THESIS
3
2001

LIBRARY
Michigan State
University

This is to certify that the

dissertation entitled

Electronic Structure of Narrow Gap Semiconductors:

Understanding Gap Formation and
Thermoelectric Properties

presented by

Paul Melvin Larson

has been accepted towards fulfillment
of the requirements for

Ph.D. degree in Physics

S. D. Mahanti
Major professor

Date 6/12/2001

MSU is an Affirmative Action/Equal Opportunity Institution

O-12771

PLACE IN RETURN BOX to remove this checkout from your record.
TO AVOID FINES return on or before date due.
MAY BE RECALLED with earlier due date if requested.

DATE DUE	DATE DUE	DATE DUE

6/01 c:/CIRC/DateDue.p65-p.15

ELECT
UNI

ELECTRONIC STRUCTURE OF NARROW GAP SEMICONDUCTORS: UNDERSTANDING GAP FORMATION AND THERMOELECTRIC PROPERTIES

By

Paul Melvin Larson

A DISSERTATION

Submitted to
Michigan State University
in partial fulfillment of the requirement for the degree of

DOCTOR OF PHILOSOPHY

Department of Physics & Astronomy

2001

ELEC

UN

Electr

stand stru

tool in the

ally narr

systems b

tant for th

Narrow

understand

in the sys

bands. W

gradient ap

been impl

method wi

accurate m

We have

ABSTRACT

ELECTRONIC STRUCTURE OF NARROW GAP SEMICONDUCTORS: UNDERSTANDING GAP FORMATION AND THERMOELECTRIC PROPERTIES

By

Paul Melvin Larson

Electronic band structure calculations are invaluable theoretical tools to understand structural, transport, and optical properties of materials. We have used this tool in the search for new high performance thermoelectric materials, which are usually narrow-gap semiconductors. We have studied the electronic structures of these systems both to understand which properties of the band structure are most important for thermoelectric properties and the nature of the gap formation.

Narrow-gap semiconductors lie between metals and wide-gap semiconductors, so understanding the nature of the gap formation is very important. The small band gaps in the systems we have studied generally arise from hybridization between different bands. We have used the local density approximation (LDA) and the generalized gradient approximation (GGA) within density functional theory (DFT). These have been implemented using the full-potential linearized augmented planewave (FLAPW) method within the WIEN97 package. This state-of-the-art method is among the most accurate methods for calculating the electronic structure of solids.

We have studied four classes of compounds. These include the half-Heusler com-

pounds. th
plex chal

The ter
show prom
starting w
Adding th
the Ferm
highly an
in the bes
ternary Zn
band gaps
usually fo
that the p
which in r

The he
genides, in
ture. Th
effects ar
We also
and highly
gap, ideal
chalcogen
in electr
similar to

pounds, the ternary Zintl-phase compounds, the simple chalcogenides, and the complex chalcogenides.

The ternary half-Heusler compounds, considered having a stuffed NaCl structure, show promising thermoelectric properties. The band gap formation is understood by starting with the semi-metallic binary NaCl compounds from which they are formed. Adding the transition (or noble) metal atom causes a strong *p*-*d* hybridization near the Fermi energy which opens up the band gap. This hybridization also leads to highly anisotropic effective masses at the conduction band minimum which are found in the best thermoelectric materials. Similar band gap formation is found in the ternary Zintl-phase compounds which are considered a stuffed Th_3P_4 structure. The band gaps in these ternary compounds are larger than experiment, unlike what one usually finds in LDA/GGA calculations. We explain this discrepancy by the noting that the position of the *d*-levels are too high in energy in LDA/GGA calculations which increases the hybridization near the Fermi energy and gives a larger gap.

The best known thermoelectric materials belong to the class of simple chalcogenides, including Bi_2Te_3 for room temperature (300 K) and PbTe for high temperature (700 K) applications. In contrast to the previous materials, here the relativistic effects are important and the band gaps are found to agree very well with experiment. We also find that the band structure of these materials show large band degeneracy and highly anisotropic effective masses at the band extrema as well as a narrow band gap, ideal for good thermoelectrics. We have searched for these properties in complex chalcogenides $BaBiTe_3$, $CsBi_4Te_6$, and $K_2Bi_8Se_{13}$. We have found that the best thermoelectric of these three, $CsBi_4Te_6$, has the highest anisotropic effective mass ratio, similar to what we had found for Bi_2Te_3.

DEIDICATION

To my parents

ACKNOWLEDGMENTS

I would like to acknowledge the immeasurable support from my advisor, Professor S.D. Mahanti. I would also like to acknowledge Professor Mercouri G. Kanatzidis in Chemistry and Dr. Tim Hogan in Engineering for collaborations on the thermoelectricity project. Especially helpful have been Dr. Duck-Young Chung and Dr. Sandrine Sportouch. I would like to acknowledge the collaborations with the photoemission experimentalists Dr. Rong Liu, Viktoria Greanya, and Wayne C. Tonjes.

I would finally like to acknowledge funding from DARPA Grant No. DAAG55-97-0184.

LIST

LIST

LIST

CHAP
INTR

CHAP
THER

CHAP
FIRST

TABLE OF CONTENTS

LIST OF TABLES....................xi

LIST OF FIGURES....................xiii

LIST OF SYMBOLS OR ABBREVIATIONS....................xxi

CHAPTER 1.
INTRODUCTION....................1

CHAPTER 2.
THERMOELECTRICITY....................4

- 2.1. GENERAL PRINCIPLES....................4
- 2.2. MAXIMIZING COP AND EFFICIENCY....................11
- 2.3. ZT FROM BOLTZMANN TRANSPORT EQUATIONS....................14
- 2.4. GUIDANCE FOR BAND STRUCTURE....................17

CHAPTER 3.
FIRST-PRINCIPLES *AB INITIO* ELECTRONIC STRUCTURE CALCULATIONS....................22

- 3.1. SOLVING THE DIRAC EQUATION....................23
  - 3.1.1. FULLY-RELATIVISTIC ONE-PARTICLE EQUATIONS....................23
  - 3.1.2. SCALAR RELATIVISTIC APPROXIMATION....................24
- 3.2. DENSITY FUNCTIONAL THEORY (DFT)....................27
  - 3.2.1. DERIVATION OF KOHN-SHAM (KS) EQUATIONS....................27

CHA
HAL

3.2.2. PHYSICAL PROPERTIES OF DFT CALCULATIONS 32

3.3. METHODS OF CALCULATION (DFT)........................... 33

3.3.1. PLANEWAVES AND ATOMIC ORBITALS............ 34

3.3.2. LINEARIZED MUFFIN TIN ORBITAL METHOD WITHIN THE ATOMIC SPHERE APPROXIMATION (LMTO-ASA)........................ 35

3.3.3. FULL-POTENTIAL LINEARIZED AUGMENTED PLANEWAVE METHOD (FLAPW)) 38

3.4. OTHER METHODS OF CALCULATION (NON-DFT)... 40

3.4.1. HARTREE-FOCK (HF) METHOD........................... 40

3.4.2. GW METHOD... 41

CHAPTER 4. HALF-HEUSLER COMPOUNDS.. 44

4.1 GAP FORMATION AND ELEMENTAL REPLACEMENTS.. 46

4.1.1. GAP FORMATION IN YNiSb AND ZrNiSn 46

4.1.2. ELEMENTAL REPLACEMENTS: CHANGING THE PNICTIDES.. 55

4.1.3. ELEMENTAL REPLACEMENTS: CHANGING THE TRANSITION METAL................................. 57

4.1.4. ELEMENTAL REPLACEMENTS: ROLE OF FILLED, UNFILLED AND PARTIALLY-FILLED *f*-LEVELS... 59

4.1.5. ELEMENTAL REPLACEMENTS OF Ni^0 WITH $Au^{1+}/Ag^{1+}/Cu^{1+}$... 64

4.1.6. ELEMENTAL REPLACEMENTS OF Ni^0 WITH Co^{1-}/Rh^{1-} 67

4.1.7. ELEMENTAL REPLACEMENTS OF Ni^0 WITH Fe^{2-}/Ru^{2-} 69

4.1.8 ELEMENTAL REPLACEMENTS OF Ni^0 WITH Mn^{3-} 70

4.2. STRUCTURAL STABILITY OF HALF-HEUSLER COMPOUNDS 72

4.2.1. TOTAL ENERGY OF THE TERNARY SYSTEMS IN DIFFERENT CONFIGURATIONS....................72

4.2.2. ANALYSIS OF THE STABILITY OF THE TERNARY COMPOUNDS BASED ON STABILITY OF BINARY PAIRS....................82

4.2.3. ENERGETICS OF ANTI-SITE DEFECTS....................87

4.3. THERMOELECTRIC PROPERTIES OF HALF-HEUSLER COMPOUNDS 94

CHAPTER 5.
TERNARY ZINTL PHASE COMPOUNDS....................99

5.1. CRYSTAL STRUCTURE AND ZINTL CONCEPT........100

5.2. ELECTRONIC STRUCTURE OF ZINTL PHASE (STUFFED Th_3P_4) COMPOUNDS............103

5.2.1. GAP FORMATION AND ROLE OF *d*-HYBRIDIZATION....................103

5.2.2. COMPARISON OF Zr_3Ni_3Sb WITH HALF-HEUSLER COMPOUND ZrNiSn.....104

CHA

SIMP

5.2.3. UNUSUAL DISCREPANCY BETWEEN THE BAND GAPS FROM THEORY (LDA/GGA)AND EXPERIMENT...............108

5.2.4. COMPARISON OF $Zr_3Ni_3Sb_4$ WITH $Hf_3Ni_3Sb_4$ AND $Ti_3Ni_3Sb_4$...110

CHAPTER 6.
SIMPLE CHALCOGENIDES...114

6.1. PbS, PbSe, PbTe...114

6.1.1. BAND STRUCTURES OF PbS, PbSe, AND PbTe 114

6.2.2. THERMOELECTRIC PROPERTIES OF LEAD SALTS...122

6.2. Bi_2Te_3, Sb_2Te_3, Bi_2Se_3, AND RELATED SYSTEMS........123

6.2.1. Bi_2Te_3 CRYSTAL STRUCTURE..............................123

6.2.2. BAND STRUCTURE AND GAP FORMATION IN Bi_2Te_3...126

6.2.3. BAND STRUCTURE AND GAP FORMATION OF Bi_2Te_3 ANALOGS..................................133

A. Bi_2Se_3 AND Sb_2Te_3 133

B. Bi_2Te_2Se, Bi_2Te_2S, Bi_2Se_2Te AND Sb_2Se_2Te 136

C. Bi_2S_3 140

6.2.4. EFFECTIVE MASSES OF THE BAND EXTREMA OF Bi_2Te_3................................143

6.2.5. COMPARISON OF THE BAND STRUCTURE WITH PHOTOEMISSION EXPERIMENTS...........148

CHA
COM

CHAPT
CONCL

BIBL

CHAPTER 7.

COMPLEX CHALCOGENIDES....164

7.1. $BaBiTe_3$....165

7.1.1. GENERAL FEATURES OF THE BAND STRUCTURE OF $BaBiTe_3$....165

7.1.2. EFFECTIVE MASSES AND THERMOELECTRIC PROPERTIES OF $BaBiTe_3$....172

7.2. $CsBi_4Te_6$....175

7.2.1. CRYSTAL STRUCTURE AND OBSERVED PROPERTIES....175

7.2.2. GENERAL FEATURES OF THE BAND STRUCTURE AND GAP FORMATION OF $CsBi_4Te_6$....179

7.2.3. EFFECTIVE MASSES AND THERMOELECTRIC PROPERTIES OF $CsBi_4Te_6$....181

7.3. $K_2Bi_8Se_{13}$....187

7.3.1. α-$K_2Bi_8Se_{13}$....188

7.3.2. β-$K_2Bi_8Se_{13}$....193

CHAPTER 8

CONCLUSIONS....201

BIBILIOGRAPHY....206

Table I
Table II
Table II
Table I
Table V
Table VI
Table VI
Table VI
Table IX
Table X

LIST OF TABLES

Table I. 8-Electron Rule of Elemental Covalent Crystals[64] 46

Table II. Experimental and calculated equilibrium lattice parameters and total-energy differences for half-Heusler systems (GGA) 76

Table III. Muffin-tin radii of half-Heusler systems 80

Table IV. Total-energy differences for NiZrSn and different binary systems with fixed lattice parameters calculated using the pseudopotential LDA [Ogut and Rabe[59]] and using LAPW within LDA and GGA 83

Table V. Relaxed equilibrium lattice parameters and total-energy differences for NiZrSn and different binary subsystems calculated using LAPW within LDA and GGA 85

Table VI. Energetics of site-switching on NaCl substructure of NiZrSn supercell (GGA) 89

Table VII. Energetics of site-switching on Ni sublattice of NiZrSn supercell (GGA) 92

Table VIII. Calculated reciprocal effective masses of $Zr_3Ni_3Sb_4$, $Hf_3Ni_3Sb_4$, and $Zr_3Pt_3Sb_4$ 113

Table IX. Experimental energy gaps for PbS, PbSe, and PbTe as a function of T (For experimental references, see Dalven[101]) 116

Table X. Comparison of calculated components of the reciprocal effective mass tensor with experiment[122] ($\alpha_l = [m_l/m_e]^{-1}$ and $\alpha_t = [m_t/m_e]^{-1}$) 123

Table

Table

Table

Table

Table

Table

Table XI. Lattice constants in atomic units (a.u.) and u and v parameters for Bi_2Te_3 analogs in the combined representation of the unit cell with hexagonal lattice constants and rhombohedral atomic coordinates used in these calculations (Bi at $\pm(u, u, u)$, Te1 at $\pm(v, v, v)$, and Te2 at (0, 0, 0) in Bi_2Te_3. For details see Wyckoff[63]).....134

Table XII. Theoretical and experimental values of the effective mass tensor parameters associated with the conduction band minima and valence band maxima for Bi_2Te_3..................146

Table XIII. Comparison of the photoemission and calculated DOS peaks for (a) Bi_2Te_3 (b) Bi_2Te_2Se, (c) Bi_2Se_3, and (d) Bi_2S_3. For a, b, and c the theoretical reference energies are chosen such that the highest valence band peak positions coincided with experiment.[149] For d, the theoretical reference energies are chosen so that the top two theoretical bands lie equidistant from the highest experimental peak..........160

Table XIV. Theoretical values of inverse effective mass parameters associated with the conduction and valence band extrema of $BaBiTe_3$ 174

Table XV. Effective mass associated with the valence and conduction band extrema along three principapl axes and the angles these axes make with a set of three suitably chosen orthogonal axes (see text) 183

Table XVI. Components of the reciporal effective mass tensor for α-$K_2Bi_8Se_{13}$..192

LIST OF FIGURES

Figure 1. Schematic of a two-leg thermoelectric device. Current travels from the right to the left, up through the n-type leg and down the p-type leg to produce cooling on the upper surface[1]........5

Figure 2. Reduced coefficient of performance η_{max}/η_{Carnot} ($\equiv \phi_r$) for various values of ZT[17]........9

Figure 3. Reduced efficiency $\varepsilon_{max}/\varepsilon_{Carnot}$ ($\equiv \eta_r$) for various values of ZT[17]........10

Figure 4. Plot of S, σ, κ, and ZT for an idealized semiconductor as a function of carrier concentration, n. S decreases with n while σ and κ increase. The maximum ZT occurs near $n = 10^{19}/cm^3$[2]........13

Figure 5. Plot of ZT vs. B parameter (Equation 23)[24]........16

Figure 6. Conduction and valence bands of HgTe (left) and CdTe (right). Upon alloying ($Cd_{1-x}Hg_xTe$) the bands cross[18]........18

Figure 7. Semiconducting gap opening due to p-d hybridization........19

Figure 8. Off-axis gap formation due to spin-orbit hybridization........20

Figure 9. Overlapping atomic spheres surround each atom of a crystal in the ASA[50]........35

Figure 10. Partitioning of the unit cell into atomic spheres (I) and an interstitial region (II)[53]........38

Figure 11. Comparison of characteristic direct and indirect LDA, GW, and experimental energy gaps for all semiconductors for which GW calculations have been reported (For references see Aulbur[31])........43

Figur

Figur

Figur

Figur

Figur

Figure

Figure

Figure

Figure

Figure

Figure

Figure 12. Two different perspectives of the cubic half-Heusler structure (YNiSb) Left: Ni atoms inserted in a YSb NaCl-type lattice. Right: Y atoms inserted in a NiSb ZnS-type lattice.........45

Figure 13. FCC Brillouin zone.........45

Figure 14. Comparisons of the Ni *d* orbital characters in YNiSb and YNi_2Sb. The size of the circles is proportional to the orbital character.........48

Figure 15. Electronic structure of ZrNiSn and YNiSb.........49

Figure 16. Comparison of the different orbital characters of ZrSn (a) Sn *p* and (b) Zr *d*, and YSb (c) Sb *p* and (d) Y *d*. The size of the circles is proportional to the orbital character.........51

Figure 17. Comparison of the different orbital characters of ZrNiSn (a) Sn *p*, (b) Zr *d*, and (c) Ni *d*, and YNiSb (d) Sb *p*, (e) Y *d*, and (f) Ni d. The size of the circles is proportional to the orbital character.........53

Figure 18. The electronic structures of ZrHeSn and ZrNiSn using the same lattice parameter.........54

Figure 19. Comparison of the electronic structures of YNiAs, YNiSb, and YNiBi. The size of the circles is proportional to the pnictide *s* orbital character.........56

Figure 20. Comparison of the electronic structures of YNiSb, YPdSb, and YPtSb. The size of the circles is proportional to the metal *s* orbital character.........58

Figure 21. Electronic structures of (a) YNiSb, (b) FCC LaNiSb, (c) LuNiSb, and (d) hexagonal LaNiSb. The Ni *d* bands and La and Lu *f* bands are shown.........60

Figure 22. Electronic structures of YbSb (a) without and (b) with SOI. The corresponding DOS (c) without and (d) with SOI are also given.........61

Figur

Figur

Figur

Figur

Figur

Figur

Figur

Figu

Figu

Fig

Fig

Fig

Figure 23. Electronic structures of YbNiSb (a) without and (b) with SOI. The corresponding DOS (c) without and (d) with SOI are also given....63

Figure 24. Electronic structures of semimetallic MgCuBi and MgAgAs....65

Figure 25. Electronic structures of LuAuSn and LuNiSb. The Ni *d* bands lie closer to E_F than the Au *d* bands. The size of the circles is proportional to the orbital character....66

Figure 26. Electronic structures of TiCoSb and TiNiSn. The Co *d* bands lie closer to E_F than the Ni *d* bands. The size of the circles is proportional to the orbital character....68

Figure 27. Electronic structures of TiRhSb....69

Figure 28. Electronic structures of NbFeSb and YNiSb. Note the difference in curvature near the X point in the LCB....70

Figure 29. Calculated DOS of half-metallic MnNiSb for (a) up and (b) down spin states....71

Figure 30. Half-Heusler crystal structure (a) XYZ, (b) ZYX, and (c) YXZ....74

Figure 31. Total energies as a function of lattice parameter for the three different configurations of NiTiSn (the lowest energy is set to zero)....75

Figure 32. Total energies as a function of lattice parameter for the three different configurations of NiZrSn (the lowest energy is set to zero)....75

Figure 33. The electronic structures of (a) XYZ, (b) ZYX, and (c) YXZ configurations of NiTiSn....77

Figure 34. The electronic structures of (a) XYZ, (b) ZYX, and (c) YXZ configurations of NiZrSn....78

Figur

Figur

Figure

Figure

Figure

Figure

Figur

Figur

Figu

Fig

Fig

Fig

Fig

Figure 35. The electronic structures of (a) XYZ, (b) ZYX, and (c) YXZ configurations of NiZrSn. The size of the circles overlying band structure is directly proportional to the strengths of the Ni *d* orbital character..81
Figure 36. Crystal structures of (NiMP)$_4$ supercell for (a) $Ni_4(Zr_3Sn)(Sn_3Zr)$, (b) $(Ni_3Sn)Zr_4(Sn_3Ni)$, and (c)$(Ni_3Zr)(Zr_3Ni)Sn_4$..88

Figure 37. Electronic structures of (a) $Ni_4Zr_4Sn_4$, (b) $Ni_4(Zr_3Sn)(Sn_3Zr)$, (c) $(Ni_3Sn)Zr_4(Sn_3Ni)$, and (d)$(Ni_3Zr)(Zr_3Ni)Sn_4$..90

Figure 38. Crystal structures of (NiMP)$_4$ for rearrangements of the Ni lattice..91

Figure 39. Electronic structures of (a) $Ni_4Zr_4Sn_4$ - 38a, (b) $Ni_4Zr_4Sn_4$ - 38b, and (b) $Ni_4Zr_4Sn_4$ - 38c..93

Figure 40. Electronic structures of ThRhSb. Note the off-axis LCB..97

Figure 41. Electronic structures of ThNiSn. Note the LCB at a general point..98

Figure 42. (a) Crystal structure of Y_3Sb_4 and (b) $Y_3Ni_3Sb_4$...............101

Figure 43. BCC Brillouin zone. 101

Figure 44. The (a) Zr *d* and (b) Sb *p* orbital characters of Zr_3Sb_4..105

Figure 45. The (a) Zr *d*, (b) Sb *p*, and (c) Ni *d* orbital characters of $Zr_3Ni_3Sb_4$..107

Figure 46. Electronic structures of (a) $Zr_3Ni_3Sb_4$, (b) $Hf_3Ni_3Sb_4$, and (c) $Zr_3Pt_3Sb_4$..111

Figure 47. Electronic structures of (a) PbS, (b) PbSe, and PbTe, using the experimental lattice parameters (corresponding to 4 K)......117

Figur

Figur

Figur

Figur

Figur

Figu

Fig

Fig

Fig

F

F

F

F

F

Figure 48. Total energy of PbS as a function of lattice parameter (in a.u.) obtained in GGA. The points were plotted using the computer program KALEIDAGRAPH.[120] The experimental value is given by the arrow..120

Figure 49. Electronic structures of (a) PbS, (b) PbSe, and PbTe, using the relaxed lattice parameters...121

Figure 50. Crystal structure of Bi_2Te_3 along the XZ plane showing the quintuple layer leaves of Te-Bi-Te-Bi-Te separated by a Van der Waals gap..124

Figure 51. (a) Rhombohedral and (b) hexagonal representations of the unit cell of Bi_2Te_3. In (b) the Te atoms are open circles and the Bi atoms are shaded circles...125

Figure 52. Brillouin zone of Bi_2Te_3 (corresponding to the rhombohedral unit cellthe Bi atoms are shaded circles...............125

Figure 53. Band structure of Bi_2Te_3 without SOI................................128

Figure 54. Band structure of Bi_2Te_3 with SOI.....................................128

Figure 55. Band structure of Bi_2Te_3 with SOI. Included are (a) total band structure and the orbital characters of the bands: (b) Bi *p*, (c) Tel *p*, and (d) Te2 *p*. The size of the circles overlying band structure is directly proportional to the strengths of the orbital character...131

Figure 56. Total and partial DOS for Bi_2Te_3 with SOI. Included are (a) total DOS partial DOS: (b) Bi *p*, (c) Tel *p*, and (d) Te2 *p*..132

Figure 57. Band structure of Bi_2Se_3 (a) without and (b) with SOI.......135

Figure 58. Band structure of Sb_2Te_3 (a) without and (b) with SOI......136

Figure 59. Band structures of Bi_2Te_2Se (a) without and (b) with SOI and Bi_2Te_2S (c) without and (d) with SOI................................137

Figure 60. Band structure of Sb_2Te_2Se (a) without and (b) with SOI..139

Figure 61. Band structures of Bi_2Se_2Te (a) without and (b) with SOI and Sb_2Se_2Te (c) without and (d) with SOI..............................140

Figu

Figur

Figur

Figur

Figur

Figur

Figu

Fig

Fig

Figure 62. (a) Orthorhombic unit cell of Bi_2S_3 (shown in the a-b plane) and its (b) corresponding Brillouin zone...141

Figure 63. Band structure of Bi_2S_3 (a) without and (b) with SOI...........142
Figure 64. Fitting of the energy band near the conduction band minimum to a parabola for Bi_2Te_3 using the computer program KALEIDAGRAPH[120]..145

Figure 65. Positions of the electron and hole pockets lying on the reflection plane of the Brillouin zone for Bi_2Te_3 for (a) CBM and (b) VBM..147

Figure 66. Valence band photoemission (UPS) and conduction band inverse photoemission (IPES) for Bi_2S_3, Bi_2Se_3, Bi_2Te_2Se, and Bi_2Te_3 crystals. UPS and IPES spectra for each crystal are connected at E_F. Energies are referred to E_F. (courtesy of Yoshifumi Ueda).[149].....151

Figure 67. Total DOS for (a) Bi_2S_3, (b) Bi_2Se_3, (c) Bi_2Te_2Se, and (d) Bi_2Te_3. The arrows indicate the positions of the photoemission peaks in the work by Ueda *et al.*[149]..152

Figure 68. Photoemission spectra for Bi_2Te_3 by Greanya *et al.* Peaks *1-6* are indicated by arrows. For the purpose of comparison, the energy reference (zero of energy) was set such that the lowest binding energy peak in the spectra coincides with the position of the corresponding peak in the data of the previous UPS experiment by Ueda *et al.*[149].........156

Figure 69. Photoemission spectra for Bi_2Se_3 by Greanya *et al.*[139] Peaks *1-9* are indicated by arrows. For the purpose of comparison, the energy reference (zero of energy) was set such that the lowest binding energy peak in the spectra coincides with the position of the corresponding peak in the data of the previous UPS experiment by Ueda *et al.*[149]..........157

Figure 70. Total DOS for (a) Bi_2Te_3 and (b) Bi_2Se_3Se. The arrows indicate the positions of the photoemission peaks seen by Greanya *et al.*[139] For the purpose of comparison, the energy reference (zero of energy) was set such that the lowest binding energy peak in the spectra coincides with the position of the corresponding peak in the data of the previous UPS experiment by Ueda *et al.*[149]............................158

Figure 71. Projection of the crystal structures in the yz plane of (a) orthorhombic $BaBiTe_3$ and (b) rhombohedral Bi_2Te_3. The Bi/Te blocks are highlighted in the shaded area for $BaBiTe_3$......167

Figure 72. Brillouin zone of $BaBiTe_3$ 167

Figure 73. Infrared absorption spectra of Bi_2Te_3 and $BaBiTe_3$. The semiconductor gaps are indicated in the spectra.................168

Figure 74. Band structure of $BaBiTe_3$ without SOI.............................170

Figure 75. Band structure of $BaBiTe_3$ with SOI..................................170

Figure 76. Monoclinic crystal structure of $CsBi_4Te_6$............................176

Figure 77. (a)Triclinic crystal structure and (b) Brillouin zone of $CsBi_4Te_6$ used in this calculation..177

Figure 78. Comparison of ZT for the best current doping of $CsBi_4Te_6$ and optimally-doped $Bi_{2-x}Sb_xTe_3$ alloy. The peak for $CsBi_4Te_6$ (ZT~0.8) occurs at 225 Kelvin..178

Figure 79. Band structure of $CsBi_4Te_6$ (a) without and (b) with SOI...180

Figure 80. Quasi-two dimensional sheets contributing to the hole transport overlying the crystal structure of $CsBi_4Te_6$..................186

Figure 81. Projection of the crystal structure of α-$K_2Bi_8Se_{13}$ viewed down the b-axis. Bi_2Te_3-, CdI_2-, and Sb_2Se_3-type building blocks in the structure are highlighted by the shaded areas.........189

Figure 82. Brillouin zone of α-$K_2Bi_8Se_{13}$...190

Figure 83. Band structure of α-$K_2Bi_8Se_{13}$ (a) without and (b) with SOI...191

Figure 84. Crystal structure of β-$K_2Bi_8Se_{13}$..194

Figure 85. Brillouin zone of β-$K_2Bi_8Se_{13}$...195

Figure 86. Band structure of β-$K_2Bi_8Se_{13}$ - Configuration1 (a) without and (b) with SOI..196

Figure 87. Orbital characters of (a) Bi8 and (b) Se10 overlying the band structure of β-$K_2Bi_8Se_{13}$ - Configuration1 with SOI. The size of the circles overlying the band structure is directly proportional to the strength of the orbital character.........197

Figure 88. Band structure of β-$K_2Bi_8Se_{13}$ - Configuration2 (a) without and (b) with SOI..198

Figure 89. Band structure of β-$K_2Bi_8Se_{13}$ - Configuration3 (a) without and (b) with SOI..199

a_t =

κ =

τ =

μ =

σ =

Δ =

a.u. =

A =

ASA

BCC

BZ =

c =

E =

e =

eV

E =

G

I =

J

k

LIST OF SYMBOLS OR ABBREVIATIONS

$\alpha_i = [m_i/m_e]^{-1}$ = Reciprocal effective mass associated with m_i
$\alpha_{ij} = [m/m_e]_{ij}^{-1}$ = Effective inverse mass tensor
γ = Band degeneracy factor
κ = Thermal conductivity
ε = Energy or efficiency
η = Coefficient of performance
κ_{ph} = Phonon thermal conductivity
μ = Chemical potential
ρ = Electrical resistivity
σ = Electrical conductivity
Δ_{xc} = LDA/GGA band gap correction
a.u. = Atomic unit (0.529177 Å)
A = Electron affinity
ARPES = Angle resolved photoemission spectroscopy
ASA = Atomic sphere approximation
BCC = Base centered cubic
BZ = Brillouin zone
c = Speed of light
CBM = Conduction band minimum
COP = Coefficient of performance
$\mathbf{E}$ = Electric field
e = Electron charge
eV = Electron-volts
DFT = Density functional theory
DOS = Density of states
E = Energy
E_F = Fermi energy
E_{gap} = Band gap
FCC = Face centered cubic
FLAPW = Full-potential linearized augmented planewave
$\mathbf{G}$ = Reciprocal lattice vector
GGA = Generalized gradient approximation
$\hbar$ = Planck's constant/2π
HF = Hartree-Fock
HVB = Highest valence band
I = Ionization energy
$\mathbf{J}$ = Electric current
$\mathbf{k}$ = momentum vector
k_B = Boltzmann constant

K = Thermal conductance or Kelvin degrees
$\mathbf{K} = \mathbf{k} + \mathbf{G}$
KS = Kohn-Sham
LAPW = Linearized augmented planewave
LCB = Lowest conduction band
LDA = Local density approximation
LMTO = Linearized muffin-tin orbital
m_e = Bare electron mass
m_i = Band effective mass in direction i
MTR = Muffin-tin radius
OR = Ogut & Rabe
P = Power
PES = Photoemission spectroscopy
$\mathbf{Q}$ = Thermal current
$q_{Peltier}$ = Peltier heat
R = Electrical resistance
S = Seebeck coefficient
T = Temperature
TB = Tight-binding
TDOS = Total density of states
SOI = Spin-orbit interaction
UPS = Ultraviolet photoemission spectroscopy
VBM = Valence band maximum
XC = Exchange-correlation
XPS = X-ray photoemission spectroscopy
ZT = $S^2\sigma T/\kappa$ = Thermoelectric figure of merit

Techn

materials

pr

parts, pr

in any s

and as

in a w

than

As w

ZT giv

where

also

are fou

large S

Finding

several

of ZT w

CHAPTER 1

INTRODUCTION

Technological needs have fueled a search for new thermoelectric materials. These materials, which can be used in either solid state refrigeration or power generation, produce a temperature gradient from an applied electric current or, conversely, an electric current from an applied temperature difference. These devices have no moving parts, produce no waste products to be released into the environment, and are scalable to any size needed. They have been used as power generation in deep space probes and as cooling units in portable refrigerators. The problem of using these materials on a wider scale is that their coefficient of performance (or efficiency) is much lower than current technologies.[1, 2, 3]

As will be discussed in detail in the next chapter, the coefficient of performance (or efficiency) of a thermoelectric device is determined by the dimensionless quantity ZT given by

$$\mathrm{ZT} = \mathrm{S}^2\sigma\mathrm{T}/\kappa, \tag{1}$$

where S is the Seebeck coefficient, σ is the electrical conductivity, T is the average absolute temperature, and κ is the thermal conductivity. The highest values of ZT are found to be about 1 and are seen in doped narrow-gap semiconductors having a large Seebeck coefficient and electrical conductivity but a low thermal conductivity. Finding a material with ZT $\approx$ 3 would make thermoelectric devices competitive with several existing technologies for cooling and power generation, but any improvement of ZT would lead to immediate applications.[1, 2, 3]

The search for new thermoelectric materials requires both experimental (synthesis and measurement) and theoretical studies, especially electronic structure calculations.[4] Thermoelectric properties depend on subtle features of the electronic structure near the Fermi energy (E_F), so electronic structure calculations provide a method to predict and understand new thermoelectric materials. The optimum materials usually have band gaps on the order of $10k_BT$ (where T is the operating temperature), degenerate bands near E_F, and anisotropic transport of the doped system.[1, 2, 3, 4]

In this dissertation, we will discuss the band structure of four general classes of narrow-gap semiconductors to understand both the formation of their semiconducting gaps and their thermoelectric properties. These materials are synthesized based on the guiding principle of combining simple structures, such as cubic or rhombohedral, to form more complex structures with a more glass-like thermal conductivity and yet maintaining the high electrical conductivity of a simple crystal[5] (electron crystal/phonon glass[6]). The first of these classes of materials is the half-Heusler compounds formed by stuffing transition metal ions into the pockets of a NaCl lattice.[7, 8, 9] This class provides numerous elemental replacements of individual atoms which can affect the electronic structure. The half-Heusler compounds are closely related to the next class, the ternary Zintl phase compounds, where Ni atoms are stuffed in a more complex Th_3P_4 lattice in order to produce lower values of κ.[10] The third class consists of the simple chalcogenides, the best known bulk thermoelectric materials for almost 40 years, including PbTe at high temperatures and Bi_2Te_3 at room temperature.[11, 12] The final class consists of complex structures formed from combinations of units with the crystal structure of the cubic PbTe and the rhombohedral Bi_2Te_3, such as $BaBiTe_3$[11, 13], $CsBi_4Te_6$[14, 15], and $K_2Bi_8Se_{13}$[16].

Understanding the electronic structure of these materials gives us an insight into which features of the electronic structure, such as band degeneracies, size of band gap, and anisotropic effective masses, are most important for high values of ZT. We hope to show that electronic structure calculations provide an invaluable theoretical tool to understand the properties of thermoelectric materials.

CHAPTER 2.

THERMOELECTRICITY

2.1. GENERAL PRINCIPLES

Thermoelectricity is a transport property which relates the thermal gradient to the electrical current in a material. Thermoelectric devices can be used either to transform an induced electric current into a temperature gradient in a material, used for refrigeration, or transform an induced temperature gradient into an electric current, used for power generation.[1, 2, 3, 4]

Figure 1 shows a schematic of a two-leg thermoelectric device which can be used for heating or cooling. The device consists of an n-doped sample, where the carriers are electrons, and a p-doped sample, where the carriers are holes. As the current enters the device from the right, the slightly more energetic electrons (for a typical doping, $10^{19}/\mathrm{cm}^3$, $E\sim 0.1$ eV) travel against the current, thereby heating the bottom of the device and leaving the top cooler. As the current goes down the left leg, the slightly more energetic holes ($E\sim 0.1$ eV) travel in the direction of the current, again heating the bottom of the device and leaving the top cooler. An equilibrium is reached as phonons transmit the heat back through the lattice from the hot end to the cold end. A large temperature difference can be best maintained if the system has a low thermal conductivity.[17, 18]

The main disadvantage of thermoelectric devices is their low coefficient of performance (efficiency) for use in refrigeration (power generation) compared with more conventional technologies, such as Freon cooling. The best thermoelectric devices have only about 1/3 the efficiency of Freon refrigerators. Thermoelectric devices fill a make m

use in

Figu

If we c

rents depe

where J

niche market for cooling computer chips and infrared detectors as well as their largest use in automobile beverage coolers which plug into the car's cigarette lighter.[19]

Figure 1. Schematic of a two-leg thermoelectric device. Current travels from right to left, up through the n-type leg and down the p-type leg to produce cooling on the upper surface.[1]

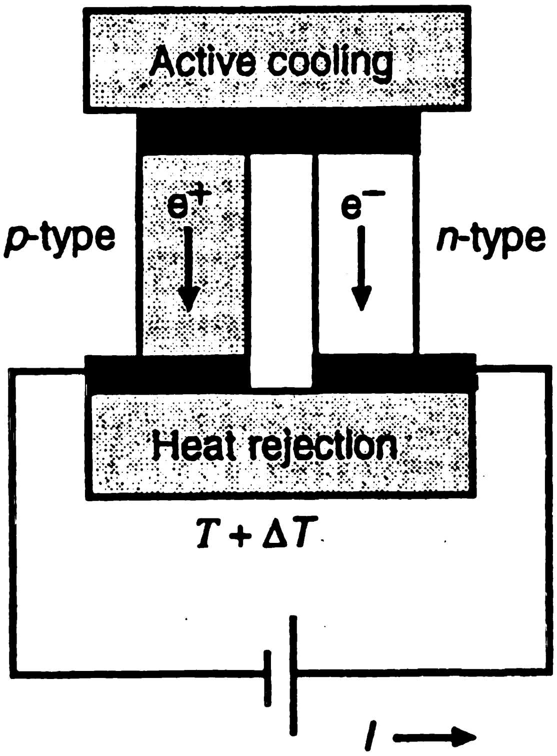

If we consider no coupling between these currents, the electrical and thermal currents depend on their sources of the electric field and thermal gradient, respectively,

(2)

$$\mathbf{J} = \sigma \mathbf{E},$$

$$\mathbf{Q} = -\kappa \nabla \mathrm{T},$$

(3)

where **J** is the electrical current, **Q** is the thermal current, **E** is the electric field,

and V
cases
other
a move
this
called
the th
the tem

The
solving
ature T
of the

The
heat.

Here R

and ∇T is the temperature gradient. In any real material, the electrical current flow causes slightly more energetic electrons to move from one end of the material to the other, producing a temperature gradient. Conversely, a temperature gradient induces a movement of electrons opposite the direction of this gradient. In order to explain this interrelation, one defines a quantity S known as the Seebeck coefficient (also called the thermoelectric coefficient or the thermopower) as a coupling term between the thermal and electrical currents produced and the sources of the electric field and the temperature gradient[17, 18, 20, 21], i.e.,

$$\mathbf{J} = \sigma[\mathbf{E} - \mathrm{S}\nabla \mathrm{T}] \tag{4}$$

$$\mathbf{Q} = (\sigma \mathrm{TS})\mathbf{E} - \kappa\nabla \mathrm{T} \tag{5}$$

The coefficient of performance can be derived for a thermoelectric material by studying the rate at which heat is removed only from the cold reservoir (at temperature T_c). This rate can be written as a sum of three terms. The first is the Peltier cooling due to the current in the material

$$q_{Peltier} = ST_cJ. \tag{6}$$

The second term is the Joule heating, written as a negative quantity since it adds heat.

$$q_{Joule} = -\tfrac{1}{2}JR^2 \tag{7}$$

Here R is the resistance rather than the resistivity ($R = (\sigma\ A/L)^{-1}$ where L is the length and A the area of the device). The third term is the heat due to thermal transport due to both electrons (or holes) and phonons which move from the hot reservoir to the cold reservoir. This is also written as negative since it adds heat to the cold resevoir.

$$q_{Thermal} = - K \triangle T \tag{8}$$

Here K is the total thermal conductance rather than the thermal conductivity ($K = \kappa$ A/L where L is the length and A the area of the device) and $\triangle T$ is the temperature difference across the device. The total heat removed from the cold reservoir is then[17]

$$q_c = q_{Peltier} + q_{Joule} + q_{Thermal} = ST_cJ - \tfrac{1}{2}JR^2 - K \triangle T. \tag{9}$$

Integrating both sides of Equation 4 , we can get a relationship for the voltage in the system.

$$V = S\triangle T + JR \tag{10}$$

The power necessary to remove q_c from the cold reservoir is the product of the voltage and the current.

$$P = VJ \quad \Rightarrow \quad (S\triangle T + JR)J \quad \Rightarrow \quad SJ\triangle T + J^2R \tag{11}$$

The coefficient of performance (COP) is defined as the ratio of the heat removed and the power necessary to remove the heat, a quantity which may be larger than 1.

$$\eta = q_c/P = (ST_cJ - \tfrac{1}{2}JR^2 - K\triangle T)/(SJ\triangle T + J^2R) \tag{12}$$

It is inconvenient for the COP to depend on the current. For given system parameters (S, κ, R), the optimum COP can be found by defining $m = JR/S$ so that

$$\eta = (mT_c - \tfrac{1}{2}m^2 - (KR\triangle T/S^2))/(m\triangle T + m^2) \tag{13}$$

Maximizing η with respect to m ($\frac{d\eta}{dm} = 0$) solves for the m which maximizes the COP in Equation 13 to obtain

$$\eta_{max} = (T_c/\ \triangle T)\ \{[\omega - (T_h/T_c)]/(\omega + 1)\}, \tag{14}$$

where the Carnot efficiency ($T_c/\ \triangle T$) is modified by the factor $\{[\omega - (T_h/T_c)]/(\omega + 1)\}$, where

$$\omega = (1 + ZT)^{\frac{1}{2}}, \tag{15}$$

the factor $ZT = S^2\sigma T/\kappa$ (defined in Chapter 1). This modifying factor approaches 1 as $\omega \rightarrow \infty$. A graph of η_{max}/η_{Carnot} ($\equiv\phi_r$) as a function of ZT for different values of the ratio T_h/T_c is shown in Figure 2 (T_h is the temperature of the hot end of the device).[17] A conventional Freon compressor refrigerator, in order to maintain an air temperature of 270 K, must have the two sides of the compressor cool from 330 K to 250 K. These refrigerators, with $T_h/T_c \doteq 1.3$, have $\eta_{max}/\ \eta_{Carnot}$ ($\equiv\phi_r$) = 0.26.[21]

Figure 2 Reduced coefficient of performance η_{max}/η_{Carnot} ($\equiv\phi_r$) for various values of ZT.[17]

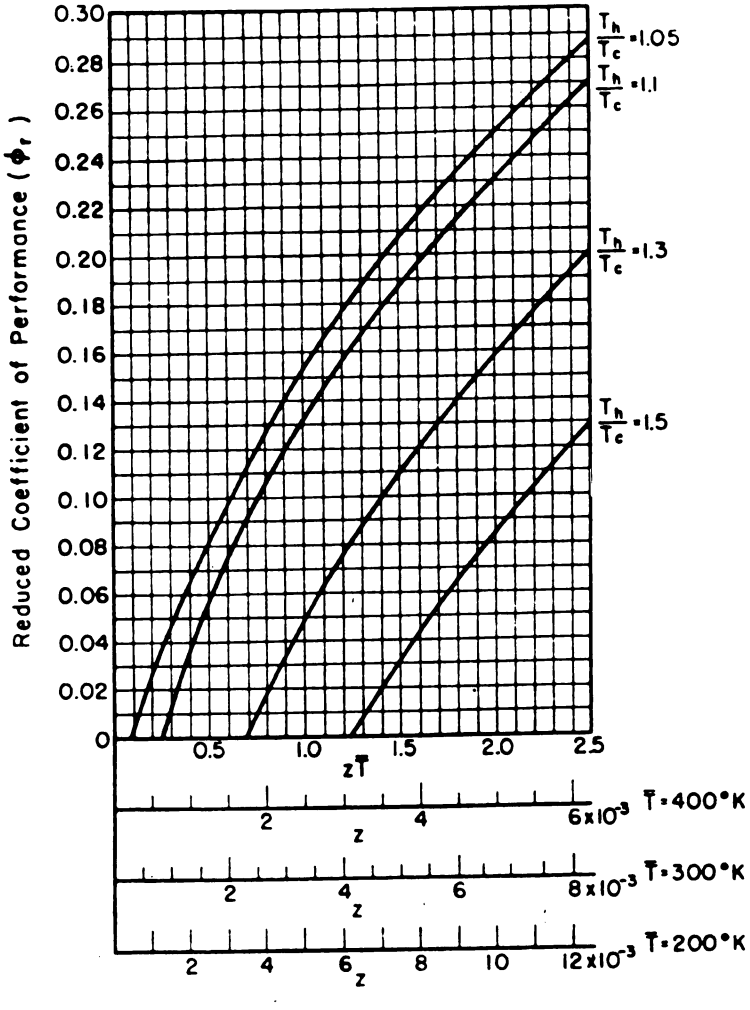

A similar derivation for the efficiency, ϵ, of a thermoelectric power generator yields

(16)

$$\epsilon_{max} = P/q_h = (\Delta T/T_h)\ \{(\omega - 1)/[\omega + (T_c/T_h)]\},$$

where P is the power output and q_h is the rate of heat observed at T_h. Again the

Carnot

approa

in Figu

a good

central

Figu

Carnot value ($\Delta T/T_h$) is modified by a factor $\{(\omega - 1)/[\omega + (T_c/T_h)]\}$. This factor approaches 1 as $\omega \to \infty$. A graph of $\epsilon_{max}/\epsilon_{Carnot}$ ($\equiv \eta_r$) as a function of ZT is shown in Figure 3.[17] The typical efficiency in a temperature range from 300 K to 900 K of a good thermoelectric device made out of PbTe is about 19% while that of a modern central power steam engine is about 40%.[21]

Figure 3 Reduced efficiency $\epsilon_{max}/\epsilon_{Carnot}$ ($\equiv \eta_r$) for various values of ZT.[17]

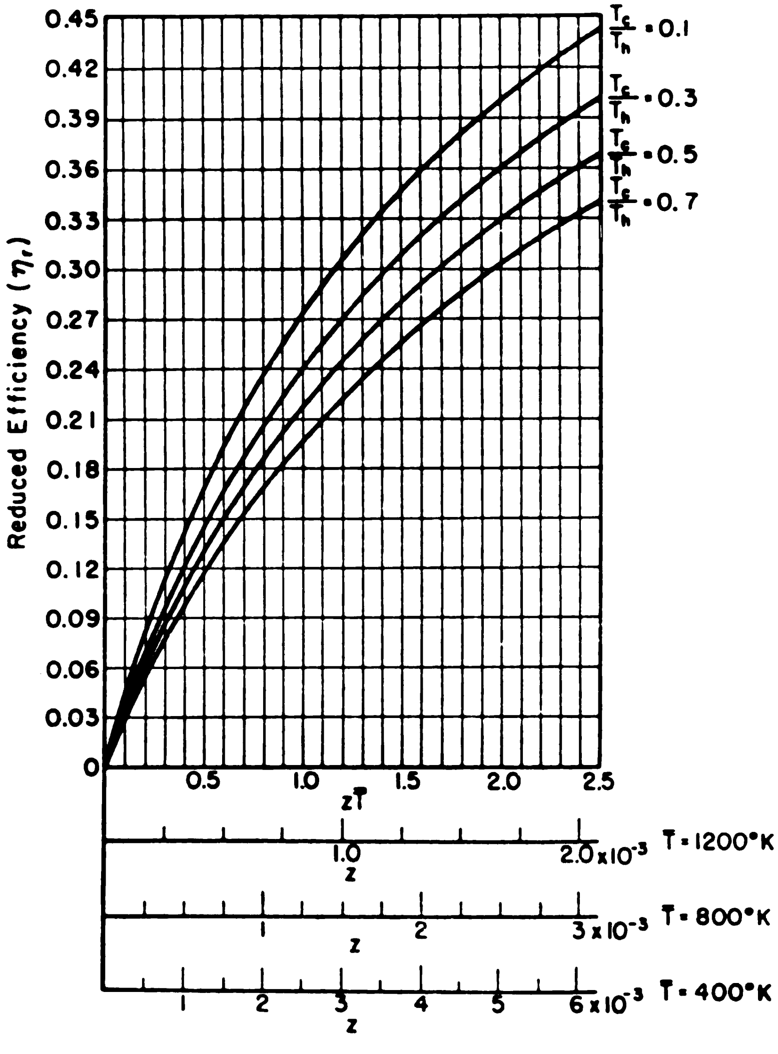

2.2 MAXIMIZING COP AND EFFICIENCY

From our previous discussions, it is is evident that to maximize the COP (efficiency) of a thermoelectric refrigerator (power generator), one must maximize the dimensionless quantity ZT, known as the thermoelectric figure of merit. The largest value of ZT found experimentally for bulk systems is on the order of 1 (for Bi_2Te_3 alloys at room temperature), but must be about equal to 3 to have a comparable COP to a conventional compressor refrigerator.[1, 2]

In order to maximize ZT at a given T, one must not only have a large Seebeck coefficient, but the electrical conductivity must be large while the thermal conductivity remains small. This is difficult since most materials with large electrical conductivities, such as metals, also have large thermal conductivities, while systems with a small thermal conductivities, such as insulators, also have small electrical conductivities.[2] One must be careful to realize that, in the case of metals, the Wiedemann-Franz law states that there is a limiting relationship between the thermal conductivity and the electrical conductivity (where k_B is the Boltzmann constant and e the electron charge)

$$\frac{\kappa}{\sigma} = \frac{\pi^2}{3} \left(\frac{k_B}{e}\right)^2 T \tag{17}$$

which means that the thermal conductivity can be reduced only so far before reducing the electrical conductivity. All of the materials which we will discuss have a larger thermal conductivity than given by this limiting relationship.[22]

To bypass the limitations of the Wiedemann-Franz law, one needs a material where the electrons travel freely as if through a crystal, to increase the electrical conductivity, but pl

Stark

them

crystals

found

The

electro

tions of

The

metall

equal

conduc

function

It can

increas

the con

(σ should be small enough so that κ is dominated by phonons instead of electrons), but phonons are scattered as if through a glass, to reduce the thermal conductivity. Slack's electron crystal/phonon glass concept[6, 23] has been central in finding new thermoelectric materials, although different groups have used different methods to achieve this goal. One tries to use systems with complex unit cells since high thermal conductivity is found for systems containing light elements, forming densely packed crystals, and formed largely through covalent bonds. Lower thermal conductivity is found for systems containing heavier elements with more ionic bonding.[20]

The best thermoelectric materials tend to be narrow-gap semiconductors. The electrical conductivity (σ) and electron thermal conductivity (κ) are increasing functions of carrier concentration (n).

$$\sigma = \mathrm{ne}\mu \tag{18}$$

$$\kappa = \sigma\frac{\pi^2}{3}\left(\frac{k_B}{\epsilon}\right)^2\mathrm{T} = \mathrm{ne}\mu\frac{\pi^2}{3}\left(\frac{k_B}{e}\right)^2\mathrm{T} \tag{19}$$

The Seebeck coefficient (S) is a more complicated function of carrier concentration (n), but increases for decreasing n and becomes very small ($\sim\frac{k_BT}{E_F}$ 80 μV/K) for metallic systems where n reaches 10^{22}/cm^3.[21] Calculations of the electrical resistivity (equal to the reciprocal of the electrical conductivity), Seebeck coefficient, thermal conductivity, and ZT are shown in Figure 4 for an idealized semiconductor as a function of carrier concentration.[2]

It can be seen that S decreases with increasing carrier concentration while σ and κ increase. A maximum for ZT = $S^2\sigma T/\kappa$ is found near 10^{18} carriers/cm^3, which is the concentration associated with doped, narrow gap semiconductors.[2]

Figure 4 Plot of ρ ($= 1/\sigma$), S, κ, and ZT for an idealized semiconductor as a function of carrier concentration, n. S decreases with n while σ and κ increase. The maximum ZT occurs near n = $10^{19}/\text{cm}^3$.[2]

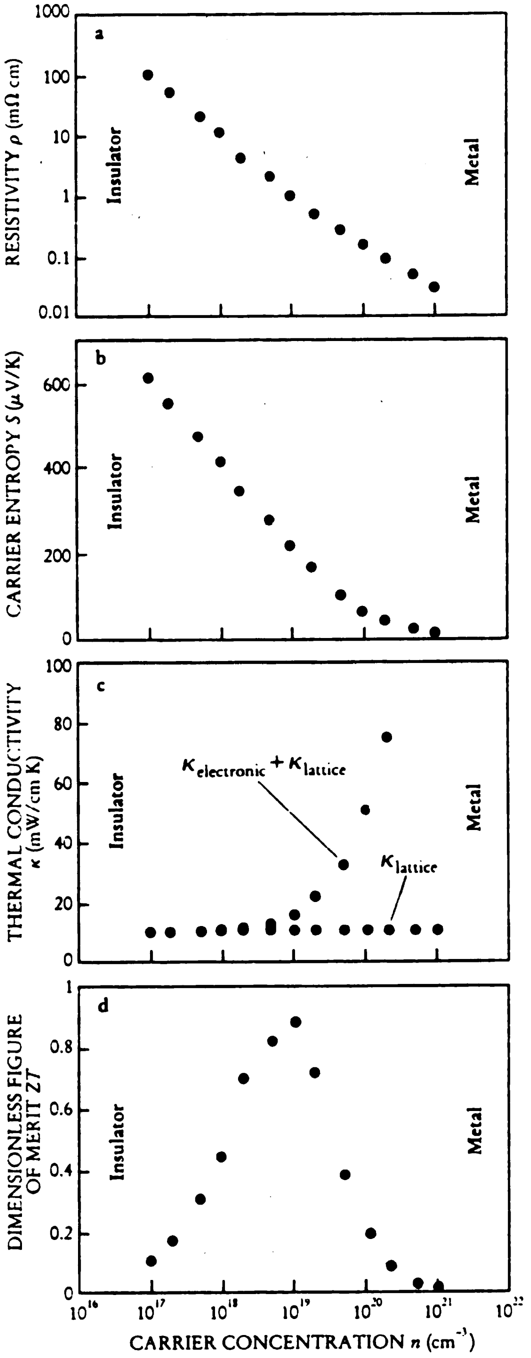

F

with

coeffi

wh

in t

a sam

sh

band

them

in N

Figure

each p

experi

Start

has a n

itself

are mea

2.3

Since

we can

For semiconductors, one must in general consider transport of both electrons, with Seebeck coefficient S_e and electrical conductivity σ_e, and holes, with Seebeck coefficient S_h and electrical conductivity σ_h. The total Seebeck coefficient is

$$S_{tot} = \frac{\sigma_e S_e + \sigma_h S_h}{\sigma_e + \sigma_h}, \tag{20}$$

where S_e is negative and S_h is positive. In order for the hole and electron transport not to cancel each other due to intrinsic electron-hole excitations, but to allow for a large enough electrical conductivity (by doping), the band gap of the material should be on the order of 10 $k_B T$.[1, 2, 3] Further, if there are a multiply-degenerate band extrema, such as when one lies at a general point in the Brillouin zone, the thermopower adds up as before for each extrema. For the same carrier concentration in N identical pockets, the carrier concentration for each pocket is lower. As seen in Figure 4, a lower carrier concentration corresponds to a larger Seebeck coefficient in each pocket which gives a larger total Seebeck coefficient. Therefore, degenerate band extrema also are expected to increase the Seebeck coefficient for a material.[11, 24]

Scattering, due to impurities, grain boundaries, etc., greatly affects σ and κ, but has a much less of an effect on S. $S = \lim_{\Delta T \to 0} \frac{\Delta V}{\Delta T}$ which makes this quantity fairly insensitive to morphology while σ and κ are very sensitive to the direction which they are measured.[21]

2.3. ZT FROM BOLTZMANN TRANSPORT EQUATION

Since S, σ, and κ, which control the ZT parameter, are transport coefficients, one can solve the Boltzmann transport equations in order to better understand their behav

func

part

of th

ZT

an

When

with

undergo

As B inc

Hicks

phonon

behavior as a function of material parameters. The details of the derivation can be found elsewhere.[24] Using the electronic dispersion relation for a single anisotropic parabolic band in the energy independent relaxation-time approximation as a function of the momentum k_i and effective masses m_i (ε_0 is an offset energy)

$$\varepsilon(k_x,\, k_y,\, k_z) = \frac{\hbar^2 k_x^2}{2m_x} + \frac{\hbar^2 k_y^2}{2m_y} + \frac{\hbar^2 k_z^2}{2m_z} + \varepsilon_0 \tag{21}$$

ZT can be written in terms of Fermi-Dirac integrals F_i, where

$$F_i = F_i(\zeta^*) = 4\pi\ (\frac{2k_BT}{h^2})^{\frac{3}{2}}(m_x m_y m_z)^{\frac{1}{2}} \int_o^{\infty} \frac{x^i dx}{e^{(x-\zeta^*)}+1} \tag{22}$$

and $\zeta^* = \zeta/k_BT$ where ζ is the chemical potential so that ZT is[24]

$$ZT = \frac{\frac{3}{2}(\frac{5F_{\frac{3}{2}}}{3F_{\frac{1}{2}}}-\zeta^*)^2 F_{\frac{1}{2}}}{\frac{1}{B}+\frac{7}{2}F_{\frac{5}{2}}-\frac{25F_{\frac{3}{2}}^2}{6F_{\frac{1}{2}}}}, \tag{23}$$

Where the quantity B appears in the denominator of Equation 23 is given by

$$B = \frac{1}{3\pi^2}\ \gamma\ (\frac{2k_BT}{\hbar^2})^{\frac{3}{2}}(m_x m_y m_z)^{\frac{1}{2}} \frac{k_B^2 T \mu_x}{e\kappa_{ph}}, \tag{24}$$

with band degeneracy γ, mobility in the direction of transport μ_x, phonon thermal conductivity κ_{ph}, and effective masses m_i (the other terms are fundamental constants). As B increases, ZT also increases, as shown in Figure 5.[24]

Hicks and Dresselhaus pointed out that to increase B, one must reduce κ_{ph}, the phonon contribution to the thermal conductivity, as expected, but also maximize the p

ba

di

F

This

to maxi

transpor

of the ba

the val

ionatel

thermo

the sho

direction

product of the effective masses multiplied by the mobility in the direction of transport (here chosen to be along x). However, the mobility is inversely proportional to the effective mass parallel to the direction of transport.[24]

$$\mu_x \propto \frac{1}{m_x} \tag{25}$$

Figure 5 Plot of ZT vs. B parameter (Equation 23).[24]

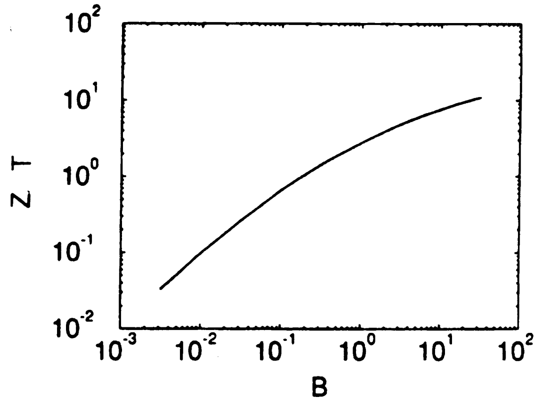

This implies that the effective mass in the direction of transport should be small to maximize the mobility, but the effective masses perpendicular to the direction of transport should be large. As already mentioned, one wants a large degeneracy (γ) of the band extrema for both the conduction and valence bands to increase S. While the value of γ has a maximum of 48 in cubic systems, this effect does not proportionately increase ZT by a factor of 48 but has a more subtle effect on increasing the thermopower.[11] Mahan and Sofo[25] have also predicted that a good thermoelectric should have a narrow distribution of carriers with a high carrier velocity in the direction of the applied field, which again can be obtained in anisotropic systems.

2.4

In

the

for

the

the

of the

also

the

also

will

In

tempera

transfers

= 1.02

through

Hybri

also with

CHF is

gap when

2.4. GUIDANCE FOR THE BAND STRUCTURE

In order to search for new materials with high ZT, electronic structure calculations cannot give us directly the transport coefficients such as thermopower or thermal and electrical conductivity. However, several properties which appear to be important for good thermoelectric materials can be discovered from electronic structure calculations. We look for systems with a semiconducting band gap on the order of $10k_BT$[1, 2, 3], degenerate band extrema[11, 24], and anisotropic effective masses at the band extrema[24]. Electronic structure calculations of the best known thermoelectric materials can be used to see if the band gaps are about $10k_BT$, to check if the high ZT arises from degenerate band extrema, to calculate the effective mass anisotropy by fitting a the calculated energies to second order polynomials, and use the information about the wavefunctions to understand the transport in these materials. Understanding how these properties lead to a large ZT in these known materials will allow for making predictions in the most promising new thermoelectric materials.

In order to find systems with band gaps on the order of $10k_BT$ (~0.25 eV for room temperature applications), we should not look for semiconductors with large charge transfers since the gaps in these systems are generally too large (i.e. $Ga^{1-}As^{1+}$: Gap = 1.52 eV[29]). Therefore, it is best to look at semiconductors whose gaps form through some sort of hybridization mechanism.

Hybridization may also be key in forming the anisotropic effective masses associated with these materials. Let us consider the band structure of $Hg_{1-x}Cd_xTe$ alloy. CdTe is a typical semiconductor while HgTe is semimetallic with an inverted band gap where the *s* level is energetically beneath the *p* level at the Γ point (Figure 6).

The m

lying b

positio

Fig

This

In system

Addition

and more

eg semi

non-disp

direction

formation

This will

The more dispersive *s* levels lie above and below E_F with less a dispersive *p* level lying between. Changing the value of x can finely tune the band gap by shifting the position of the *p* level with respect to the *s* level.[19]

Figure 6. Conduction and valence bands of HgTe (left) and CdTe (right). Upon alloying ($Cd_{1-x}Hg_xTe$) the bands cross.[19]

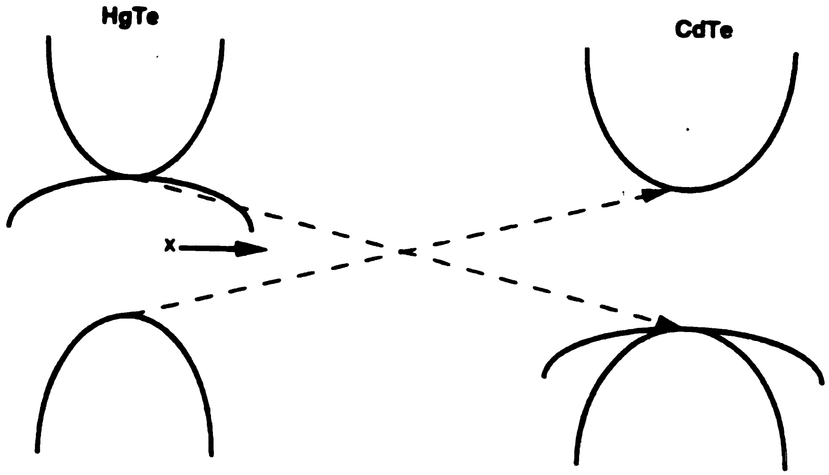

This logic can also be applied to systems with narrow *d* levels. Consider a semimetallic system where the overlapping bands lie at different positions in the Brillouin zone. Addition of a *d* level to this semiconductor can produce hybridization between the *d* and more dispersive *p* orbitals. The resulting hybridization may produce a narrow-gap semiconductor where the hybridized *p*-*d* level may have *d*-like character and be non-dispersive in one direction of **k**-space but more *p*-like and dispersive in another direction in **k**-space. This satisfies two criterion for good thermoelectric materials, formation of a narrow-gap semiconductor and highly anisotropic effective masses. This will be the reasoning behind looking at the half-Heusler compounds.[7]

Figure 7. Semiconducting gap opening due to p-d hybridization.

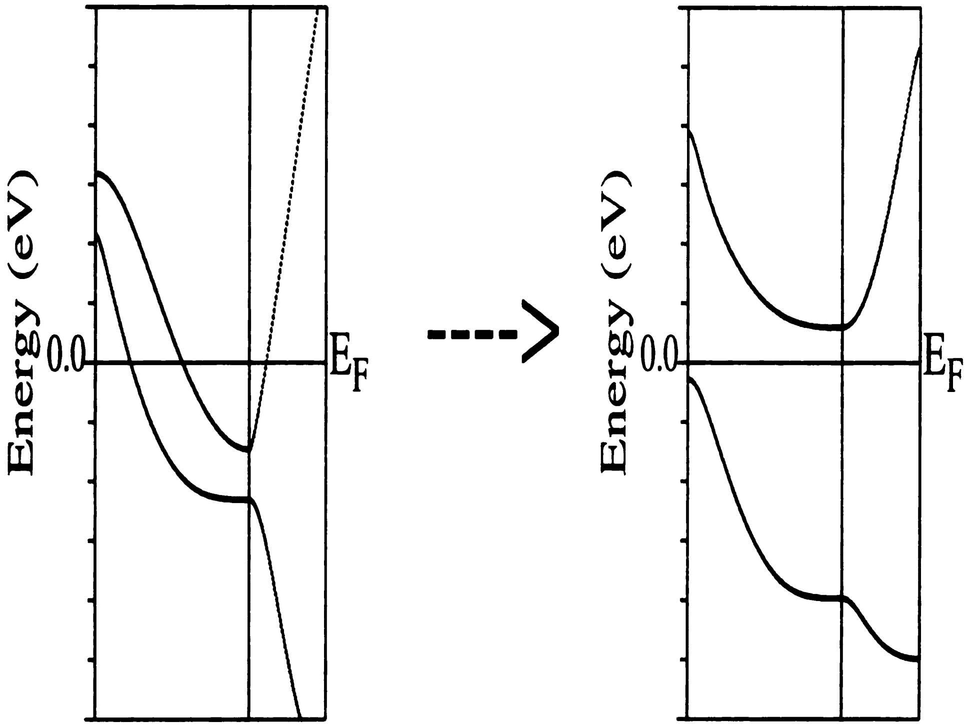

The schematic of *p*-*d* hybridization (Figure 7) shows two *p*-bands which both cross the Fermi energy at different positions. After hybridization with an added non-dispersive *d*-band, a gap opens in the spectrum. For simplicity, the details of the *d*-bands have been left out of the picture.

The presence of off-axis band extrema can come about due to strong spin-orbit hybridization. Consider the band structure for a narrow-gap semiconductor before the inclusion of spin-orbit interaction. While there may be several off-axis extrema, consider the semiconducting gap forming at the Γ point. It is well known that the spin-orbit interaction generally reduces the band gap, so a rigid shift may cause a hybridization of the bands forming the gap, leaving the off-axis extrema as the band en

in

Opt

structur

and Cd

anisotrop

the ban

The

the gap

extrema (Figure 8). This is the reasoning behind our study of Bi_2Te_3 and related materials.[11]

Figure 8. Off-axis gap formation due to spin-orbit hybridization.

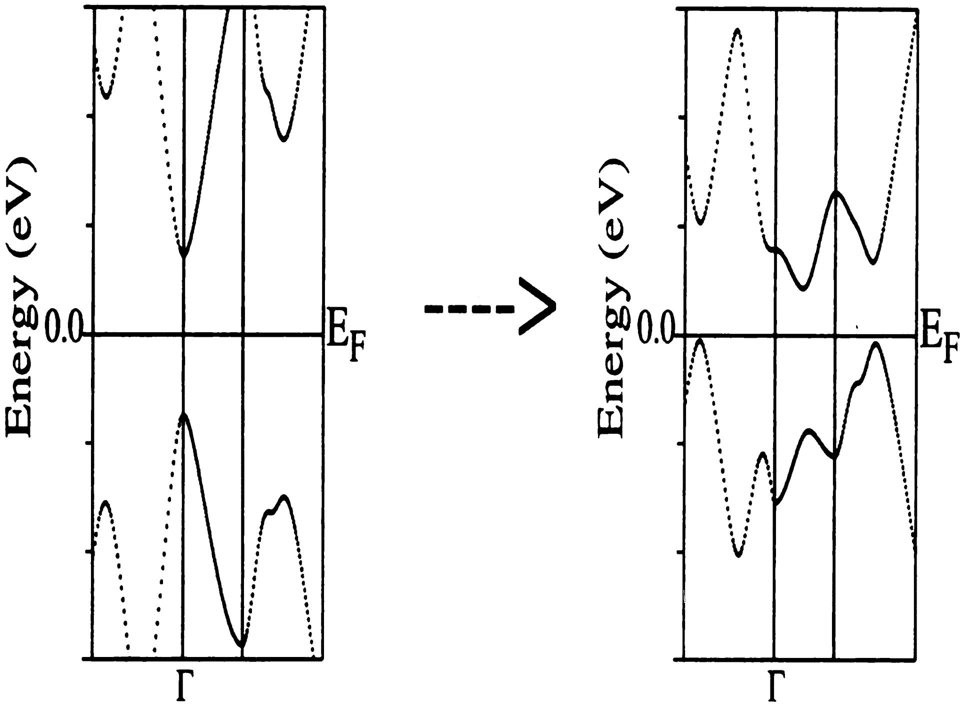

Optimum characteristics in the band structure may be a result of the crystal structure itself. Layered structures, such as those seen in Bi_2Te_3[11], $BaBiTe_3$[11], and $CsBi_4Te_6$[15] suggest that the transport (effective masses) should be highly anisotropic. It is, therefore, important to compare the calculated anisotropy found in the band structure with experiment.

The different physical reasons discussed above will be shown to be important for the gap formation of promising thermoelectric materials. An important focus of this work is to study the electronic structure of known thermoelectric materials as well as promising new thermoelectric materials in order to understand which features, such as a narrow band gap, anisotropic effective masses, and off-axis band extrema, are indeed seen in the electronic structure calculations. With this information it will be then possible to predict which are the best new thermoelectric materials.

In order to be considered for thermoelectric applications, a new system must be comparable with the previously studied materials. The best room temperature thermoelectric materials for nearly 40 years are Bi_2Te_3 alloys which have ZT$\sim$1. The best high temperature thermoelectric materials are PbTe with ZT$\sim$0.8 at about 700 K and Si-Ge alloys with ZT$\sim$1 at about 1200 K. $CsBi_4Te_6$ has a maximum ZT$\sim$0.8 at 225 K[26] and Bi-Sb alloys have ZT$\sim$0.6 at about 100 K, lower due to the the reduced value of T (in ZT) and the lower electron mobility at low temperatures.[3] High values of ZT have also been reported in PbTe-Pb(Se,Te) quantum-dot superlattices by Harman *et al.*[27] and in p-type Bi_2Te_3/Sb_2Te_3 superlattice films by Venkatasubramanian[28].

CHAPTER 3.

FIRST-PRINCIPLES *AB INITIO* ELECTRONIC STRUCTURE CALCULATIONS

Electronic structure calculations are a valuable tool to understand the structural, transport, and optical properties of materials. Recent improvements in calculational methods and computer speeds have made these calculations not only a more powerful predictive tool but also have allowed for larger and more complex systems to be studied.[30]

The basis of electronic structure calculations lies in the nature of electrons in solids. Electrons interact through strong Coulomb repulsions which makes it seem difficult at first to describe them as distinct entities. However, electrons in solids do not act as "bare" particles, rather surrounding themselves with positively charged polarization clouds. The electron and screening cloud form a "quasiparticle" which weakly interacts with other quasiparticles in the solid. Despite the strong interactions between the bare particles, the weak interaction of the quasiparticles allows for an effective single particle approximation, particularly for low energy properties where they can be treated as acting in the mean field of the other quasiparticles in the solid. Such an approximation appears to be valid in a large class of solids (simple metals, semiconductors, and insulators) but not in systems with strong electron-electron interactions and weak screening, such as in magnetic insulators.[31]

Electronic structure calculations involve solving a single particle Dirac equation within a single-particle approximation. This involves forming a one-particle potential and technical methods for solving the single-particle equations.[31] We will discuss

these aspects separately.

3.1. SOLVING THE DIRAC EQUATION

3.1.1. FULLY-RELATIVISTIC ONE-PARTICLE EQUATIONS

Assuming that a single particle description is valid, one still has to solve the Dirac equation for an electron because the full relativistic effects applied to electronic structure are included in this equation[32, 33]. The Dirac Hamiltonian is given by

$$\mathrm{H}_D = \mathrm{c}\alpha \cdot \mathbf{p} + (\beta - 1)\mathrm{m}_e\mathrm{c}^2 + \mathrm{V}(\mathbf{r}) \tag{26}$$

where α and β are 4 x 4 matrices

$$\alpha = \begin{pmatrix} 0 & \sigma \\ \sigma & 0 \end{pmatrix} \qquad \beta = \begin{pmatrix} I & 0 \\ 0 & -I \end{pmatrix} \tag{27}$$

σ_x, σ_y, and σ_z being Pauli spin matrices. $\mathbf{p}$ is the four-component momentum, m_e is the free-electron mass, c is the speed of light, and $\mathrm{V}(\mathbf{r})$ is the effective single-particle potential. The eigenvectors, Ψ, of the Dirac Hamiltonian can be written as four component spinors consisting of two component spinors, Φ (the large component) and χ (the small component).

$$\Psi = \begin{pmatrix} \Phi \\ \chi \end{pmatrix} \tag{28}$$

This leads to a set of coupled equations

(29)

$$c(\sigma \cdot \mathbf{p})\chi = (\varepsilon - \mathrm{V})\Phi$$

$$c(\sigma \cdot \mathbf{p})\Phi = (\varepsilon - \mathrm{V} + 2\mathrm{m}_e\mathrm{c}^2)\chi$$

(30)

Solving for χ in Equation 29 and inserting this into Equation 30 yields an equation for Φ alone,

(31)

$$\frac{1}{2m_e}(\sigma \cdot \mathbf{p})(1 + \frac{\varepsilon - V}{2m_e c^2})^{-1} (\sigma \cdot \mathbf{p})\Phi + \mathrm{V}\Phi = \varepsilon\Phi$$

3.1.2. SCALAR RELATIVISTIC APPROXIMATION

Equation 31 is still the exact Dirac equation. This equation serves as the basis for relativistic electronic structure calculations which have been increasing in popularity in recent years.[34] However, for valence electrons in solids, where the relativistic effects are not usually strong, one can make the following approximation

(32)

$$(1 + \frac{\varepsilon - V}{2m_e c^2})^{-1} \approx (1 - \frac{\varepsilon - V}{2m_e c^2})$$

and use the relationships

(33)

$$\mathbf{p}\mathrm{V} = \mathrm{V}\mathbf{p} - \mathrm{i}\hbar\nabla\mathrm{V}$$

$$(\sigma \cdot \nabla\mathrm{V})\ (\sigma \cdot \mathbf{p}) = (\nabla\mathrm{V} \cdot \mathbf{p}) + \mathrm{i}\sigma \cdot [\nabla, \mathbf{p}]$$

(34)

so that Equation 31 can be written as a linear, second-order differential equation in Φ.

$$[(1- \frac{\varepsilon-V}{2m_ec^2})\frac{p^2}{2m_e} + V]\Phi - \frac{\hbar^2}{4m_e^2c^2}(\nabla V\nabla\Phi) + \frac{\hbar^2}{4m_e^2c^2}(\sigma[\nabla V,\mathbf{p}]\Phi) = \varepsilon\Phi \tag{35}$$

In a spherically symmetric potential, V(r), this equation can be simplified further.

$$[\frac{p^2}{2m_e} + V - \frac{p^4}{8m_e^3c^2} - \frac{\hbar^2}{4m_e^2c^2}\frac{dV}{dr}\frac{\partial}{\partial r} + \frac{1}{2m_e^2c^2}\frac{dV}{dr}\frac{1}{r}(\mathbf{l}\cdot\mathbf{s})]\Phi = \varepsilon\Phi \tag{36}$$

The first two terms are the nonrelativistic Schroedinger Hamiltonian while the third and fourth terms are the mass velocity and Darwin terms, respectively. The last term is the spin-orbit interaction (SOI). Due to this SOI term, **l** and **s** are not good quantum numbers while their sum, **j** = **l** + **s**, is a good quantum number. In practice one solves a new equation which is Equation 36 without the last term[32, 33]

$$[\frac{p^2}{2m_e} + V - \frac{p^4}{8m_e^3c^2} - \frac{\hbar^2}{4m_e^2c^2}\frac{dV}{dr}\frac{\partial}{\partial r}]\phi = \varepsilon\phi \tag{37}$$

called the scalar relativistic Schroedinger equation where **l** and **s** are still good quantum numbers. However, spin-orbit effects are important, especially in heavier elements (which are present in most thermoelectric materials with high values of ZT[4]). The first thing that is done is to write ϕ in terms of radial functions (f(r) and g(r)) multiplied by spherical Harmonics, Y_{lm}.

$$\phi = \begin{pmatrix} g(r)Y_{lm} \\ -if(r)Y_{lm} \end{pmatrix} \tag{38}$$

The scalar relativistic equations are then solved with this choice of ϕ. To include SOI, one method is to double the entire basis set to accommodate H_{so}

$$H_{so} = \frac{\hbar}{2Mc^2}\frac{dV}{dr}\frac{1}{r}\begin{pmatrix} l\cdot s & 0 \\ 0 & 0 \end{pmatrix} \tag{39}$$

where M is the relativistic mass $M = m_e + \frac{\varepsilon - V}{2c^2}$. This approach is usually computationally expensive. An alternative, called the second variational method, does not involve doubling the size of the basis. Rather, spin up and spin down states are considered separately using the eigenvectors of the scalar relativistic calculation, but for a finite number of states near E_F. This reduces the number of basis sets involves in the calculation of the energy bands in the presence of SOI.

$$\phi^{\uparrow} = \begin{pmatrix} g^{\uparrow}(r)Y_{lm} \\ -if^{\uparrow}(r)Y_{lm} \end{pmatrix} \qquad \phi^{\downarrow} = \begin{pmatrix} g^{\downarrow}(r)Y_{lm} \\ -if^{\downarrow}(r)Y_{lm} \end{pmatrix} \tag{40}$$

The states denoted in Equation 40 are used as the new basis set for the expansion of the wavefunction Φ in Equation 36. The total Hamiltonian including SOI can be solved with less effort since the number of $\phi^{\uparrow}$ and $\phi^{\downarrow}$ in the space of orbitals of the low lying bands (reduced vectors space) are usually much less than in the original eigenvalue problem.[32, 33, 35]

One shortcoming of the second variational method was found in the case of metallic Pb where there were significant differences between the results using this method and a fully-relativistic calculation. The Pb $6p_{\frac{1}{2}}$ state strongly mixes with the $6s_{\frac{1}{2}}$, the latter coming very close to the nucleus where relativistic effects are strong. The p states used as basis functions in the second variational treatment do not approach the nucleus like the s states, since the good quantum numbers in the scalar relativistic calculation are **l** and **s**, not **j**. The strong mixing of the $6p_{\frac{1}{2}}$ and $6s_{\frac{1}{2}}$ orbitals should

also in principle affect the band structures of Bi, Hg, and Tl, though these effects have not been explicitly studied[36]. However, the second variational method has found to be quite successful in predicting the band structures of PbTe[37, 38, 39] and Bi_2Te_3[11, 12, 13, 40], so the applicability of the second variational method to semiconducting compounds containing heavy atoms has not yet been critically examined. In this dissertation, second variational procedure for spin-orbit will be used due to the simplicity of its implementation and we will check its reliability by comparing our calculations with published fully-relativistic calculations (i.e. solving the Dirac equation) wherever available.

3.2. DENSITY FUNCTIONAL THEORY (DFT)

3.2.1. DERIVATION OF KOHN-SHAM (KS) EQUATIONS

A major theoretical and computational advance in the electronic structure of solids was made by Pierre Hohenberg and Walter Kohn[41] and later by Walter Kohn and Lu Sham[42] with the advent of density functional theory (DFT). This theory states that the ground state electronic properties of a material are determined solely through its electron density.[30] The Hohenberg-Kohn proof starts from a Hamiltonian for M nuclei and N electrons with the form

$$\begin{aligned} H_e &= \Sigma_{i=1}^{N} \tfrac{1}{2} \nabla_i^2 + \Sigma_{i=1}^{N} \Sigma_{j>i}^{N} \frac{1}{|r_i - r_j|} - \Sigma_{i=1}^{N} \Sigma_{A=1}^{M} \frac{Z_A}{|R_A - r_i|} \\ &\equiv T + V_{Coul} + \Sigma_{i=1}^{N} V_{ext}(\mathbf{r}), \end{aligned} \tag{41}$$

where the first term, T, is the kinetic energy, the second, V_{Coul}, is the electron-electron Coulomb repulsion, and the third, $\Sigma_{i=1}^{N} V_{ext}(\mathbf{r})$, is the nuclear-electron at-

traction (Z_A is the atomc number and R_A the nuclear position). The Hamiltonian depends on the positions of the nuclei which create an external potential, $V_{ext}(\mathbf{r})$, on the electrons. The essence of DFT is the fact that the terms T and V_{Coul} are the same in *all* N-electron systems, and the external potential, which differs from system to system, can be written as a single-particle function. The universality of T and V_{Coul} are the basis of the universal functional F[n] (using wavefunctions Ψ).

$$F[n] = min_{\psi^2 \rightarrow n(r)} < \Psi \mid T + V_{Coul} \mid \Psi >, \tag{42}$$

where the Kohn-Sham total energy can be written as

$$E_{KS}[n] = F[n] + \int V_{ext}(\mathbf{r})\, n(\mathbf{r})\, d\mathbf{r} \tag{43}$$

The Kohn-Sham energy must be minimized under the constraint $N = \int n(\mathbf{r})\, d\mathbf{r}$

$$\delta[E_{KS}[n] - \mu\, (N - \int n(\mathbf{r})\, d\mathbf{r})] = 0 \tag{44}$$

While μ is a Lagrange multiplier in Equation 44, the functional derivative defines the chemical potential, μ_N, in DFT.

$$\frac{\delta E_{KS}[n]}{\delta n(r)}\Big|_{n(r)=n_0(r)} = \mu_N \tag{45}$$

In order to obtain the Kohn-Sham equations, the kinetic energy operator, $T_0[n]$, is written separately from $E_{KS}[n]$.

$$T_0[n] = min_{\psi^2 \rightarrow n(r)} < \Psi \mid -\tfrac{1}{2}\nabla^2 \mid \Psi > \tag{46}$$

It is customary to separate F[n] into a Hartree piece where the Hartree energy, E_H[n] (derived from the Hartree potential, V_H[n]), is

(47)

$$E_H[n] = \tfrac{1}{2}\int\int \frac{n(r)n(r')}{|r-r'|}\,\mathbf{dr}\,\mathbf{dr'} = \tfrac{1}{2}\int V_H(\mathbf{r})\,\mathbf{dr},$$

so that the difference between F[n] and T_0[n] is E_H[n] and a remainder, E_{xc}[n], which is called the exchange-correlation energy.

(48)

$$F[n] - T_0[n] = E_H[n] + E_{xc}[n]$$

The exchange-correlation potential, V_{xc}[n], is derived from E_{xc}[n]

(49)

$$\frac{\delta E_{xc}[n]}{\delta n(r)}\Big|_{n(r)=n_0(r)} = V_{xc}[n]$$

In order to satisfy the fermion nature of the electrons, the total wavefunction must be antisymmetric, and to accommodate this requirement, it is convenient to write the total wavefunction, Ψ, as the Slater determinant of single particle wavefunctions, ζ_{ij}.

(50)

$$\Psi = \frac{1}{\sqrt{N!}}\det\begin{bmatrix} \zeta_{11} & \zeta_{12} & \cdot & \cdot & \zeta_{1N} \\ \zeta_{21} & \cdot & \cdot & \cdot & \cdot \\ \cdot & \cdot & \cdot & \cdot & \cdot \\ \cdot & \cdot & \cdot & \cdot & \cdot \\ \zeta_{N1} & \cdot & \cdot & \cdot & \zeta_{NN} \end{bmatrix}$$

so that the total density is a sum of the squares of these one-electron wavefunctions[43]

$$n_\sigma(\mathbf{r}) = \Sigma_{i,k}|\zeta^\sigma_{ik}(\mathbf{r})|^2 \tag{51}$$

This choice of Ψ makes it possible to calculate $T_0[n]$ and the minimization over all Ψ such that $|\Psi|^2 \rightarrow n(\mathbf{r})$ gives rise to the following one-particle equations (known as the Kohn-Sham equations)

$$[-\tfrac{1}{2}\nabla^2 + V_{Ne} + V_H + V^\sigma_{xc}[n]]\zeta^\sigma_{ik}(\mathbf{r}) = \varepsilon^\sigma_{ik}\zeta^\sigma_{ik}(\mathbf{r}) \equiv H_{KS}\zeta^\sigma_{ik}(\mathbf{r}) \tag{52}$$

In Equation 52, $-\frac{1}{2}\nabla^2$ is the single particle kinetic energy, V_{Ne} is the nuclear-electron attraction, V_H is the Hartree potential, and $V^\sigma_{xc}[n]$ is the exchange-correlation (XC) potential. The single particle states, $\zeta^\sigma_{ik}(\mathbf{r})$, are called the Kohn-Sham orbitals and ε^σ_{ik} are the Kohn-Sham energies. The XC potential depends on the electron density, $n(\mathbf{r})$, but the density is obtained from the solutions of the one-particle Schroedinger equations, ζ^σ_{ik}.[43, 44] Since the XC potential is a part of the Hamiltonian, it affects the wavefunctions, and the wavefunctions determine the charge density and, hence, the XC potential. This means that the electron density and XC potential must be solved self-consistently.[35, 43, 44]

The XC potential includes correlation effects, which keep electrons of opposite spin from coming too close to each other, and exchange effects, arising from the fermion nature of electrons. V_{Ne} and V_H are local, i.e. $(V_{Ne}f)(\mathbf{r}) = V_{Ne}(\mathbf{r})f(\mathbf{r})$ and $(V_H f)(\mathbf{r}) = V_H(\mathbf{r})f(\mathbf{r})$, but the XC potential is inherently non-local, i.e. $(V_{xc}f)(\mathbf{r}) = \int V_{xc}(\mathbf{r},\mathbf{r}')f(\mathbf{r}')d\mathbf{r}'$. One of the most commonly used exchange-correlation potentials is the local density approximation (LDA) where V_{xc} depends only on the density n at position $\mathbf{r}$.[44]

$$\mathrm{LDA} \Rightarrow \mathrm{V}_{xc}(\mathrm{n}_\uparrow(\mathbf{r}),\, \mathrm{n}_\downarrow(\mathbf{r})) = \mathrm{f}(\mathrm{n}_\uparrow(\mathbf{r}),\, \mathrm{n}_\downarrow(\mathbf{r})) \tag{53}$$

LDA does not always do a good job in finding the ground state properties of materials. An important example of this is that LDA finds that ferromagnetic FCC Fe has a lower energy than BCC Fe by about 6 mRy, contradicting experimental evidence.[45, 46] Some of the non-local nature of the XC potential can be incorporated by including derivatives of the charge density in what is called the generalized gradient approximation (GGA). This approximation is developed by expanding the XC potential to second order in gradients of the density (∇n) and cutting off spurious long-range contributions in real space. This leads to a fairly complicated expression which favors a less homogeneous electron density than LDA.[47, 48]

$$\mathrm{GGA} \Rightarrow \mathrm{V}_{xc}(\mathrm{n}_\uparrow(\mathrm{r}),\, \mathrm{n}_\downarrow(\mathrm{r})) = \mathrm{f}(\mathrm{n}_\uparrow(\mathrm{r}),\, \mathrm{n}_\downarrow(\mathrm{r}),\, \nabla\mathrm{n}_\uparrow(\mathrm{r}),\, \nabla\mathrm{n}_\downarrow(\mathrm{r})) \tag{54}$$

In many cases, GGA improves the values of calculated properties compared to experiment, such as cohesive energies, total energies, and work functions.[46] While LDA predicted the wrong ground state for Fe, GGA correctly predicts that BCC Fe has a lower energy than FCC Fe by about 11 mRy.[45] However, GGA tends to overestimate lattice parameters while LDA tends to underestimate them. Most of the improvements of GGA over LDA are modest, and sometimes GGA does not explain properties of some materials as well as LDA, so special care should be taken that spurious results do not occur due to the choice of the XC potential.[29, 46]

3.2.2. PHYSICAL PROPERTIES OF DFT CALCULATIONS

In DFT, the Kohn-Sham eigenfunctions, $\zeta_{ik}^{\sigma}(\mathbf{r})$, solved in Equation 52 have no rigorous physical meaning; they are simply functions calculated in an intermediate step to solve for the charge density in Equation 51. The eigenvalues found in equation 52 are not single-particle excitation energies, although they are often compared to experimental results as if they were. Surprisingly, DFT results often agree very well with experiments. However, one should not overlook some of the general results of DFT which have direct physical interpretation.[31]

The ionization energy, I, is the energy required to remove an existing electron from a solid while the electron affinity, A, is the energy gained by adding an electron to a solid. These can be identified in an N-electron system as[31]

$$\mathrm{I} = \mathrm{E}_{N-1} - \mathrm{E}_N \qquad\qquad \mathrm{A} = \mathrm{E}_N - \mathrm{E}_{N+1} \tag{55}$$

where E_M is the ground-state energy of an M-electron system. In a metal, one can associate (Equation 45) the chemical potential, μ_N, or the Fermi energy, E_F, with the highest occupied Kohn-Sham orbital. In a semiconductor one has[31]

$$\mathrm{I} = -\varepsilon_{N,N} \qquad\qquad \mathrm{A} = -\mu_{N+1} = -\varepsilon_{N+1,N+1}, \tag{56}$$

and the band gap, E_{gap}, is given by the difference of I and A,[31]

$$\mathrm{E}_{gap} = \mathrm{I} - \mathrm{A} = \varepsilon_{N+1,N+1} - \varepsilon_{N,N} = \Delta_{xc} + \varepsilon_{N,N+1} - \varepsilon_{N,N}. \tag{57}$$

In the above, $\varepsilon_{N,M}$ is the M^{th} Kohn-Sham eigenvalue of an N-particle system and

$\Delta_{xc} = \varepsilon_{N+1,N+1}$ - $\varepsilon_{N,N+1}$ is the energy difference between the highest occupied Kohn-Sham orbital in the (N + 1)-electron system and the lowest unoccupied Kohn-Sham orbital in the N-electron system. This difference arises from a discontinuous jump in the XC potential, V_{xc}, when adding an electron.[31]

$$\Delta_{xc} = V_{xc,N+1}(\mathbf{r}) - V_{xc,N}(\mathbf{r}) \tag{58}$$

This difference, Δ_{xc}, is positive and usually position independent, so the XC potential changes only by a constant. This is the source of the "band-gap problem" in DFT where the band gaps can be 0.5 -2 eV smaller than experiment[31]. In most of the band gap calculations in this dissertation, we will ignore this correction and only use E $\approx \varepsilon_{N,N+1}$ - $\varepsilon_{N,N}$ as an estimate of the band gap.

3.3. METHODS OF CALCULATION (DFT)

There are many methods to solve the Kohn-Sham equations in a solid. In order to solve for $\zeta^{\sigma}_{ik}(\mathrm{r})$ self-consistently, one must start with a reasonable trial function which satisfies the crystalline periodicity and appropriate boundary conditions. Planewaves and atomic orbitals form complete basis sets which are often used in several methods to expand the wavefunctions[35, 49]. To simplify the numerical alculation, several methods, such as the linearized muffin-tin orbital method in the omic sphere approximation (LMTO-ASA), make approximations to the interatomic tential, V(r)[50, 51]. The method which we have used, the full potential linearized newave (FLAPW), makes no approximations to the shape of the potential and arates the space into two regions, spheres about the atomic positions and an inter-

stitial region. The wavefunctions are expanded in atomic orbitals inside the spheres and in planewaves in the interstitial region.[35, 51, 52, 53] We will briefly discuss these expansions and see how they are implemented in LMTO-ASA and FLAPW.

3.3.1. PLANEWAVES AND ATOMIC ORBITALS

Planewaves form a complete basis, easily programmable, and describe well nearly-free electron states. The most general type of expansion in a planewave basis can be written as follows in terms of the reciprocal lattice vectors **G**. ($c_G(\mathbf{k})$ are expansion coefficients)

$$\zeta(\mathbf{r}) = e^{ik\cdot r} \, \Sigma_G \, c_G(\mathbf{k}) \, e^{iG\cdot r} \tag{59}$$

The major strength of the planewave expansion is the ability to expand in the omplete basis of planewaves to achieve greater improvements in approximating the avefunctions. This also turns out to be the major weakness, since it may take from everal thousand to several million planewaves to adequately represent the localized ates associated with the atomic orbitals near the atomic positions.[35]

Atomic orbitals and planewaves prove to be the most important basis set for ex- nsion of the wavefunctions within DFT, but the method of calculation used is often med after the method to approximate the potential. Tight-binding calculations are e most direct application of using atomic orbitals, but require a large number of pansion coefficients since the atomic orbitals cannot describe the regions far from atomic positions.[22] The pseudopotential method (used with both atomic orbital d planewave expansions) is a very successful scheme to reduce the time necessary

in the calculations. In this method the potential associated with the core electrons is replaced by a function which reproduces the full-electron result when solving for the valence electrons self-consistently.[35, 49, 54]

3.3.2. LINEARIZED MUFFIN-TIN ORBITAL METHOD WITHIN THE ATOMIC SPHERE APPROXIMATION (LMTO-ASA)

An important and popular method of solving the Kohn-Sham equations within DFT is the linearized muffin-tin orbital method within the atomic sphere approximation (LMTO-ASA) which arose from the previously used cellular method.[22] In this method, approximations are made to the interatomic potential, V($\mathbf{r}$), which drastically reduce the computational time while still giving reliable results. The solid is separated into two regions, overlapping spherical regions around the atomic positions and the region outside of these spheres(Figure 9).

Figure 9. Overlapping atomic spheres surrounding each atom of a crystal in the ASA.[50]

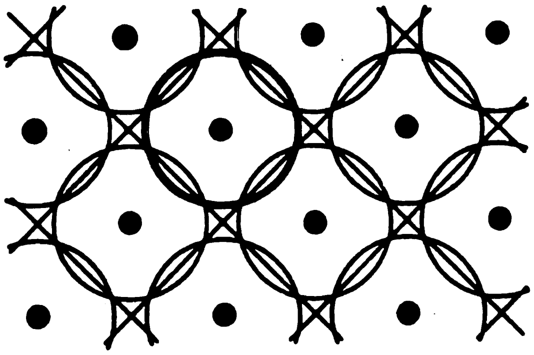

The total potential is kept the same as the actual potential inside the atomic sphere radius, r_{as}, but becomes a constant value, V_{MTZ}, outside the spheres.

$$V(r) = \begin{cases} V(r) & r < r_{as} \\ V_{MTZ} & r > r_{as} \end{cases} \tag{60}$$

The wavefunctions are defined in terms of atomic orbitals (ϕ_l(E,r)) and power law terms.

$$\zeta_{lm}(E, \mathbf{r}) = i^l Y_l^m(\mathbf{r}) \begin{cases} \phi_l(E,r) + p_l(E)\ (r/r_{as})^l & r < r_{as} \\ (r_{as}/r)^l & r > r_{as} \end{cases} \tag{61}$$

The term p_l(E) is required to keep the solution continuous and differentiable in all space where

$$p_l(E) = \frac{D_l(E)+l+1}{D_l(E)-l} \qquad D_l(E) = \frac{r_{as}}{\phi_l(E,r_{as})} \frac{\partial \phi_l}{\partial r}\bigg|_{r=r_{as}} \tag{62}$$

This method has solutions for the region outside of the spheres which extends into ie other spheres, as can be seen by Equation 61. The correct one-center expansion in ie sphere is in terms of atomic orbitals for $r < r_{as}$ is (a_{lm}^{jk} are expansion coefficients),

$$\zeta_{lm}(E, \mathbf{r}) = \Sigma_{lm}\ a_{lm}^{jk}\ i^l Y_l^m(\mathbf{r})\ \phi_l(E,r). \tag{63}$$

The tails from the expansions for all of the other spheres ($r > r_{as}$) must cancel ide the sphere for Equation 63 to be the correct expansion.

$$\zeta_{lm}(\mathrm{E}, \mathbf{r}) = \Sigma_{lm}\ \mathrm{a}_{lm}^{jk}\ \mathrm{i}^l \mathrm{Y}_l^m(\mathbf{r})\ \mathrm{p}_l(\mathrm{E})\ (\mathrm{r}/\mathrm{r}_{as})^l \tag{64}$$

The expansions outside the spheres (Equation 64) must be cancelled by $\mathrm{S}_{l',m',l,m}^k$

$$\Sigma_{lm}\ \mathrm{a}_{lm}^{jk}\ [2(2\,\mathrm{l} + 1)\ \mathrm{p}_l(\mathrm{E})\ \delta_{l'l}\ \delta_{m'm}\text{-}\ \mathrm{S}_{l',m',l,m}^k] = 0 \tag{65}$$

where $\mathrm{S}_{l',m',l,m}^k$ is called the structure matrix which contains the information about the atomic positions given by[50]

$$\mathrm{S}_{l',m',l,m}^k = \mathrm{g}_{l',m',l,m}\ \Sigma_{R\neq 0}\ \mathrm{e}^{ikR}\ (\tfrac{r_{as}}{R})^{l''+1}[\sqrt{4\pi}\ \mathrm{i}^l\ \mathrm{Y}_{l''}^{m''}(\mathbf{r})]^* \tag{66}$$

where $\mathrm{g}_{l',m',l,m}$ are Gaunt coefficients, $\mathrm{l}'' = \mathrm{l}' + \mathrm{l}$, and $\mathrm{m}'' = \mathrm{m}' - \mathrm{m}$. Finding he eigenfunctions (and eigenvalues) of the Schroedinger equation within this method equires solving for the tail cancellation in Equation 65. However, $\mathrm{p}_l(\mathrm{E})$ explicitly depends upon energy. The linearization in LMTO comes about by expanding these unctions about specific energies near the center of the bands as in Equation 67. This s done by introducing linearization energies, E_l, at the middle of the bands so that ${}_m(\mathbf{r})$ does not explicitly depend on E.[51]

$$\begin{aligned} \zeta_{lm}(\mathbf{r}) = \mathrm{i}^l \mathrm{Y}_l^m(\mathbf{r})\ &\{\ \mathrm{A}_{lm}\phi_l(\mathrm{E}_l,\mathrm{r}) + \mathrm{p}_l(\mathrm{E}_l)\ (\mathrm{r}/\mathrm{r}_{as})^l && \mathrm{r} < \mathrm{r}_{as} \\ &\{\ (\mathrm{r}_{as}/\mathrm{r})^l && \mathrm{r} > \mathrm{r}_{as} \end{aligned} \tag{67}$$

3.3.3. FULL-POTENTIAL LINEARIZED AUGMENTED PLANEWAVE METHOD (FLAPW)

The method which we have used, the full-potential linearized-augmented planewave (FLAPW) method, incorporates several of the aspects of the methods described before. Similar to the LMTO-ASA method, the space is separated into two regions, non-overlapping spheres about the atomic positions and the regions between the spheres (Figure 10).

Figure 10. Partitioning of the unit cell into atomic spheres (I) and an interstitial region (II).[53]

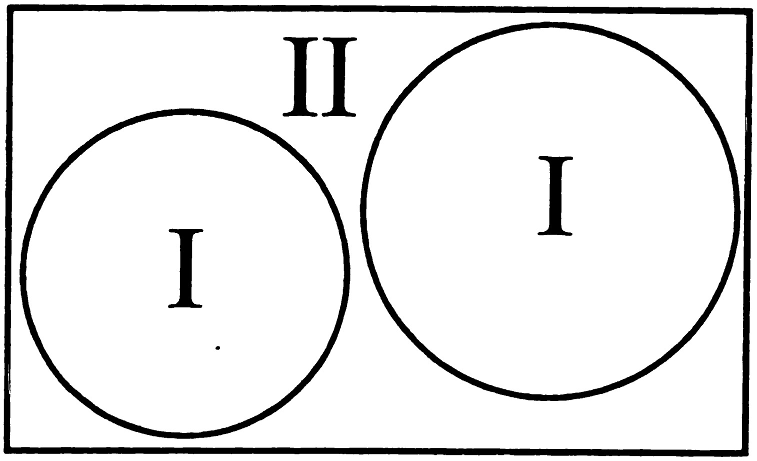

The wavefunctions are expanded with atomic orbitals inside the spheres and planewaves in the interstitial region between the spheres, combining the expansions of the tight-binding and planewave methods. Like the pseudopotential method, the electrons are separated into core and valence states, but the core states are not replaced but are kept within the self-consistent cycle and affect the final band structure.[35]

LAPW is a linearized version of the augmented planewave (APW) method. In the PW method, the wavefunctions are expanded in terms of basis functions which deend explicitly on the energies (Equation 68). Region I is inside the spheres while RegIon II is the interstitial region (with volume V and expansion coefficients $C^{\sigma}_{lm}(k_n)$)[52]

$$\begin{aligned} \text{Region I} \Rightarrow \zeta^{\sigma}_{K}(\mathbf{r},E) &= \Sigma_{lm} C^{\sigma}_{lm}(\mathbf{K}) \phi_l(r,E)\ Y_{lm}(r) \\ \text{Region II} \Rightarrow \zeta^{\sigma}_{K}(\mathbf{r}) &= \frac{1}{\sqrt{V}} e^{iK \cdot r} \end{aligned} \tag{68}$$

where $\mathbf{K} = \mathbf{k} + \mathbf{G}$. In order that the basis functions do not depend explicitly on energy (so that Ψ in $H\Psi = E\Psi$ is linear in energy), the radial parts of the wavefunction are expanded about specific linearization energies (E_l) which lie near the center of the bands, as in the LMTO method. In order to have the function and the derivative equal at the sphere boundaries, the function and its derivative are included in the expansion (for expansion coefficients A^{σ}_{lm} and B^{σ}_{lm}).[51, 53]

$$\begin{aligned} \text{Region I} \Rightarrow \zeta^{\sigma}_{k_n}(\mathbf{r}) &= \Sigma_{lm}[A^{\sigma}_{lm} \phi_l(r,E_l) + B^{\sigma}_{lm} \dot{\phi}_l(r,E_l)] Y_{lm}(r) \\ \text{Region II} \Rightarrow \zeta^{\sigma}_{ik}(\mathbf{r}) &= \frac{1}{\sqrt{V}} e^{ik_n r}, \end{aligned} \tag{69}$$

where $\dot{\phi}_l(r,E_l) = \frac{d}{dE} \phi_l(r,E_l)|_{E=E_l}$. The full-potential LAPW (FLAPW) method has been put in a convenient collection of programs which we have used, WIEN97[55]. This package contains SOI as a second variational method and solves for the full potential with no approximations to shape. Both the LDA of Perdew and Wang[47] and the GGA of Perdew, Wang, and Ernzerhof[48] has been used for the XC potential.

To further improve the convergence, the LAPW basis set can be expanded to include a radial function at a second energy ($E_{2,l}$), called a local orbital (LO).

$$\textbf{Region I} \Rightarrow \zeta^{\sigma}_{k_n}(\mathrm{r}) = \Sigma_{lm}[\mathrm{A}^{\sigma}_{lm}\phi_l(\mathrm{r},\mathrm{E}_{1,l}) + \mathrm{B}^{\sigma}_{lm}\dot{\phi}_l(\mathrm{r},\mathrm{E}_{1,l}) + \mathrm{C}^{\sigma}_{lm}\phi_l(\mathrm{r},\mathrm{E}_{2,l})]\mathrm{Y}_{lm}(\mathrm{r}) \tag{70}$$

Since there are no approximations to the potential or core electrons, the FLAPW method is a very useful method to obtain highly accurate electronic structures. However, this progress comes at a price of longer times for convergence compared to the pseudopotential or LMTO-ASA methods. This means that large systems, containing perhaps 100's of atoms, cannot be achieved using the level of accuracy in LAPW methods due to the problem of N^3 scaling with the total number of electrons.[35]

3.4. OTHER METHODS OF CALCULATION (NON-DFT)

There are other electronic structure methods beyond DFT which can either be used separately or in conjunction with DFT methods in order to better describe correlation effects within the material. Some of these methods have similar time and size requirements as most DFT methods while others, though improving the quality of the results, are so computationally demanding that they can only be used only for simple systems.

3.4.1. HARTREE-FOCK (HF) METHOD

One of the earliest methods is the Hartree-Fock (HF) method where the N-particle wavefunction, Ψ, is written, as the Slater determinant of the individual single particle wavefunctions.[56]

$$\Psi_{HF} = \frac{1}{\sqrt{N!}} \det \begin{bmatrix} \zeta_{11} & \zeta_{12} & \cdot & \cdot & \zeta_{1N} \\ \zeta_{21} & \cdot & \cdot & \cdot & \cdot \\ \cdot & \cdot & \cdot & \cdot & \cdot \\ \cdot & \cdot & \cdot & \cdot & \cdot \\ \zeta_{N1} & \cdot & \cdot & \cdot & \zeta_{NN} \end{bmatrix} \tag{71}$$

where $\zeta_i(\mathbf{r}_j) \equiv \zeta_{ij}$ describes the jth electron occupying the orbital $\zeta_i(\mathbf{r})$. These wavefunctions are used to solve the Schroedinger equation (Equation 36). Unlike in DFT where the wavefunctions were merely a construction to produce the electron density, the wavefunctions in HF have physical meaning. In HF according to Koopman's theorem[56], the ionization energy is I = -$\varepsilon_{N,N}$ and the electron affinity is A = - $\varepsilon_{N,N+1}$, so the band gap is simply E_{gap} = I - A = $\varepsilon_{N,N+1}$ - $\varepsilon_{N,N}$ with no correction as in DFT by way of the Kohn-Sham eigenvalues. The results of HF tend to overestimate the band gaps in contrast to LDA/GGA which underestimates the band gap. The overestimation of the band gaps in HF is usually associated with the omission of correlation effects.[44]

3.4.2. GW METHOD

Both LDA and HF give poor account of excitation energies in solids, particularly he band gaps in semiconductors. In recent years, a Green function approach for the quasiparticle excitations which was originally developed for interacting homogeneous electron gas problem has been applied to real solids. An approximate version, called GW method has been proven to be quite successful for a large class of semiconductors. The single particle Green function, G($\mathbf{r}$,$\mathbf{r}'$;E), which contains the information about quasiparticle excitations is given by

$$G^{-1}(r,r';E) = G_0^{-1}(r,r';E) - \Sigma(r,r';E), \tag{72}$$

where $G_0^{-1}(r,r';E)$ is the reciprocal of the Green function for a reference system and $\Sigma(r,r';E)$ is the self-energy correction. The GW method gets its name from calculating the self energy ($\Sigma(r,r';E)$) as the product of a dressed Green function ($G(r,r';E - \omega)$) and the dynamically screened Coulomb interaction ($W(r,r';\omega)$). In this approximation, the self-energy correction $\Sigma(r,r';E)$ is given by[31, 57, 58]

$$\Sigma(r,r';E) = \frac{i}{2\pi}\int d\omega\, e^{-i\delta\omega} G(r,r';E - \omega)\, W(r,r';\omega) \tag{73}$$

Starting either from the Kohn-Sham or HF eigenvalues and eigenfunctions, one can construct the self energy, $\Sigma(r,r';E)$. The GW method produces values of gaps (E_{gap}) and band dispersions for a wide range of semiconductors which are much closer to experiment than LDA/GGA (see Figure 11. Note $E_{gap}^{LDA} < E_{gap}^{GW} \approx E_{gap}^{exp}$). Unfortunately, this method is computationally very expensive, with most results found on fairly simple monatomic or diatomic crystalline systems. While this approach is quite useful in understanding the gap structure of semiconductors, it cannot be readily applied to the complex systems which we have studied in this dissertation.[31, 57, 58]

Figure 11. Comparison of characteristic direct and indirect LDA, GW, and experimental energy gaps for all semiconductors for which GW calculations have been reported (For references see Aulbur[31]).

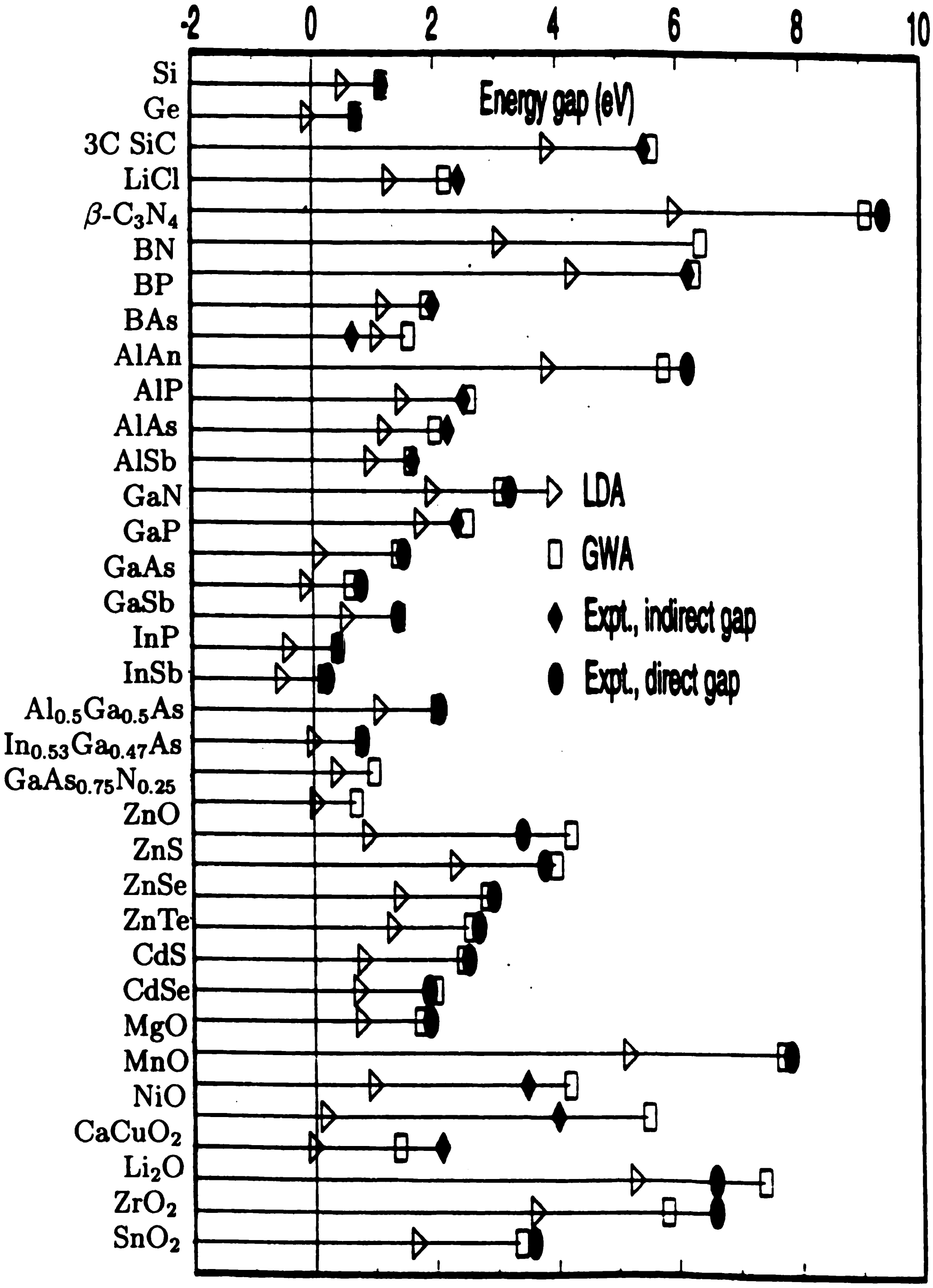

CHAPTER 4.

HALF-HEUSLER COMPOUNDS

Half-Heusler compounds are among the most common and versatile intermetallic materials. These compounds can be semiconducting (such as in the MNiSn (M = Ti, Zr, Hf))[7, 59], metallic (such as in MCoSb (M = V, Nb))[60], and even may display half-metallic ferromagnetic behavior (MMnSb (M = Co, Ni)).[61] Some of these systems also display heavy-fermion characteristics (MYbBi (M = Pt, Ni))[62] The semiconducting half-Heusler systems are interesting from a thermoelectric perspective due to the large power factors (PF = $S^2\sigma$) observed in several of these semiconductors (MNiSn (M = Ti, Zr, Hf)).[61] An interesting feature of these semiconductors is the nature of the gap formation. The full-Heusler alloys with two Ni atoms/formula unit (such as MNi_2Sn (M = Ti, Zr, Hf)) are weakly semi-metallic as are the binary compounds MSn where the Ni atoms are completely removed. This means that the inclusion of the Ni atom has a subtle effect in opening the gap, an effect which will be explored in detail in this dissertation.[7, 59]

The half-Heusler structure (*F4-3m*) can be described as a filled NaCl structure (of YSb in Figure 12) where transition metal atoms are inserted in the octahedrally-coordinated interstitial sites. In this description, Ni atoms can be considered as guest atoms in a $Y^{3+}Sb^{3-}$ network. In the full-Heusler compounds, the Ni atoms occupy all of the tetrahedral holes in the lattice. An alternate way to describe the half-Heusler structure is to consider this as a filled adamantane, $[NiSb]^{3-}$, ZnS zinc-blend-type lattice in which the Y^{3+} occupy the octahedral holes in a diamond lattice.[63] The FCC Brillouin zone used for the electronic structure calculations of the half-Heusler compounds is given in Figure 13.

Figure 12. Two different perspectives of the cubic half-Heusler structure (YNiSb).

Left: Ni atoms inserted in a YSb NaCl-type lattice.

Right: Y atoms inserted in a NiSb ZnS-type lattice.

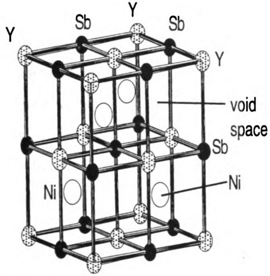
Y
Sb
Y
Sb
Y
void
space
Sb
Ni
Ni

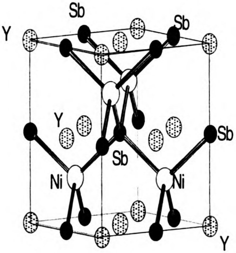
Sb
Y
Sb
Y
Sb
Sb
Ni
Ni
Y

Figure 13. FCC Brillouin zone.

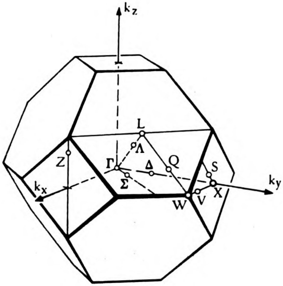
k_z
L
Λ
Z
Γ
Δ
Q
S
Σ
k_x
W
V
X
k_y

4.1. GAP FORMATION AND ELEMENTAL REPLACEMENTS

4.1.1. GAP FORMATION IN YNiSb AND ZrNiSn

The half-Heusler crystal structure includes many constituent compounds due to the large number of elements which can form the NaCl substructure and the transition (or noble) metal atoms which can go into the octahedrally-coordinated pockets. In order to find narrow-gap semiconductors for thermoelectric applications[25], it is necessary to know which combination of elements may produce semiconductors. In systems with *s*-*p* bonding there is the well known 8-electron rule which states that the valence electron count (EC) should equal 8 as seen in several semiconductors, where the binary compound can be written as $A^N B^{8-N}$ where element A has N valence electrons and element B has 8-N. Typical examples are given in Table I.[64]

Table I. 8 Electron Rule of Elemental Covalent Crystals[64]

Elements in Semiconductor AB	A Electron Count= N	B Electron Count= 8-N
A) & B) C, Si, Ge, α-Sn	4	4
A) P, As, Sb; B) Al, Ga, In	5	3
A) S, Se,Te; B) Zn, Cd, Hg	6	2
A) Br, I; B) Cu, Ag, Au	7	1

A similar electron-rule has been suggested for ternary systems which have filled *d* shells. One can imagine placing atoms with filled *d* shells into known binary semiconductors to form ternary semiconductors, assuming that the *d* orbitals interact very weakly with the *s*-*p* bonds. The filled *d* shell adds 10 valence electrons to the bi-

y semiconductor, which follows the 8 EC rule, to yield the 18 EC rule for ternary npounds.[65] This explanation has been applied to a wide variety of ternary sysns, including half-Heusler compounds. All known half-Heusler compounds which e semiconductors have EC = 18, while those known systems where EC $\neq$ 18 are mi-metallic, half-metallic, or metallic.[60, 61] To understand the gap formation of he half-Heusler compounds, one must determine whether EC = 18 is sufficient for he formation of the band gap or if it is only a necessary component.

One of the first semiconducting half-Heusler compounds which has been studied extensively for thermoelectric applications was ZrNiSn.[59, 66] This material has EC = 18 and a simple charge balance argument suggests the valences should be $Zr^{4+}Ni^{0}Sn^{4-}$. In the ternary compound ZrSn forms a NaCl lattice with the Ni atoms entering in an FCC configuration within the octahedrally-coordinated pockets. This material forms a semiconducting gap of about 0.17 eV[59, 66], in the right range for thermoelectric applications.[1, 2, 3] An obvious avenue to look for new semiconductors is to find new half-Heusler compounds where the valence of the atoms in the NaCl structure is changed without changing the transition metal atom so that EC = 18. One such system is YNiSb, where EC = 18 and a simple charge balance argument should yield $Y^{3+}Ni^{0}Sb^{3-}$, which will be discussed here.[7, 8, 67, 68, 69]

Before investigating the similarities and differences between ZrNiSn and YNiSb, it is important to understand the differences between the full-Heusler (*Fm-3m*) YNi_2Sb and half-Heusler (*F-43m*) YNiSb. According to the nominal valence count, i.e., Y^{3+}, Ni^{0}, and Sb^{3-}, both of these systems should be semiconducting, but, as one can see in Figure 14, the full-Heusler YNi_2Sb is metallic while the half-Heusler YNiSb is semiconducting, the same results seen in $ZrNi_2Sn$ and ZrNiSn.[59] The *d*-bands in the half-Heusler compound are about the same width in both compounds. The Ni *d*

itals interact with Y d orbitals the in the half-Heusler compound (Figure 14) while se bands simply cross in the full-Heusler compound. This appears to be due to higher symmetry of the full-Heusler compounds which does not allow for the oridization of the flat Ni d bands with the more dispersive Y d bands. A periodic ray of vacancies within the half-Heusler lattice, increasing the interaction of the Ni and Y d orbitals, appears to be necessary for the formation of the semiconducting ap.[70]

Figure 14. Band structure and comparison of the Ni d orbital characters in YNiSb and YNi_2Sb. The size of the circles is proportional to the orbital character.

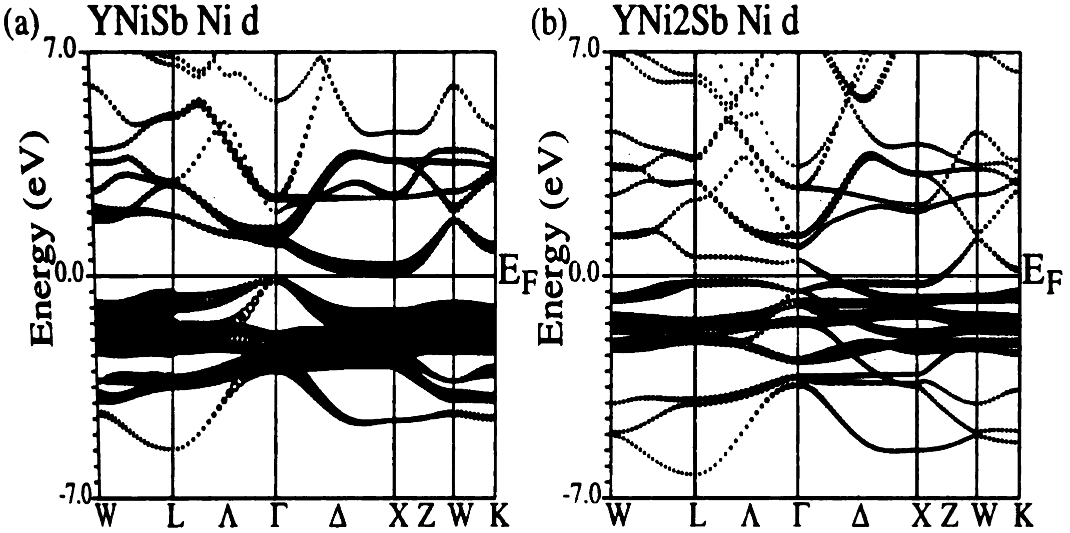

The electronic structure calculation of ZrNiSn (along with that of HfNiSn and TiNiSn) have been performed previously using a pseudopotential method by Ogut & Rabe[59, 66]. We have performed FLAPW calculations in these materials and in a new set of compounds, YNiSb and related systems.[7, 9] Our FLAPW calculations agree scale, the electronic structures of these two materials look very similar (Figure 15). The valence band maximum (VBM) forms at the Γ point while the conduction band minimum (CBM) is at the X point. The dispersion about this minimum is highly anisotropic, very flat along XΓ but much more dispersive along XW (Figure 15).[7, 8] Photoemission studies of ZrNiSn show that the Ni *d* peak appears approximately 2 eV below E_F[71] as predicted by our and previous calculations[7, 11, 59]. However, the TB-LMTO-ASA band structure for ZrNiSn provided by Slebarski *et al.* appears to be incorrect, the VBM forming along either ΓM or ΓK instead of at the Γ point.[7, 11, 59]

Figure 15. Electronic structure of ZrNiSn and YNiSb.

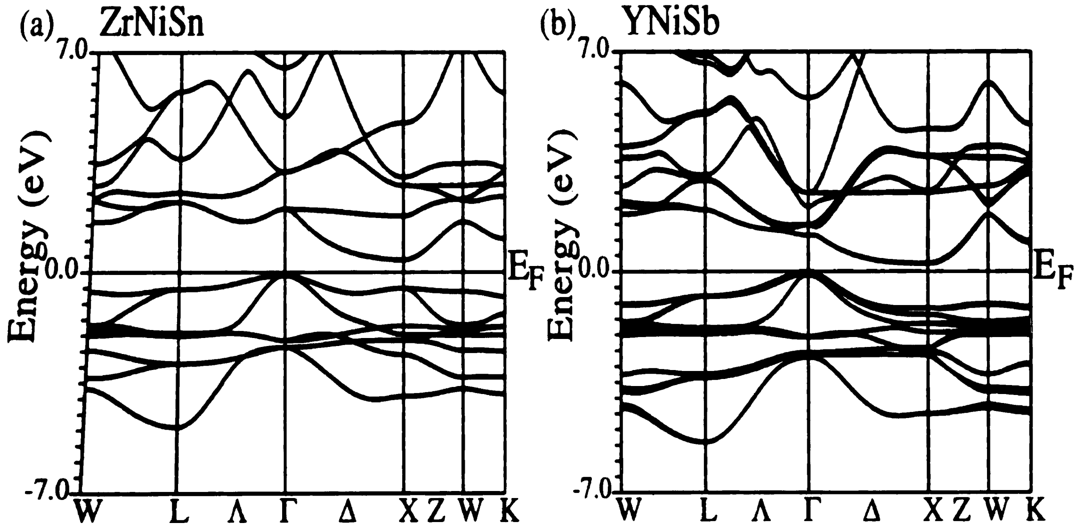

he half-Heusler compounds ZrNiSn and YNiSb contain parent binary compounds and YSb, respectively, as part of their NaCl sublattice. These compounds should miconducting according to a nominal valence count ($Zr^{4+}Sn^{4-}$and $Y^{3+}Sb^{3-}$) and C = 8 rule[64], but our calculations, performed at the ternary's equilibrium parameter (Figure 16), show semi-metallic behavior, violating the EC = 8 rule. The number of states at E_F for YSb is found to be 0.19 states/eV, a factor of 2.5-3 smaller than the earlier LDA results.[72] Ogut and Rabe (OR)[59] pointed out the significance of p-d hybridization along the ΓX direction on the energy gap of ZrSn. They argued that a strong **k**-dependent hybridization between Zr d_{xz} and d_{yz} and Sn p_x and p_y along (001) is one of the two reasons behind the gap formation at E_F. The strength of the Sn p and Zr d orbitals are shown in Figure 16a, and 16b, the strengths of the orbital characters being proportional to the size of the circles. The band labeled 2′ starts out with Sn p character at the Γ point and changes over to Zr d character at the X point. The band labeled 2 shows just the opposite behavior, evidence of strong **k**-dependent p-d hybridization between bands 2 and 2′, as pointed out by OR[59]. In YSb, however, this Sn p-Zr d hybridization is very weak, as seen in Figure 16c and 16d, yet the addition of Ni to form the half-Heusler structure opens very similar band gap. Therefore, it appears that, contrary to the suggestion of R[59], strong p-d hybridization is not a prerequisite for the formation of the band p in the half-Heusler compounds. Rather, as we argue in this dissertation, the esence of Ni d orbitals plays a significant role in the gap formation.[7]

Figure 16. Comparison of the different orbital characters of ZrSn (a) Sn p and (b) Zr d, and YSb (c) Sb p and (d) Y d. The size of the circles is proportional to the orbital character.

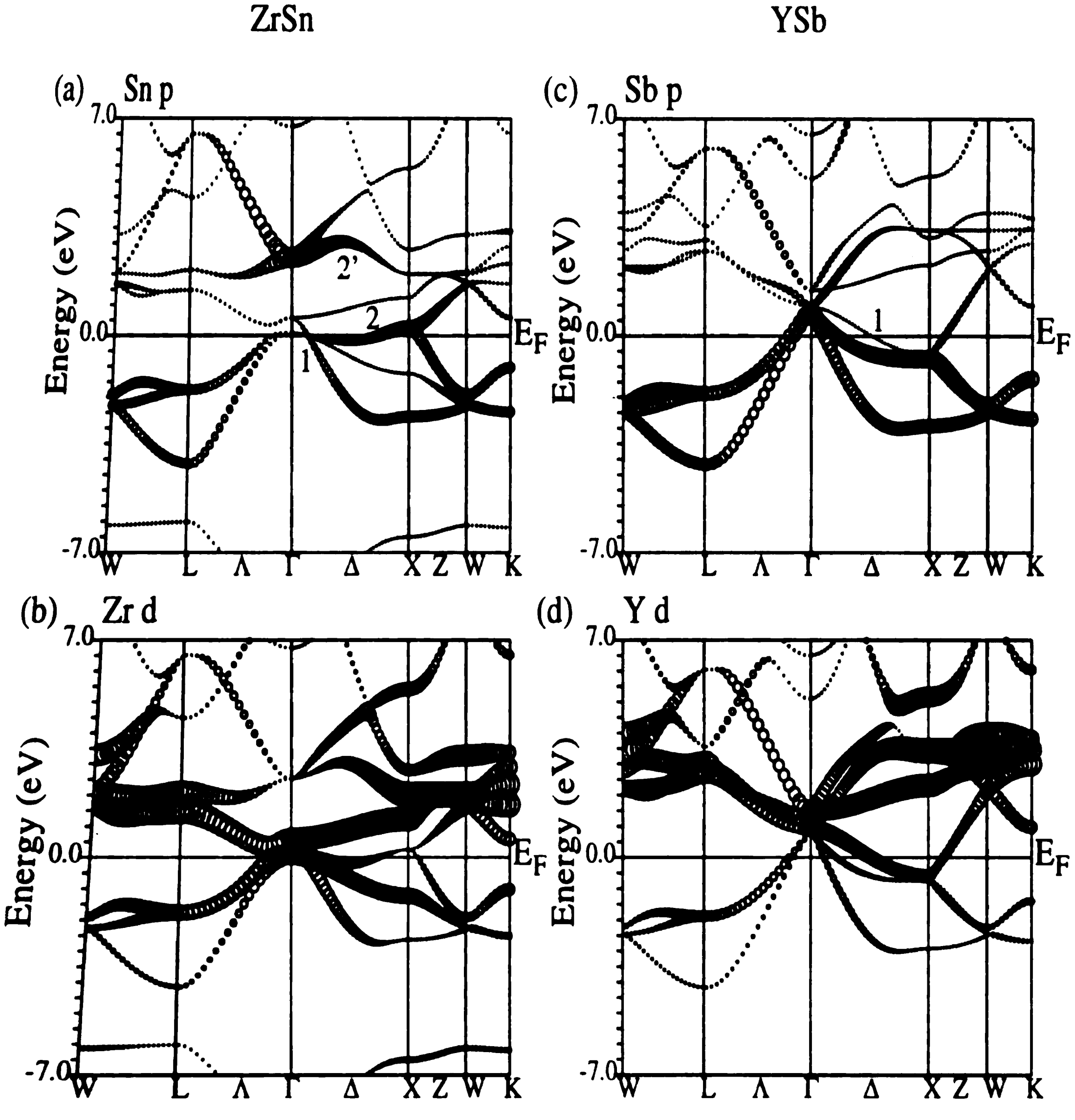

n ZrNiSn the Ni d orbitals affect the band structure in two ways. The hybridized -Zr d band with a large dispersion (labeled 1 in Figure 17a, which starts from Γ point with Γ_{12} symmetry at ~0.5 eV and goes to ~-2.5 eV at the X point $X_{4'}$ symmetry) in ZrSn hybridizes strongly with the Ni d orbitals (Figure 17c) and become the lowest conduction band (also labeled 1 in Figure 17a, along ΓX with X_3 symmetry at the X point). In addition, the strongly hybridized Sn *p*-Zr *d* band (labeled 2 in Figure 17a, which starts from the Γ point at ~0.0 eV and goes to ~0.1 eV at the X point) gets slightly modified. The energy of this band at the X point drops below that at the Γ point by about ~0.5 eV. The net effect is the formation of an indirect gap semiconductor with a gap of 0.50 eV, which agrees very well with the previous calculation.[59]

The situation appears to be different in YNiSb. The lowest Y *d* band, which has a downward dispersion from Γ to X (labeled 1 in Figure 17d) strongly hybridizes with the Ni *d* band and somewhat weakly with the Sb *p* band. This hybridization pushes the CBM at the X point above the VBM at the Γ point. The net result is the formation of an indirect narrow gap semiconductor, but in this case the gap is 0.28 eV, almost a factor of two smaller than that of the isoelectronic compound ZrNiSn. In spite of the basic differences in the nature of bonding, the electronic band structure in the neighborhood of the Fermi energy is remarkably similar in ZrNiSn and YNiSb. (*Figure 17*)[7]

Figure 17. Comparison of different orbital characters between ZrNiSn (a) Sn *p*, (b) Zr *d*, (c) Ni *d*, and YNiSb (d) Sb *p*, (e) Y *d*, (f) Ni *d*. the size of the circles is proportional to the orbital character.

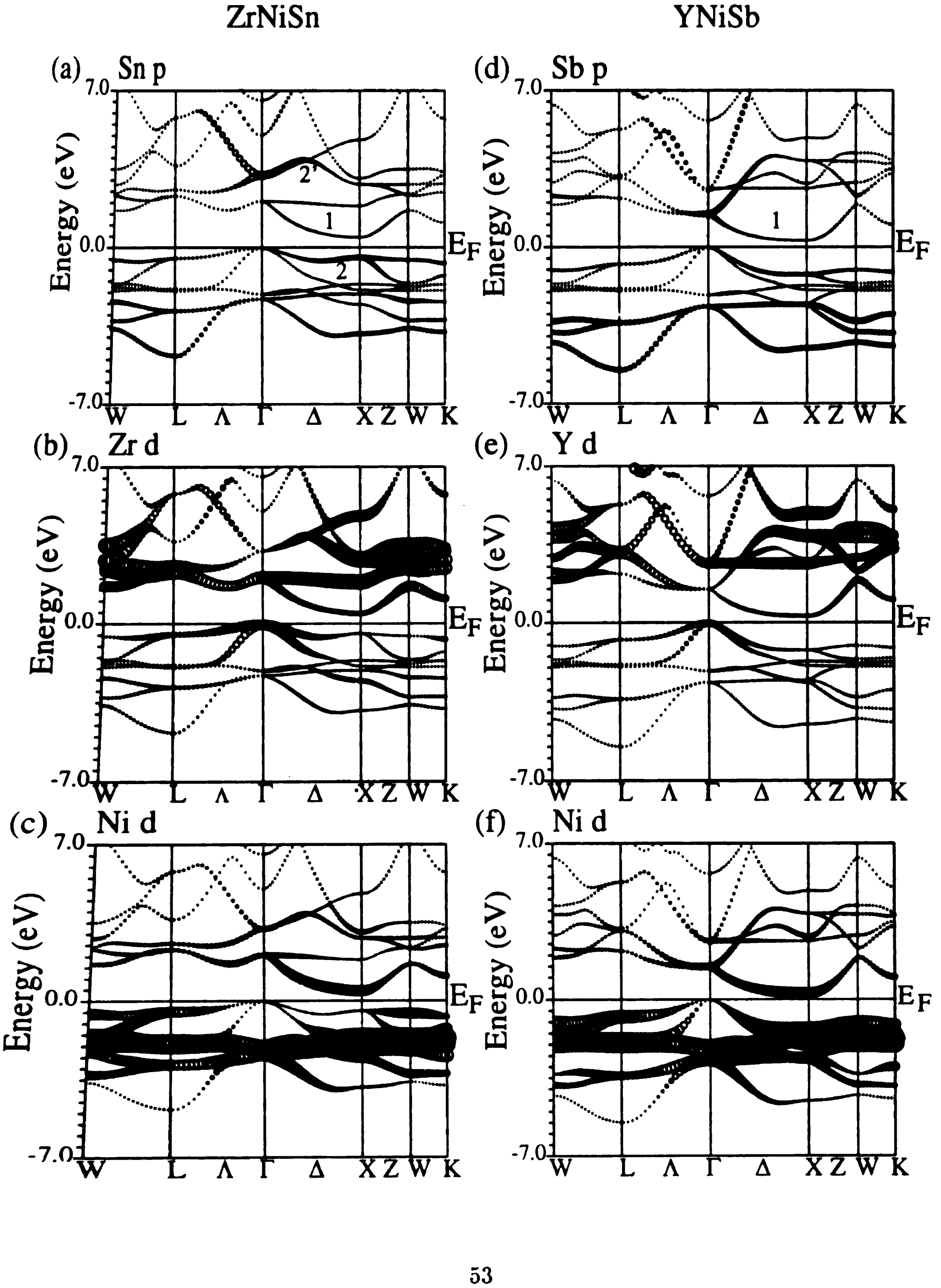

OR stated that the gap formation in ZrNiSn was due to the both strong Sn p-Zr d hybridization and the reduction of the crystal symmetry when a neutral Ni atom enters half of the octahedrally-coordinated sites of ZrSn.[59] In order to test this idea, we have placed He atoms in the Ni positions of ZrNiSn to form the hypothetical compound ZrHeSn. He will not contribute any orbitals to hybridize with ZrSn, but will reduce the crystal symmetry from NaCl to half-Heusler. No gap exists in ZrHeSn (Figure 18) since He has no d orbitals to hybridize with the Zr d orbitals. Thus the presence of Ni d orbitals to hybridize with Y/Zr d orbitals, rather than only lowering the symmetry produced by adding Ni to the NaCl sublattice to form the half-Heusler structure[59], is necessary for the formation of the small band gap in ZrNiSn and YNiSb.

Figure 18. The electronic structures of ZrHeSn and ZrNiSn using the same lattice parameter

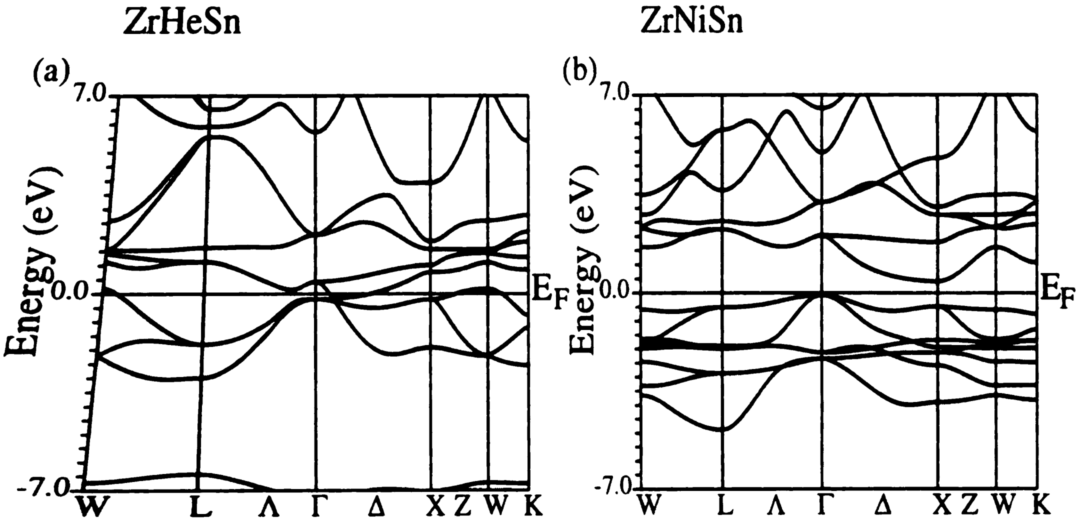

4.1.2. ELEMENTAL REPLACEMENTS: CHANGING THE PNICTIDES

It is well known that thermoelectric properties depend sensitively on the details of the electronic structure near E_F. The half-Heusler structure allows for a wide variety of elemental replacements which may affect these subtle features of the band structure while maintaining a semiconducting gap. We will discuss several of such replacements.

The first of these modifications which we will discuss is the change of the pnictides from As to Sb to Bi. Band structure calculations for YNiAs, YNiSb, and YNiBi show that all three are narrow-gap semiconductors (Figure 19). The band structures near E_F remain very similar, but the effects of SOI become more prominent in going from As to Bi. This is seen in the band gaps which decrease from 0.53 eV (YNiAs) to 0.31 eV (YNiSb) to 0.13 eV (YNiBi) in this series. The reduction in the band gap appears to correlate with the lowering of the pnictide s band (Figure 19), lying above E_F, and moving closer to E_F near the Γ point in going from As to Bi. In YNiAs, the As s orbital is nearly degenerate with the Y d orbitals at the Γ point but move down further in YNiSb and YNiBi. As these pnictide s levels become lower at the Γ point, the band along ΓX becomes flatter and the gap decreases.

Figure 19. Comparison of the electronic structures of YNiAs, YNiSb, and YNiBi. The size of the circles is proportional to the pnictide *s* orbital character.

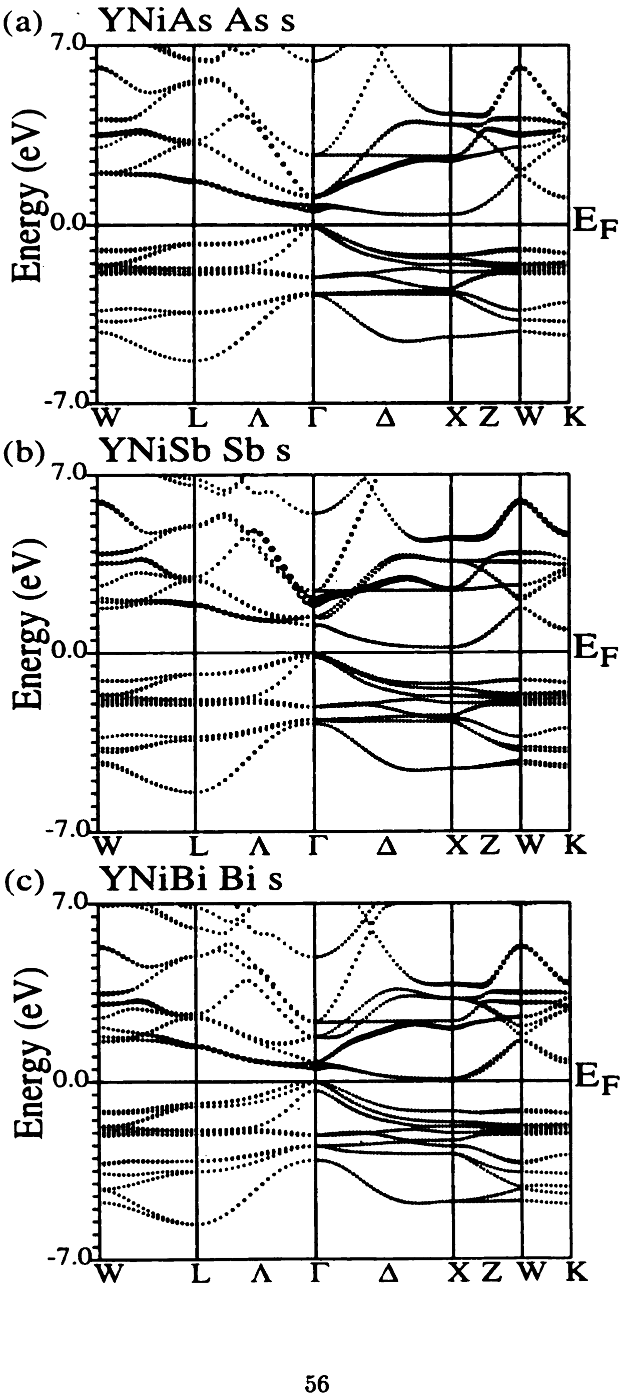

4.1.3. ELEMENTAL REPLACEMENTS: CHANGING THE TRANSITION METAL

The second type of elemental replacement we discuss is the change of the transition metal from Ni to isoelectronic Pd and Pt. In YNiSb, the Ni *d* orbitals lie approximately 2 eV below E_F while in YPdSb and YPtSb they are lower in energy, approximately 4 eV below E_F (Figure 20). Therefore, we would expect that the band gaps for YPdSb and YPtSb would be smaller than that for YNiSb since the Y *d*-Pt/Pd *d* hybridization in YPdSb and YPtSb would be weaker than the Y *d*-Ni *d* hybridization in YNiSb. However, the band gaps change from 0.31 eV (YNiSb) to 0.15 eV (YPdSb) to 0.21 eV (YPtSb), so that the Pd compound conforms to our expectations but the Pt compound does not. A second effect is also seen, stronger relativistic splitting at the valence band maximum (VBM) at the Γ point. The SOI splitting increases from 0.13 eV in YNiSb to 0.24 eV in YPdSb to 0.64 eV in YPtSb. A third effect is also present, which was also seen in the substitution of the pnictides, where the transition metal valence *s* orbitals move down closer to E_F. It is important to note that the gap becomes direct at the Γ point in YPtSb while the CBM is at the X point. Combination of these effects in YPtSb, including greater splitting of the VBM which moves down this peak, and the CBM moving from the X point to the Γ point due to the lowering of the Pt *s* band, explain the lower Pt d levels do not lead to a reduced band gap.

Figure 20. Comparison of the electronic structures of YNiSb, YPdSb, and YPtSb. The size of the circles is proportional to the transition metal *s* orbital character.

(a) YNiSb Ni s

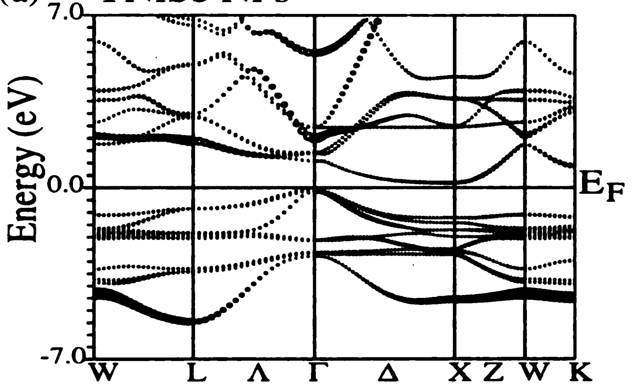

(b) YPdSb Pd s

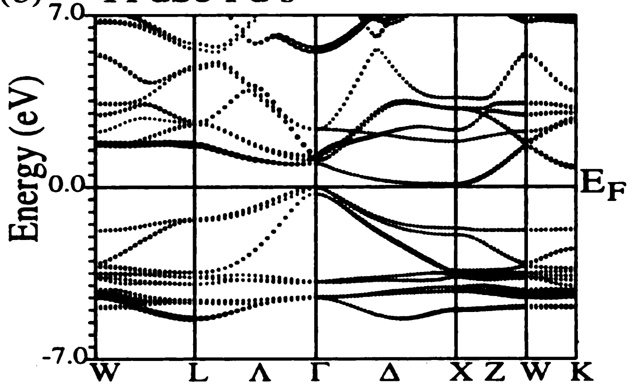

(c) YPtSb Pt s

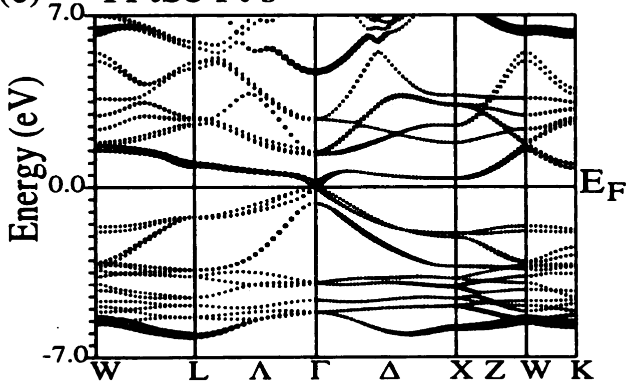

4.1.4. ELEMENTAL REPLACEMENTS: ROLE OF FILLED, UNFILLED, AND PARTIALLY FILLED f-LEVELS

A third type of elemental replacement comes from changing Y to a rare-earth element. It is well known that LDA/GGA calculations have difficulty with highly localized partially-filled f-shells, where the Fermi energy (E_F) is always placed in the middle of the very narrow f-band. Corrections such as LSDA+U can be introduced to partially correct for this in an *ad hoc* manner.[73] We have avoided this problem by replacing Y (Figure 21a) with atoms with either filled f-levels (Lu) or empty f-levels (La). The empty f-levels in LaNiSb lie approximately 3 eV above the Fermi energy, and have little effect on the band structure near the Fermi energy. (Figure 21b) On the other hand, the filled f-levels in LuNiSb, which lie at approximately -4.5 eV and -6 eV below E_F with a SOI splitting of 1.52 eV, push up the conduction band states slightly to reduce the band gap in this material. (Figure 21c) This can be seen in the band gaps going from 0.31 eV (YNiSb) to 0.40 eV (LaNiSb) to 0.19 eV (LuNiSb).[7] The observation that the empty Lu f-levels do not affect the band structure as much as the filled La f-levels may be due to greater f-d hybridization in the Lu compound or a lack of splitting of the La f-levels in the conduction band states which are not treated correctly in DFT[31].

The experimental structure for LaNiSb is actually known to be hexagonal instead of half-Heusler. The difference in the coordination of the Ni d orbitals and different hybridization between the Ni d and La d orbitals lead to a metallic instead of semiconducting behavior in this compound (Figure 21d).[69]

Figure 21. Electronic structures of (a) YNiSb, (b) FCC LaNiSb, (c) LuNiSb, and (d) hexagonal LaNiSb. The Ni *d* bands and La and Lu *f* bands are shown.

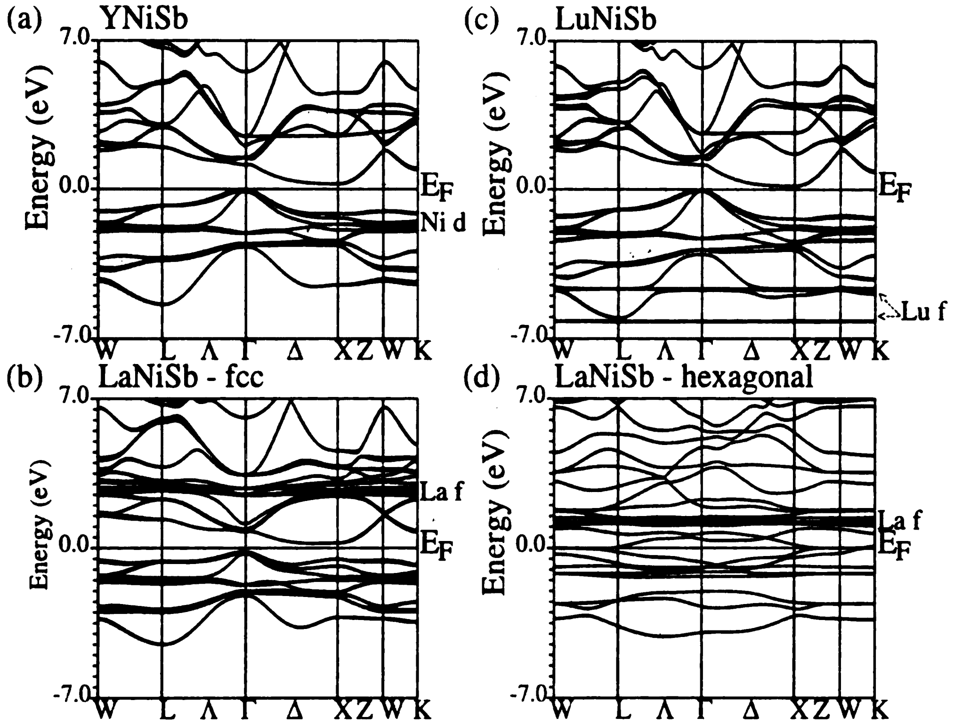

Although LDA/GGA is not adept for partially-filled, narrow-band systems, it has shown some success in handling *f*-electron systems with one electron (Ce) or one hole (Yb). In YbNiSb, Yb has one hole in the *f*-shell and is most likely a mixed-valence, heavy-fermion system.[68] Similar attempts to study the band structure of mixed-valence systems have been successfully made in CeRu$_2$Si$_2$.[74] The only previously published electronic structure of YbNiSb[67] (aside from our own[7]) was carried out at the scalar relativistic level within LDA using LMTO-ASA. Unfortunately, these results differ significantly from that of a closely related system, YbPtBi[62], and the calculated band structure[67] appears strange with several flat portions, implying a lack of convergence in the band structure calculation.

The metallic behavior of YbNiSb can be understood using the same technique as in the semiconducting compounds YNiSb and ZrNiSn by first studying the parent NaCl binary compound YbSb. YbSb displays a strong *f*-*p* hybridization near E_F although the majority of the *f*-levels are below E_F (Figure 22a). The SOI is quite strong for the *f*-levels and the splitting between $f_{\frac{5}{2}}$ and $f_{\frac{7}{2}}$ is about 1.25 eV (Figure 22b). The *f*-levels also become flatter as seen in the increase in the density of states (DOS) with SOI (Figure 22c, d).

Figure 22. Electronic structure of YbSb (a) without and (b) with SOI. The corresponding DOS (c) without and (d) with SOI are also given.

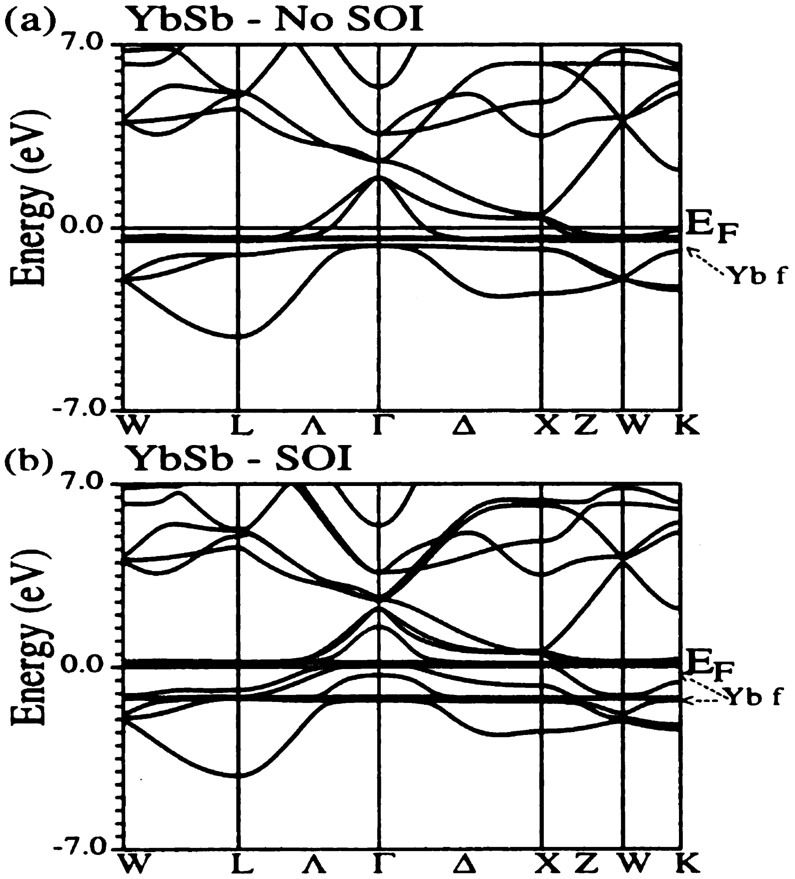

(c)

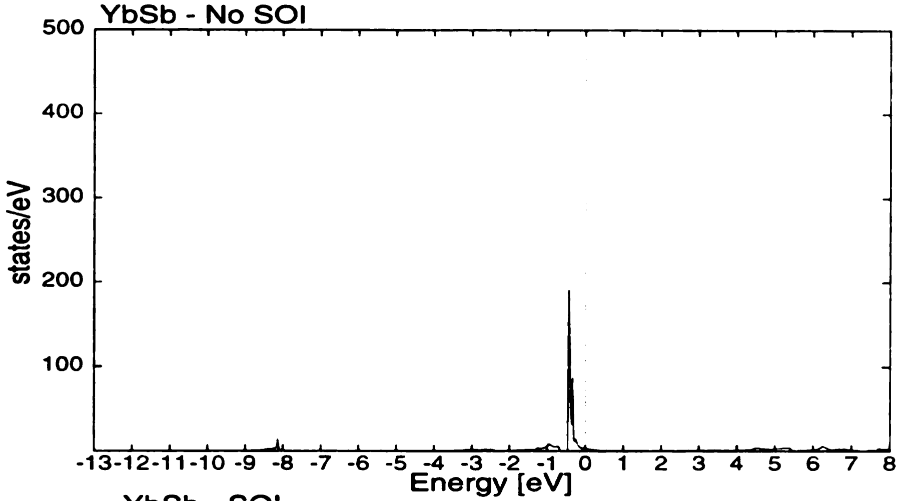

(d)

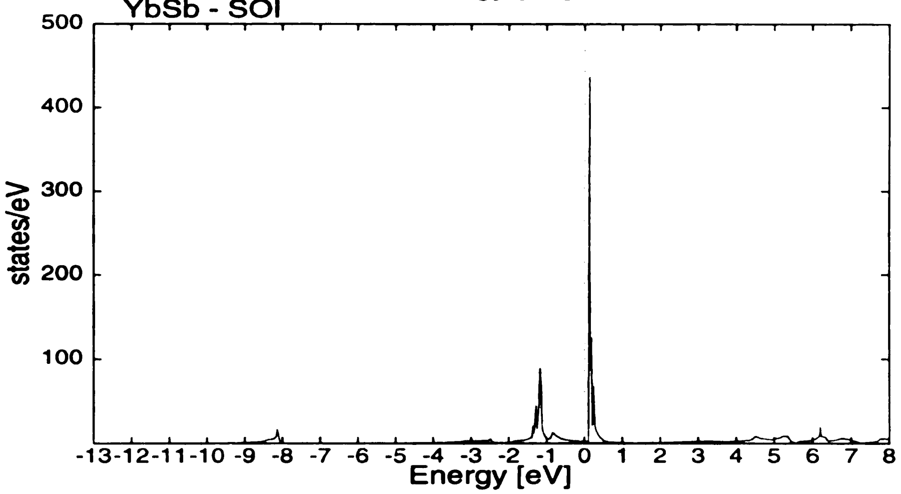

Insertion of Ni in the lattice to form YbNiSb places the Ni *d* orbitals below the *f* levels, which get pushed up in energy. As a result, there is a partial charge flow from the Yb *f* levels into the Sb *p* bands. (Figure 23a) Yb *f* levels become partially occupied and YbNiSb acquires a heavy fermion character much like YbPtBi, the splitting between $f_{\frac{5}{2}}$ and $f_{\frac{7}{2}}$ remaining about 1.25 eV (Figure 23b), in agreement with the calculations for YbPtBi.[62] The total density of states (TDOS) (Figure 23d) at the Fermi level, $N(\epsilon_F)$, is 12.6 states/eV, 77% of which is of Yb f character. In comparison, the corresponding numbers for YbPtBi are 4.5 states/eV and 60%, respectively.[62]

It should be emphasized that if we do not include SOI (Figure 23c), $N(\epsilon_F)$ reduces to about 6.9 states/eV and the *f* character is also reduced to about 61%. Therefore, SOI should play an important role in the low-energy properties (the linear term in the heat capacity and the transport properties) of this system.

Figure 23. Electronic structure of YbNiSb (a) without and (b) with SOI. The corresponding DOS (c) without and (d) with SOI are also given.

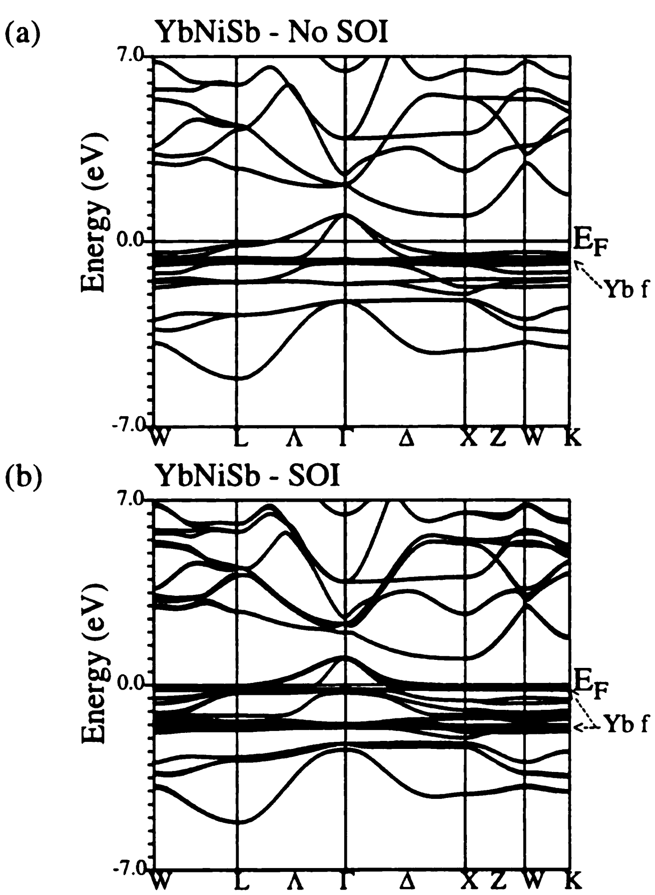

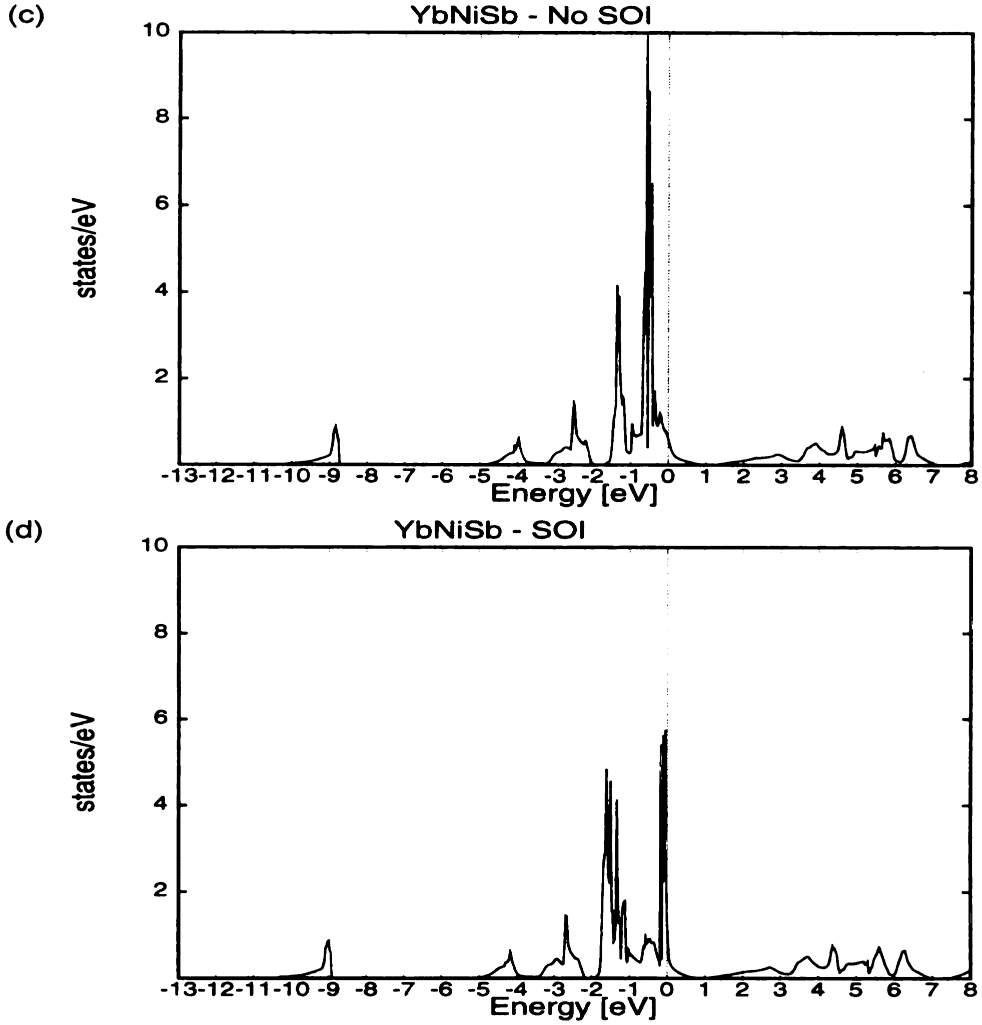

4.1.5 ELEMENTAL REPLACEMENTS OF Ni^0 WITH $Au^{1+}/Ag^{1+}/Cu^{1+}$

More semiconducting half-Heusler phases can be found if the transition metal is changed from Ni to another transition or noble metal with a valence other than 0 (+1, -1, +2, -2, etc.) with a corresponding change in the valence of the elements in the NaCl substructure so as to maintain EC = 18. When changing Ni to Cu (Ag,

Au), the valence goes from Ni^0 to Cu^{+1}(Ag^{+1}, Au^{+1}). Curiously, MgCuBi is the only Cu containing and MgAgAs the only Ag containing half-Heusler compounds which might be semiconductors, but no gap opens in either of these materials (Figure 24). It is clear that the EC = 18 rule does not work in these cases (Mg: N = 2, Cu: N = 11; Bi: N = 5; Mg: N = 2, Ag: N = 11; As: N = 5).[65, 70] It is important to note the lack of empty *d* valence orbitals in Mg compared to Zr, Y, La, Lu, etc., which were found to be the predominant factor in the gap formation of YNiSb and ZrNiSn.[7] It seems that the EC = 18 rule is a necessary but not sufficient condition for the opening of a semiconducting band gap.

Figure 24. Electronic structure of semi-metallic MgCuBi and MgAgAs.

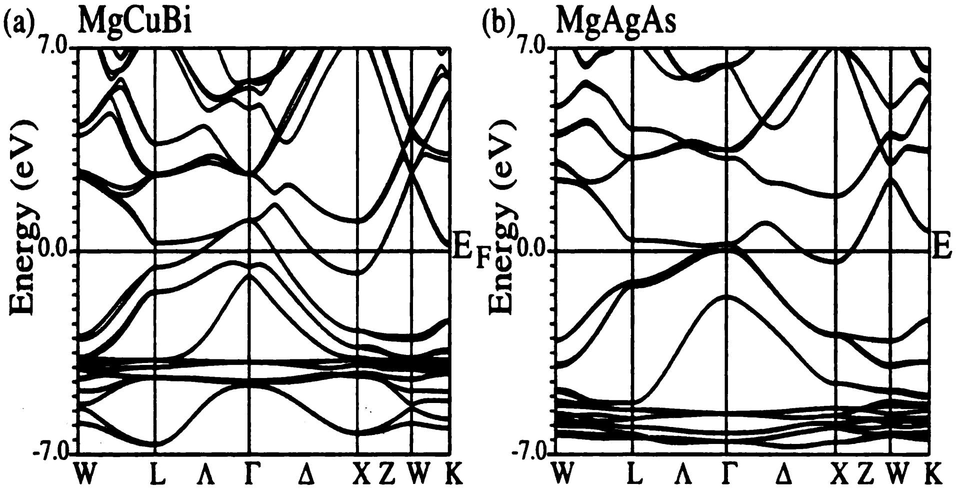

There are several potential semiconducting half-Heusler compounds containing Au. We will compare one of interest, Lu^{3+}Au^{1+}Sn^{4-} to the previously studied Ni compound Lu^{3+}Ni^{0}Sb $^{3-}$. The Au *d* orbitals appear at approximately 6.0 eV below E$_F$ (Figure 25a) compared to the Ni *d* orbitals which appear at approximately 2.0

eV below E_F (Figure 25b). Consequently, the hybridization of the Au *d* levels with the *d* orbitals of Lu is much smaller compared to that with the Ni *d* levels. The Au *d* contribution to the CBM at the X point in LuAuSn (Figure 25a) is much smaller than the Ni *d* contribution to the CBM at the X point in LuNiSb (Figure 25b). The strength of the Au *d* or Ni *d* characters in Figure 25 are proportional to the size of the circles. The weaker hybridization leads to a reduction in the band gap, becoming slightly negative in LuAuSn compared to 0.19 eV in LuNiSb (Figure 25).

Figure 25. Electronic structure of LuAuSn and LuNiSb. The Ni *d* bands lie closer to E_F than the Au *d* bands. The size of the circles is proportional to the orbital character.

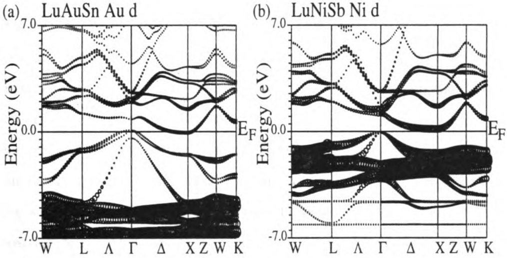

4.1.6. ELEMENTAL REPLACEMENTS OF Ni^0 WITH Co^{1-}/Rh^{1-}

Replacing Ni^0 by Co^{1-} and Rh^{1-} has the opposite effect of replacing Ni^0 by Au^{1+}. We will consider a representative compound, $Ti^{4+}Co^{1-}Sb^{3-}$, whose band structure can be compared with that of Ni-containing $Ti^{4+}Ni^0Sn^{4-}$. The band structure of TiNiSn is roughly the same as that of ZrNiSn with nearly the same band gap, 0.50 eV (Figure 26b).[59] The calculated band gap for TiCoSb is significantly larger, 1.08 eV (Figure 26a). The band structure for TiCoSb is different from all the semiconducting half-Heusler systems discussed so far. Its VBM moves from the Γ point, still predominantly of Sb *p* character, to the L point, primarily of Co *d* and Zr *d* character, as is the case for the CBM at the X point. The Co *d* level not only has a significant contribution below E_F, around -1 eV, but also above E_F around 2 eV. The flat Co *d* levels lying about 1.5 eV below E_F along WL push up the hybridized Co *d* and Ti *d* orbitals at the L point above the Sb *p* levels at the Γ point. The greater hybridization of the Ti *d* orbitals with Co *d* (Figure 26a) compared to Ni *d* orbitals (Figure 26b) near E_F leads to an increase in the band gap.

This relationship between the position of the transition (or noble) metal *d* orbitals and the band gap could be modeled by an effective Hamiltonian. The size of the band gap for a generic half-Heusler system could be predicted by knowing, for instance, the position of the Ni *d* orbitals in relation to the Zr *d* orbitals in ZrNiSn, and by comparing the calculated values of the band gaps. While we will not do this, our results suggest that such a modeling would be useful in further understanding the band gaps of the half-Heusler compounds.

Figure 26. Electronic structure of TiCoSb and TiNiSn. The Co *d* bands lie closer to E_F than the Ni *d* bands. The size of the circles is proportional to the orbital character.

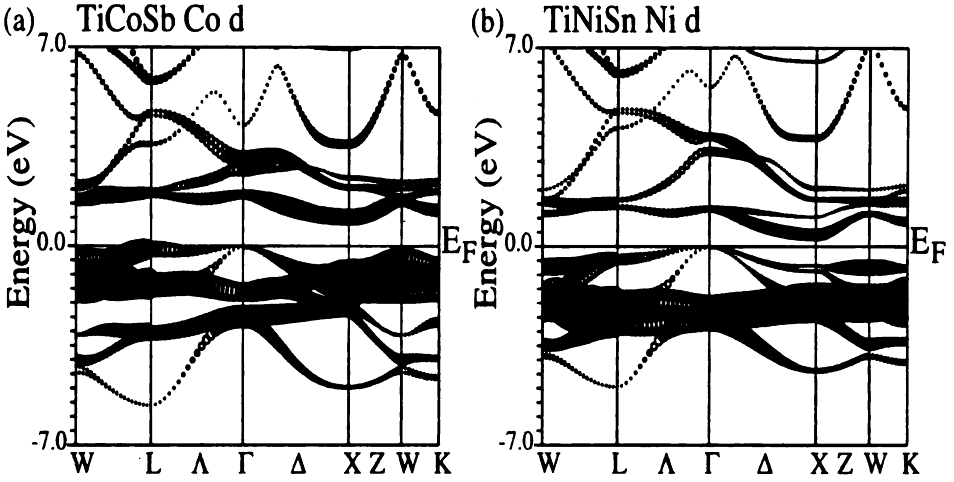

Unlike TiCoSb, in $Ti^{4+}Rh^{1-}Sb^{3-}$ the VBM moves back to the the Γ point from the L point as in $Ti^{4+}Ni^{0}Sn^{4-}$, with an even larger gap, 1.16 eV (Figure 27). The band along WL, which was pushed up to form the maximum in TiCoSb, is not pushed up as much in TiRhSb. The CBM also changes significantly in TiRhSb. In both of these materials, there are two bands near the CBM, a flat hybridized band of Rh *d* and Ti *d* and a more dispersive unhybridized Ti *d* band. In TiCoSb, this more dispersive band is 0.25 eV below the less dispersive band at the X point while in TiRhSb the flatter band is below the more dispersive band by about the same amount. This change in the dispersion in the conduction band should have an important effect on the thermoelectric properties of the electron doped system.

Figure 27. Electronic structure of TiRhSb.

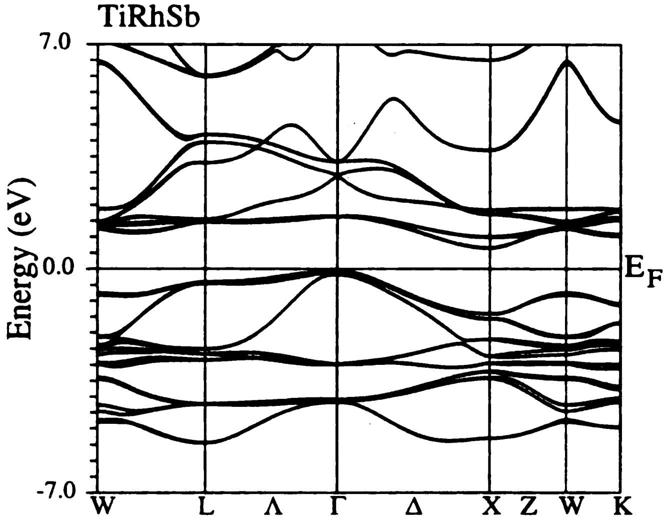

4.1.7. ELEMENTAL REPLACEMENTS OF Ni^0 WITH Fe^{2-}/Ru^{2-}

The last elemental replacement we will discuss is changing Ni^0 to Fe^{2-} and Ru^{2-}. Again we will compare $Y^{3+}Ni^0Sb^{3-}$ with a representative material, $Nb^{5+}Fe^{2-}Sb^{3-}$. As in TiRhSb, the LCB consists of two bands, a more dispersive unhybridized Fe *d* band and a flatter hybridized Fe *d*-Nb *d* band. The more dispersive Fe *d* band lies below the flatter hybridized Nb *d* and Fe *d* band, now by about 1 eV. As in TiCoSb, Fe *d* orbitals in NbFeSb split at about -0.5 eV to push up the bands between WL, producing a VBM at the L point. The calculated band gap is 0.53 eV, larger than the value of 0.28 in YNiSb.

Figure 28. Electronic structure of NbFeSb and YNiSb. Note the difference in curvature near the X point in the LCB.

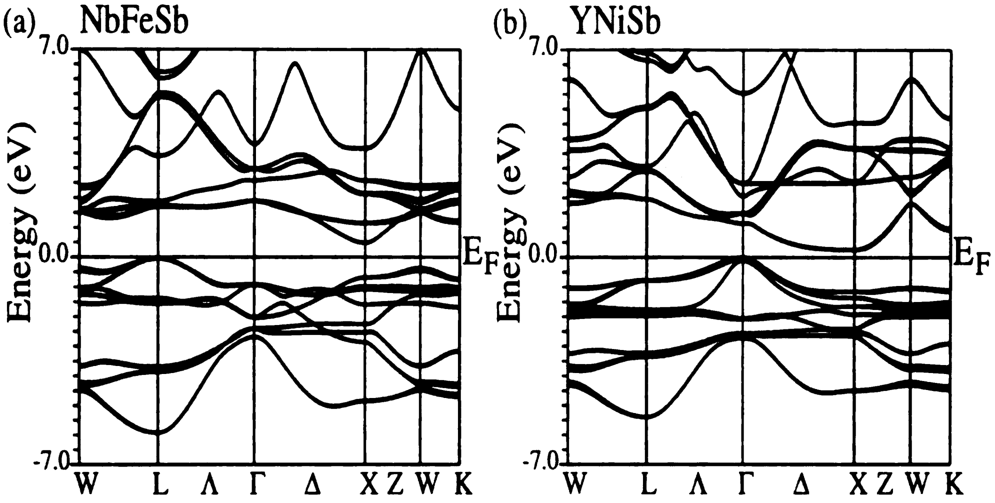

4.1.8. ELEMENTAL REPLACEMENTS OF Ni^0 WITH Mn^{3-}

Finally, the logical extension is to try Mn^{3-} as the transition metal in the half-Heusler structure. This does not yield any new semiconductors, since Mn often has a mixed valence. However, half-metallicity has been predicted in MnNiSb, where Mn forms part of the NaCl substructure rather than replacing the transition metal Ni atoms.[75] Half-metallic systems have a metallic majority spin (here *up*) state with a semiconducting minority (here *down*) spin state (Figure 29). Subsequent photoemission and transport measurements have found that the polarization, unlike the 100% which should exist in a truly half-metallic system, is only about 50%.[76] In the presence of weak Mn-Sb disorder (even on the order of 5%) the semiconducting gap seen in the minority spin channel disappears and the system becomes completely metallic (though still ferromagnetic)[75], consistent with nearly 10% Mn-Sb disorder which is seen experimentally.[76]

Figure 29. Calculated DOS of half-metallic MnNiSb for (a) up and (b) down spin states.

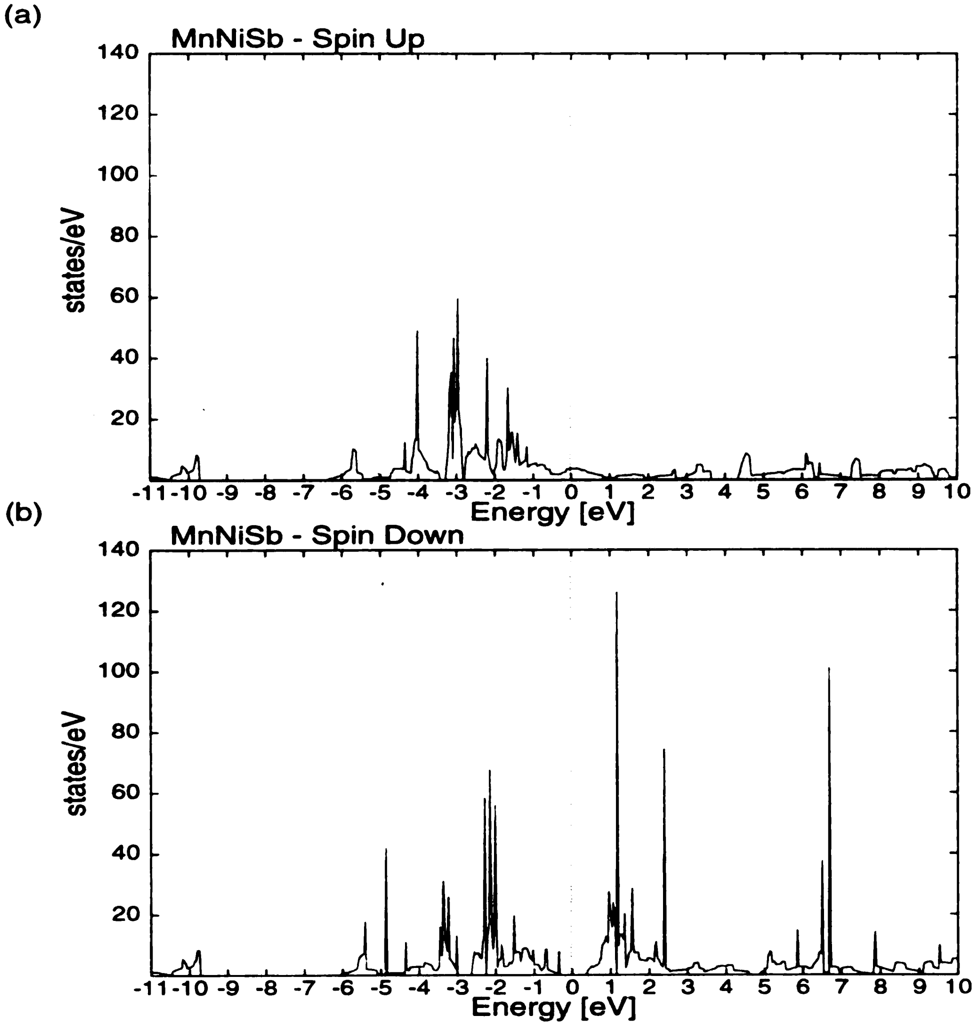

4.2. STRUCTURAL STABILITY OF HALF-HEUSLER COMPOUNDS

4.2.1. TOTAL ENERGY OF THE TERNARY SYSTEMS IN DIFFERENT STRUCTURAL CONFIGURATIONS

We have studied elemental replacements as important for the gap formation, but the positions of the atoms in the unit cell of the half-Heusler compounds also play an important role in the semiconducting gap formation and structural stability. There has been some confusion regarding the nature of the ordering of the atoms within the unit cell and which ordering gives the lowest energy. Ogut and Rabe (OR) have studied the stability of ZrNiSn, using LDA and the pseudopotential plane-wave method, within three possible configurations. They correctly identified the configuration of atoms with the lowest energy, the same configuration seen experimentally.[59] They, however, concluded that the inclusion of Ni atoms into the octahedrally coordinated pockets of the NaCl-type basis structure ZrSn had energetically very little effect on the stability of the final compound ZrNiSn. This would imply that Ni atoms essentially enter the above pockets as neutral atoms and do not take part in any sort of bonding with the neighboring Zr and Sn atoms. However, in the previous section we showed that hybridization of Ni atoms played a significant role in the gap formation. The effect of Ni atoms was not just simply to lower the local symmetry compared to the binary compounds, thereby leading to additional hybridization between Zr and Sn orbitals, forbidden in the absence of Ni, as envisaged by OR.[7, 9]

A recent paper by Ishida *et al.*[77] analyzed the structural stability of a series of half-Heusler compounds (without reference to the results of OR), using the LMTO-ASA method and LDA, and found that the lowest-energy configurations for most members studied were different from those seen experimentally.[66] This has led us to reevaluate the question of structural stability of the half-Heusler semiconductors using FLAPW.[11] To this end we have investigated the energetics of the same six systems studied by Ishida *et al.*[77]: NiTiSn, NiZrSn, NiHfSn, NiScSb, NiScSn, and NiTiSb.

Within this section only, the possible configurations of the constituent atoms inside the unit cell can be written in the same shorthand notation used by Ishida *et al.*[77] For a half-Heusler compound NiMP (M = Ti, Zr, Hf, Sc; P = Sn, Sb), this notation denotes the Ni atom as X, the M atom as Y, and the P atom as Z. The order of X, Y, and Z tells the relative positions of the atoms within the cell. The first letter refers to the atoms within the octahedrally coordinated pockets located at the position ($\frac{1}{4}$, $\frac{1}{4}$, $\frac{1}{4}$) while the second refers to the atom at position ($\frac{1}{2}$, $\frac{1}{2}$, $\frac{1}{2}$) and the third to the atom at position (0, 0, 0). Therefore, a configuration designated by XYZ has the Ni atom in the octahedrally coordinated pocket with the M and P atoms forming the NaCl substructure (written as NiMP) while YXZ exchanges the position of the Ni and M atoms within the cell (written as $M$Ni$P$) (Figure 30). These different configurations can also be distinguished by the Greek nomenclatures (α, β, γ) where α refers to the XYZ configuration, β refers to the ZYX configuration, and γ refers to the YXZ configuration, respectively.[59]

Figure 30. Half-Heusler crystal structures (a) XYZ, (b) ZYX, and (c) YXZ.

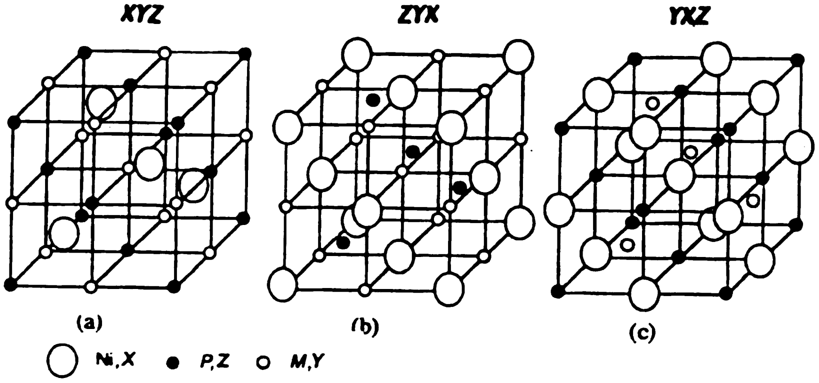

The total LAPW-GGA energies of one system of interest, NiTiSn, for these three different configurations of the constituent atoms in the unit cell as functions of the lattice parameter are given in Figure 31 (the lowest energy is set to zero).

Due to symmetry, interchanging the positions of the atoms comprising the NaCl substructure without changing the position of the atom within the octahedrally coordinated pocket gives the same energy within the convergence prescribed by the self-consistent iterations. The configuration which has the lowest energy is XYZ where the Ni atoms lie in the octahedrally coordinated pockets. The energy difference between this lowest-energy structure (XYZ) and the other two structures is about 2 eV/unit cell. The equilibrium lattice parameters for the YXZ and ZYX configurations also differ by about 0.2 A from that of the XYZ. The XYZ structure is the most compact, and there is a small energy difference between the YXZ and ZYX arrangements which is less than 0.1 eV/ unit cell. These results hold for all of the systems studied, including NiZrSn (Figure 32), whose results are consistent with the earlier pseudopotential calculation[59].

Figure 31. Total energies as a function of lattice parameter for the three different configurations of NiTiSn (the lowest energy is set to zero).

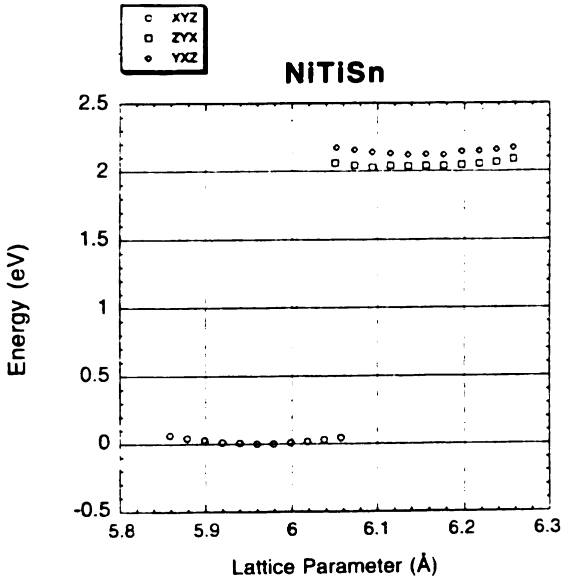

Figure 32. Total energies as a function of lattice parameter for the three different configurations of NiZrSn (the lowest energy is set to zero).

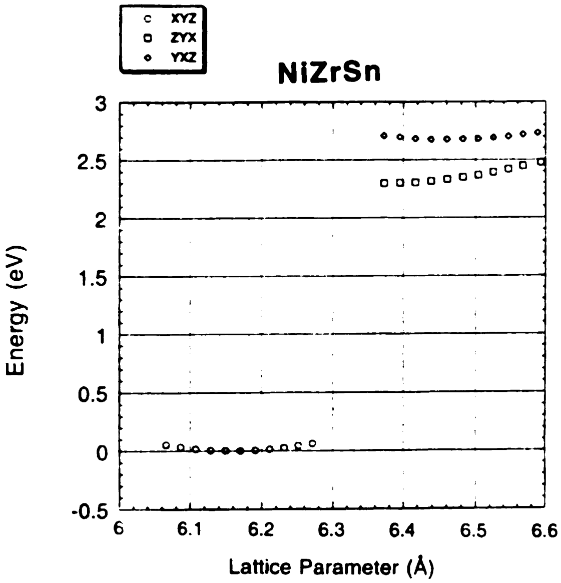

Our LAPW-GGA results for the six different compounds investigated by Ishida *et al.*[77] are listed in Table II. The first column lists the systems (XYZ) and their experimental lattice parameters (in a.u.), where available. The next three columns give the calculated equilibrium lattice parameters of the three types of atomic arrangements while the final three columns give the energy differences (in eV) between these different configurations. The configuration for each compound which Ishida *et.al.*[77] found to have the lowest energy is italicized. The results of LAPW-GGA differ dramatically from those of LMTO-ASA LDA, but these LAPW-GGA results for NiZrSn agree very well with those obtained with the pseudopotential LDA.[59] In order to see whether these differences were caused by LDA/GGA, both LDA and GGA were tested for NiZrSn. The differences between these two methods showed energy differences only on the order of 1-2%.

Table II. Experimental and calculated equilibrium lattice parameters and total-energy differences for half-Heusler systems (GGA).

System	Exp. (XYZ)	XYZ (α)	ZYX (β)	YXZ (γ)	ZYX-XYZ	YXZ-XYZ	YXZ-ZYX
	(a.u.)	(a.u.)	(a.u.)	(a.u.)	(eV)	(eV)	(eV)
NiZrSn	11.187	*11.261*	11.516	11.595	2.03	2.12	0.09
NiHfSn	11.463	11.572	11.955	*12.150*	2.43	2.67	0.24
NiZrSn	11.546	11.607	*12.042*	12.168	2.30	2.68	0.38
NiScSb	11.442	11.607	*11.942*	12.107	1.66	2.39	0.74
NiScSn	NA	11.690	*12.080*	12.121	2.23	2.19	-0.01
NiTiSb	11.187	11.291	11.589	*11.663*	1.51	1.37	-0.14

Figure 33. The electronic structures of (a) XYZ, (b) ZYX, and (c) YXZ configurations of NiTiSn.

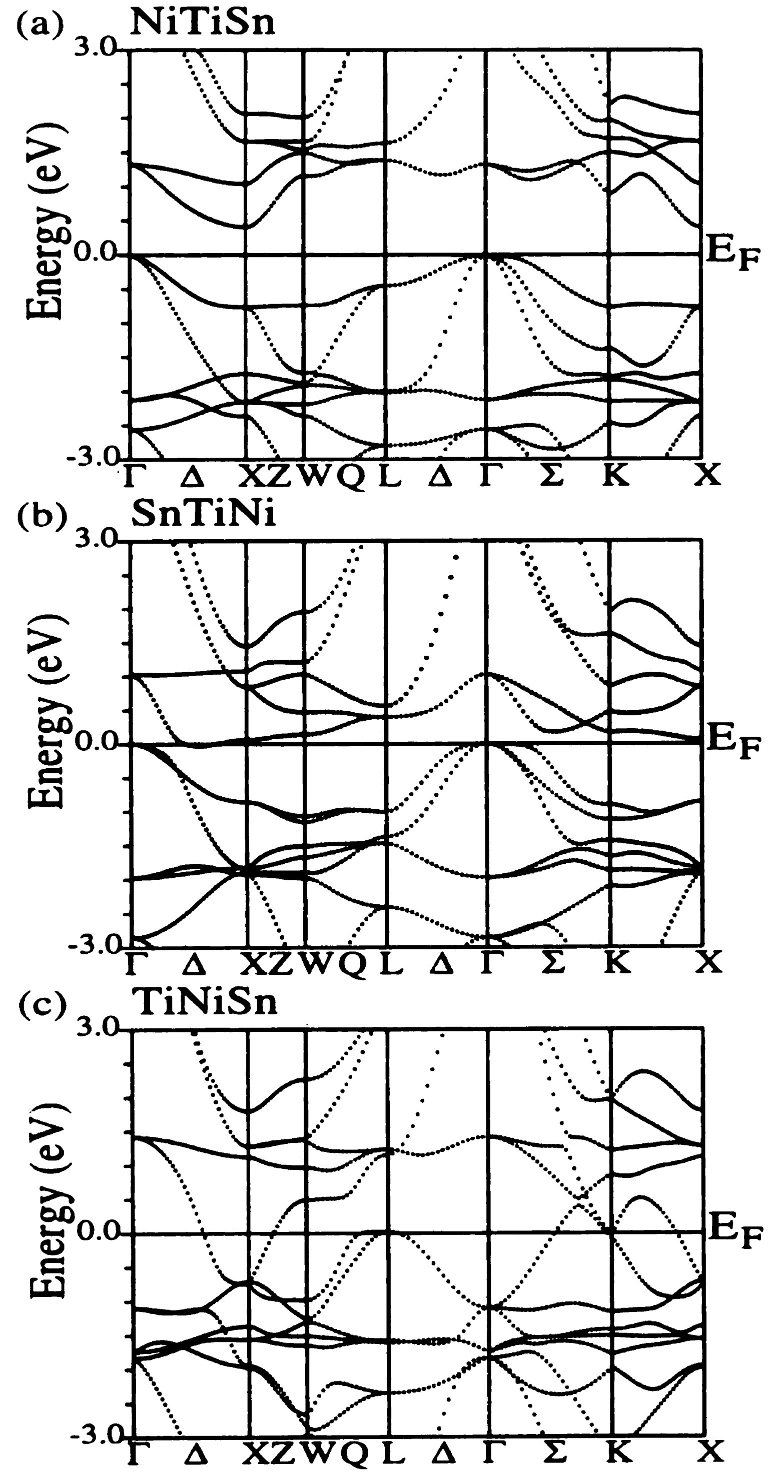

Figure 34. The electronic structures of (a) XYZ, (b) ZYX, and (c) YXZ configurations of NiZrSn.

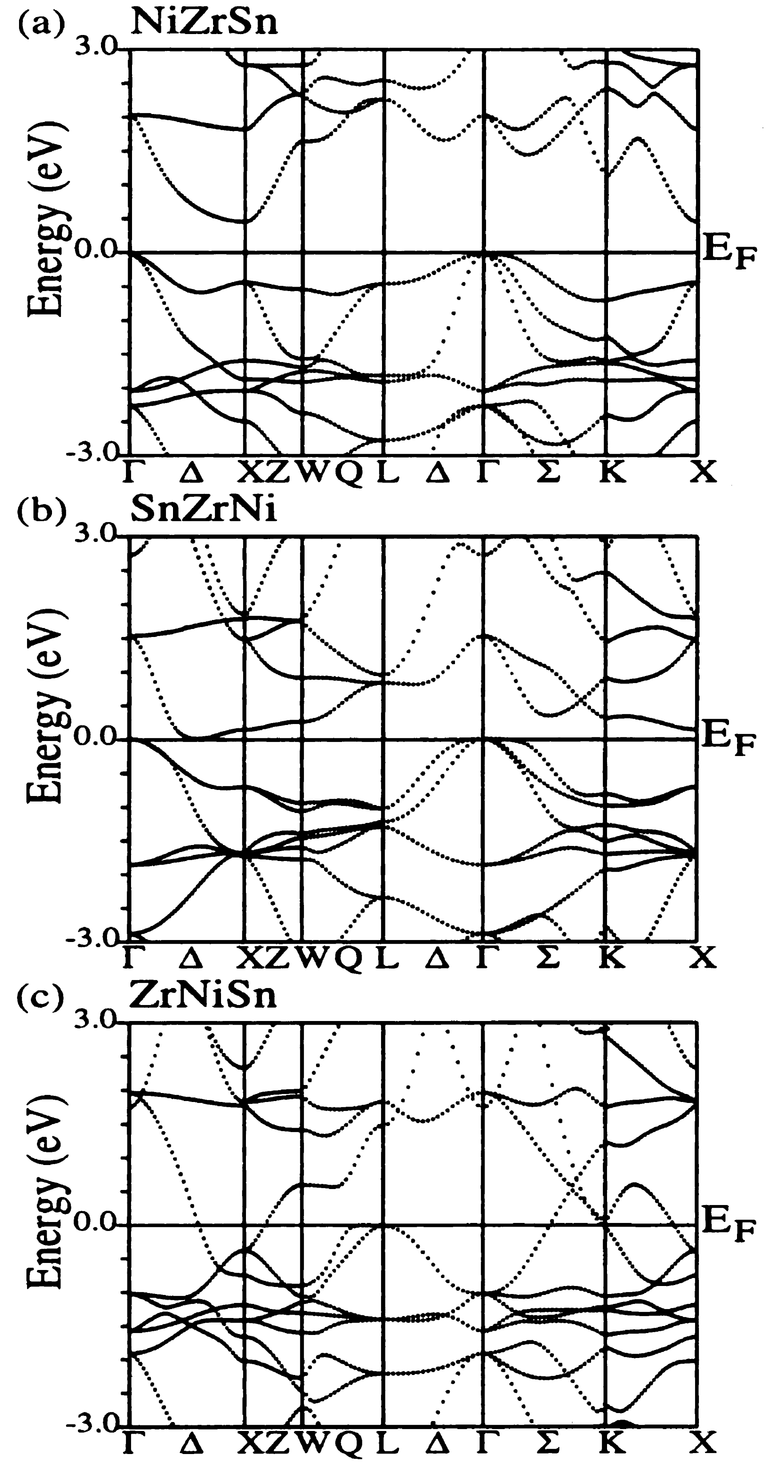

Comparison of the electronic structure in these three configurations shows a drastic effect. The electronic structures for NiTiSn in the XYZ (NiTiSn), ZYX (SnTiNi), and YXZ (TiNiSn) configurations are given in Fig. 32. As can be seen, the lowest energy configuration, NiTiSn, is a semiconductor with the VBM at the Γ point and the CBM at the X point, as seen in the previous calculations.[77] In SnTiNi, the lowest conduction band (LCB) along ΓX drops to form a zero-gap semiconductor. In TiNiSn, the LCB moves below E_F while the highest valence band (HVB) shifts away from the Γ point to the K point and moves above E_F to form a metallic system.[11]

These results also hold for the other semiconducting systems studied (NiZrSn, NiHfSn, NiScSb). The results for the different configurations of NiZrSn in Figure 34 agree with the pseudopotential calculations by OR.[59]

It is unclear from the paper by Ishida *et al.*[77] which lattice constants were used in their calculations. Also, the values of the energy differences between the different configurations were not given and the nature of the electronic states of these half-Heusler compounds in configurations other than XYZ were not discussed. They claimed that their results were sensitive to the muffin-tin radii (MTR) chosen, so the same MTR was kept the same for each configuration of the individual systems, given in Table III. In view of our present calculations, their suggestion that these half-Heusler systems can exist in configurations other than XYZ is not likely. Also it would disagree with several experiments on these materials.[66]

In order to understand the reason for the gap reduction in the ZYX and YXZ configurations, we have investigated the orbital character of the band structure at the relaxed lattice positions for the three configurations. A significant difference is seen in the position of the Ni *d* orbitals in each of these configurations (Figure 35). In the XYZ configurations, where Ni lies in the octahedrally coordinated pockets, the Ni *d* orbitals lie about 2 eV below E_F. In the ZYX configuration, where Ni forms part of the NaCl substructure with Ti and Sn is in the octahedrally coordinated pockets, the Ni *d* orbitals play a more prominent role in the valence band with less importance in the lowest conduction band which moves down to reduce the gap. In the YXZ configuration, where Ni forms in the NaCl substructure with Sn and Ti is in the octahedrally-coordinated pockets, the Ni *d* orbitals hybridize less with the Ti *d* orbitals and become prominent both above and below E_F, the system becoming metallic (Figure 35).

Table III. Muffin-tin radii of half-Heusler systems.

System	Muffin-tin radii (a.u.)
NiTiSn	2.33
NiHfSn	2.30
NiZrSn	2.36
NiScSb	2.31
NiScSn	2.37
NiTiSb	2.24

A few words should be said about NiTiSb and NiScSn, the two metallic half-Heusler structures which we have studied. As in the semiconducting cases, the lowest energy configuration is the XYZ, the same as seen experimentally. This means that the stability of this configuration need not be due to the formation of a band gap in the system. However, the YXZ has a lower energy than the ZYX in these two cases. In comparison, when XYZ was semiconducting, ZYX was a zero-gap semiconductor while the YXZ was metallic, while in these two systems all configurations are metallic.[11]

Figure 35. The electronic structures of (a) XYZ, (b) ZYX, and (c) YXZ configurations of NiZrSn. The size of the circles overlying the bandstructure are directly proortional to the with the Ni *d* character at each point.

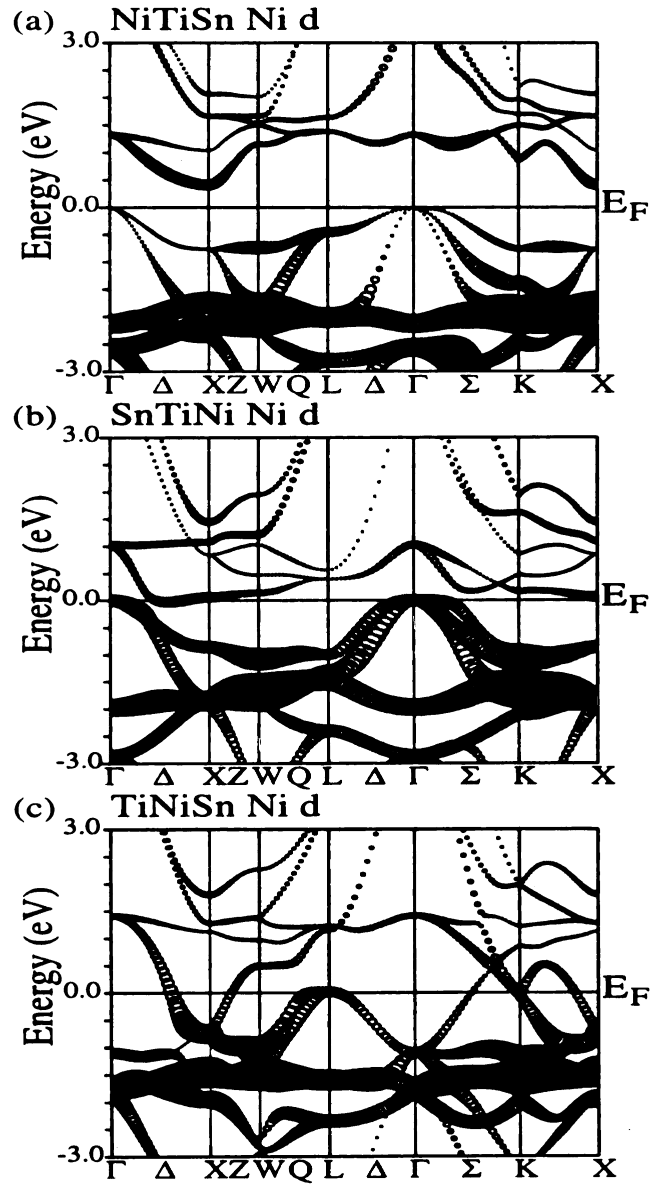

4.2.2. ANALYSIS OF THE STABILITY OF THE TERNARY COMPOUNDS BASED ON THE STABILITY OF THE BINARY PAIRS

Since we have found that the XYZ configuration has the lowest energy, we will follow the analysis by OR[59] who studied the energetics of the binary compounds which form in three different configurations in order to see which types of bonds lead to the stability of the ternary compounds. The half-Heusler compounds can be considered either as a NaCl lattice with atoms placed in half of the octahedrally-coordinated pockets or as a ZnS lattice with atoms placed within the voids of this network (Figure 12). The lowest energy configuration should in principle lower the interaction energy between all three components in the structure, so it is worthwhile to understand how each pair of atoms within the lattice interact in order to form the lowest energy configuration. In NiZrSn (XYZ), NiZr forms a diamond structure while ZrSn for a NaCl structure while in ZrNiSn(YXZ) ZrSn and NiZr both form diamond structures. In the calculation of OR[59], first the energies of the binary compounds were studied at a "fixed" lattice parameter for all three ternary configurations and were then compared to energies obtained at "relaxed" lattice parameters. We will show that a better understanding of the energetics arises from using the relaxed lattice parameters appropriate for these different configurations.

The energy differences between different configurations of the binary compounds are given in Table IV using LDA and the fixed lattice parameter, as was used by OR.[59] In the top third of the table, the results of the pseudopotential calculation of OR, in the middle third our LAPW-LDA results at the fixed lattice parameter. and in the final third our LAPW-GGA results at the fixed lattice parameter. The first column gives the binary system studied, the next three columns gives the crystal structure within the XYZ, ZYX, or YXZ configuration of the half-Heusler system, and the energy differences are tabulated in the last three columns, first between the half-Heusler systems and then between the binary systems from which it is composed.

Table IV. Total-energy differences for NiZrSn and different binary systems with fixed lattice parameters calculated using the pseudopotential LDA [Ogut and Rabe[59]] and using LAPW within LDA and GGA

NiZrSn	XYZ	ZYX	YXZ	ZYX-XYZ	YXZ-XYZ	YXZ-ZYX
			OR [59]	Pseudopotential	(LDA)	
11.546 a.u.				2.28 eV[a]	2.85 eV[a]	0.57 eV[a]
				Diamond-NaCl	Diamond-NaCl	Diamond-diamond
ZrSn	NaCl	Diamond	Diamond	2.03 eV	2.03 eV	0 eV
				NaCl-diamond	Diamond-diamond	Diamond-NaCl
NiZr	Diamond	NaCl	Diamond	0.26 eV	0 eV	-0.26 eV
				Diamond-diamond	NaCl-Diamond	NaCl-diamond
NiSn	Diamond	Diamond	NaCl	0 eV	0.23 eV	0.23 eV

NiZrSn	XYZ	ZYX	YXZ	ZYX-XYZ	YXZ-XYZ	YXZ-ZYX
				LAPW (LDA)		
11.546 a.u.				2.63 eV	3.29 eV	0.66 eV
				Diamond-NaCl	Diamond-NaCl	Diamond-diamond
ZrSn	NaCl	Diamond	Diamond	2.03 eV	2.03 eV	0 eV
				NaCl-diamond	Diamond-diamond	Diamond-NaCl
NiZr	Diamond	NaCl	Diamond	0.50 eV	0 eV	-0.50 eV
				Diamond-diamond	NaCl-Diamond	NaCl-diamond
NiSn	Diamond	Diamond	NaCl	0 eV	0.76 eV	0.76 eV

NiZrSn	XYZ	ZYX	YXZ	ZYX-XYZ	YXZ-XYZ	YXZ-ZYX
				LAPW (GGA)		
11.546 a.u.				2.60 eV	3.25 eV	0.65 eV
				Diamond-NaCl	Diamond-NaCl	Diamond-diamond
ZrSn	NaCl	Diamond	Diamond	2.33 eV	2.33 eV	0 eV
				NaCl-diamond	Diamond-diamond	Diamond-NaCl
NiZr	Diamond	NaCl	Diamond	0.22 eV	0 eV	-0.22 eV
				Diamond-diamond	NaCl-Diamond	NaCl-diamond
NiSn	Diamond	Diamond	NaCl	0 eV	0.51 eV	0.51 eV

[a]Energy differences for ternary compounds calculated by OR[59] computed at relaxed lattice parameters

Overall, the calculated energy differences between the different configurations obtained using pseudopotential-LDA and LAPW-LDA agree fairly well (Table IV). The largest energy difference is seen for the ZrSn configuration in a NaCl over a diamond structure. However, there still are differences between the methods. The difference in the energies between the NaCl and diamond structures in NiZr is found to be 0.50 eV in LAPW compared to 0.26 eV in the pseudopotential method. Also, the energy difference between the NaCl and diamond structures in NiSn is found to be 0.76 eV in LAPW compared to 0.23 eV in the pseudopotential method. As has been noted before, this pseudopotential calculation missed a significant contribution to the CBM above E_F which came from the Ni *d* orbitals. Comparison of the pseudopotential-LDA and LAPW-GGA finds that these actually have better agreement compared to the pseudopotential-LDA and LAPW-LDA. The difference between NiZr in the NaCl and diamond phases is only 0.22 eV in the LAPW-GGA compared to 0.26 eV in the pseudopotential calculation and for NiSn it is only 0.51 eV in the LAPW-GGA compared to 0.23 eV in the pseudopotential calculation.[59]

Table V. Relaxed equilibrium lattice parameters and total-energy differences for NiZrSn and different binary subsystems calculated using LAPW within LDA and GGA.

NiZrSn	XYZ	ZYX	YXZ	ZYX-XYZ	YXZ-XYZ	YXZ-ZYX
				LAPW (LDA)		
11.546 a.u.[a]	11.429 a.u.	11.735 a.u.	11.928 a.u.	2.50 eV	2.98 eV	0.48 eV
				Diamond-NaCl	Diamond-NaCl	Diamond-diamond
ZrSn	NaCl	Diamond	Diamond	1.99 eV	1.89 eV	-0.10 eV
				NaCl-diamond	Diamond-diamond	Diamond-NaCl
NiZr	Diamond	NaCl	Diamond	1.08 eV	0.72 eV	-0.37 eV
				Diamond-diamond	NaCl-Diamond	NaCl-diamond
NiSn	Diamond	Diamond	NaCl	0.32 eV	1.49 eV	1.17 eV

NiZrSn	XYZ	ZYX	YXZ	ZYX-XYZ	YXZ-XYZ	YXZ-ZYX
				LAPW (GGA)		
11.546 a.u..[a]	11.261 a.u.	12.042 a.u.	12.168 a.u.	2.30 eV	2.68 eV	0.38 eV
				Diamond-NaCl	Diamond-NaCl	Diamond-diamond
ZrSn	NaCl	Diamond	Diamond	1.78 eV	1.71 eV	-0.07 eV
				NaCl-diamond	Diamond-diamond	Diamond-NaCl
NiZr	Diamond	NaCl	Diamond	1.16 eV	0.68 eV	-0.47 eV
				Diamond-diamond	NaCl-Diamond	NaCl-diamond
NiSn	Diamond	Diamond	NaCl	0.36 eV	1.30 eV	0.95 eV

[a] Experimental value.[59]

These energetics are found to be dependent also on the lattice parameters chosen.

Table V is set up in the same way as Table IV except that the lattice parameters for the minimum energy configurations for the three different arrangements (XYZ, ZYX, YXZ) are used in the calculation of the energetics of the ternary and binary systems in our LAPW calculations.

For NiZrSn the energy difference between the XYZ and ZYX (YXZ) configuration for LDA is 2.50 eV (2.98 eV)/unit cell and for GGA is 2.30 eV (2.68 eV)/unit cell, whereas the energies of the ZrSn substructure originating from the XYZ and ZYX (YXZ) configurations for LDA is 1.99 eV (1.89 eV)/unit cell and for GGA is 1.78 eV (1.71 eV)/unit cell, about three-fourths of the energy gain found in the ternary. The energy difference between the XYZ and ZYX structures for NiZr is 1.08 eV for LDA and 1.16 eV for GGA, 30-50% less than that for ZrSn. Similarly, the energy difference between the XYZ and YXZ structures for NiSn is 1.49 eV for LDA and 1.30 eV for GGA, each about 25% less than that for ZrSn. Comparing these numbers to those obtained at fixed lattice parameters, it is clear that the relaxation has a strong effect on the relative energies of the binary compounds. For example, comparing the NaCl and diamond phases of NiZr and ZrSn, for GGA the NiZr energy difference is only 10% of that for ZrSn using the fixed lattice parameters but becomes 65% that of ZrSn using the relaxed parameters. Similar values are found for both LAPW-LDA and LAPW-GGA. Also, we have showed that the LAPW-LDA and LAPW-GGA give similar results to the previous pseudopotential calculation at fixed lattice parameters, so the difference in the analysis is due to the effects of lattice relaxation.[59]

The energy differences for NiTi and NiSn in the incorrect configuration using the relaxed parameters showed that they were an appreciable part of the relaxation energy, much more than obtained using the fixed lattice parameters. Also, the pseudopotential calculation by OR[59], which attributed so much to having TiSn in the NaCl configuration as the main lowering in energy in the half-Heusler structure, missed the important contribution of the Ni *d* orbitals in the CBM which are so important to the gap formation. Therefore, in the structural stability of the half-Heusler system, the Ni *d* orbitals play an important, although secondary role to the configuration of TiSn, in the structural stability of the half-Heusler system.

4.2.3. ENERGETICS OF ANTI-SITE DEFECTS

Anti-site defects within Ni*MP* compounds have been used to explain why the calculated band gaps of the half-Heusler systems are larger than the experimental values[81], an unusual property since LDA usually underestimates the band gaps of semiconductors. OR performed a series of calculations within the virtual-crystal approximation for $\mathrm{Ni(Sn_{1-x}Zr_x)(Sn_xZr_{1-x})}$ for a few values of x lying between $x = 0$ and $x = 0.5$. They found that the band gap indeed decreased with increasing x to produce a semi-metal when $x = 0.15$.[59]

This argument for the band gap reduction is based on x-ray diffraction studies done at low temperatures (<250 K) which found anti-site disorder in the NaCl sublattice of ZrNiSn (ZrSn) but no disorder in the Ni sublattice after annealing.[78] The temperature range in which these materials are expected to be used for thermoelectric applications is anywhere from 300 to 700 K[66], where the structure has not been fully investigated. In fact, a Ni-defect phase was detected before annealing with different lattice parameters a_I and a_{II} which disappears after annealing.[79] Therefore, defects in the Ni sublattice and within the *MP* framework and their effect on the electronic structure need to be investigated.

We have investigated the effects of Ni and Zr-Sn disorder in the simple cubic supercell $\mathrm{(NiZrSn)_4}$. This allows for changing the positions of the 12 atoms (4 Ni, 4 Zr, and 4 Sn) to see the effects of disorder within the lattice either by exchanging their positions or moving atoms from their ideal positions to one of the 8 octahedrally-coordinated sites (4 of which are occupied in the ideal structure). Configurations of these atoms with disorder in the ZrSn sublattice are shown in Figure 36.

Figure 36. Crystal structures of (NiMP)$_4$ supercell for (a) $Ni_4(Zr_3Sn)(Sn_3Zr)$, (b) $(Ni_3Sn)Zr_4(Sn_3Ni)$, and (c) $(Ni_3Zr)(Zr_3Ni)Sn_4$.

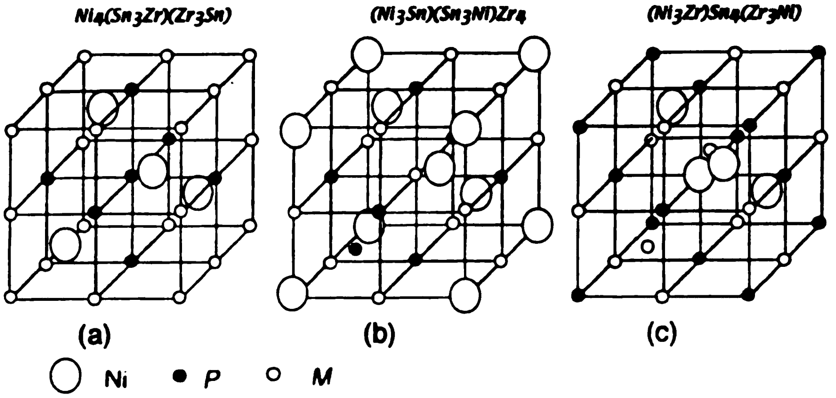

We find that exchanging the positions of Sn/Zr atoms with the Ni atoms or other Sn/Zr atoms within the supercell (to produce a different configuration) produces a fairly substantial increase in the energy. Using the relaxed parameters and atomic radii used for the lowest energy configuration, the total energy differences are given in Table VI. Switching one Ni and one Zr (Sn) atom increases the energy by a fairly large amount, 1.71 (1.98) eV/FCC unit cell while switching one Zr atom with one Sn atom has a smaller energy increase (1.25 eV/FCC unit cell). This is in agreement with our calculations for the structural stability of *MP* NaCl and the greater stability of Ni within the octahedral pockets of *MP*. In order to understand the effects of Ni when switching the Zr and Sn positions, we have also calculated the difference in energy in switching the position of one Zr and one Sn atom in $Ni_4Zr_4Sn_4$ and compared that with the energy change when the same positions where switched in Zr_4Sn_4. The energy difference was 1.25 eV/FCC unit cell in $Ni_4Zr_4Sn_4$ compared to 1.10 eV/FCC unit cell in Zr_4Sn_4, the Ni contributing 0.15 eV/unit cell due to the changed Zr/Sn environment.

Table VI. Energetics of site-switching on NaCl substructure of NiZrSn supercell (GGA).

System	Energy - energy $Ni_4Zr_4Sn_4$ (eV)	ΔE/FCC unit cell (eV)
$Ni_4Zr_4Sn_4$	0	0
$Ni_4(Zr_3Sn)(Sn_3Zr)$	4.99	1.25
$(Ni_3Sn)Zr_4(Sn_3Ni)$	6.82	1.71
$(Ni_3Zr)(Zr_3Ni)Sn_4$	7.93	1.98
Zr_4Sn_4	0	0
$(Zr_3Sn)(Sn_3Zr)$	4.39	1.10

In each of the cases where the positions have been changed, the band structure becomes metallic (Figure 37). OR claimed that the band gap closed for 15% Sn-Zr disorder[59], whereas we have studied only 25% disorder in the supercell.

Figure 37. Electronic structures of (a) $Ni_4Zr_4Sn_4$, (b) $Ni_4(Zr_3Sn)(Sn_3Zr)$, (c) $(Ni_3Sn)Zr_4(Sn_3Ni)$, and (d) $(Ni_3Zr)(Zr_3Ni)Sn_4$.

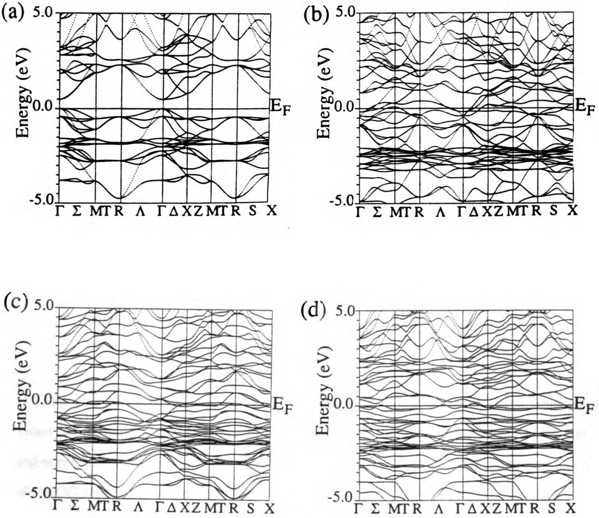

A different scenario for anti-site defects in half-Heusler is for the Ni atoms, within the octahedrally-coordinated pockets, to lie outside an FCC configuration by exchanging positions with the unoccupied sites. In order to investigate this possibility, the total energies of several rearrangements of the Ni sublattice have been calculated, again using the same lattice parameter and atomic radii for the relaxed FCC cell. (Figure 38) The first configuration is obtained by moving one Ni atom into one of the four empty sites; the second configuration is obtained by moving two Ni atoms into empty sites to form an eclipsed arrangement; and the third configuration is obtained by moving two Ni atoms into empty sites to form a staggered configuration.

Figure 38. Crystal structures of (NiMP)$_4$ supercell for rearrangements of the Ni lattice.

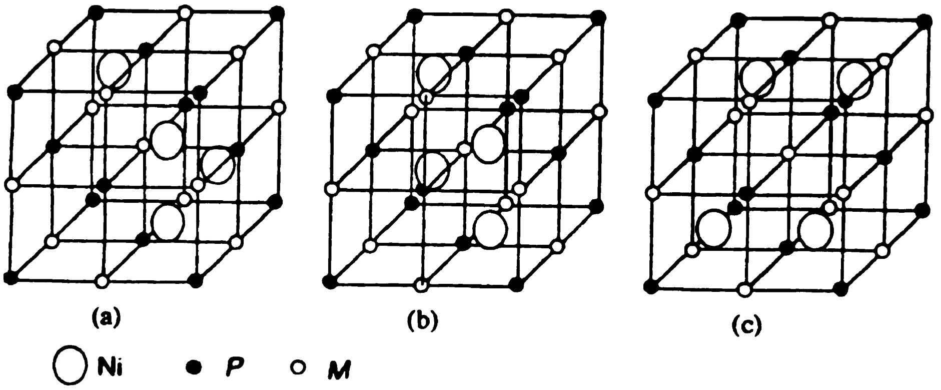

The energy increases above the half-Heusler structure of these three configurations are much smaller than those associated with the rearrangements of the NaCl substructure by about a factor of 2 (0.6-0.8 eV/FCC unit cell compared to 1.3-2.0 eV/FCC unit cell), shown in Table VII.

Table VII. Energetics of site-switching on Ni sublattice of NiZrSn supercell (GGA).

System	Energy - energy ($Ni_4Zr_4Sn_4$) (eV)	ΔE/FCC unit cell (eV)
$Ni_4Zr_4Sn_4$	0	0
$Ni_4Zr_4Sn_4$ - 35a	2.37	0.59
$Ni_4Zr_4Sn_4$ - 35b	2.66	0.67
$Ni_4Zr_4Sn_4$ - 35c	3.14	0.78

These systems are also metallic, but there are fewer bands crossing E_F compared to systems with disorder in the NaCl sublattice for the three configurations given in Figure 38 (Figure 39). The reduced formation energy and less metallic behavior seems to imply the configurations containing disorder in the Ni lattice would be preferred over those with disorder in the NaCl substructure, contradicting what is seen experimentally.[78]

The results of this analysis do not agree with experimental measurements which find that there is Zr/Sn disorder in NiZrSn but no disorder of the Ni atoms out of an FCC configuration.[78] It is possible that Ni defects have been annealed out of these samples while the Zr-Sn defects, perhaps due to large energy barriers, are quenched at low temperatures.

Figure 39. Electronic structures of (a) $Ni_4Zr_4Sn_4$ - 38a, (b) $Ni_4Zr_4Sn_4$ - 38b, and (c) $Ni_4Zr_4Sn_4$ - 38c.

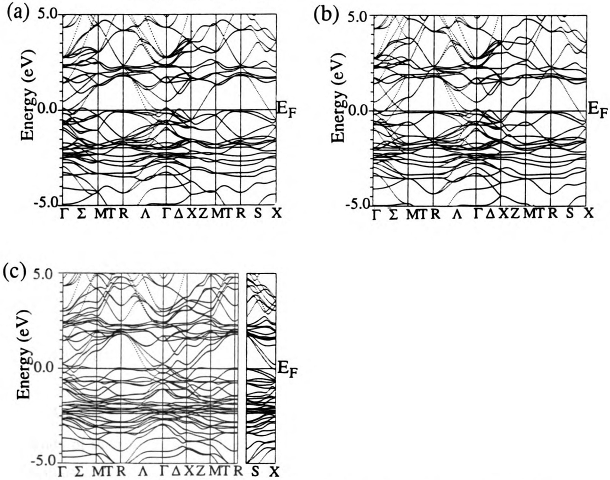

The Zr/Sn disorder in NiZrSn is believed to be due to the similarity of the atomic radii of Zr (0.160 nm) and Sn (0.158 nm) and has been suggested as the mechanism to reconcile the differences between the band gaps found experimentally from that in the electronic structure calculations of the ordered NiZrSn.[81] The effect of Ni disorder within the octahedrally-coordinated pockets should also reduce the band gaps of the half-Heusler compounds. The experimental value for the band gap (0.19 eV) for NiZrSn is much smaller than the value obtained from electronic structure calculations (0.51 eV). The electronic structure calculations performed by OR[59] in the virtual-crystal approximation found that the band gap decreased to zero for about 15% Zr/Sn anti-site disorder. On the other hand, the atomic radii of Ti (0.147 nm) and Sn (0.158 nm) are different enough that anti-site defects should be extremely rare in NiTiSn.[79] However, the experimental value for the band gap in this compound (0.12 eV[79]) is also much smaller than that of the ordered NiTiSn obtained in electronic structure calculations (0.51 eV[59]). Since one system displays anti-site disorder on the NaCl sublattice while the other does not, while the calculated and experimental values are nearly the same, it seems unlikely that anti-site disorder can completely explain the band gap difference in these materials. One cannot blame LDA/GGA which usually underestimates rather than overestimates the band gaps in binary or covalent semiconductors. We will return to this question after discussion our calculation of the other ternary compounds in the Zintl phase.

4.3. THERMOELECTRIC PROPERTIES OF HALF-HEUSLER COMPOUNDS

An understanding of the band structure of the half-Heusler compounds allows for study of their thermoelectric properties. Half-Heusler compounds have been studied extensively for their thermoelectric properties.[59, 80] With the considerable variety of changes seen in the band structure in the semiconducting half-Heusler phases, it is necessary to understand what properties would be best for thermoelectric applications. In order to maximize $ZT = S^2\sigma T/\kappa$, it is necessary to have a large S and σ and a low κ. From the derivation of ZT from the Boltzmann transport equations, the B parameter (Equation 24 in Chapter 2) gives insight about how to increase ZT.[24] As stated before, to increase B, which then increases ZT, one needs to look for systems with low κ_{ph}, multiply degenerate band extrema to increase γ, and highly anisotropic effective masses, small effective masses in the direction of transport in order to maximize and large effective masses perpendicular to the direction of transport.[24]

Several of the half-Heusler systems seem to be ideal candidates for electron-doped thermoelectric materials based on the concept of anisotropic effective masses since there is a very flat band along the ΓX direction which becomes more dispersive along XW. Recently, Uher *et al.*[81] have studied the transport properties of ZrNiSn and related compounds. They have estimated the effective mass of the states near the bottom of the conduction band to be about $2\text{-}3m_e$, where m_e is the free-electron mass. We have calculated the effective masses associated with the conduction band minimum (at the X point) and find the effective mass along ΓX to be about $10m_e$, whereas along the other directions are about m_e. This gives an average effective mass of $10^{\frac{1}{3}}m_e$ which is consistent with Uher *et al.*'s findings.[81] Similar effective mass values have been found in YNiSb where the heavy electron mass along the ΓX direction is a factor of 2 larger. In contrast, the hole effective masses are not as large and nearly isotropic.

Experimentally, these systems display a large S ($\sim$-40 to -250 μV/K) and large σ (0.1-10/mΩ-cm) in the electron-doped regime. This gives a large power factor (PF) ($S^2\sigma T\sim$0.8-1.4 W/mK).[80] This is consistent with our calculation for a system with highly anisotropic effective masses. Unfortunately, κ is very large in these materials ($\sim$10 W/mK compared to 1.5 W/mK for Bi_2Te_3), leading to values of ZT of around 0.03 near room temperature (RT) and 0.29 (TiNiSn), 0.26 (ZrNiSn), and 0.22 (HfNiSn) obtained at 700K using the RT values for the thermal conductivity.[66, 81, 82, 83]

In order to reduce κ and further increase the power factor, many studies of ZrNiSn, HfNiSn, and TiNiSn alloys have been performed.[66, 81, 82, 83] Doping on the Ni site shows little improvement of PF, but doping of the Sn site by Bi and of an alloyed site of Zr, Hf, and Ti by Nb and Ta show marked improvements in PF by as much as an order of magnitude. However, the phonon thermal conductivity is not substantially reduced, leading to ZT at RT which is nearly an order of magnitude smaller than that of Bi_2Te_3.[66, 81, 82, 83] One possibility to reduce κ is to use this materials in multilayer systems which have been shown to improve ZT in PbTe-PbSeTe quantum-dot superlattices[27] and in p-type Bi_2Te_3/Sb_2Te_3 superlattice films[28], mainly through reduction of κ.

The effective masses in YNiSb are larger and more anisotropic than those in ZrNiSn, but these improvements are not sufficient to expect dramatic improvements in ZT. One of the reasons for the high thermal conductivity is the higher symmetry of the half-Heusler crystal structure. This high symmetry can be used to our advantage by increasing the band degeneracy factor, γ, to a maximum value of 24 provided the extrema occur at a general point in the Brillouin zone.

In ZrNiSn and YNiSb, the CBM lies at a high symmetry point X where $\gamma = 3$. The degeneracy factor, and hence S, can be increased if the minimum were to lie at a more general point in the Brillouin zone (BZ).[7] This feature was found in ThRhSb (Figure 40) with the CBM moving to halfway between Γ and X, which increases its degeneracy factor to $\gamma = 6$. The VBM at the W point is nearly degenerate VBM at X and Γ. We find a gap of 0.68 eV which is larger than measured value of 0.44 eV for the isostructural URhSb.[84]

Figure 40. Electronic Structure of ThRhSb. Note the off-axis LCB.

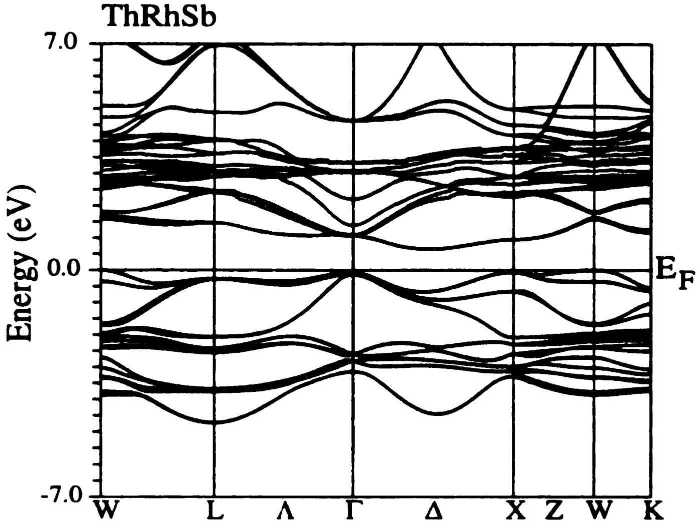

This off-axis CBM was also seen in ThNiSn. The previous calculation[10], without the inclusion of SOI, showed a band structure very similar to that of ThRhSb with the CBM forming halfway between Γ and X, but here the SOI is very important. The inclusion of SOI reduces the band gap to less than zero, which is smaller than the measured value of about 0.06 eV[85], but the CBM has shifted closer toward the X point which increases the degeneracy factor to $\gamma = 12$ (Figure 41). Unfortunately, this material has not been studied yet for its thermoelectric properties.

Figure 41. Electronic structure of ThNiSn. Note the LCB lies at a general point.

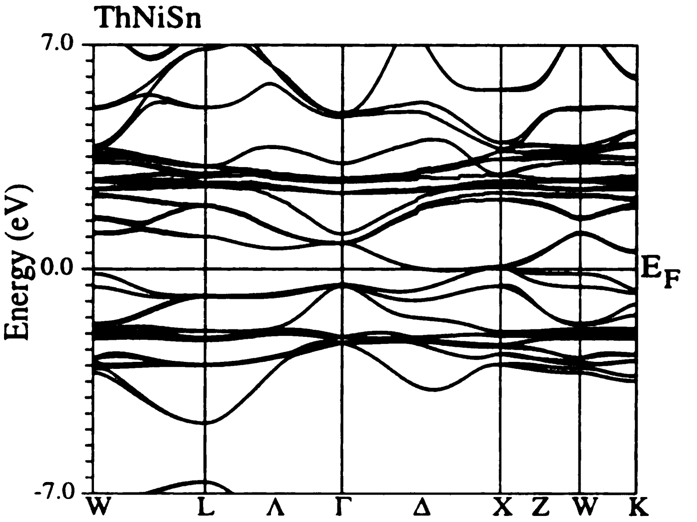

In summary, the half-Heusler compounds are still interesting for their potential thermoelectric properties provided that their κ can be reduced by a factor of 5 to 10.

CHAPTER 5.

TERNARY ZINTL PHASE COMPOUNDS

As discussed in detail in the last chapter, the half-Heusler structure has been described as a stuffed NaCl structure where transition metal ions form an FCC lattice within the pockets of a NaCl structure (Figure 12).[7, 59] With different chemical constituents within the structure, half-Heusler compounds can display semiconducting[7, 59], half-metallic[75, 76], or metallic behavior[62, 67, 74]. The narrow gap semiconductors of this class have been studied for thermoelectric applications.[4] While these materials have respectable values for their thermopower (S) and electrical conductivity (σ)[4, 80] which lead to a large power factor (PF $= S^2\sigma$), due to their simple, isotropic crystal structure, their thermal conductivity, κ, has been fairly large.[4, 66, 81, 82, 83]

Since the thermoelectric efficiency of a material depends on the dimensionless thermoelectric figure of merit, ZT$= S^2\sigma T/\kappa$[1, 2, 3], attempts to reduce the thermal conductivity in half-Heusler compounds have proven only moderately successful since the power factor has been observed to also reduce with alloying.[4, 66, 81, 82, 83] The large values of κ in the half-Heusler alloys have proven the major difficulty in using these materials for thermoelectric devices. A similar class of materials, Zintl phase compounds in the structure $Y_3Au_3Sb_4$, contain several of the same elements as the half-Heusler compounds, have similar bonding and gap formation, but, due to their cage-like structure and complex units cells, have a low κ.[4] Due to their potentially high ZT values, a thorough understanding of this new class of potential thermoelectric materials is therefore needed through electronic structure calculations, and is the topic of this chapter.

5.1. CRYSTAL STRUCTURE AND ZINTL CONCEPT

Zintl ions and Zintl phases have been studied for over a century, but their properties are not widely known.[86] Zintl ions are clusters or aggregates of "polar" intermetallic ions with strong charge transfer between elements. Zintl phases form out of Zintl ions arranged to produce polar or salt-like compounds which include binary or ternary compounds formed between alkali or alkali-earth elements and the main-group elements from group IV on. Most of these compounds are expected to be semiconducting or semimetallic due to the inherent charge balance necessary for their formation.[87]

Zintl phase compounds of the form $Y_3Au_3Sb_4$ are understood as a stuffed Th_3P_4 structure. Cubic Y_3Sb_4 (Th_3P_4 structure) derives from doubling the unit cell of BCC Sb (2 Sb atoms/unit cell) in all three directions to produce a Sb supercell (16 Sb atoms/unit cell). The Sb atoms are then displaced slightly along the 111 direction of the supercell to produce two different types of Sb polyhedra: regular disphenoids[88] and distorted tetrahedra. The Y atoms enter the center of the disphenoids and are 8-fold coordinated to Sb to form Y_3Sb_4 (Figure 42a). The noble (or transition) metal atoms, such as Au, enter the distorted Sb_4 tetrahedra in Y_3Sb_4 to form the ternary compound $Y_3Au_3Sb_4$ (Figure 42b). After Au is added, Y is 4-fold coordinated to Sb and 4-fold coordinated to Au, Au is 4-fold coordinated to Sb and 4-coordinated to Y, and Sb is 3-fold coordinated to Au and 4-fold coordinated to Y. In the half-Heusler compounds such as YNiSb, Ni is 4-fold coordinated to Y and 4-fold coordinated to Sb, and the Ni-Sb and Ni-Y distances are the same. However, in the $Y_3Au_3Sb_4$ structure, due to the distortions of the tetrahedra, the different coordinations of the elements are at slightly different distances.[89] The BCC Brillouin zone used in the electronic structure calculations for the Zintl phases is given in Figure 43.

Figure 42.(a) Crystal structure of Y_3Sb_4 and (b) crystal structure of $Y_3Ni_3Sb_4$. The large open circles are Sb, the small open circles are Y, and the filled circles are Ni.

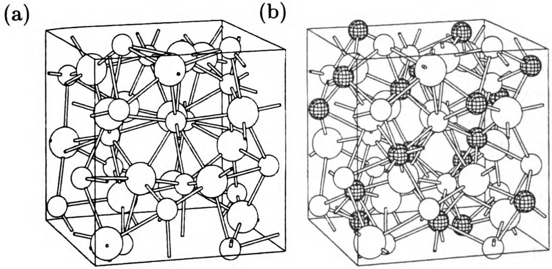

Figure 43. BCC Brillouin zone.

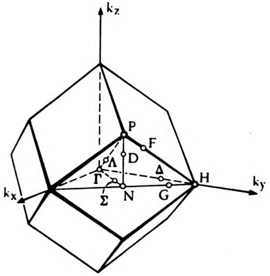
kz
P
F
D
Λ
Δ
Γ
H
ky
kx
Σ
N
G

Zintl phases and half-Heusler compounds share many similarities including the formation of their crystal structure from parent binary structures and the nature of the opening of their band gaps.[90, 91, 92, 93] Both of these structures contain a backbone compound which is predicted to be either semiconducting or semimetallic (such as ZrSn or Zr_3Sb_4 (isostructural to Y_3Sb_4)) where transition (or noble) metal atoms enter into the octahedrally-coordinated pockets of this parent compound. In both the half-Heusler and Zintl phases, Ni is octahedrally coordinated to 4 Zr and 4 Sn (Sb) atoms, while 4 Ni atoms form a tetrahedra about the Zr atoms. However, there is a fundamental difference between these two structure types in regard to the Ni coordination with Sn (Sb). In the half-Heusler phase, Ni forms tetrahedra about Sn, but in these Zintl phases there are only 3 Ni atoms about the Sb positions, even though the corresponding Ni-Sb-Ni angle (114.88°) is close to the tetrahedral angle. This difference in local coordination may be the reason certain noble or transition metals appear to prefer one structure over the other. While Ni prefers to form semiconductors in the half-Heusler structure, Cu forms more stable semiconducting compounds in this Zintl phase configuration for $R_3Cu_3Sb_4$ (R = Y, La, Ce, Pr, Nd, Sm, Gd, Tb, Dy, Ho, Er).[93] In fact, some of the U-containing compounds can be in either phase (UNiSn and $U_3Ni_3Sn_4$, UPtSn and $U_3Pt_3Sn_4$, URhSb and $U_3Rh_3Sb_4$).[93]

As discussed in Chapter 2, the search for new thermoelectric materials involves finding new narrow-gap semiconductors.[1, 2, 3] Several semiconducting members of this class of Zintl compounds have been found and studied experimentally.[10, 89, 90, 91, 92, 93, 94] $Th_3Ni_3Sb_4$[10] has been found both experimentally and theoretically to be a narrow-gap semiconductor. Both $U_3T_3Sb_4$ (T = Ni, Pd, Pt)[90] and $Ce_3Pt_3Bi_4$[91] are heavy-fermion, narrow-gap semiconductors with magnetic moments on the U and Ce sites, respectively. However, these heavy-fermion, narrow-gap semiconductors do not have large thermoelectric coefficients at room temperature.[95]

In this dissertation we will present our investigations of the electronic structure of three Zintl phase compounds of the $Y_3Au_3Sb_4$ structure type, namely $Zr_3Ni_3Sb_4$, $Hf_3Ni_3Sb_4$, and $Zr_3Pt_3Sb_4$. The reasons for studying these systems is (i) to understand the role in the gap formation of Ni/Pt *d* hybridization in comparison with the half-Heusler compounds, such as ZrNiSn, and (ii) to understand the electronic origin of their thermoelectric properties.

5.2. ELECTRONIC STRUCTURE OF ZINTL PHASE (STUFFED Th_3P_4) COMPOUNDS

5.2.1. GAP FORMATION AND THE ROLE OF *d*-HYBRIDIZATION

The gap formation in the half-Heusler compounds $Y^{3+}Ni^{0}Sb^{3-}$and $Zr^{4+}Ni^{0}Sn^{4-}$ derives from a charge transfer between the elements of the NaCl substructure combined with the strong interaction of the Ni *d* and Y/Zr *d* orbitals.[7, 59] Similarly, in the Zintl compounds the charge transfer in the binary parent compound $(Zr^{4+})_3(Sb^{3-})_4$ to form the ternary $(Zr^{4+})_3Ni_3^0(Sb^{3-})_4$ should be important in understanding the gap formation in these materials. The only previous electronic structure study of $Zr_3Ni_3Sb_4$, $Hf_3Ni_3Sb_4$, and $Ti_3Ni_3Sb_4$, is the calculation of the DOS using extended Huckel calculations[94], with their inherent limitations.

$Zr_3Ni_3Sb_4$, $Hf_3Ni_3Sb_4$, and $Zr_3Pt_3Sb_4$ were identified by Wang *et al.*[94] to have the same crystal structure as the better studied $Y_3Au_3Sb_4$, the first compounds in this structure type to not contain Y or an *f*-electron element. As discussed for $Y_3Au_3Sb_4$, in $Zr_3Ni_3Sb_4$ Ni has 4 Zr and 4 Sb neighbors, Zr has 4 Ni and 4 Sb neighbors, and Sb has 4 Zr and 3 Ni neighbors. The shortest Zr-Sb distance is 2.9144 Å, the shortest Zr-Ni distance is 2.7746 Å, and the shortest Ni-Sb distance is 2.4858 Å.[94]

In their analysis of $Zr_3Ni_3Sb_4$, Wang *et al.*[94] claim that, in a Zintl-phase concept, Sb is considered a nonmetallic element since it is the most electronegative component. They claim the observed short Zr-Ni distance, 2.7746 Å, produces a strong covalent bonding between Zr and Ni, so that Zr_3Ni_3 forms the covalent network which then has a predominantly ionic bonding with the interpenetrating Sb atoms. This picture is consistent with their extended Huckel calculation which showed a reduced charge on Zr. However, this description disagrees with Jingtai *et al.*[96] who studied similar metallic rare-earth (RE)-copper Zintl phases, $RE_3Cu_3Sb_4$. They claim that, due to the shorter Cu-Sb distance (2.630 A compared to the Cu-RE distance of 2.868 Å), Cu_3Sb_4 forms the covalent network, and the interpenetrating RE atoms, in the distorted octahedra of Cu_3Sb_4, have ionic bonding with the Cu_3Sb_4 covalent network. As in $Zr_3Ni_3Sb_4$, the electronegativity of Sb is larger than that of the rare-earth atom.[96] Both Wang *et al.*[94] and Jingtai *et al.*[96] agree that there should be a strong charge transfer between Zr and Sb in $Zr_3Ni_3Sb_4$.

5.2.2. COMPARISON OF $Zr_3Ni_3Sb_4$ WITH THE HALF-HEUSLER COMPOUND ZrNiSn

Due to the similarities between the half-Heusler and Zintl phase compounds, we find the gap formation of these two classes of materials to be very similar. Let us briefly review the gap formation in the half-Heusler compound ZrNiSn (for details see Chapter 4). The gap formation in the half-Heusler compounds has been understood by first studying the parent binary compound ZrSn and then investigating the effects of the inclusion of the Ni *d* levels in the gap formation in the ternary compound. In ZrNiSn, there is a strong Ni *d*-Zr *d* hybridization in the conduction band near the

X point which is important for the formation of the band gap.[7, 59] An important question to ask is whether it is possible to understand the gap formation of $Zr_3Ni_3Sb_4$ by studying what effect the Ni *d* orbitals would have on semimetallic Zr_3Sb_4. Using the experimental value of the lattice constant of the ternary compound[7], we have calculated the band structure of Zr_3Sb_4 (Figure 44). It can be seen that the electronic structure of Zr_3Sb_4 is slightly semimetallic with a conduction band crossing E_F near the Γ point and a valence band crossing above E_F along ΓH and along ΓN (Figure 44). This is consistent with the self-consistent APW calculation for Th_3Sb_4, which is a known existing compound.[10] As can be seen, the majority of Zr *d* bands lie above E_F, the majority of the Sb *p* bands below, consistent with the view that these are mostly polar salts in the Zintl phase.[87] The important question is how the inclusion of Ni changes the bonding within this network.

Figure 44. The (a) Zr *d* and (b) Sb *p* orbital characters of Zr_3Sb_4.

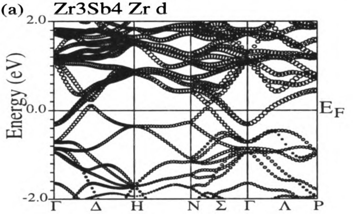

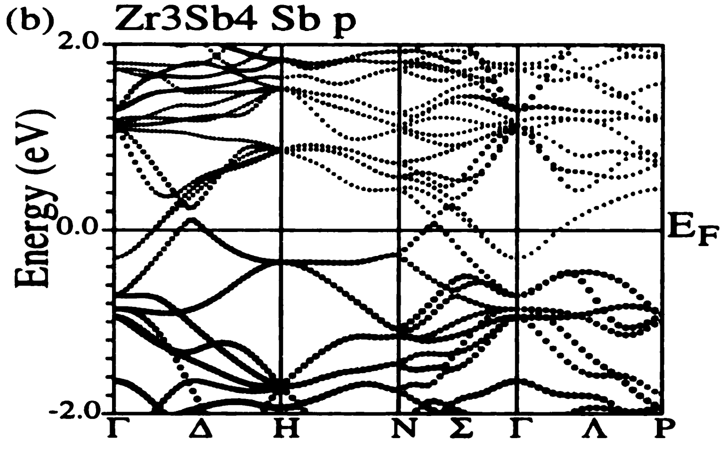

In $Th_3Ni_3Sb_4$[10], it has been found that the Th *d*-Ni *d* hybridization at the Γ point was much stronger than the Sb *p*-Ni *d* hybridization and that the former hybridization leads to the formation of the semiconducting gap. This is true even though the Ni-Sb distance (2.644 Å) is smaller than the Ni-Th distance (2.874 Å).[10] Therefore, the interatomic distance is not a clear indicator of the local bonding, as is commonly used. We also find that, when Ni is added to Zr_3Sb_4 to form $Zr_3Ni_3Sb_4$, the gap formation is similar to that of the half-Heusler compounds, when Ni is added to ZrSn to form ZrNiSn. The strengths of the orbital characters in $Zr_3Ni_3Sb_4$ (Figure 45) show that the Ni *d* hybridizes more strongly with Zr *d* than with Sb *p*. The Zr *d*-Ni *d* hybridization at the Γ point is much stronger than the Sb *p*-Ni *d* hybridization and leads to the formation of the semiconducting gap in $Zr_3Ni_3Sb_4$. Again, the Ni-Sb distance (2.4858 Å) is smaller than the Ni-Zr distance (2.7746 Å). The physics of the gap formation in the half-Heusler and Zintl-phase compounds is very similar: the introduction of Ni atoms into the semi-metallic binary compound (ZrSn, YSb, or Zr_3Sb_4) results in a strong Ni *d*-Y/Zr *d* hybridization which opens a narrow band gap. Since Zr, Sb, Sn, and Ni are not heavy elements, the inclusion of SOI has only a small effect on the band structure, such as minor splitting of degenerate bands and a small reduction of the band gap, but with no change in the shape of the LCB or HVB.[7]

Figure 45. The (a) Zr *d*, (b) Sb *p*, and (c) Ni *d* orbital characters of $Zr_3Ni_3Sb_4$.

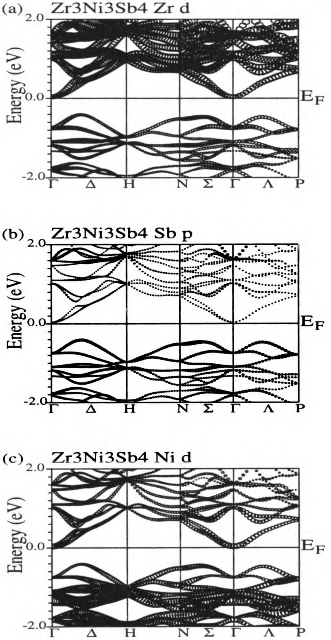

Y

Y

V

at

La

wa

d

com

in b

A

expe

than

LDA

comp

The similarity between the gap formation in these Zintl-phase compounds and the half-Heusler compounds also can be seen when changing the transition metal atom from Ni to Au or Cu. In the half-Heusler compounds, such as LuAuSn, the reduced Au *d*-La *d* hybridization compared to the Ni *d*-La *d* hybridization in LuNiSb led to a reduction of the band gap in the former material (note that for charge compensation that Sb → Sn if Ni → Au). Weaker Au/Cu *d*-Y *d* hybridization has been seen in $Y_3Au_3Sb_4$ and $Y_3Cu_3Sb_4$.[89] $Zr_3Ni_3Sb_4$ has a band gap of 0.39 eV compared to 0.23 eV for $Y_3Cu_3Sn_4$ and $Zr_3Pt_3Sb_4$ has a band gap of 0.78 eV compared to 0.61 eV in $Y_3Au_3Sn_4$.[89] In these compounds, the Au and Cu *d* levels lie about 5 eV below the VBM[89], while the Ni *d* levels lie only about 2 eV below and Pt *d* levels lie only about 3-4 eV below the VBM[7, 59] Previous calculations of the band structure of $La_3Au_3Sb_4$ found that the gap was 0.17 eV, half of that for $Th_3Ni_3Sb_4$. This difference was attributed directly to the reduced Au *d*-La *d* hybridization due to the lower Au *d* levels in the former compound.[10] Reduced Zr/Y/La *d*-Cu/Au *d* hybridization compared to Zr/Y/La *d*-Ni/Pt *d* hybridization leads to a reduction of the band gap in both the half-Heusler and Zintl phase compounds.

5.2.3. UNUSUAL DISCREPANCY BETWEEN THE BAND GAPS FROM THEORY (LDA/GGA) AND EXPERIMENT

As in the half-Heusler structure, there seems an unusual discrepancy between the experimental and theoretical band gaps, the theoretical values being much larger than the experimental values[7, 10, 59], the opposite of what is usually found in LDA/GGA calculations.[31] The situation seems even more confusing due to the comparisons of the electronic structure calculations of the binary compounds Th_3X_4

(X = P, As) with the ternary $Th_3Ni_3Sb_4$. The calculated band gap for the binary system Th_3P_4 by Takegahara *et al.*[10] gives 0.007 eV compared to the experimental value of 0.40 eV, whereas in Th_3As_4 they find 0.05 eV compared to the experimental value of 0.43-0.44 eV. For Th_3Sb_4 they find a negative gap (semimetal) compared to the experimental value of 0.48 eV. The reason for this discrepancy was attributed the inadequate treatment of the XC potential in LDA/GGA. The trend for the band gaps in the ternary compounds is just the opposite. The calculated value of the gap for the ternary $Th_3Ni_3Sb_4$ is 0.36 eV compared to the experimental value of 0.07 eV. These calculations were performed without the inclusion of SOI which can be important for heavy atoms like Th and are likely to play an important role in changing the band gap.[10]

The discrepancy of finding a larger band gap in a band calculation than found experimentally has been seen also in the half-Heusler compounds. Ogut & Rabe[59] tried to explain the observed smaller values of the band gap in ZrNiSn by invoking disorder in the ZrSn lattice. Similar arguments have been put forward to explain the observed smaller gap in these Zintl-phase compounds.[10] However, our supercell calculations for the half-Heusler compounds[11] (Chapter 4) showed that this type of disorder is found to be energetically unfavorable compared to Ni disorder. Also, while disorder of the ZrSn lattice has been seen in ZrNiSn[78], there is no experimental evidence of disorder in these Zintl-phase compounds, where the Zr and Sn sites are not equivalent. Therefore, we will try to understand this dramatic discrepancy between theory and experiment from a different perspective.

The observed discrepancy between the experimental and theoretical band gaps may lie in the uncertainty in the positions of the Ni d orbitals in different calculations. As seen in Chapter 4, when the transition metal d orbitals lie closer to E_F, such as

in TiCoSb[80], the Ti *d*-Co *d* hybridization is stronger, leading to a larger band gap in the material. It is well known that LDA/GGA calculations place the *d* orbitals of transition metals too high in energy while other methods, namely Hartree-Fock, place these *d* orbitals too low in energy.[97] Only a small shift, less than 0.5 eV, in the position of the *d* orbitals changes the gap from 0.51 eV in TiNiSn[59] to 1.08 eV in TiCoSb[80]. Shifting of the *d* levels down reduces the band gaps. In the Zintl phases, we find that $Zr_3Ni_3Sb_4$ has a band gap of 0.39 eV compared to 0.23 eV for $Y_3Cu_3Sn_4$ and $Zr_3Pt_3Sb_4$ has a band gap of 0.78 eV compared to 0.61 eV in $Y_3Au_3Sn_4$.[89] In these compounds, the Au and Cu *d* levels lie about 5 eV below the valence band maximum[89] while the Ni *d* levels lie only about 2 eV below the valence band maximum.[7, 59] The position of the Ni *d* level[97] may be the source of the overestimation of the band gap in the half-Heusler and Zintl phase compounds, not disorder between Zr and Sn/Sb.[10, 59]

5.2.4. COMPARISON OF $Zr_3Ni_3Sb_4$ WITH $Hf_3Ni_3Sb_4$ AND $Zr_3Pt_3Sb_4$

$Zr_3Ni_3Sb_4$, $Hf_3Ni_3Sb_4$, and $Ti_3Ni_3Sb_4$ are isoelectronic Zintl-phase compounds, the first compounds in the $Y_3Au_3Sb_4$ structure type not containing Y or an *f*-electron atom. The electronic structures of all three compounds show small semiconducting gaps (Figure 46). We find that the effect of SOI is to lower the band gap from 0.58 eV to 0.51 eV in $Hf_3Ni_3Sb_4$, from 0.45 eV to 0.39 eV in $Zr_3Ni_3Sb_4$, and from 0.86 eV to 0.78 eV in $Zr_3Pt_3Sb_4$. Though extended Huckel calculations rarely do a good job in predicting band gaps, the previous calculation for $Zr_3Ni_3Sb_4$ (without SOI) gave a gap of 0.57 eV, consistent with our results.[94]

Figure 46. Electronic structures of (a) $Zr_3Ni_3Sb_4$, (b) $Hf_3Ni_3Sb_4$, and (c) $Zr_3Pt_3Sb_4$.

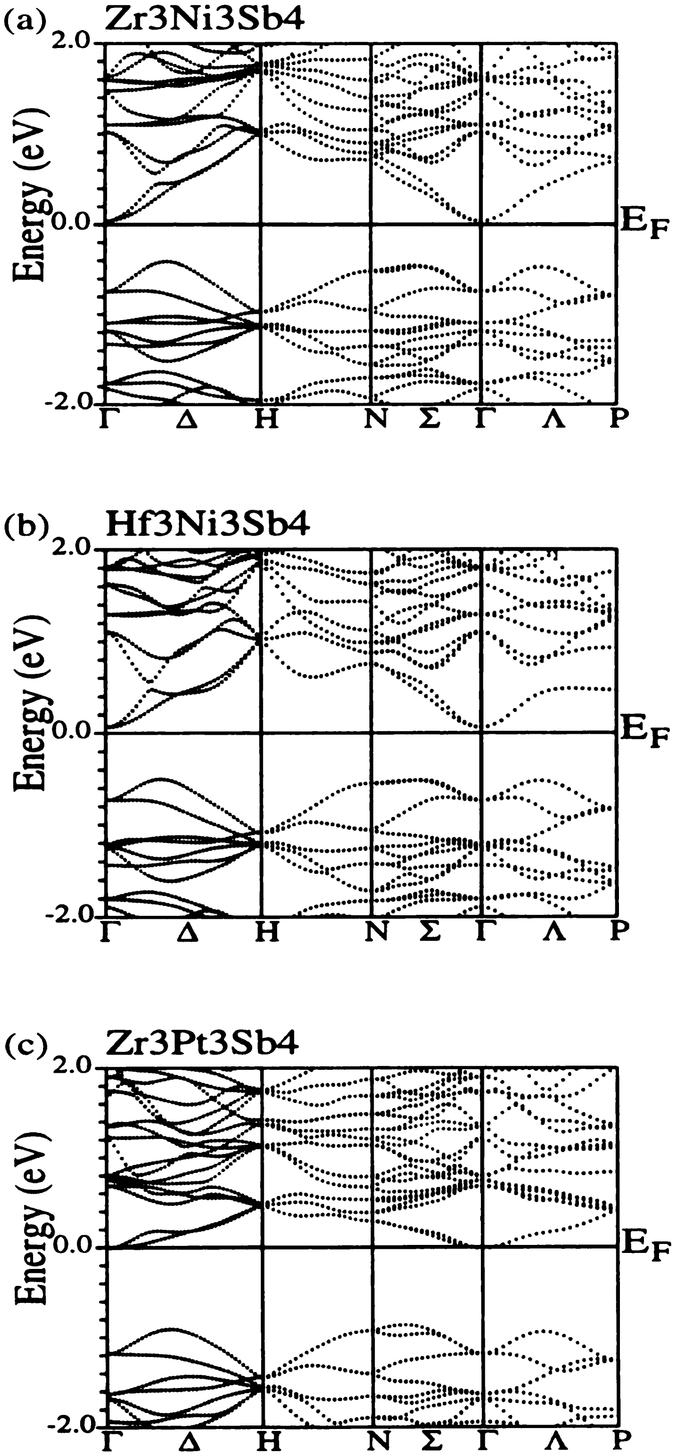

The electronic structures of $Zr_3Ni_3Sb_4$, $Hf_3Ni_3Sb_4$, and $Zr_3Pt_3Sb_4$ are remarkably similar with valence band maxima forming along the same directions in **k**-space. The HVB in each of the compounds is apparently multiply degenerate with maxima along ΓN, ΓH, and ΓP (Figure 46). These bands arise primarily from Hf/Zr *d*-Ni/Pt *d* hybridization, with some Sb *p* hybridization. In each case, the effect of SOI is to remove degeneracies from the bands and reduce the observed band gap by about 0.07 eV. As in the half-Heusler systems, the bands near E_F arise due to a strong hybridization of the three metallic elements.

A closer study of the effective masses of these materials shows that there are only two VBM along ΓH and ΓP in $Zr_3Ni_3Sb_4$, and $Hf_3Ni_3Sb_4$, the supposed maxima along ΓN in these two compounds, which has a slightly lower energy than the other two, is really a saddle point with a minimum along the z-direction. The calculated reciprocal values of the effective masses ($\alpha_i = [m_i/m_e]^{-1}$) are given in Table VII. These effective masses have not been measured experimentally. The CBM at the Γ point is doubly degenerate, one band more dispersive than the other. The values of the reciprocal effective masses are very similar in the three compounds, except that the Pt compound has heavier CBM effective masses and no saddle point along ΓN.

Table VIII. Calculated reciprocal effective masses of $Zr_3Ni_3Sb_4$, $Hf_3Ni_3Sb_4$, and $Zr_3Pt_3Sb_4$.

	$\alpha_i = [m_i/m_e]^{-1}$	$Zr_3Ni_3Sb_4$	$Hf_3Ni_3Sb_4$	$Zr_3Pt_3Sb_4$
CBM(Γ)	$\alpha_x = \alpha_y = \alpha_z$	1.46	1.53	0.07
	$\alpha_x = \alpha_y = \alpha_z$	0.72	0.57	0.08
VBM (ΓN)	$\alpha_x = \alpha_y$	0.21	0.27	0.50
	α_z	-0.04	-0.23	0.54
VBM(ΓH)	$\alpha_x = \alpha_y = \alpha_z$	0.17	0.19	0.12
VBM (ΓP)	$\alpha_x = \alpha_z$	0.47	0.40	0.26
	α_y	1.26	1.24	0.88

$Zr_3Ni_3Sb_4$, $Hf_3Ni_3Sb_4$, and $Zr_3Pt_3Sb_4$ have a low κ due to the complex unit cells.[94, 95] Our calculations also show anisotropic effective masses, though much less anisotropic than the half-Heusler compounds. As pointed out for $Y_3Au_3Sb_4$ and $Y_3Cu_3Sb_4$[89], the multiply degenerate VBM away from the high symmetry points leads to a large thermopower in these systems.[11, 24] The different values for the band gaps allows for shifting the temperature range at which the materials are useful. These Zintl-phase compounds have promising power factors, like the half-Heusler compounds, however with a much lower κ due to the more complex crystal structure.[94, 95] Further experimental studies of these materials for their thermoelectric properties is warranted.

CHAPTER 6.

SIMPLE CHALCOGENIDES

Both half-Heusler compounds (Chapter4) and Zintl-phase compounds (Chapter 5) are potential candidates for new thermoelectric materials. However, the best currently available bulk thermoelectric materials belong to a class called simple chalcogenides.[4] These include alloys of Bi_2Te_3 with Bi_2Se_3 and Sb_2Te_3 for room temperature ($\sim$300K) and PbTe for higher temperatures ($\sim$600K) applications.[3, 25] The search for new thermoelectric materials has focused on using these materials as building blocks for synthesizing novel materials with complex structures which will have high ZT values.[4]

While there are general expectations about what one should look for in a good thermoelectric material (Chapter 2), studying the electronic structure of known thermoelectrics allows one to see which mechanisms are the most important. Also, before studying the electronic structure of complex chalcogenides, we will discuss the physics of gap formation in simple chalcogenides which have been extensively studied in the past. We will present our FLAPW results and then compare with the previous calculations which were performed using different methods, and to understand the features which are found in the electronic structure of the best known thermoelectric materials.

6.1. PbS, PbSe, PbTe

6.1.1. BAND STRUCTURES OF PbS , PbSe, AND PbTe

PbS, PbSe, and PbTe, commonly referred to as the lead salts, are compounds in the NaCl structure type with 2 atoms/FCC unit cell. The lead salts have been used in many applications, including near-infrared photoconductive detectors[98], photoconductive and photovoltaic conductors[99], and p-n injection lasers[100]. PbS, PbSe, and PbTe are also good thermoelectric materials near 700 K with a maximum ZT around 1.[3, 25] These materials have also been used in quantum dots and multilayer systems which show even higher values of ZT, mainly due to reductions in κ.[4, 27, 28]

The lead salts are among the few materials where the temperature coefficient $(\frac{\partial E_{gap}}{\partial T})$ is positive, which means that the semiconducting gap increases with temperature. Almost all other elemental or binary compound semiconductors exhibit negative values of the temperature coefficient. In fact, all three compounds have about the same temperature coefficient, $\frac{\partial E_{gap}}{\partial T} \approx 4.7 \times 10^{-4}$ eV/K (Table IX). This is related to the negative pressure coefficients $(\frac{\partial E_{gap}}{\partial P})$ for all three systems and positive volume coefficients of thermal expansion, α. Therefore, as the temperature increases, the lattice expands, acting like a negative pressure $(\frac{\partial E_{gap}}{\partial P})$, which then increases the band gap $(\frac{\partial E_{gap}}{\partial T} > 0)$. Another unusual feature is that the band gap *decreases* going from PbS to PbSe but *increases* going from PbSe to PbTe (Table IX). Generally, there is a monotonic decrease of E_{gap} with increasing atomic number.[101]

Table IX. Experimental energy gaps in eV for PbS, PbSe, and PbTe as a function of T. (For experimental references, see Dalven [101])

T(K)	PbS	PbSe	PbTe
4.2	0.286 ± 0.003	0.165 ± 0.005	0.190 ± 0.002
12	0.286	0.145	0.187
77	0.307 ± 0.003	0.176 ± 0.005	0.217 ± 0.002
300	0.41; 0.42	0.27; 0.29	0.31; 0.32
373	0.44	0.31	0.34

PbS, PbSe, and PbTe have been extensively studied in the past, and their electronic structures have been calculated by several authors using different methods. These include tight-binding (TB) calculations[102], the augmented planewave method[103, 104], the k·p method[105, 106], the Green function method[107], the orthogonalized planewave (OPW) method[108], the empirical pseudopotential method[109, 110, 111, 112, 113, 114, 115], the relativistic LMTO method[116, 117, 118], and the FLAPW method including SOI[37, 38, 39]. Early calculations[102, 103, 104, 105, 106, 107, 108, 109, 110, 111, 112, 113] correctly predicted the position of the direct gap at the L point in the BZ. However, many of these calculations included the band gap as an input parameter. The later papers[37, 38, 39, 115] note that, even after including SOI, the LDA/GGA band gaps are too small compared to experiment, which has been noted in many other semiconductors.[31]

Our FLAPW calculation of the band structures of these three compounds (including SOI) at the experimental lattice parameters (corresponding to T = 4 K) shows that the band gaps are much smaller than experiment, 0.10 eV for PbS, 0.01 eV for PbSe, and 0.09 eV for PbTe, though the trend in the bands gaps going from PbS to

PbTe is reproduced.

Figure 47. Electronic structures of (a) PbS, (b) PbSe, and (c) PbTe using the experimental lattice parameters (corresponding to 4 K).

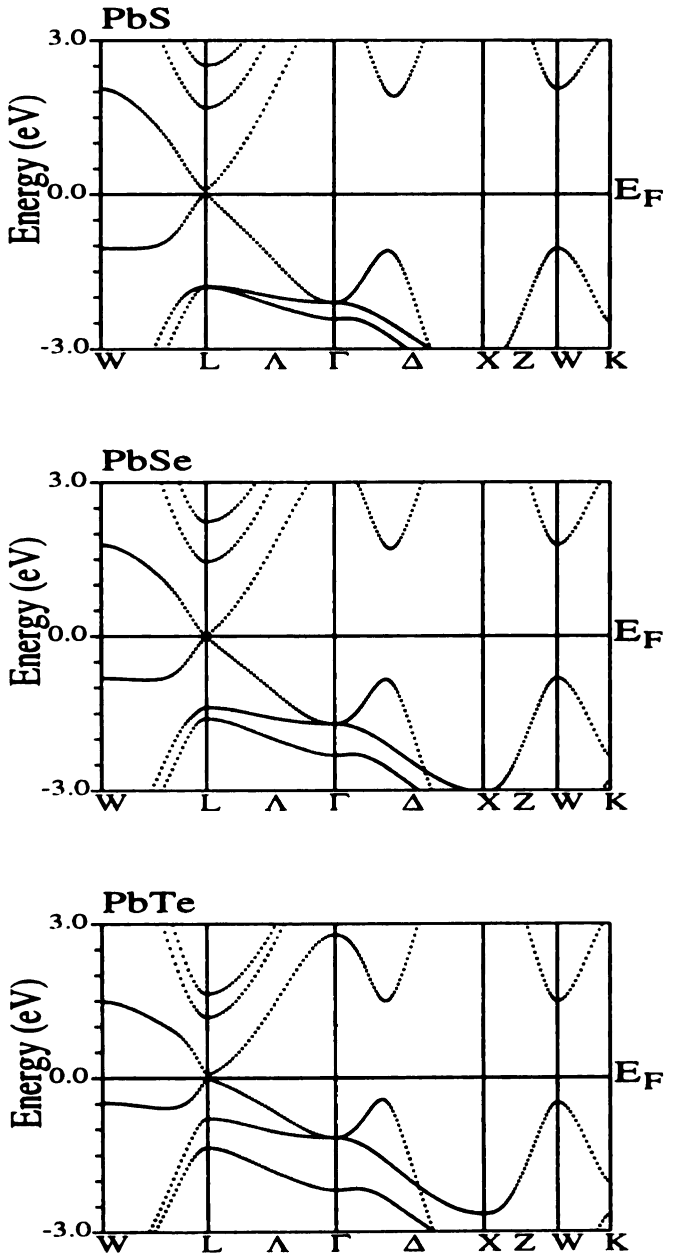

Several calculations of these materials have tried to improve the band gaps for better agreement with experiment. All of these have been zero temperature calculations, so the attempts have been to reproduce the experimental values of 0.29 eV for PbS, 0.17 eV for PbSe, and 0.19 eV for PbTe.[119] One of these calculations uses a one-dimensional multipole expansion for SOI to yield 0.24 eV for PbSe[115]. In a similar vein, another calculation expands the SOI using a Slater-Koster approach in order to fit the gap in PbTe[38]. Another adds a constant potential to the conduction-band states in an FLAPW calculation to obtain the experimental values of the gaps[37]. There is an *ab initio* relativistic full-potential LMTO calculation which yields 0.069 eV for PbS, 0.141 eV for PbSe, and 0.31 eV for PbTe[117]. Finally, one group uses the lattice parameters appropriate to the minimum energy configuration within an FLAPW-GGA calculation to yield values of the gap of 0.26 eV for PbSe and 0.15 eV for PbTe[39].

It is clear that some of these approaches seem more reasonable than others. Though the band gaps do not agree very well with experiment, the fully relativistic calculation[117] seems the most reasonable, since it is known that including SOI in a second-variational procedure has problems with Pb $6p_{\frac{1}{2}}$ states in metallic Pb[36]. The one-dimensional multipole expansion[115] and Slater-Koster expansion[38] of SOI also seem reasonable approaches, but are unduly complicated for this problem. The addition of a constant potential to the conduction-band states[37] seems rather *ad hoc*, especially within an *ab initio* FLAPW approach.

The method to obtain the gap which seems to make the most sense (in terms of computational efficiency) is calculating the band structure using a second variational approach for SOI after finding the minimum energy lattice parameters[39]. DFT calculations are only approximate solutions since the XC potential is not exactly known[31]. Therefore, one should choose a reasonable model of the system to study, which can be done by first finding the minimum energy configuration of a crystal. Also, it is known experimentally that the band gap increases with increasing lattice parameter[101], so an increase in the theoretical lattice constant is expected to also increase the calculated band gap. The minimum energy configuration for each system in GGA was found by increasing the lattice parameters which gives good agreement with the experimental band gaps. In LDA, the minimum energy configuration for each system was found by reducing the lattice parameters which further reduces the calculated band gaps.[39] We will try to reproduce the published results[39] using GGA to better understand the effects of lattice relaxation.

The total energy was calculated within GGA for PbS, PbSe, and PbTe, and is plotted as a function of lattice parameter in Figure 48 for PbS. We have found the total energy has a minimum with lattice parameters approximately 1-2% larger than the experimental value. The equilibrium lattice parameters changing in PbS from 11.204 a.u. to 11.422 a.u., in PbSe from 11.573 a.u. to 11.725 a.u., and in PbTe from 12.176 a.u. to 12.376 a.u. The arrow in Figure 48 gives the position of the experimental lattice parameter.

Figure 48. Total energy of PbS as a function of lattice parameter (in a.u.) obtained in GGA. The points were plotted using the computer program KALEIDAGRAPH[120]. The experimental value is given by the arrow.

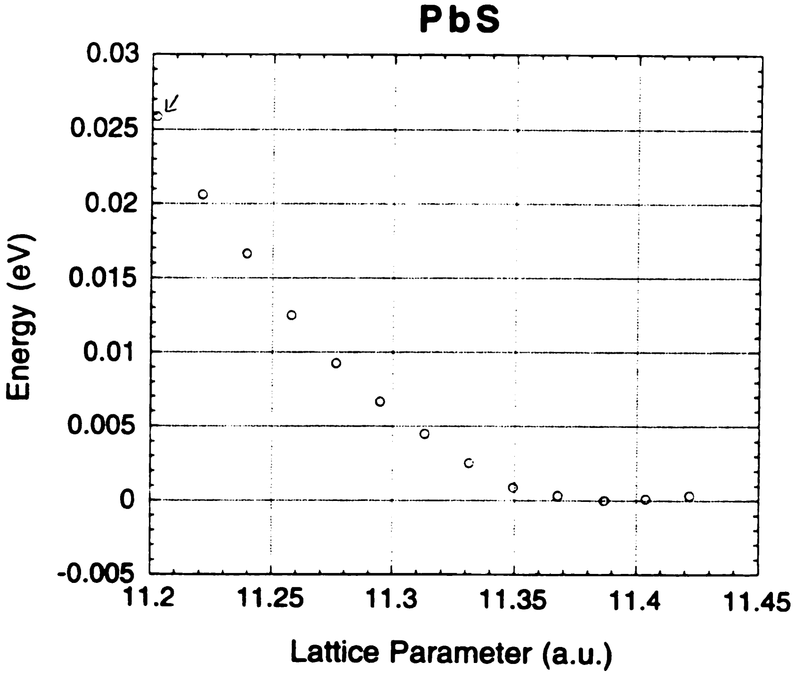

Electronic structure calculations performed at these larger lattice parameters do not change the shape of the bands appreciably, but the band gaps increase to nearly the experimental values for the three systems (Figure 49), in PbS to 0.26 eV compared to the experimental value of 0.29 eV, in PbSe to 0.08 eV compared to the experimental value of 0.17 eV, and in PbTe to 0.17 eV compared to the experimental value of 0.19 eV.[119] These calculations suggest that it might be important to calculate the energy gaps using equilibrium lattice parameters instead of experimental ones. This is also a case, such as in the determining the minimum energy configuration between BCC Fe and FCC Fe[45], where GGA better reproduces the properties of the system than LDA. We find that GGA increases the band gaps of these materials close to the experimental values while the previous LDA calculation[39] reduced the gaps even further.

Figure 49. Electronic structures of (a) PbS, (b) PbSe, and (c) PbTe using the relaxed lattice parameters from GGA and including SOI.

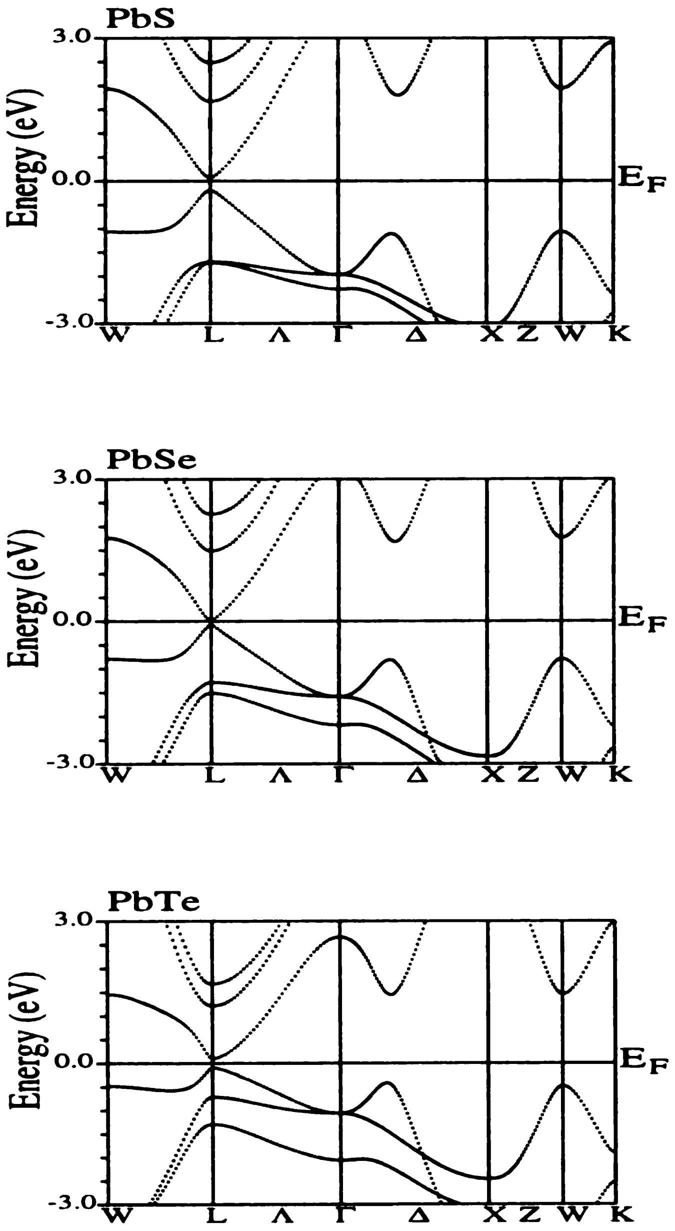

6.1.2. THERMOELECTRIC PROPERTIES OF THE LEAD SALTS

Most of the electronic structure calculations on the lead salts focused on the problem of correctly predicting the band gaps instead of using this information to better understand the thermoelectric properties of these materials. Due to the increase of the band gap with temperature[101], the band gap is on the order of about $10k_BT$ at 700 K[1, 25, 3, 4], estimated to be about 0.5 eV for a recent estimation of ZT in these materials[19]. If we assume that the CBM and VBM remain at the L point, the degeneracy of the band extrema is small, which is insufficient to explain the large ZT at high temperatures.[11, 24] One must, therefore, look at the anisotropy of the effective masses.

The effective masses in PbS, PbSe, and PbTe are known to be highly nonparabolic and temperature dependent[101, 121] as well as highly anisotropic[122]. As seen in Table X, the effective mass along the (100) direction (defined as longitudinal) is much different from that of the (111) direction (defined as transverse).[122] The effective masses have been calculated (using the band structure for the relaxed lattice), but the reciprocal values are written to compare with Bi_2Te_3 in the next section.

The agreement between the theoretical and experimental values looks reasonable. The largest anisotropy is found in PbTe, which is the best thermoelectric material of the three.[19] According to the mass dependence of the B parameter (Equation 24 of Chapter 2), higher ZT should occur in systems with large band degeneracy and highly anisotropic effective masses.[11, 24] The mechanism for the high ZT in PbTe seems to be the highly anisotropic transport mass with only a small enhancement from the band degeneracy factor.

Table X. Comparison of calculated components of the reciprocal effective mass tensor with experiment[122] ($\alpha_l = [m_t/m_e]^{-1}$ and $\alpha_t = [m_t/m_e]^{-1}$).

		PbS		PbSe		PbTe	
		Experiment	Theory	Experiment	Theory	Experiment	Theory
Conduction	α_l	7.25	13.53	16.39	18.58	30.30	24.48
	α_t	8.13	9.55	10.31	10.06	4.24	5.45
Valence	α_l	6.70	12.89	16.13	16.41	33.33	18.89
	α_t	6.13	7.91	8.33	8.19	2.39	3.55

6.2. Bi_2Te_3, Bi_2Se_3, Sb_2Te_3, AND RELATED SYSTEMS

The best room temperature thermoelectric materials are alloys of Bi_2Te_3 with Bi_2Se_3 and Sb_2Te_3. While the thermoelectric properties of these materials were optimized nearly 40 years ago[123], there is no accepted theoretical explanation of their high observed ZT values. The effects of SOI in these materials is very important to their gap formation[11, 40, 124], but only one other band structure calculation has been performed where SOI has been included self-consistently[11, 40]. Understanding the features of the band structure relevant for the high ZT in these materials is therefore important in the search for new thermoelectric materials, several of which contain portions of the Bi_2Te_3 crystal structure in their complex unit cells.[4]

6.2.1. Bi_2Te_3 CRYSTAL STRUCTURE

The crystal structure of Bi_2Te_3 is rhombohedral with the space group D_{3d}^5 (*R-3m*) with five atoms in the unit cell. These atoms form five atom layers called "quintuple-layer leaves" of Te-Bi-Te-Bi-Te along the z direction with primarily ionic and covalent bonding within the layer with Van der Waals bonding between the layers.[63]

Figure 50. Crystal structure of Bi_2Te_3 along the XZ plane showing the quintuple layer leaves of Te-Bi-Te-Bi-Te separated by a Van der Waals gap.

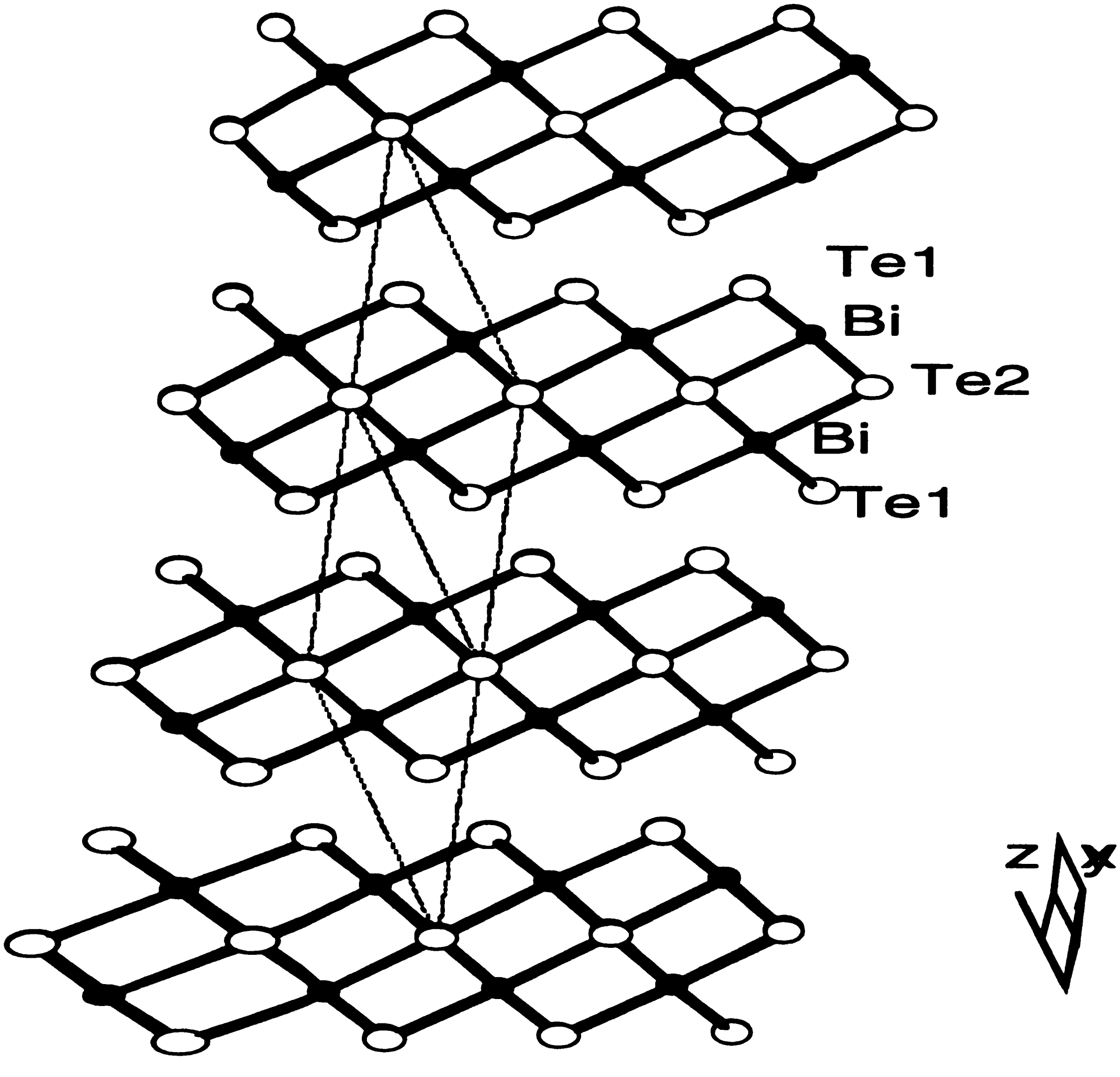

The five atoms in the unit cell reduce to three inequivalent atoms identified at Te1, Te2, and Bi as indicated in Figure 51. The corresponding Brillouin zone is given in Figure 52.

Figure 51. (a) Rhombohedral and (b) hexagonal representations of the unit cell of Bi_2Te_3. In (b) the Te atoms are open circles and Bi are shaded circles.

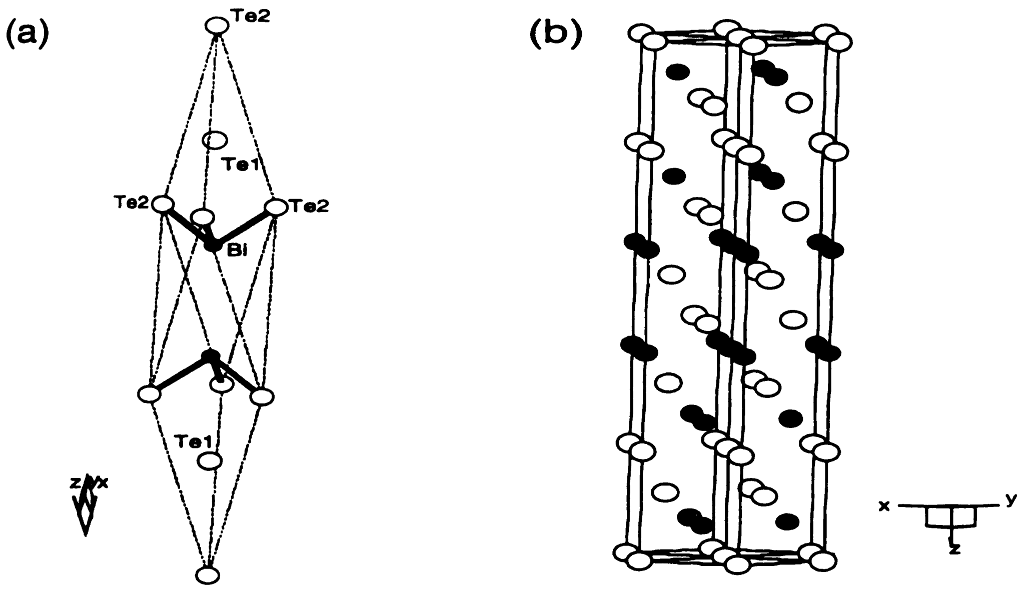
(a)
Te2
Te1
Te2
Te2
Bi
Te1
z
x
(b)
x
y
z

Figure 52. Brillouin zone of Bi_2Te_3 (corresponding to the rhombohedral unit cell).

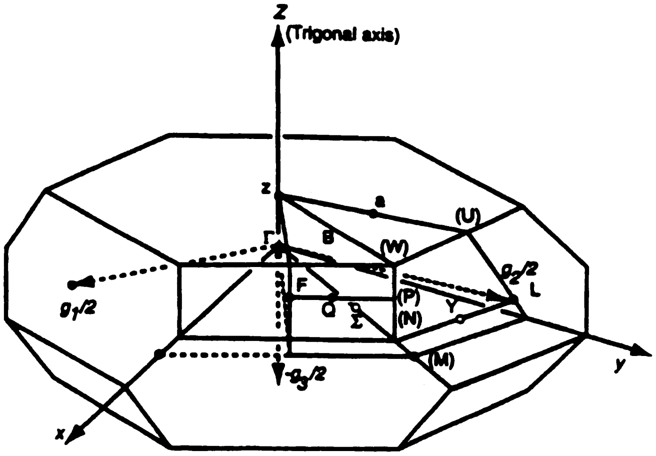
Z
(Trigonal axis)
z
a
(U)
Γ
B
(W)
$g_2/2$
L
$g_1/2$
F
Q
Σ
(P)
(N)
Y
(M)
$-g_3/2$
y
x

6.2.2. BAND STRUCTURE AND GAP FORMATION IN Bi_2Te_3

The electronic structure of Bi_2Te_3 has been studied extensively in the past[40, 124, 125, 126, 127, 128, 129, 130], but there have been few studies of the electronic structure of analogs containing either Sb or Se[40] or those containing both Se and Te. Some of these materials are found to be good thermoelectrics while others are not. Since the lattice contribution to κ depends mostly on the rhombohedral crystal structure, which is the same in all of the compounds, the differences in the thermoelectric properties must be electronic in origin and should be seen in the band structure. Before discussing the electronic structure of these structural analogs, let's first understand the electronic structure of Bi_2Te_3.

The importance of relativistic effects, especially that of SOI, has been noted in each of the previous calculations. However, several questions remain to be resolved in the band structure of Bi_2Te_3. For example, Thomas *et al.*[124] explained the physics of the gap formation by incorporating SOI, but were unable to incorporate it self-consistently into their *ab initio* LAPW calculation. Later, Mishra *et al.*[40] did include SOI self-consistently in their *ab initio* LMTO calculation, but they did not explore the nature of the bands that hybridized (leading to uncrossing) near E_F. More recently, Youn *et al.*[130] used the LAPW method with a different XC functional and a different cut-off energy between the valence and core states to find the CBM at a different location in **k**-space than the previous calculations[11, 40]. While the degeneracy of the hole pockets in the previous calculations agreed with the de Haas-van Alphen experiments[131, 132, 133, 134], only Youn *et al.*[130] found agreement with the degeneracy of the electron pockets, a result which we could not epeat using the WIEN97 program.[55] A careful study of the electronic structure of

Bi_2Te_3 is therefore needed to understand the formation of the semiconducting gap and the thermoelectric properties.

SOI affects the band structure of Bi_2Te_3 significantly. Before SOI is included, the band structure shows a direct gap semiconductor at the Γ point with a band gap of 0.37 eV. (Figure 53) This is about twice the value reported by Thomas *et al.*[124] who used a different LDA XC potential. There are two additional peaks in the HVB (along the Γa and ZF directions) and two valleys in the LCB (also along the Γa and ZF directions) which have an energy slightly lower than the VBM and slightly higher than the CBM, respectively. An orbital analysis reveals that the LCB and the HVB arise primarily from an admixture of Bi p and Te1 p bands. The conduction band is predominantly Bi p in nature whereas the valence band is predominantly Te1 p. Note that the Te1 atoms are in the layers that straddle the Van der Waals gap. Te2 p states lie primarily below the HVB although there is a small amount of Te2 p character in the HVB. In the presence of SOI, the band structure near E_F is dramatically changed. The main effect of SOI is to move the conduction band bottom down relative to the top of the valence band, due to the different SOI of Bi and Te, so that the bottom of the conduction band crosses the top of the valence band at Γ (Figure 54). The resulting hybridization, which leads to an uncrossing of the bands, opens a new gap which is indirect. This point was made by Thomas *et al.*[124] in their tight-binding parameterized calculations. They pointed out, however, the need for a complete self-consistent calculation including SOI to understand the subtle gap structure of Bi_2Te_3.[11]

Figure 53. Band structure of Bi_2Te_3 without SOI.

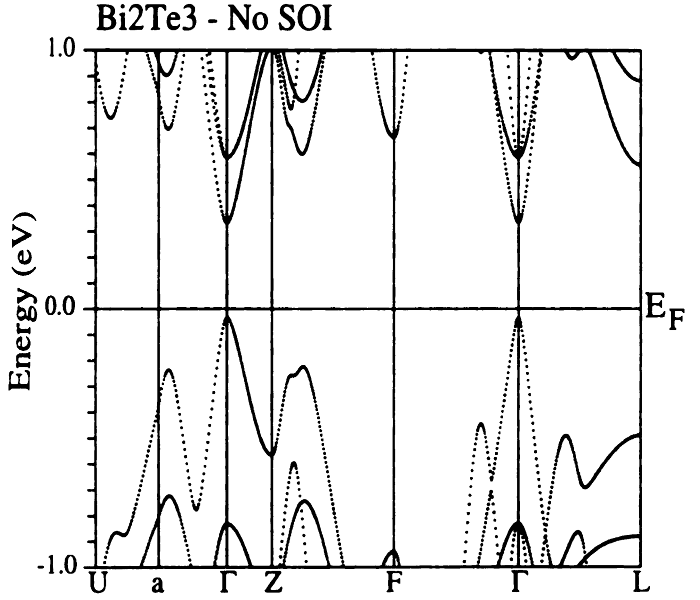

Figure 54. Band structure of Bi_2Te_3 with SOI.

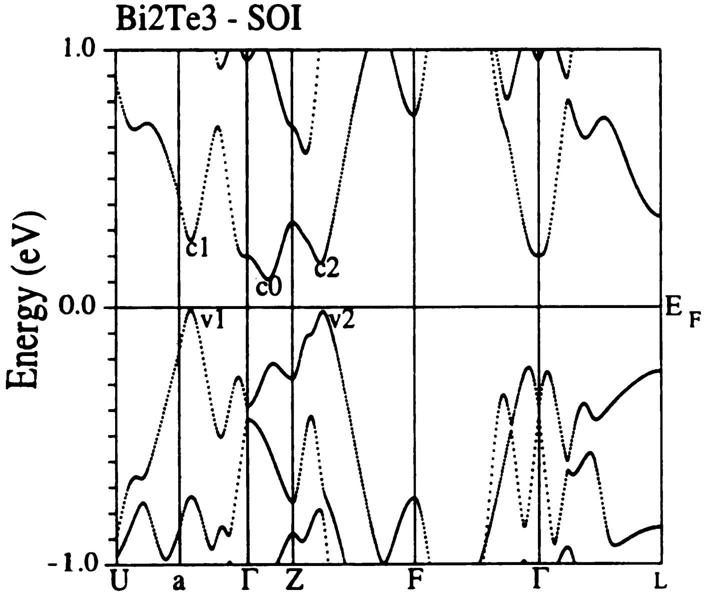

Including SOI keeps the shapes of the off-axis peaks virtually unchanged, but moves them closer by approximately 0.50 eV. The strong hybridization occurring near Γ depresses the HVB peak to such an extent that the two valence band side peaks now have higher energy and form the VBM (Figure 54). (This hybridization near Γ is much stronger than for that of the side peaks in the valence and conduction bands, so the overall shift is not rigid.) The two VBM lie on the yz plane of the BZ, which is a plane of reflection symmetry. They will be denoted as *v1* (along Γa) and *v2* (along ZF). Similarly the hybridization caused by the SOI shifts the CBM away from the Γ point to a point between Γ and Z, denoted as *c0*. The net result is an indirect-gap semiconductor with a band gap of 0.13 eV, in very good agreement with the previously published LMTO-ASA calculation[40] of 0.11 eV. In addition to this minimum, there are two higher-lying minima, *c1* (along Γa) and *c2* (along ZF). The gap between *v1* and *c1* is 0.27 eV and that between *v2* and *c2* is 0.23 eV.

Thomas *et al.*[124] have carried out optical measurements in Bi-doped Bi_2Te_3 and find an indirect gap of 0.15 ± 0.02 eV and a direct gap of 0.22 ± 0.02 eV, which agrees rather well with our values of 0.13 eV and 0.19 eV, respectively. Shubnikov-de Haas and de Haas-van Alphen measurements[131, 132, 133, 134] of both p- and n-doped Bi_2Te_3 give six-fold degenerate valence and conduction band extrema. The VBM *v2* appears to be the one seen in experiment. A recent calculation by Youn *et al.*[130] shows that, using a FLAPW method and the Hedin-Lundqvist form of the XC potential[135] for 60 special **k**-points and a cut-off energy between the valence and core states of -1.8 Ry, the band which we have called *c2* moves down by ~0.10 eV, with little difference in the rest of the band structure, to become the CBM. This point has the six-fold degeneracy for the conduction band seen experimentally, whereas our calculation does not, but their band gap has decreased to 0.06 eV. (It is interesting to note that we have better agreement with the band gap while Youn *et al.*[130] find better agreement with the degeneracy of the CBM.) They further find that the true extrema lie slightly off of the high symmetry lines which are plotted in Figure 54.[130] Using the WIEN97 program[55] and the identical input parameters, the result of a six-fold degenerate CBM could not be reproduced. As is well known, DFT calculates the occupied valence band states well, but does not do as good a job for the unoccupied conduction band, especially on the energy scale of ~0.1 eV.[31] It is disconcerting, however, that these results could not be reproduced with our program.

The orbital characters of the LCB and HVB in the presence of SOI are given in Figure 55 where the size of the circles is proportional to the orbital character. The Bi *p*, Te1 *p*, and Te2 *p* bands are all involved in different amounts in the bonding near E_F, but the LCB has a larger amount of Bi *p* character than Te1 *p* or Te2 *p* character, and the HVB has a larger Te1 *p* character than Bi *p* or Te2 *p* character.

The orbital character also can be seen in the DOS of the Bi *p*, Te2 *p*, and Te1 *p* partial densities of states (Figure 56) lying above and below E_F. Te 1 lies on the Van der Waals gap, bonded to one layer of Bi atoms below (or above) and weakly to a Te1 atom across the gap, while Te2 is bonded to two layers of Bi atoms, one above and the other below (Figure 50). The result is the stabilization of the Te2 *p* bands which lie primarily below E_F and contribute relatively less to the conduction band. The n-type transport is primarily through hybridized Bi *p* and Te1 *p* orbitals (contributing to the LCB) and p-type transport through hybridized Te1 *p*, Bi *p*, and Te2 *p* orbitals (contributing to the HVB). This is consistent with the results of carrier scattering lifetime measurements[124] and a previous calculation of electronegativity of each of the constituent atoms.[136] Finally, the Te1, Te2, and Bi valence *s* states lie approximately 10 eV below E_F and do not play any significant role in the bonding and transport properties.[11]

Figure 55. Band structure of Bi_2Te_3 with SOI. Included are (a) total band structure and the orbital characters of the bands: (b) Bi p, (c) Te1 p, and (d) Te2 p. The size of the circles overlying the band structure is directly proportional to the strength of the orbital character.

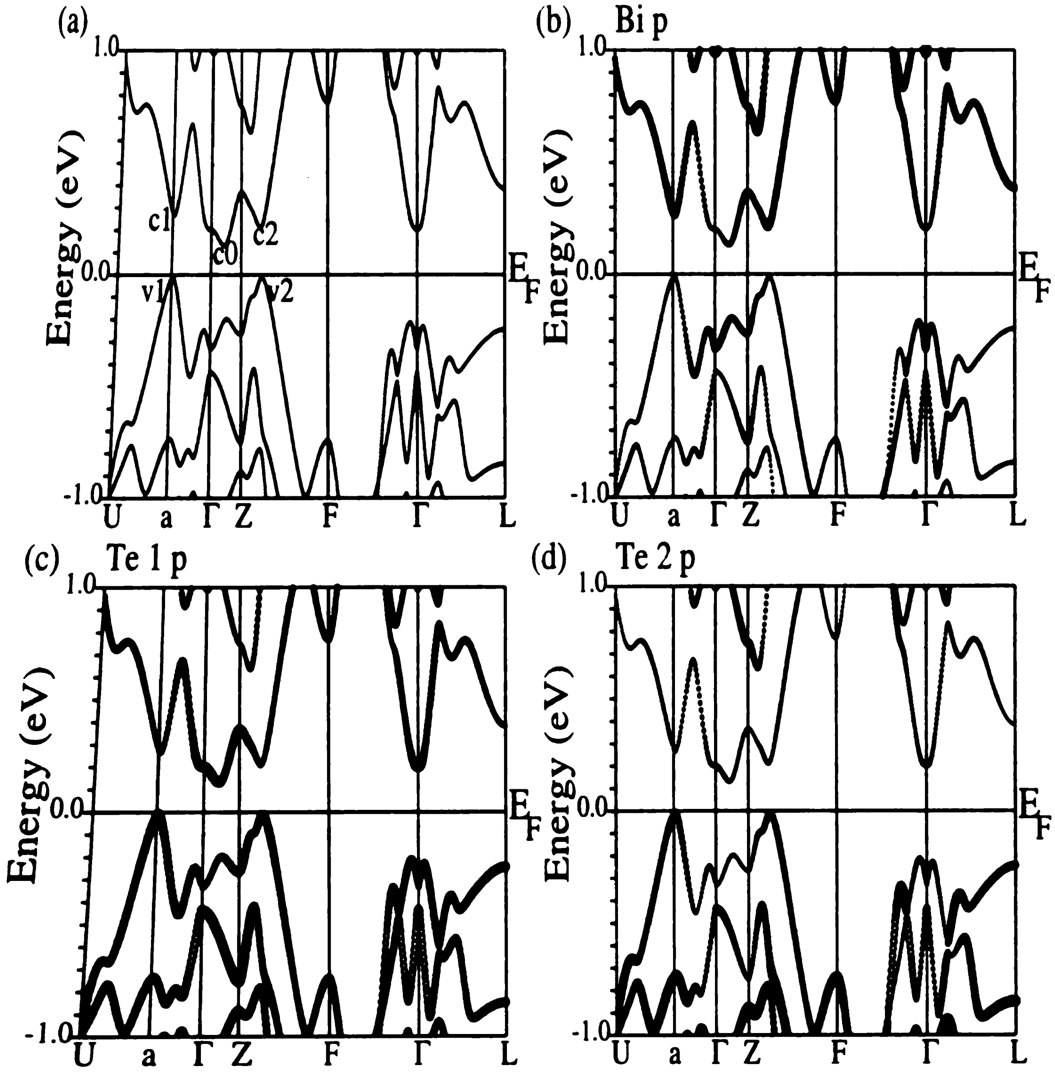

Figure 56. Total and partial DOS for Bi_2Te_3. Included are (a) total DOS and partial DOS: (b) Bi p, (c) Te1 p, and (d) Te2 p.

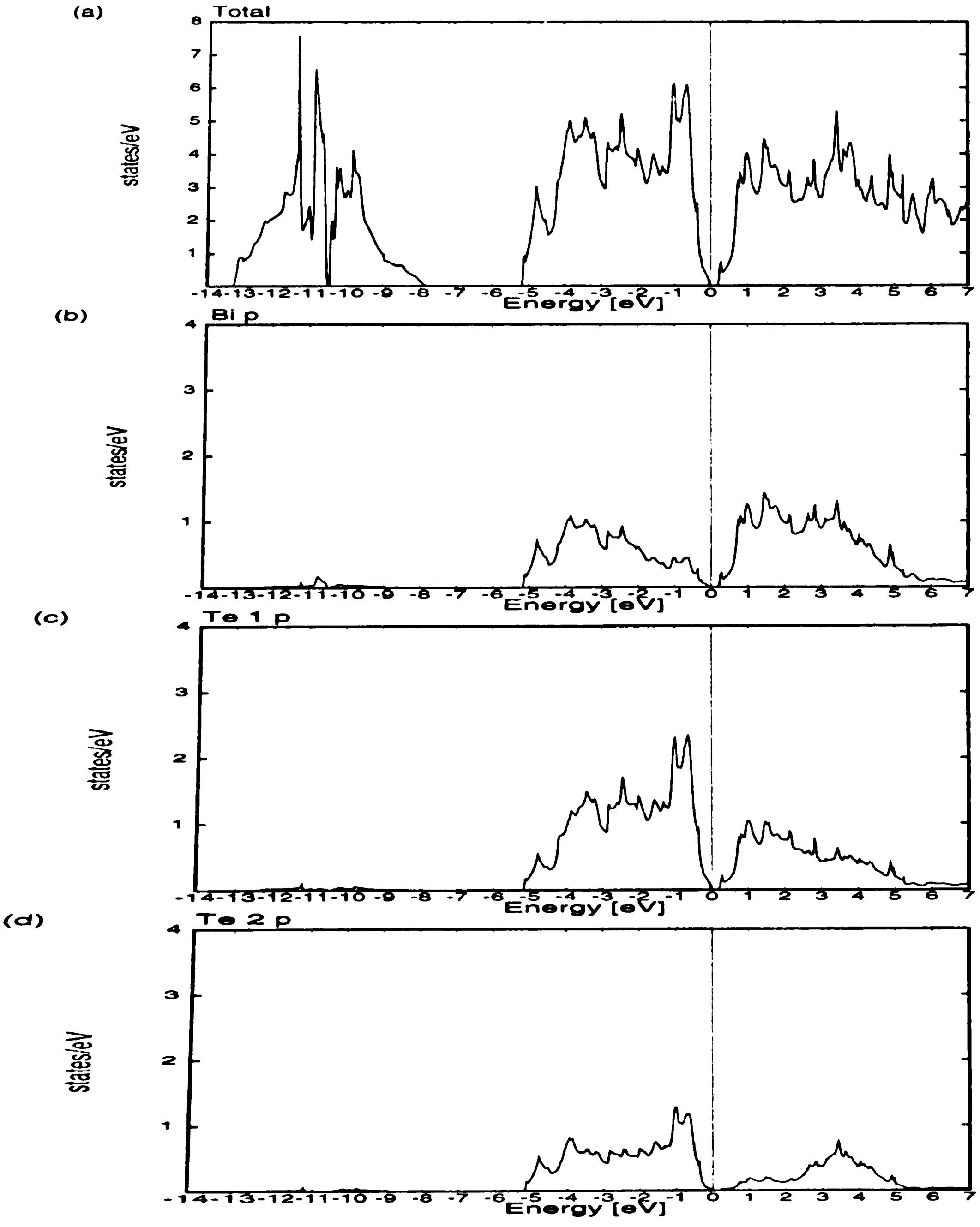

6.2.3. BAND STRUCTURE AND GAP FORMATION OF Bi_2Te_3 ANALOGS

A. Bi_2Se_3 AND Sb_2Te_3

The gap formation in Bi_2Te_3 is drastically affected by strong SOI of the Te1 p and Bi p orbitals. The SOI effects of Bi and Te cannot be separated since both are heavy elements and the LCB and HVB are strongly hybridized. We expect that the effects of SOI are larger for Bi than for Te, so that the electronic structures of Bi_2Se_3 and Bi_2Te_3 will have more similarities than those of Sb_2Te_3 and Bi_2Te_3. However, the opposite is true. This difference is important for understanding the thermoelectric properties, since Bi_2Te_3 and Sb_2Te_3 have been widely used as thermoelectric materials but Bi_2Se_3 has not.[4] The lattice constants used in the calculations within this section are given in Table XI.

The present calculation for Bi_2Se_3 (Figure 57) agrees very well on the global scale with the previous LMTO-ASA calculation.[40] Our LAPW-GGA calculations give a gap of 0.32 eV, slightly larger than the previous calculated value of 0.24 eV.[40], but both results are close to the experimental value of 0.2-0.3 eV.[137] The differences between our and the previous calculation[40] is that we find a larger lowering of the valence band peak at the Γ point (after inclusion of SOI) so that this peak has nearly the same energy as the two secondary peaks along UaΓ and ZF (Figure 57), whereas the Γ point peak was found to have a higher energy in the previous calculation.[40] In fact, in our calculation what appears to be a peak in the valence band at the Γ point is really a saddle point with a maximum only in the ΓZ direction. While electron-doped Bi_2Se_3 is known to have a minimum at the Γ point, in agreement with our and the previous calculations[40], hole-doped Bi_2Se_3 has not been studied experimentally.[138] It will be interesting to check the prediction of the theoretical results in this regard for two six-fold degenerate hole pockets at general points of the BZ and one saddle surface near the Γ point.[139]

Table XI. Lattice constants in atomic units (a.u.) and u and v parameters for Bi_2Te_3 and its analogs in the combined representation of the unit cell with hexagonal lattice constants and rhombohedral atomic coordinates used in these calculations. (Bi at $\pm(u, u, u)$, Tel at $\pm(v, v, v)$, and Te2 at $(0, 0, 0)$ in Bi_2Te_3. For details see Wyckoff.[63])

System	Lattice	constants (a.u.)	u	v
	a	c		
Bi_2Te_3	8.2836	57.6121	0.3990	0.2080
Bi_2Se_3	7.8197	54.1220	0.3990	0.2060
Sb_2Te_3	8.0313	57.4477	0.4000	0.2110
Bi_2Te_2Se	8.0880	56.4272	0.3961	0.2117
Bi_2Te_2S	8.1560	56.7107	0.3920	0.2120
Sb_2Te_2Se	7.914	56.5730	0.3942	0.7854
Bi_2Se_2Te	7.9710	55.5960	0.3985	0.2115
Sb_2Se_2Te	7.7570	55.7530	0.3953	0.2146

Figure 57. Band structure of Bi_2Se_3 (a) without and (b) with SOI.

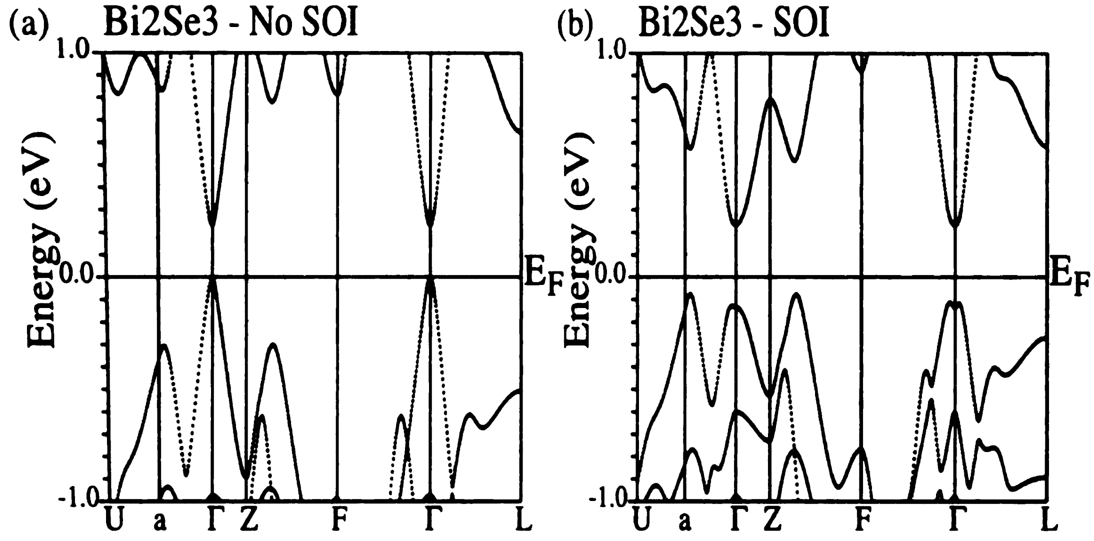

The only previous electronic structure calculation of Sb_2Te_3 was a tight-binding (TB) study which only calculated the DOS.[140] We find that the electronic structure of Sb_2Te_3 more closely resembles that of Bi_2Te_3 than Bi_2Se_3. The VBM of Sb_2Te_3 lies along UaΓ and ZF with the CBM lying along ΓZ with higher lying states along UaΓ and ZF (Figure 58), very much like that in Bi_2Te_3. Before the inclusion of SOI, Sb_2Te_3 is a zero-gap semiconductor at the Γ point with secondary peaks along UaΓ and ZF (Figure 58a). The inclusion of SOI causes the HVB to come closer relative to the LCB (and overlap) (Figure 58b) as in Bi_2Te_3. This produces an uncrossing of the bands with an opening of a new, larger gap of about 0.14 eV. While Sb p is mostly above E_F and Te p mostly below E_F, a strong hybridization of the Sb p and Te1 p occurs along ΓZ, similar to Bi_2Te_3.[11] The Te2 p orbitals do not appear to play any significant role near E_F, similar to what was found in Bi_2Te_3.[11]

Figure 58. Band structure of Sb_2Te_3 (a) without and (b) with SOI.

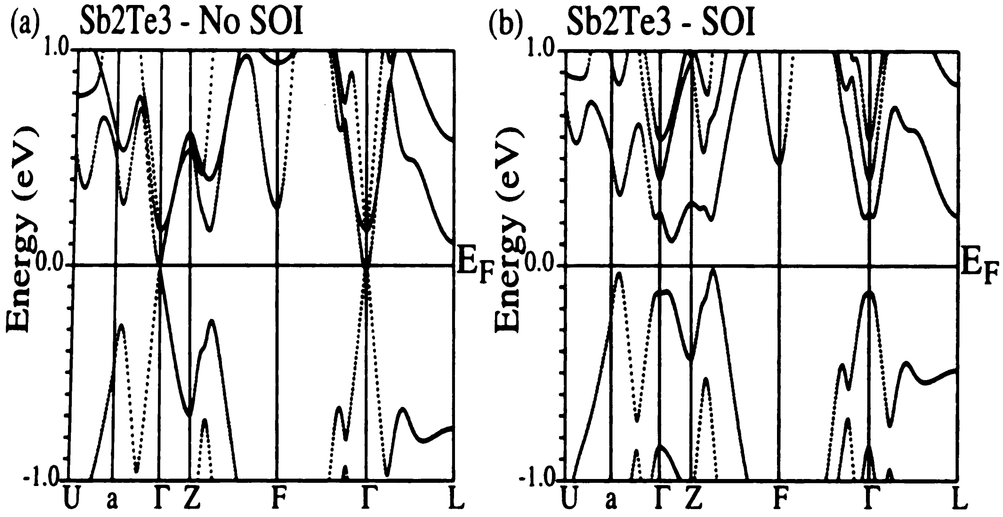

B. Bi_2Te_2Se, Bi_2Te_2S, Sb_2Te_2Se, Bi_2Se_2Te, AND Sb_2Se_2Te

There has been no theoretical or experimental studies of the band gaps in Bi_2Te_2Se, Bi_2Te_2S, Sb_2Te_2Se, Bi_2Se_2Te, or Sb_2Se_2Te. We have carried out electronic structure calculations in a series of such compounds to see how the gap structure changes when one or two of the three Te atoms are replaced by Se or S. Band structures of $Bi_2(Te,Se,S)_3$ generally resemble Bi_2Te_3 or Bi_2Se_3, depending which element is in greater abundance in the system. We find the physics of gap formation is the same in all these systems but the final band structures differ due to the size of the band gap before including SOI and the relative strengths of the Bi/Sb and Te/Se/S SOI. The crystal systems differ from that of Bi_2Te_3, Bi_2Se_3, or Sb_2Te_3 by changing the atom at the Te2/Se2 site which we did not find to play an important role in the gap formation in Bi_2Te_3.

The unit cells of Bi_2Te_2Se and Bi_2Te_2S differ from that of Bi_2Te_3 by replacing one of the three Te atoms by a Se or S atom, respectively, this atom going into the Te2 site.[141] Before the inclusion of SOI, the band gap in Bi_2Te_2Se is 0.10 eV and in Bi_2Te_2S is 0.32 eV, the gaps forming at the Γ point with secondary peaks along UaΓ and ZF (Figure 59a,c). The inclusion of SOI causes the HVB to come closer relative to the LCB (and overlap) as in Bi_2Te_3 and Sb_2Te_3. This produces an uncrossing of the bands with an opening of a new indirect gap. The HVB forms along UaΓ and ZF, while the bottom of the conduction band forms along ΓZ (Figure 59b,d). This more closely resembles the band structure of Bi_2Te_3 than Bi_2Se_3.[11, 40] While Bi p is mostly above E_F and Te p mostly below E_F, a strong Bi p-Te1 p hybridization occurs along ΓZ, similar to Bi_2Te_3.[11] The Se2 p and S2 p orbitals do not appear to play any significant role near E_F, similar to what was found for Te2 p in Bi_2Te_3 and Se2 p in Sb_2Te_3.[11]

Figure 59. Band structures of Bi_2Te_2Se (a) without and (b) with SOI and Bi_2Te_2S (c) without and (d) with SOI.

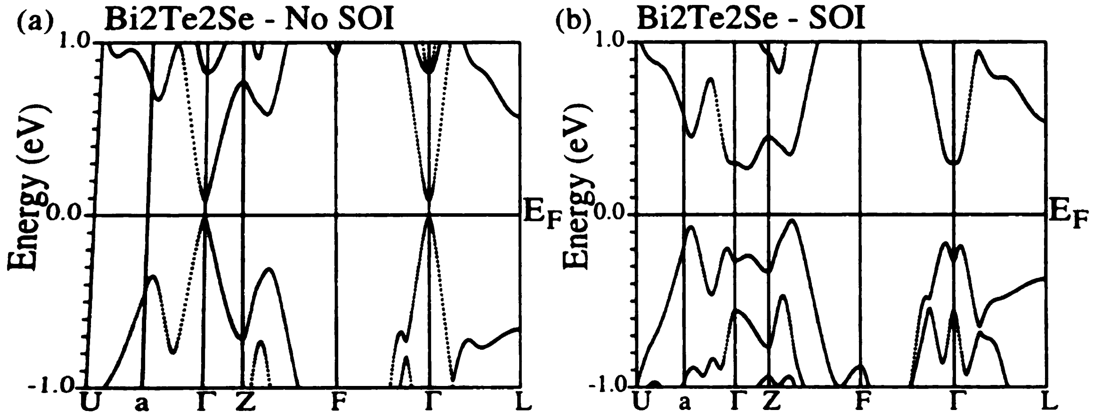

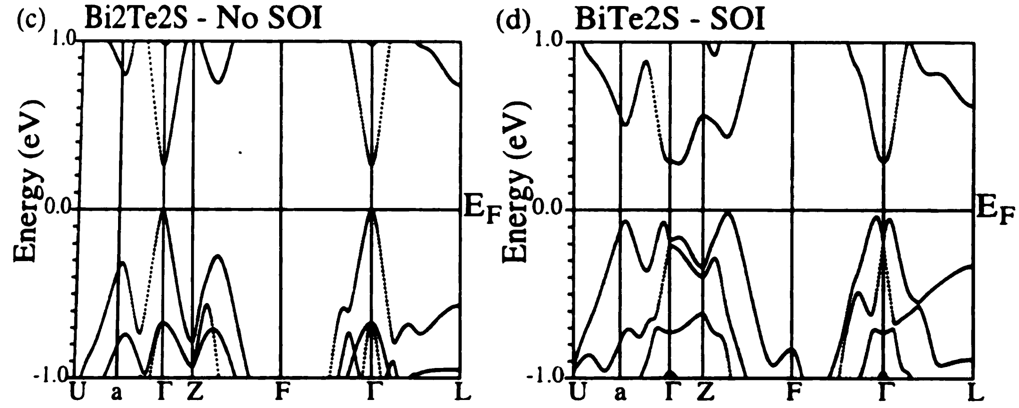

While only one atom in the unit cell of Sb_2Te_2Se differs from that of Sb_2Te_3, specifically the atom at the Te2 site[141] which does not strongly hybridize with Te1 or Sb near E_F at the Γ point in either compound, the band structures are significantly different.(Figure 58, 60). Before the inclusion of SOI, Sb_2Te_2Se has a band gap of 0.03 eV. The VBM and CBM have a maximum at the Γ point along Γa and ΓZ, with secondary peaks along UaΓ and ZF, but this point is a local minimum along ΓF and ΓL(Figure 60a). The inclusion of SOI causes the HVB to come closer relative to the LCB so that the two bands overlap, drastically changing the bands near the Γ point. The CBM moves away from the Γ point, similar to that in Bi_2Te_3 or Sb_2Te_3, but remaining closer to Γ. Due to the smaller SOI of Sb and Se in the Te2 site (and different hybridizations of Te1-Se2 compared to Te1-Te2), the VBM remains at the Γ point (Figure 60b), similar to Bi_2Se_3, and the band gap increases to 0.31 eV. Here, the atom occupying the Te2 site plays a role in the gap formation by changing the band gap before inclusion of SOI (0 in Sb_2Te_3, 0.03 in Sb_2Te_2Se) so that the degree of overlap of the LCB and HVB differs after including SOI, which then change the final band structures.

Figure 60. Band structure of Sb_2Te_2Se (a) without and (b) with SOI

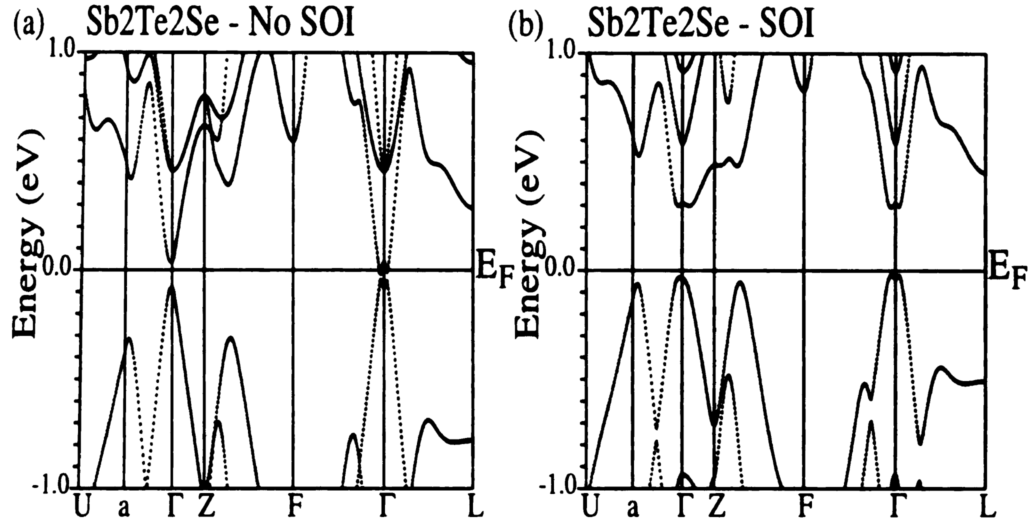

The gap formation of Bi_2Se_2Te and Sb_2Se_2Te is far simpler than those in the previously studied systems. The unit cells of Bi_2Se_2Te and Sb_2Se_2Te differ from those of Bi_2Se_3 and (hypothetical rhombohedral) Sb_2Se_3, respectively, by replacing one of the three Se atoms by a Te atom, this Te atom going into the Se2 site.[141] Before the inclusion of SOI, the band gap in Bi_2Se_2Te is 0.56 eV and in Sb_2Se_2Te is 0.18 eV, both of these gaps forming at the Γ point with secondary peaks along UaΓ and ZF (Figure 61a,c). The inclusion of SOI causes the HVB to come closer relative to the LCB but they do not overlap so the gap remains direct (Figure 61b,d), decreasing to 0.06 eV in Bi_2Se_2Te and to 0.05 eV in Sb_2Se_2Te. Again, changing the atom at the Se2 site increases the band gap before inclusion of SOI so that the LCB and HVB do not come close enough to overlap in these two systems.

Figure 61. Band structure of Bi_2Se_2Te (a) without and (b) with SOI and Sb_2Se_2Te (c) without and (d) with SOI

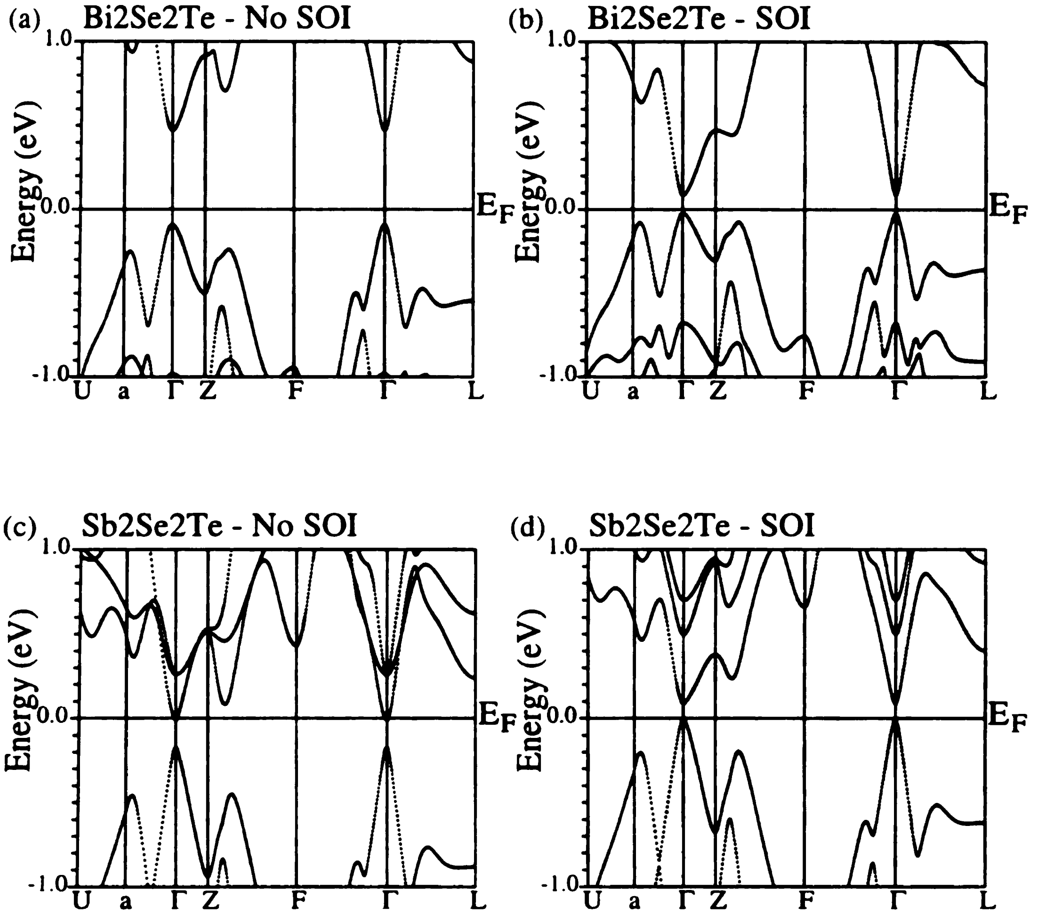

C. Bi_2S_3

While S lies in the same column as Se and Te, Bi_2S_3 forms in a different crystal structure than Bi_2Te_3 and Bi_2Se_3. Bi_2S_3 has been studied for thermoelectric applications in the past. While it was found to have promising values of thermopower and thermal conductivity, its electrical conductivity was found to be too small.[142] Due to its larger band gap, it has also been investigated as a prospective material for photovoltaic converters.[143] While this material has been studied extensively experimentally[143], its band structure has not been investigated yet.

The crystal structure of Bi_2S_3 is orthorhombic in the space group V_h^{16} (*Pbnm*) with twenty atoms in the unit cell.[63] The orthorhombic unit cell and its corresponding BZ are shown in Figure 62. The crystal structure consists of sheets of atoms parallel to the z-axis with each S surrounded by three Bi atoms and each Bi atom surrounded by three S atoms.[63] These twenty atoms reduce to five inequivalent atoms identified as Bi1, Bi2, S1, S2, and S3. The lattice parameters (a, b, c) are 11.15 Å, 11.30 Å, and 3.981 Å, the atomic positions taken from Wyckoff.[63]

Figure 62. (a) Orthorhombic unit cell of Bi_2S_3 (shown in the a-b plane) and its (b) corresponding Brillouin zone.

(a)

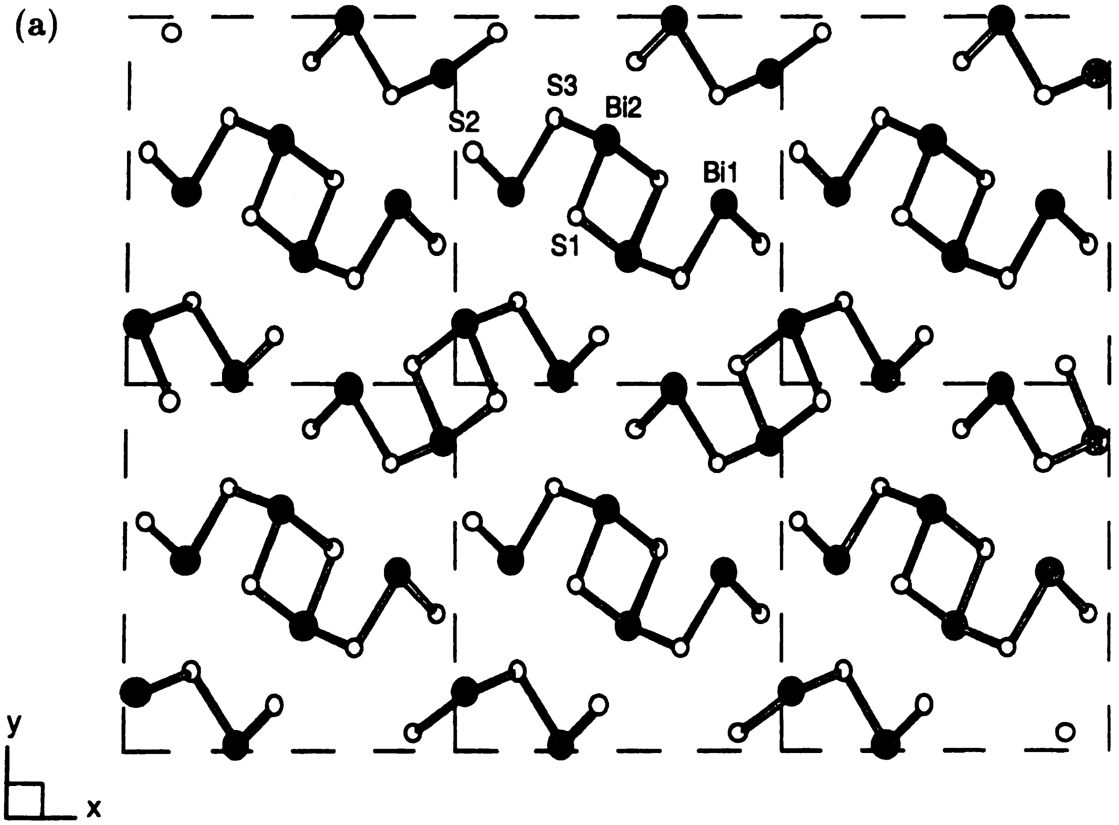

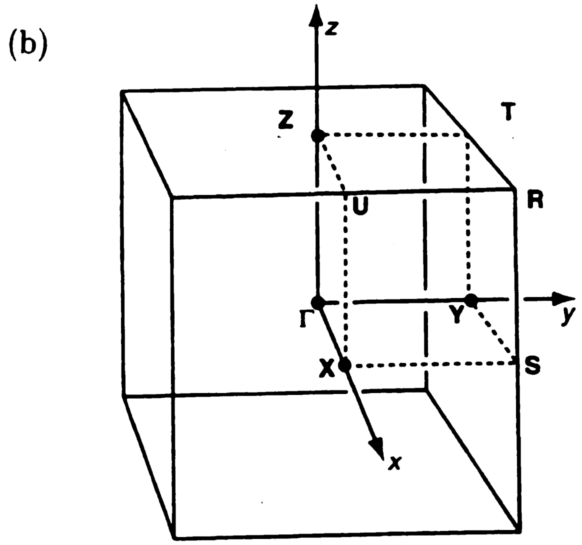

The electronic structure of Bi_2S_3 shows a large number of bands within a few eV of E_F. Before the inclusion of SOI, an indirect gap of 1.55 eV forms between the CBM at S and the VBM along ΓX (Figure 62). After the inclusion of SOI, the HVB is practically unchanged, but the CBM moves from S to a point along ΓX (Figure 63) to form a nearly direct band gap of 1.24 eV. The band gap has been measured by several groups to be between 1.2-1.7 eV[142, 144], one of the most recent measurements giving a value of 1.3 eV[142].

Figure 63. Band structure of Bi_2S_3 (a) without and (b) with SOI.

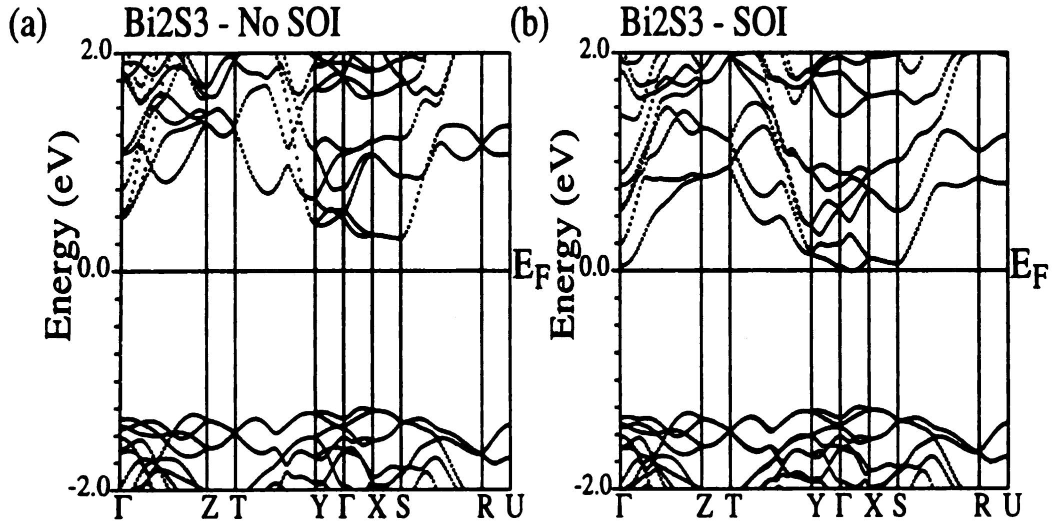

In order to understand the electronic structure of this material near the gap region, an orbital analysis of the bands near E_F was performed. We find that Bi1 and Bi2 p orbitals contribute primarily to the bottom of the conduction band while S1, S2, and S3 p orbitals contribute to the top of the valence band. While there is some hybridization between these orbitals, it is much less that that between Bi p and Te/Se p in Bi_2Te_3 and Bi_2Se_3.[11, 40] Thus, Bi_2S_3 is more ionic. These differences for Bi_2S_3, with respect to Bi_2Te_3 and Bi_2Se_3, may be due to both the different crystal structure of Bi_2S_3 compared to Bi_2Te_3 and Bi_2Se_3 and the different electronic affinities of S, Se, and Te.

6.2.4. EFFECTIVE MASSES OF THE BAND EXTREMA OF Bi_2Te_3

In the last two sections of this chapter, we will test the validity of our band structure calculations (aside from comparing the band gap values which has already been done) by comparing them with several experiments on these materials. In this section, the orientation of the carrier pockets and effective masses of the doped Bi_2Te_3, which determine the properties close to E_F (~0.1 eV), will be compared. These properties are important to understand the thermoelectric properties of these materials. The next section will compare the calculated DOS to results of photoemission studies over a larger energy range (~10 eV) in Bi_2S_3, Bi_2Se_3, Bi_2Te_2Se, and Bi_2Te_3.

Shubnikov-de Haas and de Haas-van Alphen experiments have found six-fold degenerate CBM and VBM in Bi_2Te_3. While these experiments cannot locate the position of the extrema in **k**-space, the number of extrema and the effective mass tensor associated with these extrema have been repeatedly studied in Bi_2Te_3.[131, 132, 133, 134] The effective mass tensor is defined as[22]

$$[m/m_e]^{-1}_{ij} = \alpha_{ij} = \hbar^{-2}[\frac{\partial^2 E}{\partial k_i \partial k_j}] \tag{74}$$

where m_e is the free electron mass and $2\pi\hbar$ is Planck's constant. In most cases, the off-diagonal terms of the mass tensor are small, so diagonal elements of the mass tensor, α_{ii}, accurately give the inverse of the effective mass parameters m_i ($i = 1, 2, 3$). In the general case, however, the mass tensor has to be diagonalized to obtain the effective masses associated with the principal directions. We fit the calculated E vs **k** along different orthogonal directions to parabolas and obtained the coefficients α_{ij}.

All of our calculated extrema in Bi_2Te_3 lie on planes of reflection symmetry (the z axis is the trigonal axis, the y axis is the bisectrix axis, and the yz plane is one of the three reflection planes) the energies near the top of the HVB and the bottom of the LCB can be fitted using the equation

$$2m_e/\hbar^2\ \varepsilon_k = \alpha_{xx}k_x^2 + \alpha_{yy}\ k_y^2 + \alpha_{zz}k_z^2 + 2\alpha_{yz}k_yk_z \tag{75}$$

where a constant term has been omitted and **k** is measured from the extrema. Note that the de Haas-van Alphen measurements find sixfold-degenerate hole and electron pockets lying on the reflection planes (containing the trigonal and bisectrix axes). The cross sections of these pockets in the yz plane are ellipses whose major axes make an angle θ with the y axis (the bisectrix axis). The angle θ is given by[131, 133]

$$\theta = \frac{1}{2}\arctan[2\alpha_{yz}/(\alpha_{zz} - \alpha_{yy})] \tag{76}$$

The effective masses for Bi_2Te_3 were obtained by fitting values of the energy close to different LCB minima and HVB maxima to Equation 75 while moving along suitably chosen directions in the BZ (Figure 64). The energy dispersion curves near the LCB minima and HVB maxima of Bi_2Te_3 are known to display strong nonparabolic behavior[131, 132, 133, 134], but a fair approximation to a parabolic band can be made if points are chosen close to the band extrema.

Theoretical values of the coefficients α_{ij} are given in Table XII along with their experimental values. They agree quite well with the previous LMTO calculation[40], though using the values in their paper, θ should be approximately 40° not 35° as reported in their paper. The curvature in the x direction is obtained using values very close to the HVB maximum and LCB minimum and, as we can see, the theoretical values are about a factor of 3 too large compared to experiment. For higher doping, i.e. for larger k_x, the effective mass decreases due to nonparabolic effects which improves the agreement with experimental values.

Figure 64. Fitting of the energy band near the conduction band minimum to a parabola for Bi_2Te_3 using the computer program KALEIDAGRAPH[120].

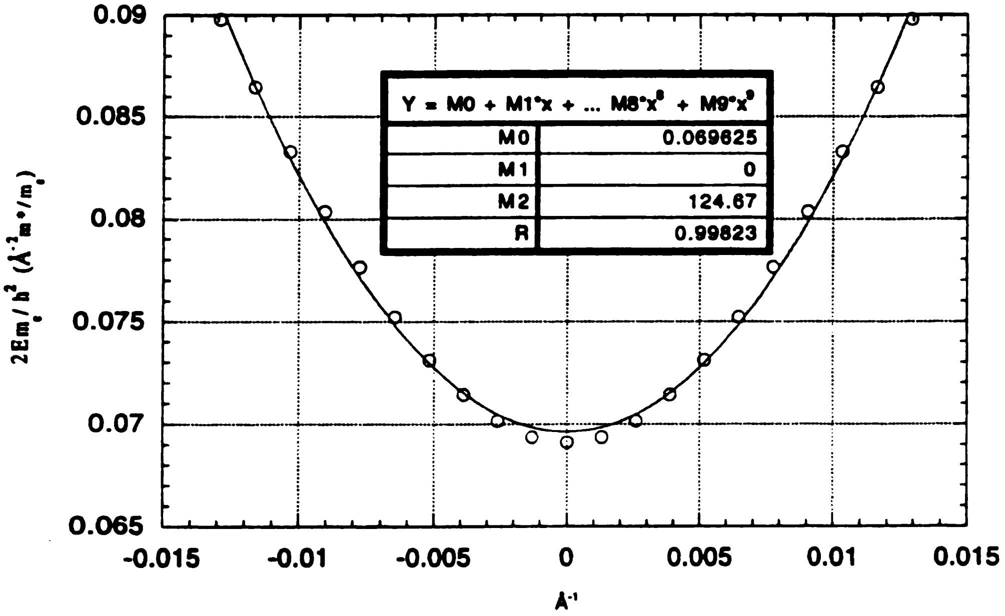

Table XII. Theoretical and experimental values of the effective mass tensor parameters associated with the conduction band minima and valence band maxima for Bi_2Te_3.

Conduction band	*c0*	*c1*	*c2*	Experiment[131] (±10%)
$\alpha_{xx} = [m/m_e]^{-1}_{xx}$	20.25	112.75	95.84	46.9
$\alpha_{yy} = [m/m_e]^{-1}_{yy}$	3.97	2.87	3.56	5.92
$\alpha_{zz} = [m/m_e]^{-1}_{zz}$	3.75	5.49	6.20	9.50
$\alpha_{yz} = [m/m_e]^{-1}_{yz}$	2.93	2.54	2.39	4.22
θ	-43.9°	31.3°	32.7°	33.5°
Valence band		*v1*	*v2*	Experiment[133] (±10%)
$\alpha_{xx} = [m/m_e]^{-1}_{xx}$		107.51	90.05	32.5
$\alpha_{yy} = [m/m_e]^{-1}_{yy}$		3.97	2.91	4.81
$\alpha_{zz} = [m/m_e]^{-1}_{zz}$		5.54	5.60	9.02
$\alpha_{yz} = [m/m_e]^{-1}_{yz}$		2.76	2.34	4.15
θ		37.1°	30.0°	31.5°

The positions of the electron and hole pockets *c1*, *c2*, *v1*, and *v2* on the reflection planes as well as the angle θ associated with these pockets are accurately reproduced compared to experiment (Figure 65). The angle θ of the electron pocket associated with the *c0* minimum is nearly 90° away from that seen in experiment. This, along with the more recent calculation[130], suggests that *c0* does not correspond to a conduction band extrema seen experimentally.[131, 132, 133, 134]

Figure 65. Positions of the electron and hole pockets lying on the reflection plane of the Brillouin zone for Bi_2Te_3 for (a) CBM and (b) VBM.

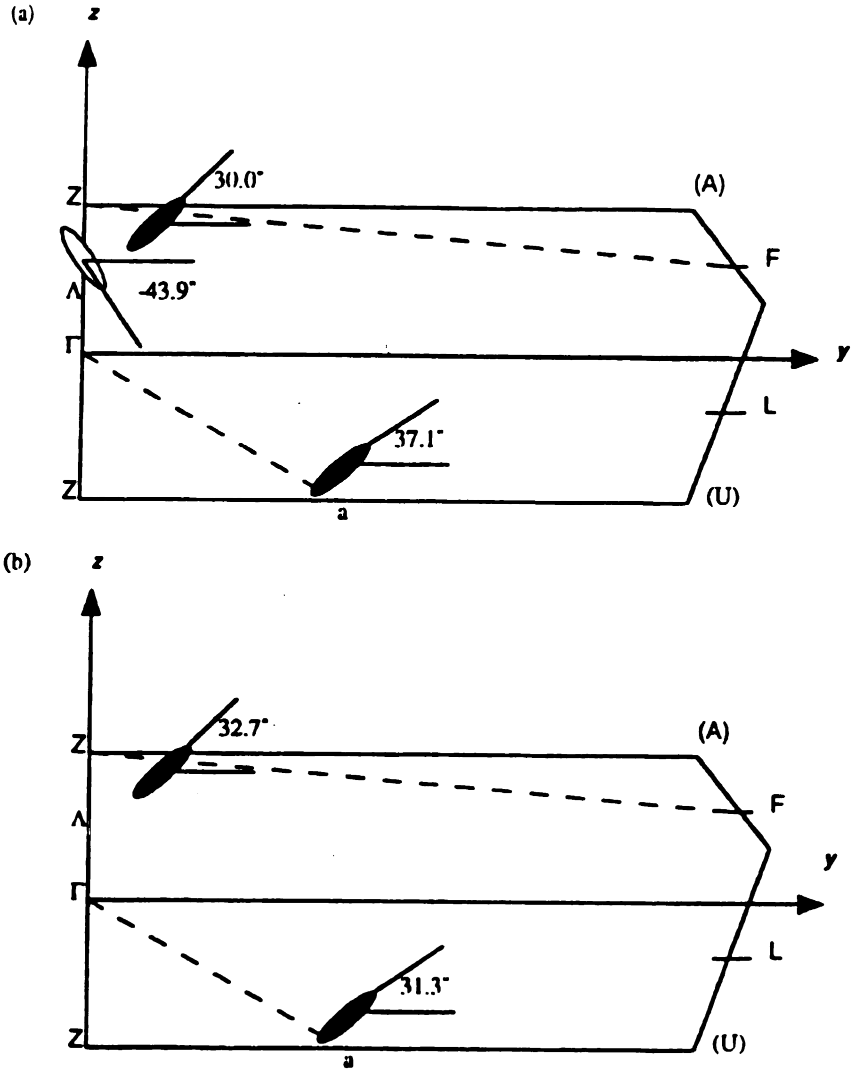

As already stated, the nature of the bands near E_F play an important role in the the observed large room temperature values of ZT in these materials. First, in applications, Bi_2Te_3 is alloyed with Bi_2Se_3 and Sb_2Te_3 to reduce κ. However, the large S and σ values must have an electronic origin. The B parameter (Equation

24 in Chapter 2)[11, 24] suggests highly anisotropic effective masses and large band degeneracy will produce high ZT. We find that in Bi_2Te_3, the effective masses, while fairly small, are highly anisotropic. Unlike the half-Heusler alloys, these masses are much closer to those found in other doped semiconductors. Further, there is a 6-fold degeneracy in the VBM and CBM which enhances the thermopower. We find that in Bi_2Se_3 the VBM and CBM have a lower degeneracy which can explain the lower value of ZT seen in this material compared to Bi_2Te_3. The combination of anisotropic (but not large) effective masses and highly degenerate band extrema, coupled with the low κ, are the reason for the large ZT values seen in Bi_2Te_3. These features should be investigated in other thermoelectric materials.[11, 12, 13]

6.2.5. COMPARISON OF THE BAND STRUCTURE WITH PHOTOEMISSION EXPERIMENTS

Photoemission experiments allow for a testing the band structure calculations over a larger energy scale. Photoemission spectroscopy (PES) is a direct probe of a material's occupied states. In these experiments, photons incident on a sample result in ejection of electrons which are then collected and energy analyzed. In the reverse experiment, inverse photoemission spectroscopy (IPES), electrons are incident on the sample while photons are ejected and studied to analyze the unoccupied states. Angle-resolved PES (ARPES) allow for a comparison with the calculated $E(\mathbf{k})$ vs. $\mathbf{k}$. On the other hand, an angle-integrated PES spectrum gives information about the occupied DOS modified by energy dependent matrix elements between initial and final states.[145]

Angle-resolved photoemission on Bi_2Te_3[146] and Bi_2Se_3[147] have been performed recently in order to compare the experimentally determined E(**k**) vs **k** with our band structure. Greanya *et al.*[146] studied the band dispersions of p- and n-doped Bi_2Te_3 along two **k**-space directions, ΓZ and UaΓ, the directions which one should find *v1*, *c0*, and *c1*. Their measured overall width of the valence band states of 5-5.5 eV for both systems agreed very well with the current calculation.[11] They found the six-fold VBM along UaΓ, consistent with the current calculation[11] and Shubnikov-de Haas and de Haas-van Alphen experiments[131, 132, 133, 134] The position of the maxima was found not at the calculated position, however, which may be due to anti-site doping of Bi into the Te sites[146] known to play a large effect in the band structure near E_F[11]. Their doping was insufficient to find the CBM. They also found that the dispersion along ΓZ, through the Van der Waals gap was much smaller than predicted[11], though this might be due to electron-phonon interaction, electron-electron interaction, anti-site defects, and the limited penetration depth of the photons into the material along this direction. Greanya *et al.*[147] also studied n-doped Bi_2Se_3 along ΓZ, ΓaU, ΓF, and ΓL to find a single VBM at the Γ point with a close lying local maximum about 0.1 eV below along ΓF. Greater dispersion is seen along ΓZ than in Bi_2Te_3, though these bands are still fairly flat. Again, the differences between the experiment and the band calculation may be due to anti-site defects and electron-electron interactions.[147]

Several angle-integrated PES studies have been performed on Bi_2X_3 (X = Te, Se, S) systems in the past[139, 148, 149, 150]. Two fairly recent photoemission studies will be compared with our calculations for Bi_2Te_3, Bi_2Te_2Se, Bi_2Se_3, and Bi_2S_3. We find that the positions of the peaks in our DOS agree rather well with the measured PES, and, in general, increases in the energy resolution of the PES spectrum tends to improve the agreement between experiment and our calculations.

While there have been several sets of photoemission data performed on Bi_2Te_3-related systems, most of these have been x-ray photoemission (XPS) measurements with a low energy resolution which makes comparison with the calculated DOS unreliable. Debies *et al.*[148] studied Bi_2O_3, Bi_2S_3, Bi_2Se_3, and Bi_2Te_3, where the energy resolution was not explicitly specified, but was fairly low. Nascimento *et al.*[150] studied Bi_2Se_3 with an energy resolution of 0.8 eV. Ueda used both PES and IPES measurements to study the filled and empty states of Bi_2S_3, Bi_2Se_3, Bi_2Te_2Se, and Bi_2Te_3 with an energy resolution of 0.2 eV for the PES experiments and 0.58 eV for the IPES experiments. More recently, Greanya *et al.*[139, 146, 147] used PES studies to understand Bi_2Se_3 and Bi_2Te_3 using an energy resolution of 0.08 eV.

Figure 66 gives the PES spectra and the positions of the dominant spectra found in the experiment of Ueda *et al.*[149] for Bi_2S_3, Bi_2Se_3, Bi_2Te_2Se, and Bi_2Te_3. In Ueda *et al.*'s[149] experiments, E_F is maintained by electrical contact between the sample and substrate on which it is mounted.[145] In the electronic structure calculations, E_F, which should be somewhere in the middle of the band gap, can be anywhere between the VBM and the CBM. Since we do not know the experimental value of E_F, its exact position depending on doping, etc., we will compare our theoretical results with experiment by rigidly shifting the theoretical DOS such that the highest valence band peak coincides with that seen in the experiment. The positions of the peaks obtained by Ueda *et al.*[149], are numbered *c1*-*c3* in the conduction band and *v1*-*vn* ($n = 3$ for Bi_2Te_3, $n = 5$ for Bi_2Se_3 and Bi_2Te_2Se , and $n = 4$ for Bi_2S_3) in the valence band, and these numbers are placed in the calculated DOS plot (Figure 67), *c1* and *v1* lying closest to E_F.

Figure 66. Valence-band photoemission (UPS) and conduction band inverse-photoemission (IPES) for Bi_2S_3, Bi_2Se_3, Bi_2Te_2Se, and Bi_2Te_3 crystals. UPS and IPES spectra for each crystal are connected at E_F. Energies are referred to E_F. (courtesy of Yoshifumi Ueda).[149]

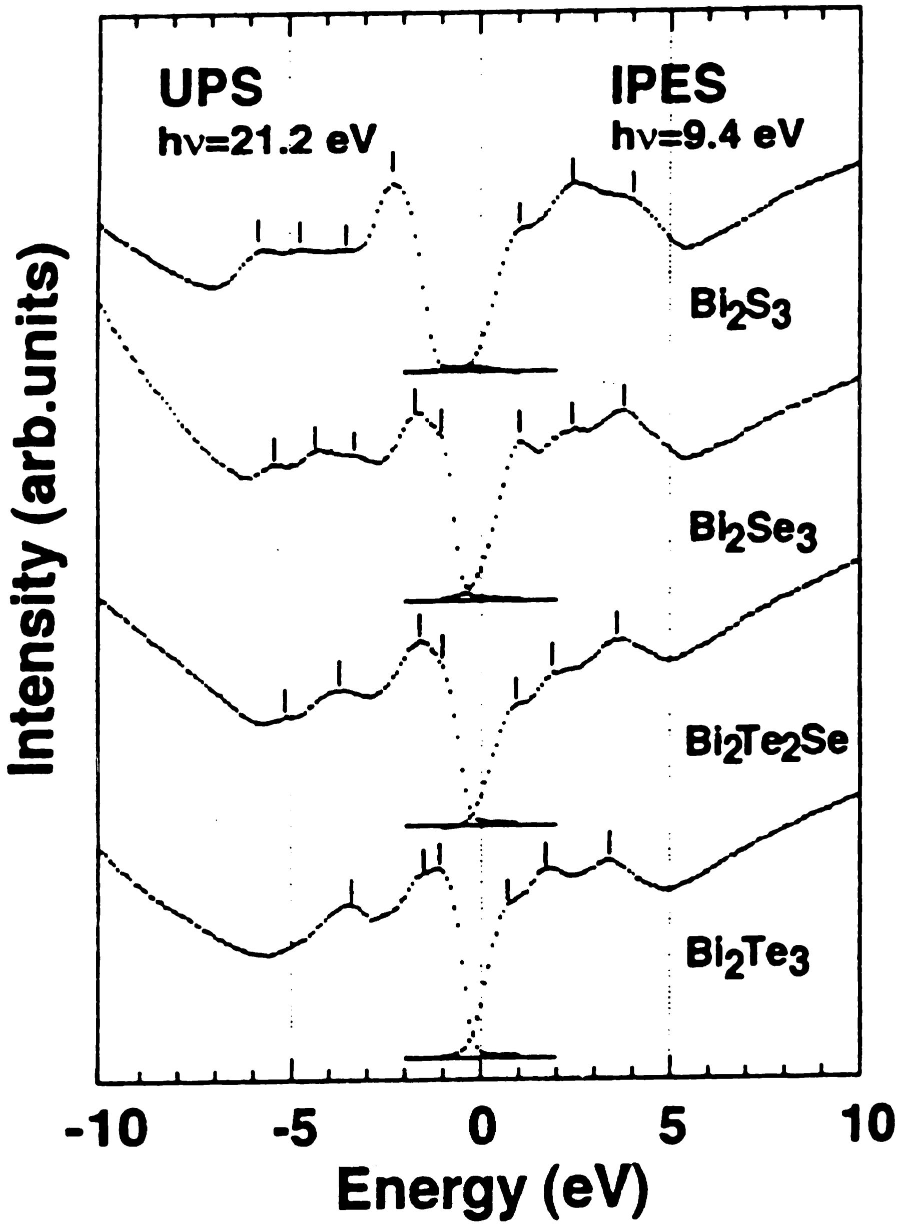

Figure 67. Total DOS of (a) Bi_2S_3, (b) Bi_2Se_3, (c) Bi_2Te_2Se, and (d) Bi_2Te_3. The arrows indicate the positions of the photoemission peaks seen in the work by Ueda.[149]

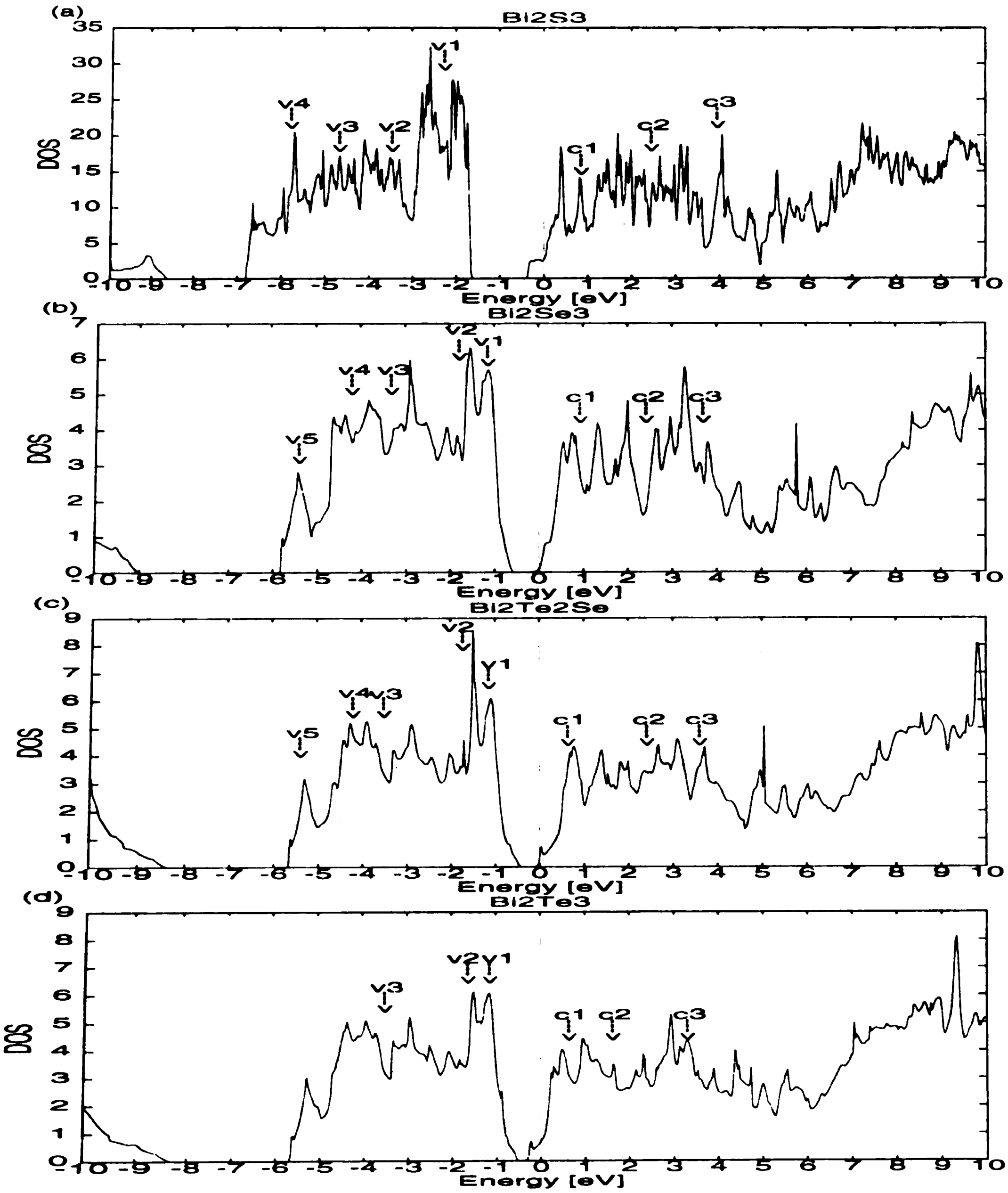

A close look at Figure 67 shows that the double-peaked structure near the VBM is found in the PES of all three compounds, Bi_2Te_3, Bi_2Te_2Se, and Bi_2Se_3, while Bi_2S_3, which has a completely different crystal structure, displays a single prominent peak in this experiment. The separation between these two peaks is 0.3-0.4 eV, very close to that seen in the calculated DOS. The DOS peak near the VBM obtained in the previous LMTO-ASA calculation had only one peak[40], in contradiction to these experiments.[139, 149] Also, this double-peak is found to come primarily from Te1/Se1 and Te2/Se2 p states. It appears that the narrow width of these two peaks is consistent with the picture proposed by Ueda *et al.*[149] who ascribed these to lone pair states of Se1 and Se2 in Bi_2Se_3. A similar picture must be true for Bi_2Te_3 and Bi_2Te_2Se which have similar local coordination geometry.

For Bi_2Te_3 the energy separation between the HVB peaks is found to be 0.5 eV in the measurement[149] compared to 0.3 eV found in our calculation.[139] There is only one peak seen at -3.5 eV. For the IPES results, within the experimental resolution (0.56 eV) the conduction band peak *c1* corresponds to the calculated peak positions at 0.5 and 1.0 eV while *c3* at 3.4 eV lies slightly below the calculated peak position at 2.9 eV. Matrix element effects and noise affect the heights and positions of the PES peaks[145], but while these have not been included in the DOS calculation, the agreement between the theoretical DOS peak positions and experiment is fairly good.

For Bi_2Se_3, the separation of the double-peaked structure is 0.5 eV compared to the calculated value of 0.4 eV. The calculated peak at -2.9 eV may correspond to *v3*. shifted by -0.5 eV, while peaks at -3.8 eV and -4.6 eV may be seen as the single peak *v4*. The calculated peak at -5.4 eV agrees well with *v5*. The two lowest peaks in the conduction band at 0.8 eV and 1.3 eV lie within the experimental resolution of *c2* and *c3*, respectively.[149] For Bi_2Se_3, the overall agreement between the theoretical DOS and experimental PES (and IPES) is very good.

In Bi_2Te_2Se, the separation between the valence band peaks *v1* and *v2*, the double-peak structure at the top of the PES spectra[149] is 0.5 eV compared to the calculated value of 0.4 eV. The peak predicted at -2.9 eV may be peak *v3* shifted by -0.5 eV, the peaks at -3.9 and -4.6 eV may correspond to the single peak *v5* at -4.2 eV, and the peak predicted at -5.3 eV correspond to *v5*. As regards to the conduction band, three peaks (*c1*, *c2*, and *c3*) are seen experimentally (0.7, 2.5, and 3.7 eV), two of which agree well with our calculated DOS peaks (0.7 and 3.7 eV).[149]

Finally, for Bi_2S_3, which has a different crystal structure than the above three compounds, the general structure of the calculated DOS (Figure 66) agrees very well with the PES spectra[149]. Experimentally one sees a dominant valence band peak below E_F, while our calculation predicts a double peak with a separation of 0.7 eV with a fairly smooth background between -3.5 and -7 eV. In order to facilitate comparison between theory and experiment, the energy reference (E_F) will be set so that v1 lies between the calculated double peak structure. It is surprising that the double peak structure could not be resolved in experiment in spite of the resolution of 0.2 eV for the valence band. Perhaps matrix element effects can explain this discrepancy. The three rather broad peaks seen in the experiment (*v2*, *v3*, and *v4*) are seen in our calculated DOS as a single broad peak. The overall agreement with the conduction band is also fairly good. Several features in the calculated DOS agree well with the positions of the measured peaks *c1*, *c2*, and *c3*, the lowest predicted conduction peak lying within the energy resolution of peak *c1*.[139]

More recently Greanya *et al.*[139, 146] have carried out high resolution angle-integrated PES experiments on Bi_2Te_3 and Bi_2Se_3. We will next compare our theoretical results with their experiment. The photoemission spectrum for Bi_2Te_3 by

Greanya *et al.*[139, 146] is shown in Figure 68, that for Bi_2Se_3 in Figure 69. The PES data was taken using a synchrotron radiation source which allows for the effects of matrix element and atomic cross-sections to be examined by measuring spectra at several different photon energies. As can be seen, six peaks (numbered *1-6* and shown by the arrows in Figure 68) were found in the valence band for Bi_2Te_3 and nine peaks for Bi_2Se_3 (numbered *1-9* and shown by the arrows in Figure 69), several of these peaks seen at certain photon energies but not at others. These measurements did not have an energy reference, so the bands were rigidly shifted so that the topmost peak agreed with the previous calculation, as had been done with the theoretical DOS.[139]

Figure 68. Photoemission spectra for Bi_2Te_3 by Greanya *et al.*[139]. Peaks *1-6* are indicated by arrows. For the purpose of comparison, the energy reference (zero of energy) was set such that the lowest binding energy peak in the spectra coincides with the position of the corresponding peak in the data of the previous UPS experiment by Ueda *et al.*[149]

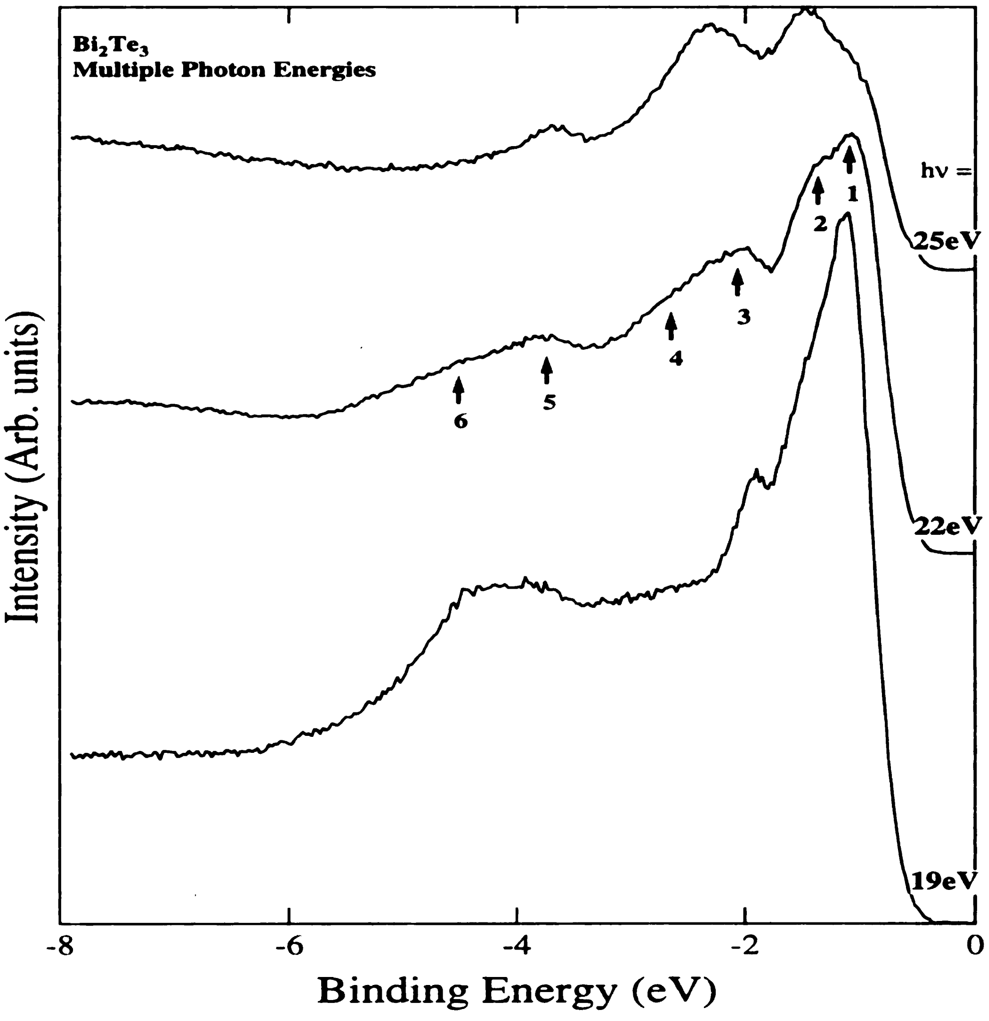

Figure 69. Photoemission spectra for Bi_2Se_3 by Greanya *et al.*[139]. Peaks *1-9* are indicated by arrows. For the purpose of comparison, the energy reference (zero of energy) was set such that the lowest binding energy peak in the spectra coincides with the position of the corresponding peak in the data of the previous UPS experiment by Ueda *et al.*[149]

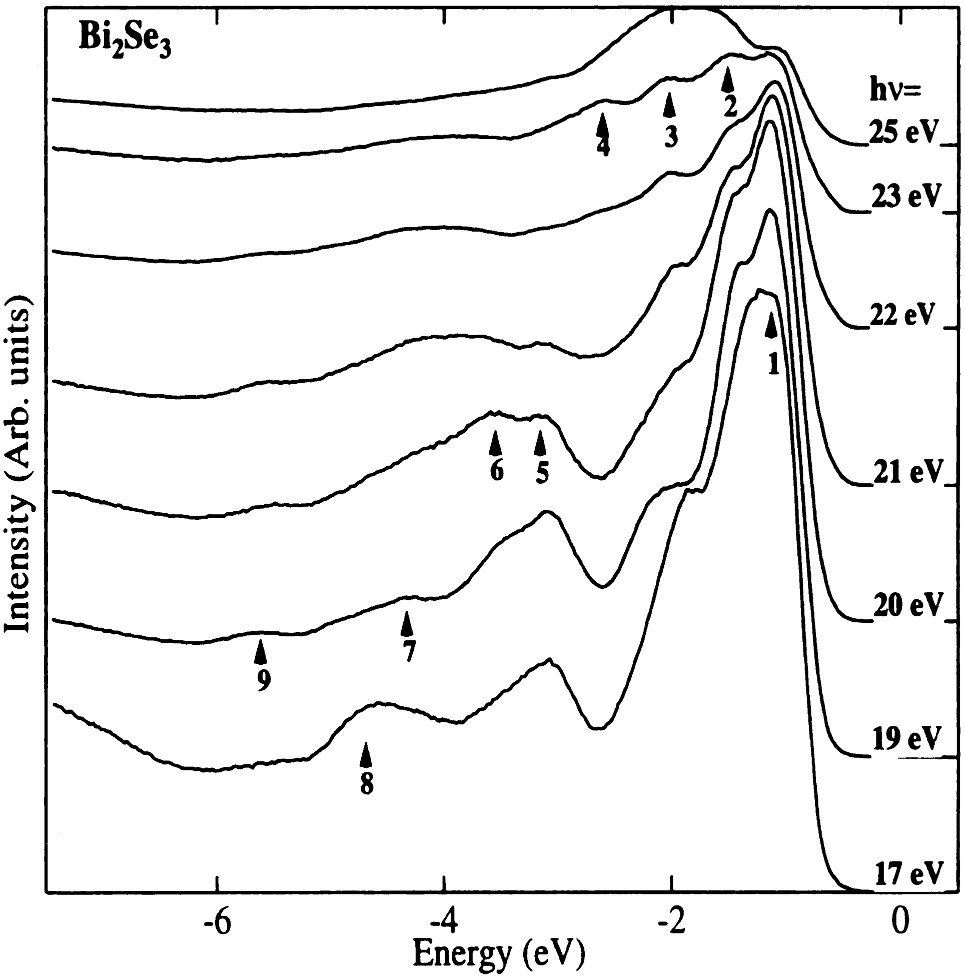

The positions of the peaks found in the PES study of Bi_2Te_3 and Bi_2Se_3 by Greanya *et al.*[139, 146] are shown in Figure 70 over our calculated DOS plots.

Figure 70. Total DOS of (a) Bi_2Te_3 and (b) Bi_2Se_3. The arrows indicate the positions of the photoemission peaks seen in Greanya *et al.*[139]. For the purpose of comparison, the energy reference (zero of energy) was set such that the highest valence band DOS peak coincides with the position of the corresponding peak in the data from the experiment of Ueda *et al.*[149]

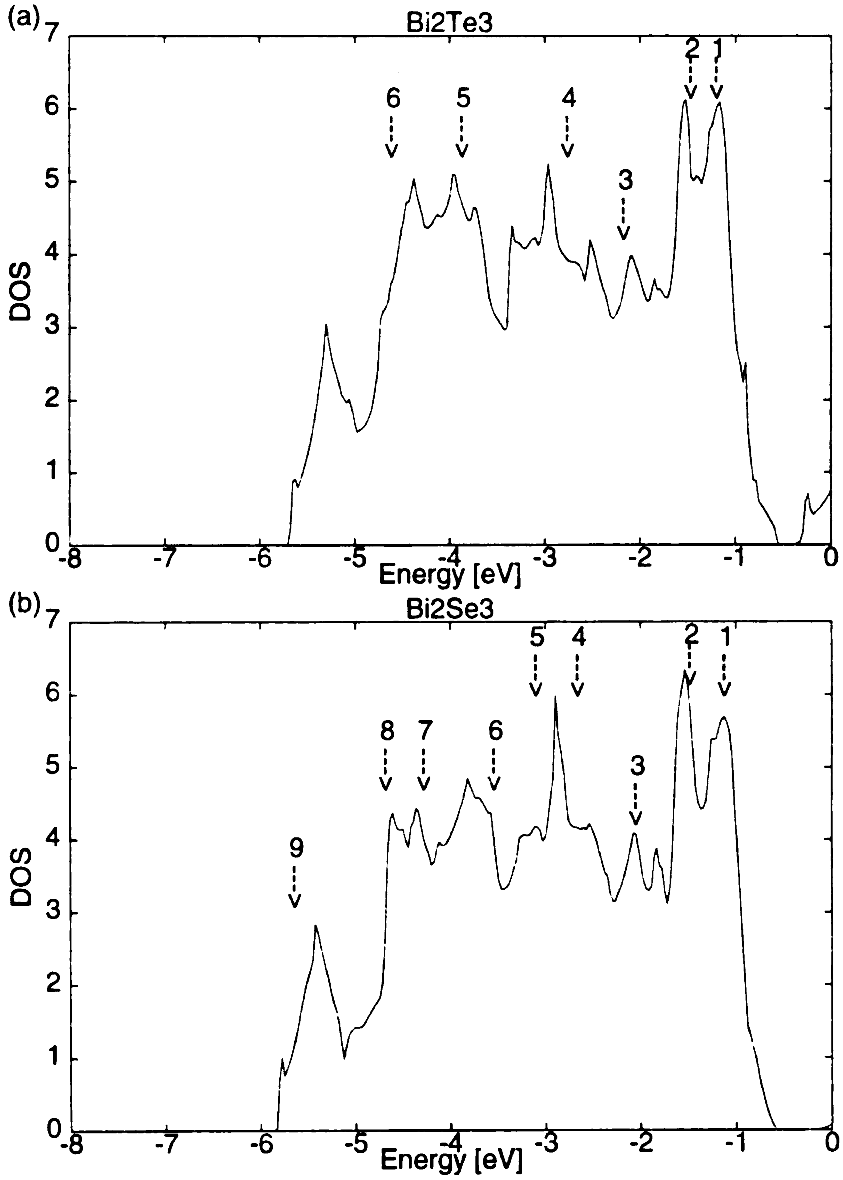

The double-peak structure at the VBM for Bi_2Te_3 has an energy separation of 0.27 eV, in much better agreement with the calculated value of 0.3 eV. The positions of the next three peaks in this experiment[139, 146] (peaks *3*, *4*, and *5*) agree very well with the calculated positions at -2.1, -2.6, and -3.9 eV, respectively. Experimental peak *6* is slightly below a DOS peak while the DOS peak at -5.3 eV is not seen in this experiment.[139, 146]

For Bi_2Se_3 this experiment[139] find nine peak positions compared with the experimentally determined eight, more than the five found by the previous experiment[149]. The double peak structure has a separation of 0.36 eV compared to the calculated value of 0.4 eV. The calculated peak at -2.9 eV corresponds well to peak *3*. The experimentally observed peaks *4* and *5*, seen at -2.64 and -3.08 eV, respectively, lie symmetrically on either side of the calculated peak at -2.9 eV. Peak *6* (-3.52 eV) lies about 0.3 eV above the calculated peak at -3.8 eV. Peaks *7*, *8*, and *9* clearly correspond to the calculated peaks at -4.4, -4.6, and -5.4 eV, respectively.[139] For both Bi_2Te_3 and Bi_2Se_3, improvements in the energy resolution[139, 149] lead to better agreement of the experimental PES and theoretical DOS peaks. Further increasing the energy resolution of the experiments and addition of matrix element effects into the calculation should further improve this agreement.

Finally, we summarize the peak positions found in the theoretical DOS and those in different PES measurements in Table XIII. The first columns of Table XIII give the peak positions for both the valence and conduction bands by Debies *et al.*[148], Ueda *et al.*[149], and Nascimento *et al.*[150], in the systems where they have been reported. In Bi_2Se_3 and Bi_2Te_3, the results of Greanya *et al.*[139] have been reported in the second to last column. The last column (with the heading "DOS") presents the positions of the peaks obtained from our electronic structure calculations. Clearly the agreement between theory and experiment improves when uses the experimental data with the best resolution.

Table XIII. Comparison of the photoemission and calculated DOS peaks for (a) Bi_2Te_3, (b) Bi_2Te_2Se, (c) Bi_2Se_3, and (d) Bi_2S_3. For a, b, and c the theoretical reference energies are chosen such that the highest valence band peak positions coincided with experiment.[149]
For d, the theoretical reference energies are chosen so that the top two theoretical bands lie equidistant from the highest experimental peak.[149]

a)

Bi_2Te_3

Valence Band	Valence Band	Valence Band	DOS
Debies[148]	Ueda[149]	Greanya[139]	
-1.2 eV	-1.1 eV	-1.10 eV	-1.1 eV
	-1.6 eV	-1.37 eV	-1.4 eV
		-2.07 eV	-2.0 eV
		-2.66 eV	-2.5 eV
-3.4 eV	-3.5 eV	-3.77 eV	-3.8 eV
		-4.51 eV	-4.2 eV
			-5.2 eV
	Conduction Band		
	Ueda[149]		DOS
	0.7 eV		0.5 eV
	1.7 eV		1.0 eV
	3.4 eV		2.9 eV

b)

Bi_2Te_2Se

Valence Band	DOS
Ueda[149]	
-1.1 eV	-1.1 eV
-1.6 eV	-1.5 eV
	-2.0 eV
	-2.9 eV
-3.5 eV	-3.9 eV
-4.2 eV	-4.6 eV
	-5.3 eV
Conduction Band	DOS
Ueda[149]	
0.7 eV	0.7 eV
	1.4 eV
	1.8 eV
2.5 eV	3.1 eV
3.7 eV	3.7 eV

c)

Bi_2Se_3

Valence Band	Valence Band	Valence Band	Valence Band	DOS
Nascimento[150]	Debies[148]	Ueda[149]	Greanya[139]	
		-1.1 eV	-1.10 eV	-1.1 eV
	-1.6 eV	-1.6 eV	-1.46 eV	-1.5 eV
-2.1 eV			-2.03 eV	-2.1 eV
			-2.64 eV	-2.9 eV
			-3.08 eV	
		-3.3 eV	-3.52 eV	-3.8 eV
-4.4 eV	-4.4 eV	-4.2 eV	-4.26 eV	-4.4 eV
			-4.66 eV	-4.6 eV
		-5.4 eV	-5.62 eV	-5.4 eV
Conduction Band		Conduction Band		DOS
Nascimento[150]		Ueda[149]		
		1.0 eV		0.9 eV
				1.4 eV
		2.5 eV		2.1 eV
3.5 eV		3.8 eV		3.1 eV

d)

Bi_2S_3

Valence Band	Valence Band	DOS
Debies[148]	Ueda[149]	
-2.2 eV	-2.2 eV	-1.9 eV
		-2.6 eV
	-3.4 eV	-3.5 eV
		-3.8 eV
		-4.1 eV
	-4.6 eV	-4.5 eV
		-5.0 eV
	-5.7 eV	-5.7 eV
		-6.7 eV
	Conduction Band	DOS
	Ueda[149]	
		0.4 eV
	0.9 eV	0.9 eV
		1.5 eV
	2.5 eV	2.7 eV
	4.0 eV	4.1 eV

CHAPTER 7.

COMPLEX CHALCOGENIDES

Technological needs have driven a search for new thermoelectric materials.[4] Since bulk materials are more easily amenable for fabrication in electronic circuitry and superconducting devices, classes of materials such as skutterudites[23], half-Heusler alloys[7, 11, 81], clathrates[151], and pentatellurides[152] are being studied both experimentally and theoretically for their potential thermoelectric properties. We have already looked at half-Heusler alloys, Zintl phases, and simple chalcogenides in previous chapters, but the best new thermoelectric materials are likely to be skutterudites, clathrates, or complex chalcogenides.[4] These systems appear to have large carrier effective masses, high carrier mobility, large degeneracy of the valence and conduction band extrema, and low lattice thermal conductivity, all of which are necessary to enhance the thermoelectric figure of merit, $ZT = S^2\sigma T/\kappa$.

Different approaches have also been attempted to look for new thermoelectric materials. Hicks and Dresselhaus[24] argued that systems displaying large anisotropy or reduced dimensionality (quantum confinement) in their charge transport can also exhibit a significant enhancement in ZT. Mahan and Sofo[25] predicted than in good thermoelectric materials the energy distribution of the carriers should be narrow and have a high carrier velocity in the direction of the applied field. Consequently, nanofabrication of one- and two-dimensional arrays of materials have been attempted, and high values of ZT have been reported in PbTe-PbSeTe quantum-dot superlattices by Harman *et al.*[27] and in p-type Bi_2Te_3/Sb_2Te_3 superlattice films by Venkatasubramanian[28]. The major source of improvement for the enhanced ZT in these superlattice systems appears to be in their reduced thermal conductivity (κ)

rather than an increase in the power factor (PF = $S^2\sigma$).

Since the best bulk materials for thermoelectric applications are simple chalcogenides, specifically PbTe and Bi_2Te_3 alloys[2, 3], complex chalcogenides provide a promising avenue for searching for new thermoelectric materials. Complex chalcogenides with large unit cells containing weakly bound atoms or molecules, called "rattlers", have been studied to reduce the phonon contribution to κ without affecting S and σ. The basic principle underlying the synthesis of new thermoelectric materials by Dr. Mercouri Kanatzidis' group in the Chemistry Department at Michigan State University is to synthesize complex bismuth chalcogenides to reduce κ while maintaining the high values of S and σ of Bi_2Te_3. This is done by combining portions of existing structures such as PbTe (FCC) and Bi_2Te_3 (rhombohedral) to form new, more complex structures with enhanced thermoelectric properties.[5] Three representatives of these systems, $BaBiTe_3$, $CsBi_4Te_6$, and $K_2Bi_8Se_{13}$ contain highly layered and anisotropic crystal structures with weakly bound Ba, Cs, and K atoms, respectively. These cations act as "rattlers" off which phonons are expected to scatter to reduce κ, but allowing for electron transport within the layers to maintain a large S and σ. Electronic structure calculations of these materials should lead to a better understanding of the transport and electronic contributions to the thermoelectric properties of these materials.

7.1. $BaBiTe_3$

7.1.1. GENERAL FEATURES OF THE BAND STRUCTURE OF $BaBiTe_3$

$BaBiTe_3$ belongs to a class of compounds which are derived from the Bi_2Te_3 crystal structure.[153] The Bi/Te building blocks from Bi_2Te_3 are arranged side by side in layers connected by Te atoms. The heavy Ba atoms lie between the layers.[153, 154, 155] The structure of $BaBiTe_3$ also contains Te_2^{2-} (Te-Te) units which serve to connect the Bi/Te blocks into layers. The unit cell of $BaBiTe_3$ is more complicated than that of Bi_2Te_3. Its crystal structure is orthorhombic rather than rhombohedral, the space group being $P2_12_12_1$ with 40 atoms in the unit cell [A = 4.47 Å, B = 16.53 Å, C = 17.89 Å][153, 154], but internal symmetries reduce the number of inequivalent atoms to ten: Ba1-2, Bi1-2, and Te1-6. The crystal structure of $BaBiTe_3$ and, for comparison with that of the parent compound, Bi_2Te_3 (projected onto the yz plane) are shown in Figure 71. The underlying local Bi_2Te_3-like structures (shown by the shaded area) connected by Te5-Te6 chains existing in $BaBiTe_3$ can easily be seen in Figure 71. The Te2 and Te4 atoms lie on the edges of the layers and are bonded to only one layer of Bi atoms while the Te1 and Te3 atoms are bonded to two layers of Bi atoms. The Te1 atom has, however, a low Bi coordination and is likely to behave more like Te2 and Te4. In Bi_2Te_3, the Te1 atom is bonded to one layer of Bi atoms and lies near the Van der Waals gap, whereas the Te2 atom is bonded to two layers of Bi atoms. As a consequence, the Te2 p bands in Bi_2Te_3 have a lower energy and appear away from E_F.[11] Therefore, one would expect that in $BaBiTe_3$, Te1, Te2, and Te4 p bands would act more like the Te1 p bands in Bi_2Te_3, contributing to the top of the valence band DOS near E_F, whereas Te3 p bands would act more as Te2 p bands in Bi_2Te_3, stabilized several eV below E_F with little contribution to the DOS near E_F. Also, Bi p states will contribute primarily to the conduction band. Since Te5 and Te6 have no counterparts in Bi_2Te_3, the bands associated with these atoms will be new features in $BaBiTe_3$.[11]

Figure 71. Projection of the crystal structures in the yz plane of (a) orthorhombic $BaBiTe_3$ and (b) rhombohedral Bi_2Te_3. The Bi/Te blocks are highlighted in the shaded area for $BaBiTe_3$.

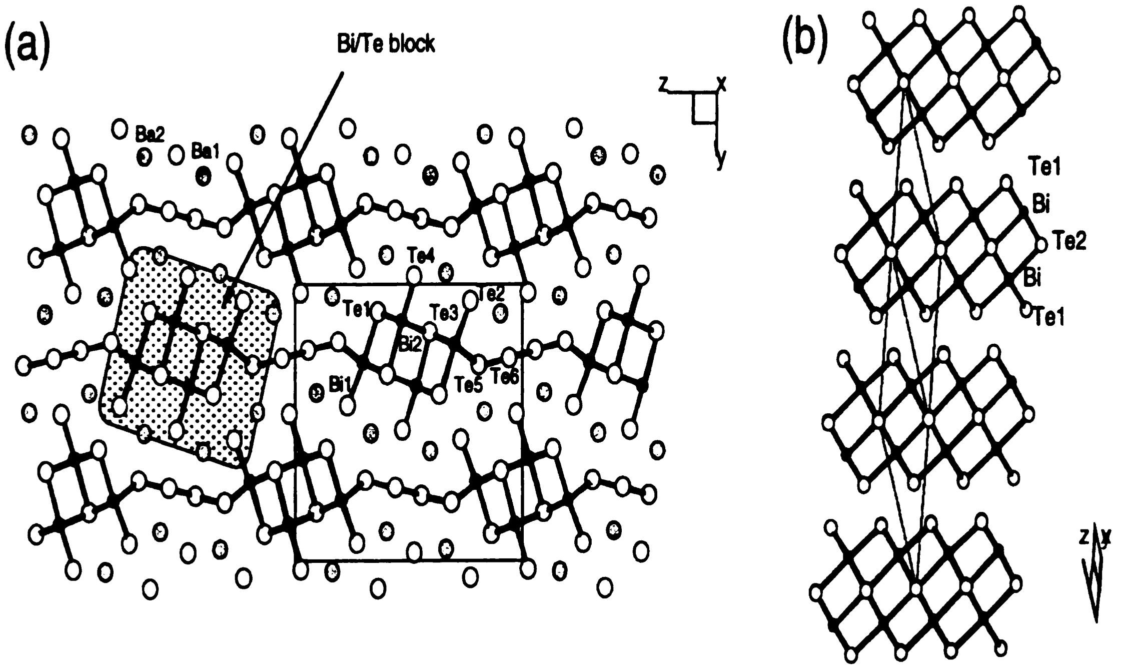
(a)
Bi/Te block
Ba2
Ba1
Te4
Te1
Te3
Te2
Bi2
Bi1
Te5
Te6
z
x
y
(b)
Te1
Bi
Te2
Bi
Te1
z
x

Figure 72. Brillouin zone of $BaBiTe_3$.

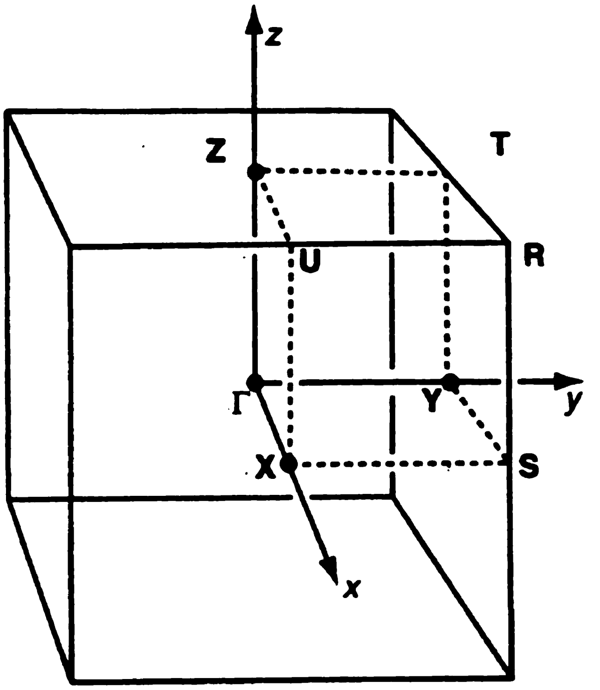
z
Z
T
U
R
Γ
Y
y
X
S
x

Electronic structure calculations were performed both with and without spin orbit interaction (SOI). The band structure of $BaBiTe_3$ is much more complicated than that of Bi_2Te_3 due to the larger number of atoms in the unit cell. We will focus, therefore, on the region close to E_F. The bands are plotted along the high symmetry directions of the orthorhombic Brillouin zone, shown in Figure 72.

Before discussing the theoretical band structure in detail, we wish to discuss the room temperature diffuse reflectance spectroscopy (Figure 73) for Bi_2Te_3 and $BaBiTe_3$. These experiments in $BaBiTe_3$ reveal absorptions at 0.42 eV (which is the intercept found by extending the linear portion to the axis) and at 0.28 eV (where the spectrum extends to zero after the linear portion). This absorption spectrum in $BaBiTe_3$ is unusual in the sense that it has two values. This was not seen in Bi_2Te_3 (Figure 73) which has one at the band gap value of 0.13 eV.

Figure 73. Infrared absorption spectra of Bi_2Te_3 and $BaBiTe_3$. The semiconductor energy gaps are indicated in the spectra.

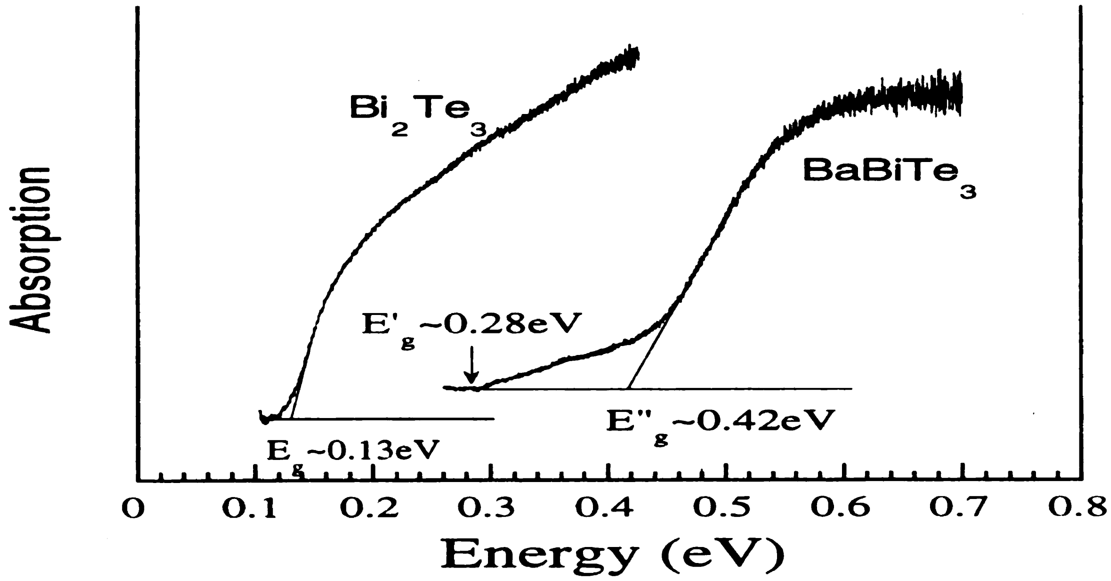

Due to the atomic arrangement inside the unit cell and the presence of the Ba^{2+} ions, the orbital characters of the HVB and LCB in $BaBiTe_3$ are distinctly different from those seen in Bi_2Te_3. As a result, the effect of SOI is not as dramatic. The energy bands without SOI centered in the range of ~2 eV about E_F are given in Figure 74. The VBM occurs at a point between Γ and Z (this HVB in the ΓZ direction is extremely flat) while the CBM lies at the Z point. The band gap at Z is calculated to be 0.45 eV, in good agreement (but see below for a discussion when SOI is included) with the larger of the two band gaps found experimentally, 0.42 eV. This, however, cannot explain a second smaller gap of 0.28 eV also seen experimentally.[153] Our results agree rather well with a previous unpublished LMTO calculation which also did not include SOI.[156]

Introducing SOI has some broad general effects, such as lifting the degeneracy of several bands and moving the CBM and VBM closer together (Figure 75). However, it has little effect on the position of the VBM, while the CBM moves to a point between Γ and Z to produce a nearly direct gap. A careful analysis of our results shows the VBM is at (0, 0, 0.325) and the CBM is at (0, 0, 0.3625), in units of the primitive reciprocal lattice vectors. The new band gap is about 0.26 eV, in good agreement with the smaller experimental value of 0.28 eV.[153] There exist several other indirect band gaps in the spectrum, such as the 0.34 eV gap between the VBM at Γ and the CBM between Γ and Δ. As pointed out before, the direct band gap at the Γ point is 0.47 eV, which is comparable to and may be identified with the larger of the experimentally observed band gaps of 0.42 eV.[153] The unusual shape of the experimental absorption spectrum near the threshold of the smaller band gap (0.28 eV) may result from the forbidden *p*-*p* transitions when $\Delta k = 0$. More accurate measurements and a detailed calculation of the optical absorption spectrum will clarify this issue.

Figure 74. Band structure of BaBiTe$_3$ without SOI.

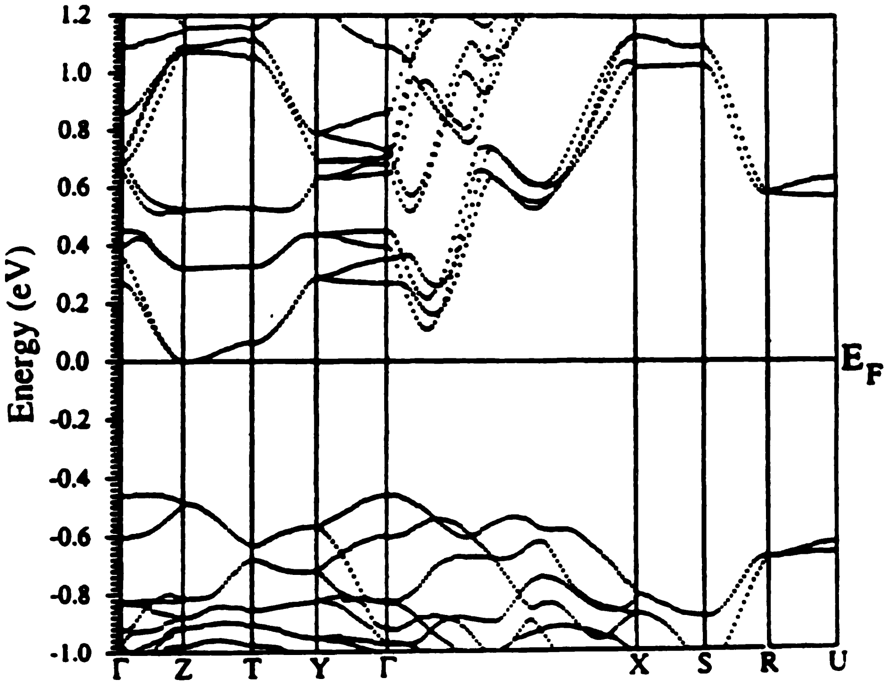

Figure 75. Band structure of BaBiTe$_3$ with SOI.

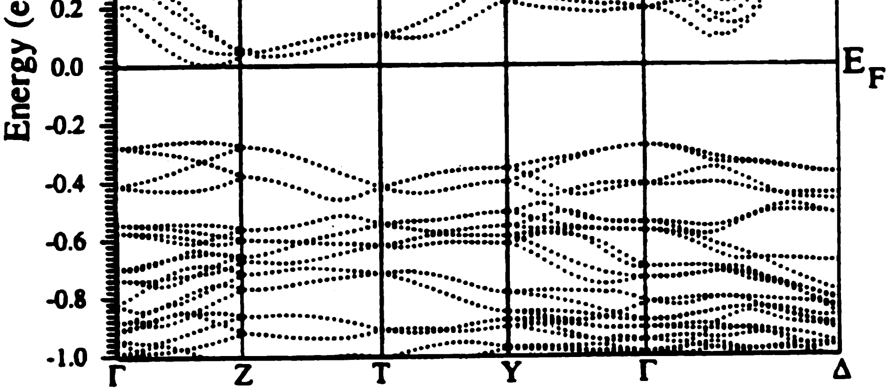

The orbital characters of the bands in the neighborhood of E_F have been carefully analyzed, but will not be shown to save space. It is observed that the main contribution in the LCB near the CBM is associated with the Bi1 p, Te5 p, and Te6 p states while the Te1 p, Te2 p, and Te4 p states contribute most strongly to the VBM. This is in agreement with the analogy made between the bonding found in Bi_2Te_3 and $BaBiTe_3$ with respect to the position of the atoms within the layers[11]. The bands contributing to the DOS near E_F consist of Te and Bi p bands, the Ba $5p$ bands lying about 13 eV below and the Ba $5d$ and $6s$ bands lying several eV above E_F. Therefore, Ba $5p$, $5d$, and $6s$ orbitals contribute very little to the states near E_F, the Ba^{2+} ion acting mainly as a spacer. The interesting case is that of the Te5 and Te6 atoms which connect the Bi/Te blocks together through the Te-Te chains along the z axis and have no analogy in Bi_2Te_3. As mentioned before, the Te 5 p and Te6 p states contribute to the LCB along with the Bi1 p and Bi2 p orbitals, primarily the former. The crystal structure of $BaBiTe_3$ can be considered as $[Bi_4Te_{10}]^{8-}$ segments separated by Ba^{2+} ions and connected by Te5-Te6 chains. The previous extended Huckel calculation assigned a 3+ oxidation state to Bi with an electronic configuration of $6s^26p^0$, the two remaining $6s$ electrons acting as a "lone pair". A strong hybridization between the "lone pair" states was found with the atoms in the Te5-Te6 chains for the lowest conduction band. Our band structure calculation finds these Te5-Te6 orbitals playing an important role in the LCB, in agreement with the "lone pair" ($2\sigma^*$) description.[154]

The nature of the charge transport in this anisotropic material depends on the dispersion of the bands along different directions. In the conduction band, the dispersion along the ΓY direction, perpendicular to the Ba^{2+} layers, is very small while that along the ΓZ direction, i.e., through the Te5-Te6 necks is appreciable. One also sees that there is a large dispersion along the $\Gamma\Delta$ direction which should be similar to that seen in the xy plane of Bi_2Te_3.[11] Thus, n-doped $BaBiTe_3$ can be treated as quasi-two-dimensional system with respect to charge transport. The valence band has what appears to be similar dispersions in several directions, so requires more careful analysis.

Since the inclusion of SOI does not cause as drastic a change in the band structure as in Bi_2Te_3[11] (Chapter 4), the position and degeneracy of the calculated CBM should be more reliable than in Bi_2Te_3. However, several off-axis minima, whose energies lie above the CBM by about 0.1 eV, will also contribute to the charge transport and effectively increase the band degeneracy, thereby leading to a higher ZT value.

7.1.2. EFFECTIVE MASSES AND THERMOELECTRIC PROPERTIES OF $BaBiTe_3$

As has been discussed in previous chapters, the thermoelectric properties of a material can be understood by studying the B parameter (Equation 24 in Chapter 2). Increasing B, by way of a large band degeneracy, increases the figure of merit, ZT. Unlike Bi_2Te_3, the lower symmetry of the more complicated unit cell of $BaBiTe_3$ implies that the degeneracy factor of the band extrema, γ, is reduced. Also, in $BaBiTe_3$ the Bi/Te blocks are connected through Te5-Te6 atom chains. Orbital analysis of the band structure shows that they contribute significantly to the CBM along with the Bi atoms. Therefore, while electrons can flow through the layers, the Te5-Te6 chains will block the holes from traveling through the Te1, Te2, and Te4 layers. It is therefore necessary to study the effective masses of the band extrema to understand how anisotropic the charge transport will be for both the holes and the electrons.[17, 18]

Since the mobility, μ, is inversely proportional to the effective mass in the direction of transport, in order to increase B (and therefore ZT), one would like to find systems with small effective masses in the direction of charge transport to increase μ and large effective masses perpendicular to the direction of transport (Equation 24 in Chapter 2). The off-diagonal terms of the mass tensor (Equation 74 in Chapter 6) must vanish due to the orthorhombic symmetry, so diagonal elements of the mass tensor, α_{ii}, give the inverse of the effective mass parameters m_{ii} (i = 1, 2, 3). These effective masses for $BaBiTe_3$ were obtained by calculating values of the energy close to different LCB minima and HVB maxima while moving along suitably chosen directions in the BZ. The α_{ii} values are given in Table XIV.

All the band extrema in $BaBiTe_3$ lie along the ΓZ direction and hence are two-fold degenerate. Large values of α_{ii} correspond to small effective masses which give a large mobility in that direction. A large mobility is found for the electrons in the XZ plane, corresponding to charge transport through the Bi/Te layers. This is similar to what is seen in Bi_2Te_3 and is consistent with the description of the Te5-Te6 chains connecting the Bi/Te blocks and contributing to the LCB. The hole transport, on the other hand, a large mobility is found in the XY plane, perpendicular to the Bi/Te layers. For the holes are unable to move through the Te5-Te6 chains, leading to their charge transport perpendicular to the Bi/Te layers. However, the values of α_{ii} in the X and Y directions are a factor of 2-3 smaller than those in the conduction band, implying that the mobility of the electrons is better than that of the holes.

Table XIV. Theoretical values of inverse effective mass parameters associated with the conduction and valence band extrema of $BaBiTe_3$.

Conduction band	ΓZ
$\alpha_{xx} = [m/m_e]^{-1}_{xx}$	11.61
$\alpha_{yy} = [m/m_e]^{-1}_{yy}$	2.79
$\alpha_{zz} = [m/m_e]^{-1}_{zz}$	13.16
Valence band	ΓZ
$\alpha_{xx} = [m/m_e]^{-1}_{xx}$	7.61
$\alpha_{yy} = [m/m_e]^{-1}_{yy}$	5.40
$\alpha_{zz} = [m/m_e]^{-1}_{zz}$	2.89

In comparison with the effective masses of Bi_2Te_3 (Table XII), the first important point is that these inverse effective mass parameters for $BaBiTe_3$ are much more symmetric. For the CBM, α_{xx} for Bi_2Te_3 is calculated to be $112.75m_e^{-1}$ compared to α_{yy} of $2.87m_e^{-1}$, a ratio of almost 40. The ratio in $BaBiTe_3$ is only about 4. Similarly for the VBM, α_{xx} for Bi_2Te_3 is calculated to be $107.51m_e^{-1}$ compared to α_{yy} of $3.97m_e^{-1}$, a ratio of about 25. The ratio in $BaBiTe_3$ is only about 1.5. Also, in Bi_2Te_3 $\alpha_{yy} < \alpha_{zz}$, the dispersion through the Bi/Te network stronger than through the Van der Waals gap for each extrema. However in $BaBiTe_3$, $\alpha_{yy} > \alpha_{zz}$ for the valence band, the hole transport blocked by the Te5-Te6 chains through the Bi/Te network.[11]

The larger band gap, the more isotropic effective masses, and the reduction in the mobility of the hole transport through the Bi/Te network due to the Te5-Te6 chains explains why $BaBiTe_3$ is not as promising a thermoelectric material as Bi_2Te_3, even though the complex unit cell reduces κ. These calculations suggest that attempts to optimize $BaBiTe_3$ should aim at preparing solid solutions of the type $BaBi_{1-x}Sb_xTe_3$, so that the Te sites are not disrupted. Given that the Te states are dominant near the VBM, Sb substitution at the Bi sites should have minimal effect on the hole mobilities. Any substitution, however, at the Te sites (e.g., Se) is expected to greatly degrade the hole mobilities. On the other hand, attempts to optimize $BaBiTe_3$ as an n-type material are expected to be more challenging because the CBM has substantial contribution from Bi and Te (Te5-Te6) states. Therefore, any substitution of either Bi or Te will likely have serious negative effects on electron mobilities.

7.2. $CsBi_4Te_6$

7.2.1. CRYSTAL STRUCTURE AND OBSERVED PROPERTIES

$CsBi_4Te_6$, like $BaBiTe_3$, belongs to a class of compounds which are derived from the Bi_2Te_3 crystal structure.[153] The unit cell of $CsBi_4Te_6$ is monoclinic with space group *C2/m* containing 88 atoms/unit cell [A = 97.425 a.u., B = 8.264 a.u., C = 27.424 a.u., β = 101.438°]. This unit cell is shown in Figure 76 where the different atoms in the cell have been numbered. It has a layered anisotropic structure with anionic [Bi_4Te_6] laths connected through Bi-Bi bridges to form two-dimensional slabs, and these Bi/Te slabs are separated by layers of Cs^+ ions. Bi-Bi bonds have not been found in chalcogenide compounds before. The axis of the laths (normal to the paper) is the direction of the highest charge mobility and is usually referred to as the needle axis.[26, 155] There is a gross structural resemblance of this compound with Bi_2Te_3 and $BaBiTe_3$ where the Bi/Te slabs are separated by a Van der Waals gap and a Ba^{++} ion layer respectively.[11]

Figure 76. Monoclinic crystal structure of $CsBi_4Te_6$.

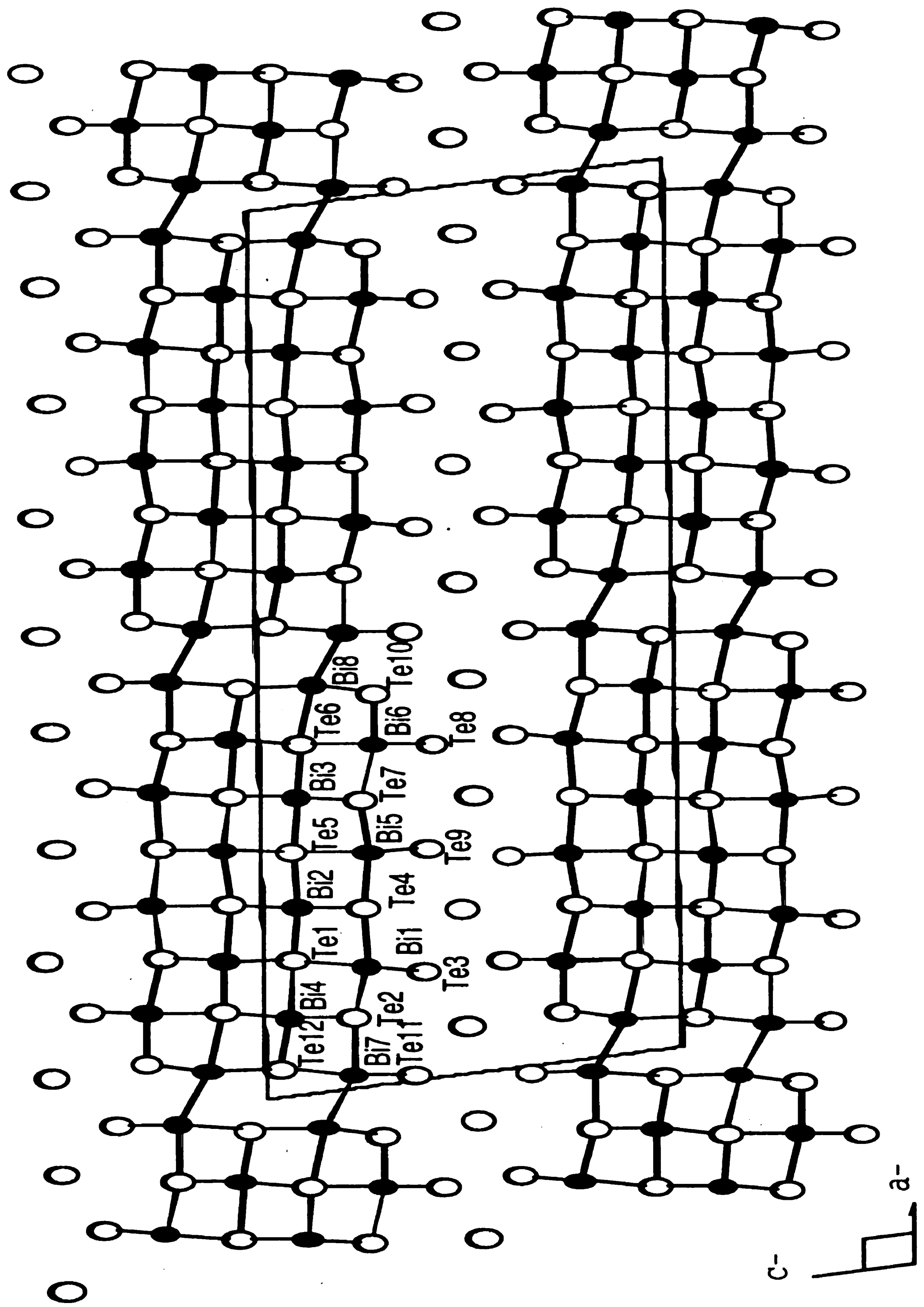
Bi8
Te10
Te6
Bi6
Te8
Bi3
Te7
Te5
Bi5
Te9
Bi2
Te4
Te1
Bi1
Te3
Bi4
Te2
Te12
Bi7
Te11
c-
a-

In order to reduce computer memory used in the electronic structure calculations, we have used an equivalent triclinic unit cell (Space group: *P-1*) with 44 atoms/unit cell was used in our electronic structure calculation [A = 49.233 a.u., B = 49.233 a.u., C = 27.424 a.u., $\alpha = 101.438°$, $\beta = 101.438°$, $\gamma = 9.693°$]. This crystal structure and its corresponding Brillouin zone are given in Figure 77.

Figure 77. (a) Triclinic crystal structure and (b) Brillouin zone of $CsBi_4Te_6$ used in this calculation.

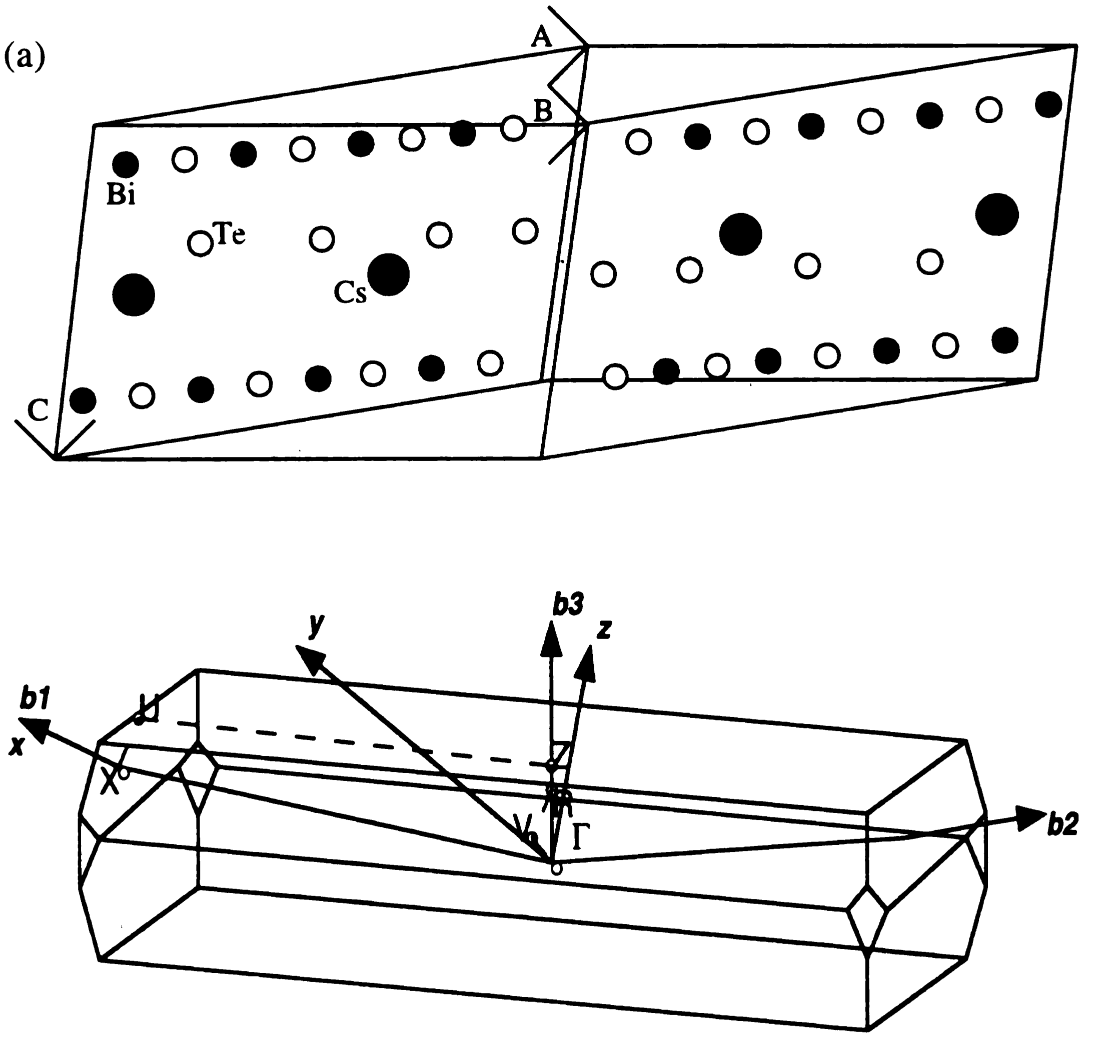

$CsBi_4Te_6$, as seen in Figure 78, has a larger figure of merit (ZT~0.8 at 225 Kelvin) than conventional optimized $Bi_{2-x}Sb_xTe_3$ alloys at these temperatures.[26] Doping studies of this material shows that the hole-doped samples show a much larger ZT than the electron-doped samples.[158] The thermal conductivities of these two materials are comparable, which suggests that the improved ZT for $CsBi_4Te_6$ is electronic in origin. Therefore, a careful analysis of the electronic structure of this material is necessary to understand the origin of the high ZT for this system.

Figure 78. Comparison of ZT for the best current doping of $CsBi_4Te_6$ and optimally-doped $Bi_{2-x}Sb_xTe_3$ alloy. The peak for $CsBi_4Te_6$ (ZT~0.8) occurs at 225 Kelvin.

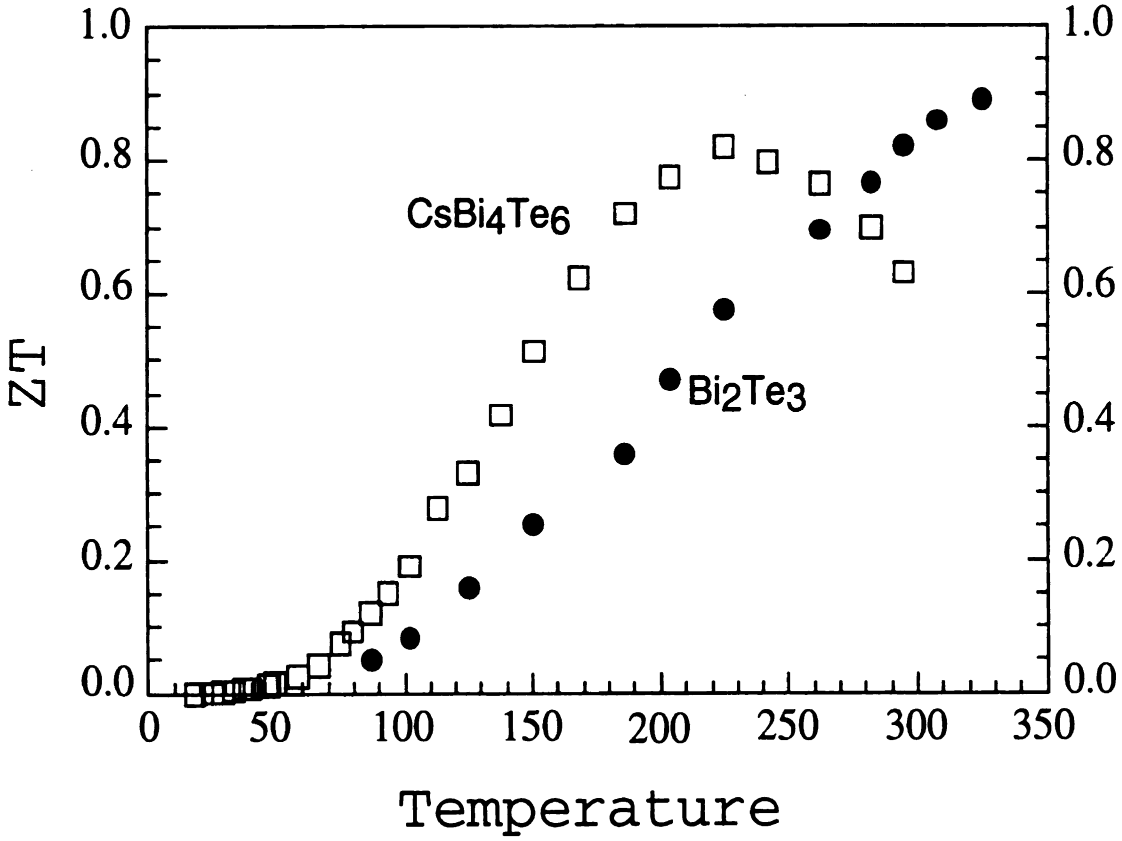

7.2.2. GENERAL FEATURES OF THE BAND STRUCTURE AND GAP FORMATION OF $CsBi_4Te_6$

Electronic structure calculations show that $CsBi_4Te_6$ is a narrow-gap semiconductor with a band gap of approximately 0.04 eV (Figure 79), smaller than the measured value of 0.05-0.11 eV[26] (usually seen in DFT calculations[31]). In the absence of SOI (Figure 79a), the band gap is 0.37 eV. The introduction of SOI (Figure 79b) produces an almost rigid shift of the conduction band toward the valence band. Similar shifts are also seen in $BaBiTe_3$ and Bi_2Te_3[11], but in Bi_2Te_3 the shift is so large that new hybridization gaps form, thereby giving completely different positions for the valence and conduction band extrema. In $CsBi_4Te_6$, the top of the valence band occurs at the Γ point while the bottom of the conduction band occurs at a general point in the Brillouin zone (denoted as C^*) ($C^* = (0.88125, 0.88125, 0.175)$ in terms of the reciprocal lattice vectors.) In addition, there are several local conduction band minima appearing slightly above this point ($\sim$0.1 eV above), along ΓZ and RV directions in the Brillouin zone, which may contribute to the charge transport. By looking at the equation for the B parameter (Equation 24 of Chapter 2), where increasing B increases the figure of merit, ZT, a large band degeneracy, γ, can give large values of ZT.[11]

Figure 79. Band structure of $CsBi_4Te_6$ (a) without and (b) with SOI.

(a) CsBi4Te6 - No SOI

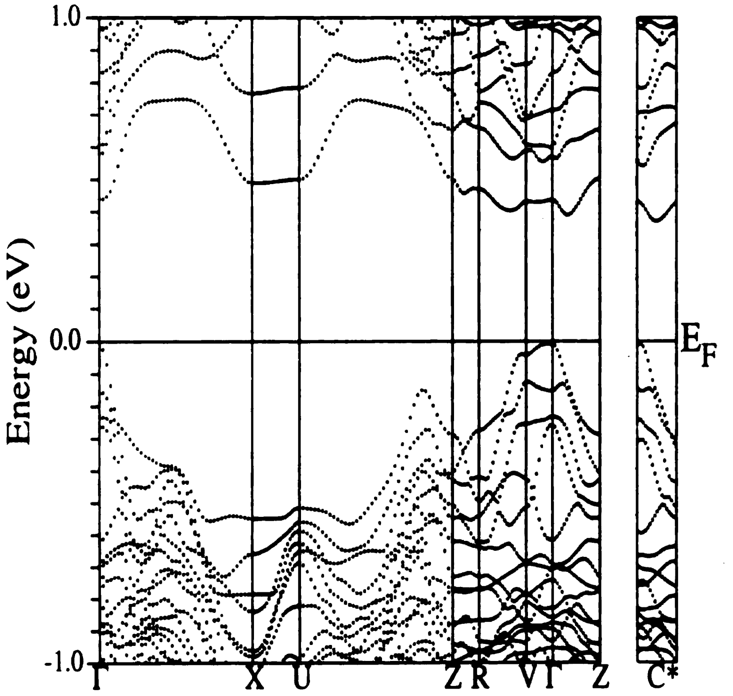

(b) CsBi4Te6 - SOI

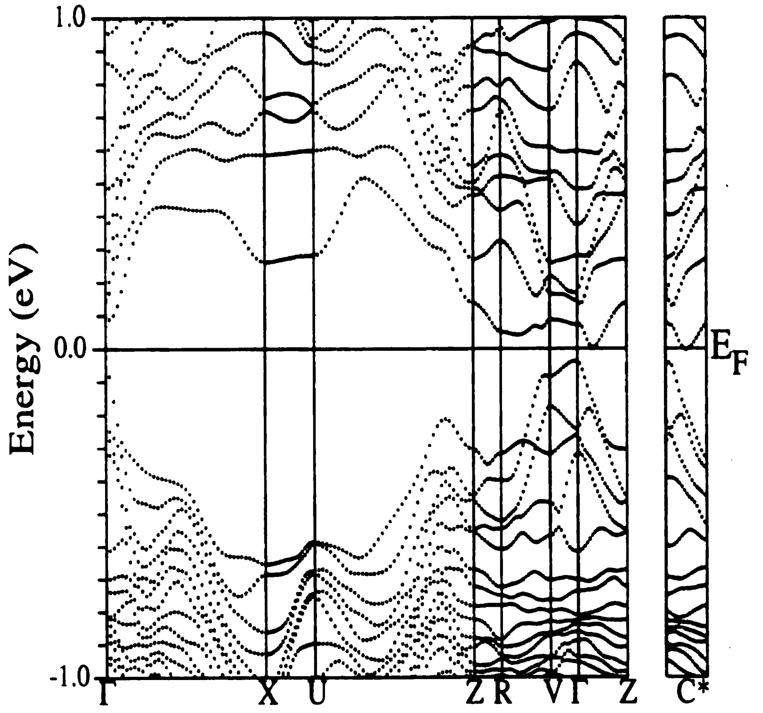

7.2.3. EFFECTIVE MASSES AND THERMOELECTRIC PROPERTIES OF $CsBi_4Te_6$

The 0.04-0.11 eV band gap in $CsBi_4Te_6$ follows the $10k_BT$ criterion for a good thermoelectric[1, 2, 3, 4] because S is expected to peak at 225 K, though it had been believed that only semimetals were good thermoelectrics below room temperature.[19] While multiple conduction band extrema may be a reason for anticipating a large ZT value in the electron-doped $CsBi_4Te_6$ (large thermopower values in n-doped systems have not yet been seen[158]), the single maximum of the valence band at the Γ point requires another explanation for the large observed values of ZT in the hole-doped compound. In order to explore whether anisotropy in the charge transport (confinement idea of Hicks & Dresselhaus[24]) may play a role, we have computed the effective carrier masses along different directions and have analyzed the detailed nature of the electronic states (orbital character and parentage, i.e, Bi *p* or Te *p*, etc.) associated with the valence band maxima (holes) and conduction band minima (electrons).

Considering the effective mass dependence of the B parameter (Equation 24 of Chapter 2), we see that since the mobility, μ_x is inversely proportional to the effective mass in the direction of transport, B depends on the effective mass parameters as $\sqrt{\frac{m_y m_z}{m_x}} = R\sqrt{m_x}$. For an isotropic system, R = 1. For an anisotropic system we can assume the smallest effective mass along the x direction, the direction of charge transport, while one or both of the effective masses associated with the other directions are larger. Considering two cases (i) $m_x = m_y = m_z/\omega$, (ii) $m_x = m_y/\omega = m_z/\omega$. $\omega > 1$, we find that the ratio R is larger than the isotropic case by a factor $\sqrt{\omega}$ for (i) and by a factor ω for (ii). (When the three masses are different one has to generalize this slightly.) Thus the effective mass anisotropy can significantly affect ZT.

In $CsBi_4Te_6$ the effective masses along three specific directions, i.e., the needle growth direction (ΓX), the direction of the Bi/Te slabs (ΓV), and through the Cs^+ atom layer (ΓZ) were computed. Since the system is triclinic, the full reciprocal mass tensor must be computed and diagonalized (Equation 74).[22] In most cases, the off-diagonal terms of the mass tensor are small, so diagonal elements of the mass tensor, α_{ii}, accurately give the inverse of the effective mass parameters m_{ii} (i = 1, 2, 3). In the general case, however, the mass tensor has to be diagonalized to obtain the effective masses associated with the principal directions. We fit the calculated E(**k**) vs **k** along different orthogonal directions to parabolas and obtained the coefficients α_{ij}.

The effective masses for $CsBi_4Te_6$ were obtained by calculating values of the energy close to different LCB minima and HVB maxima while moving along suitably chosen directions in the BZ using the equation

$$2m_e/\hbar^2\ \varepsilon_k = \alpha_{xx}k_x^2 + \alpha_{yy}\ k_y^2 + \alpha_{zz}k_z^2 + 2\alpha_{xy}k_xk_y + 2\alpha_{yz}k_yk_z + 2\alpha_{xz}k_xk_z \tag{75a}$$

where a constant term has been omitted. The three orthogonal directions lying closest to the three directions mentioned above will be denoted as X, Y, and Z, respectively. The effective masses obtained from the eigenvalues of the inverse mass tensor are given in Table XV. Due to the observed large number of hybridized bands near E_F, the band extrema rapidly become nonparabolic, so that the effective mass approximation is not expected to hold at large carrier concentrations. However, up to carrier concentrations consistent with the optimum doping of this system (~3 x $10^{18}/cm^3$[26, 158]), the agreement between the calculated dispersions and parabolic fit was found to be excellent.

Table XV. Effective masses of $CsBi_4Te_6$ associated with the valence and conduction band extrema along three principal axes and the angles these axes make with a set of three suitably chosen orthogonal axes (see text).

Valence Band (Γ)	Angle	m_{ii}/m_e
X (needle)	12.37°	0.02
Y (Bi-Bi bonds)	0.97°	0.16
Z (Cs layer)	12.35°	0.09
Conduction Band (C^*)		
X (needle)	12.38°	0.04
Y (Bi-Bi bonds)	3.17°	0.47
Z (Cs layer)	11.98°	0.16

The corresponding eigenvectors define different directions in **k**-space. For both the electrons and the holes, the lightest effective mass direction makes an angle of about 12° with the needle axis while that with the intermediate mass direction also makes an angle of 12° with the axis perpendicular to the Cs^+ atom layers. The direction of the heaviest carriers lie within 1-3° of the Y axis, i.e., parallel to the Bi-Bi bonds. The heaviest valence band mass is a factor of 50 larger than the lightest valence band mass while the heaviest conduction band mass is only a factor of 10 larger than the lightest conduction band mass. Thus the valence band holes are more spatially restricted than the electrons, particularly along the direction of the Bi-Bi bonds. These results suggest that the effective hole transport takes place not along the Bi/Te slabs but in planes nearly perpendicular to the slabs containing the needle axis. A similar situation was found in $BaBiTe_3$, but the degree of anisotropy was much smaller.[11] Also the effective masses in $BaBiTe_3$ were a factor of 5-6 higher leading to a lower overall mobility (lower conductivity). The charge transport in Bi_2Te_3 is generally along the layers with much less dispersion through the Van der Waals gap while a much stronger charge transport is seen in hole doped $CsBi_4Te_6$, perpendicular to the Cs^+ atom layer and in the needle growth direction, but not along the Bi/Te network. The effective masses in the transport directions are, however, comparable to those of $CsBi_4Te_6$.[11]

To understand the nature of the electron and hole states near the respective band extrema further we have analyzed the wave functions in some detail. When the strengths of the orbital character associated with these states are analyzed for different atoms, it is seen that the valence band charge density forms a quasi-two dimensional layer lying almost perpendicular to the $[Bi_4Te_6]$ slabs while the conduction band charge density is more three-dimensional, consistent with our effective mass calculations. We find that the states corresponding to the CBM are mostly of Bi character, especially Bi7 and Bi8, the atoms forming the Bi-Bi bond which connects the Bi/Te laths together, a bonding not before seen in chalcogenides. These arise from the anti-bonding state of the Bi-Bi pair, the bonding state lying below the valence band maxima. This may be understood in terms of the stabilization of the donor electron from Cs by this Bi-Bi bond which is necessary for the formation of a semiconductor.[26] (The Cs atoms act primarily as electron donors with little contribution near the top of the valence band or the bottom of the conduction band).

We find the states corresponding to the valence band maxima consist of Bi (Bi1, Bi6) and Te (Te1, Te3, Te6, Te8) (Figure 76) atoms, the charge density associated with these atoms forms corrugated, two-dimensional sheets separated by approximately 13

Å (Figure 80). There are very few atoms lying between the sheets with contributions to these states (which would have allowed for transport in the direction of the Bi-Bi bonds), consistent with the large effective mass found in this direction. The Bi-Bi bonds, connecting the Bi/Te network together, have their anti-bonding states in the conduction band and their bonding states deep in the valence band with only a small contribution to the states near the valence band maxima. This implies that hole transport through the Bi-Bi bonds will be blocked in this direction, explaining the large effective masses and two-dimensional sheet-like transport.[15]

Greanya *et al.*[159] recently performed an ARPES study of $CsBi_4Te_6$ to find the CBM at the Γ point, in agreement with our calculation. While they found both dispersions along ΓV and ΓZ to be much flatter than that in the ΓX direction, they were only able to obtain a few experimental points in the two nondispersive directions due to the needle-like morphology. They were also able to estimate a band gap of 0.05 eV, consistent with our calculation[15] and the previous experiments[26]. These results give further confidence in our analysis of the electronic structure of this complex novel material.

Figure 80. Quasi-two dimensional sheets contributing to hole transport overlying the crystal structure of $CsBi_4Te_6$.

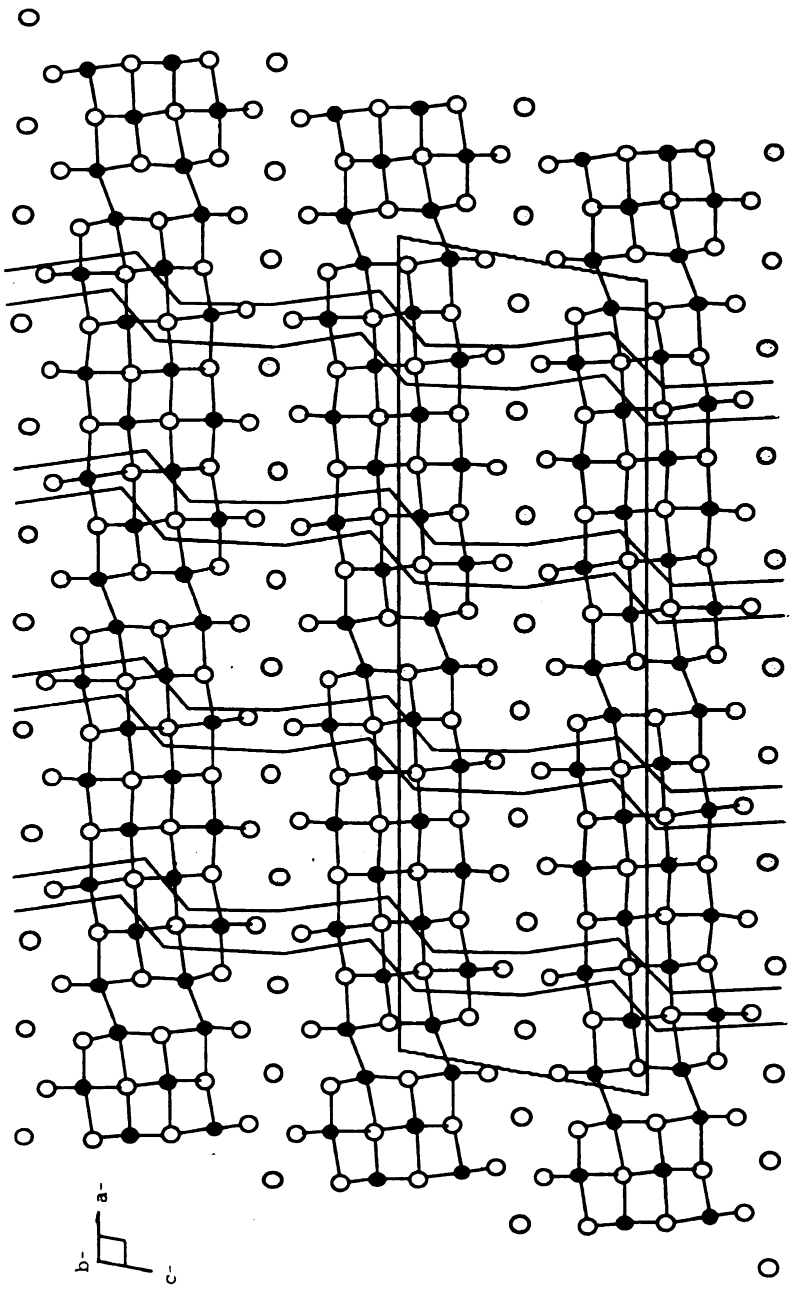

To summarize our results for $CsBi_4Te_6$, systems with different structures have been synthesized to exploit low dimensional transport which result in enhanced ZT.[27, 28, 160] The vast majority of these attempts, however, revolve around nanofabrication of quantum wells or multilayer films. $CsBi_4Te_6$, on the other hand, quite naturally displays quasi-two dimensional hole transport with regions of the crystal of several Å width participating very little in the charge transport. These "insulating" regions are sandwiched between conducting regions, leading to structures similar to quantum wells or multilayers, but in a bulk material. The source of this anisotropic hole transport arises from the Bi-Bi bonds, which are not seen in other bismuth chalcogenides. It is possible to take advantage of this novel quantum architecture in other Cs-Bi-Te compounds where the Bi-Bi bonds are closer together or further apart. While the conduction band has several degenerate minima, the transport in this band is much more isotropic. However, large values of ZT are still possible for the electron-doped systems when several of these local minima get occupied. $BaBiTe_3$, which has a strong structural similarity to $CsBi_4Te_6$, does not show as large an anisotropy as the latter compound. Furthermore the effective mass along the optimum direction (needle axis) is a factor of 10 larger in $BaBiTe_3$ than in $CsBi_4Te_6$. This may explain the low ZT values observed in $BaBiTe_3$.[11]

7.3. $K_2Bi_8Se_{13}$

The third member of the complex Bi-Te-Se systems which has great potential for high thermoelectric performance is β-$K_2Bi_8Se_{13}$[16]. $K_2Bi_8Se_{13}$ forms in two distinct crystal structures, α-$K_2Bi_8Se_{13}$ and β-$K_2Bi_8Se_{13}$, both of which are stable phases within a limited temperature window. These two systems are formed of similar building blocks, Bi_2Te_3-, NaCl-, CdI_2-, and Sb_2Se_3-type rod fragments, which arrange in the same stoichiometry but with different architecture[16]. The inclusion of alkali atoms stabilizes the covalent bonding in the Bi-chalcogen framework with cages. The K atoms occupy the positions inside these cages as K^+ ions and can act as "rattlers"[5], consistent with the concept of an electron crystal/phonon glass.[6]

In order to determine the figure of merit, $ZT = S\sigma^2T/\kappa$, in these compounds, S, σ, and κ have been measured as a function of temperature. The highest room temperature (RT) values for σ in α-$K_2Bi_8Se_{13}$ is 2 S/cm compared to β-$K_2Bi_8Se_{13}$ with 250 S/cm.[16] The largest RT value of S for both α- and β-$K_2Bi_8Se_{13}$ is -200 μV/K, which means that the carriers are electrons. The thermoelectric properties of β-$K_2Bi_8Se_{13}$ are believed to be enhanced by the disordered Bi-K sites within the lattice which reduces the phonon thermal conductivity (κ); a value of 1.28 W/m·K has been seen compared to 1.31 W/m·K for Bi_2Te_3 alloys. This yields a value of 0.22 for ZT in unoptimized β-$K_2Bi_8Se_{13}$.[16] Values of κ for α-$K_2Bi_8Se_{13}$, with no disorder, have not been measured due to the low σ values.[161]

7.3.1. α-$K_2Bi_8Se_{13}$

The crystal structure of α-$K_2Bi_8Se_{13}$ is triclinic with space group *P-1* [A = 26.108 a.u., B = 22.858 a.u., C = 7.872 a.u., $\alpha = 89.98°$, $\beta = 98.64°$, $\gamma = 87.96°$][16]. This crystal structure is given in Figure 81 with its corresponding Brillouin zone in Figure 82.

Figure 81. Projection of the crystal structure of α-$K_2Bi_8Se_{13}$ viewed down the b-axis. Bi_2Te_3-, CdI_2-, and Sb_2Se_3-type building blocks in the structure are highlighted by the shaded areas.

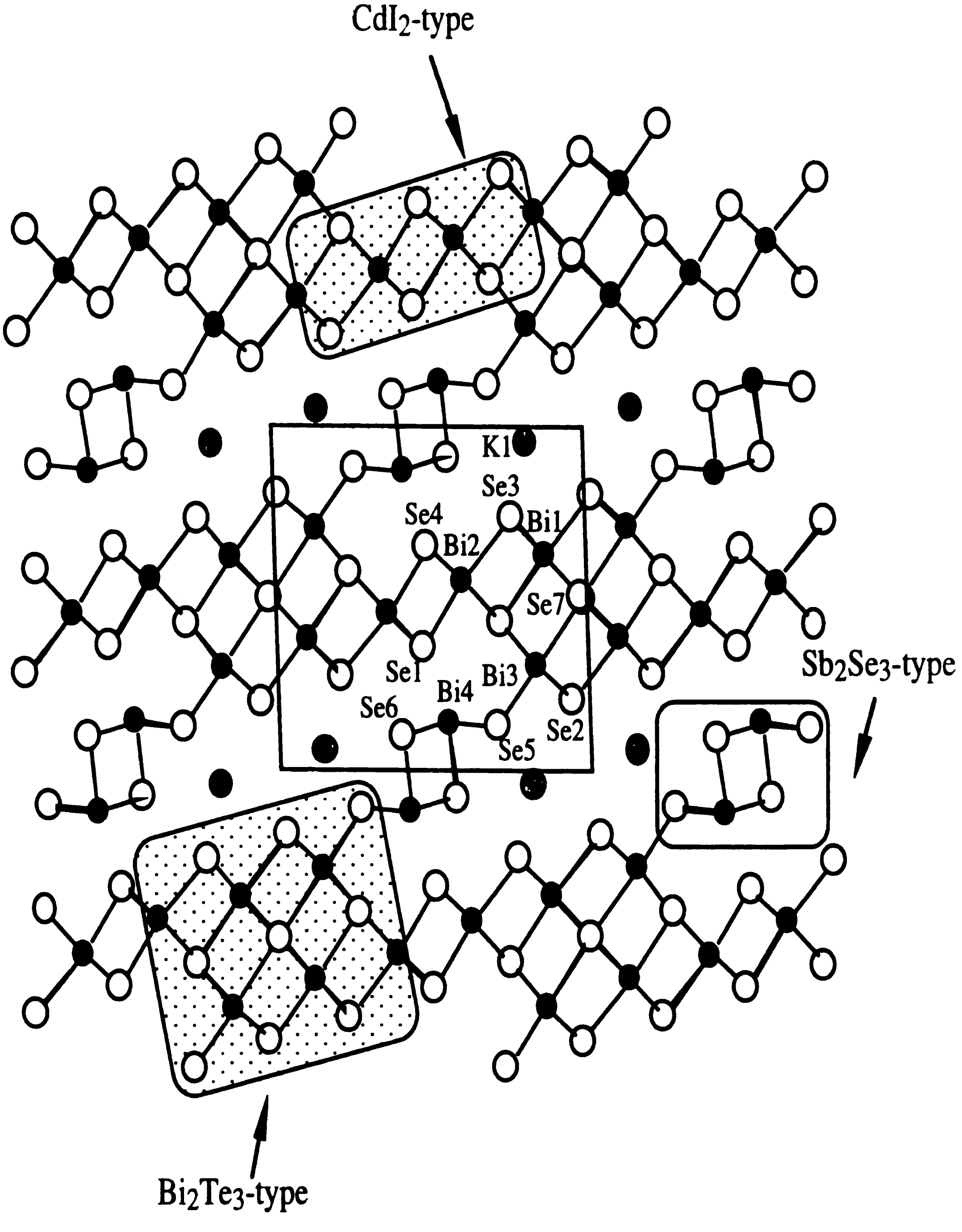
CdI2-type
K1
Se3
Se4
Bi1
Bi2
Se7
Se1
Bi3
Bi4
Se6
Se5
Se2
Sb2Se3-type
Bi2Te3-type

Figure 82. Brillouin zone for α-$K_2Bi_8Se_{13}$.

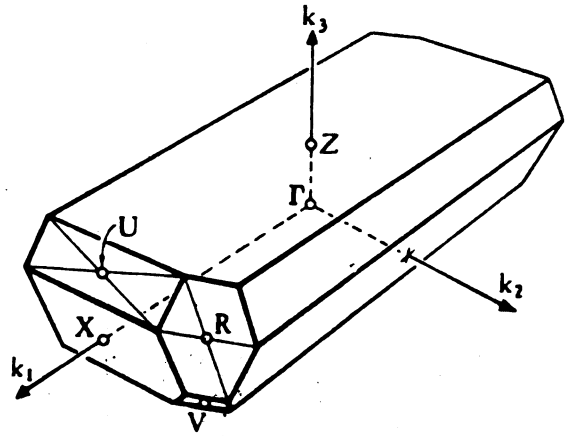

The band structure of α-$K_2Bi_8Se_{13}$ with and without SOI is given in Figure 83. The effect of SOI is to shift the conduction band down relative to the valence band and thereby decrease the gap values. Both with and without SOI, a semiconductor forms with the VBM at the Γ point and the CBM at the X point. When SOI is included the calculated band gap is 0.47 eV (Figure 83b) compared to the measured value of 0.76 eV.[161] There are however direct gaps at the X point of 0.74 eV and at the V point of 0.72 eV.

Figure 83. Band structure of α-$K_2Bi_8Se_{13}$ (a) with and (b) without SOI.

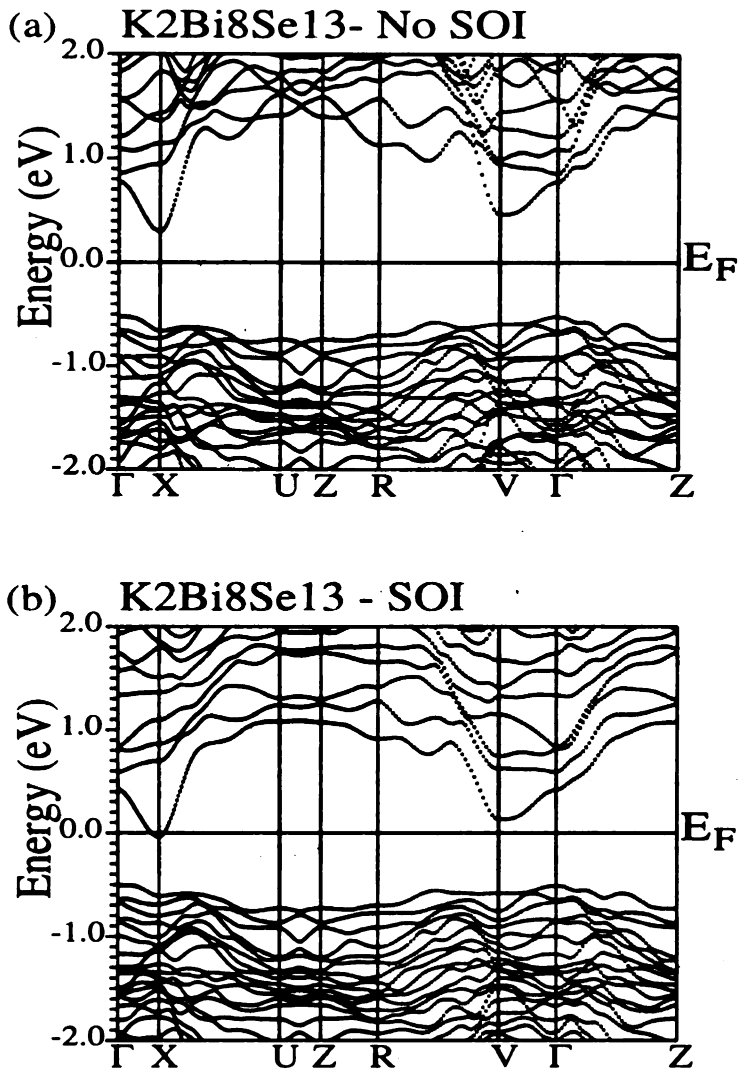

The low σ and high S are consistent with a wide-gap semiconductor found in this system. The thermoelectric properties in this material may also be influenced by anisotropic effective masses, which can lead to a high ZT.[24, 11] The effective masses of the band extrema in α-$K_2Bi_8Se_{13}$ were calculated assuming that the angles α and γ are 90°. In this approximation, the effective masses were obtained by calculating values of the energy close to different LCB minima and HVB maxima while moving along suitably chosen directions in the BZ. These values were then fitted using the equation

$$2m_e/\hbar^2\, \varepsilon_k = \alpha_{xx}k_x^2 + \alpha_{yy}\, k_y^2 + \alpha_{zz}k_z^2 + 2\alpha_{xz}k_xk_z, \tag{75b}$$

where a constant term has been omitted. Generally, the off-diagonal terms are small so the reciprocal of the diagonal terms, α_{ii} (i = 1, 2, 3), can be considered the effective mass parameters. As can be seen (Table XVI) the effective masses of the valence band maxima are fairly isotropic. We find that the Sb_2Se_3 fragments connecting the CdI_2 layers together, consisting of Se1-7 and hybridized Bi4 *p* orbitals, having a strong contribution to the HVB. On the other hand, these Sb_2Se_3 fragments do not contribute strongly to the LCB, which consist mainly of Bi1-3 *p* orbitals. This leads to a more 2D transport of the electrons within the CdI_2 layers, similar to what is seen in the layers of Bi_2Te_3.[11, 59] This suggests better thermoelectric properties from the electron-doped system compared to the hole-doped system.

Table XVI. Components of the reciprocal effective mass tensor for α-$K_2Bi_8Se_{13}$

	m_v/m_e	m_c/m_e
$\alpha_{xx} = [m/m_e]^{-1}_{xx}$	1.05	5.56
$\alpha_{yy} = [m/m_e]^{-1}_{yy}$	1.44	1.09
$\alpha_{zz} = [m/m_e]^{-1}_{zz}$	1.19	7.69
$\alpha_{xx} = [m/m_e]^{-1}_{xz}$	0.71	2.94

7.3.2. β-$K_2Bi_8Se_{13}$

While having the same stoichiometry as α-$K_2Bi_8Se_{13}$, β-$K_2Bi_8Se_{13}$ is isostructural to $K_2Bi_8S_{13}$[162] in space group $P2_1/m$ and is formed of Bi_2Te_3-, NaCl-, and CdI_2-type infinite rod-shaped blocks to form a much more 3-D structure.[16] The α form is slightly less dense than the β form, because in the α form the Bi atoms are in octahedral or higher coordination geometry compared to the β form where the Bi atoms are found in a trigonal-pyramidal geometry. The Bi_2Te_3 and CdI_2 rods in the β form are arranged side-by-side to form layers perpendicular to the c-axis where the NaCl units connect the layers to build a 3-D framework with tunnels filled with K^+ ions.[16]

The monoclinic crystal structure of β-$K_2Bi_8Se_{13}$ is closely related to that of $Sr_4Bi_6Se_{13}$, i.e., one replaces two Sr^{2+} atoms with two K^+ atoms and the remaining two Sr^{2+} atoms with Bi^{3+} atoms[163]. This leads to a mixed occupancy of Bi and K atoms within the crystal structure. The K2 position is fully occupied by K^+ atoms and Bi1-7 are fully occupied by Bi^{3+}atoms. However, the site K1/B9 has 62% K and 38% Bi occupancy while the K3/Bi8 site has 62% Bi and 38% K occupancy.[16] A very similar type of disorder is found in the isostructural compound $K_2Bi_8S_{13}$, but in this compound the disorder is between K1/Bi9, K3/Bi8, and K2.[162] The K1/Bi9 site has three bonds ranging from 2.85 to 3.07 Å and five longer ones from 3.44 to 3.70 Å, while the K3/Bi8 site has three bonds from 2.84 to 3.04 Å and five longer ones from 3.31 to 3.68 Å.[16] However, the two sites are not equivalent to each other. The Bi8/K3 site lies at the corner of one of the NaCl blocks while the Bi9/K1 site lies along the side of the block next to Se9 which lies on the corner. Electronic structure calculations of β-$K_2Bi_8Se_{13}$ should in principle incorporate the Bi9/K1 and Bi8/K3 disorder. The monoclinic crystal structure [A = 33.056 a.u., B = 7.914 a.u., C, = 34.804 a.u., β = 90.49°] is given in Figure 84 and the corresponding Brillouin zone in Figure 85.

Figure 84. Crystal structure of β-$K_2Bi_8Se_{13}$.

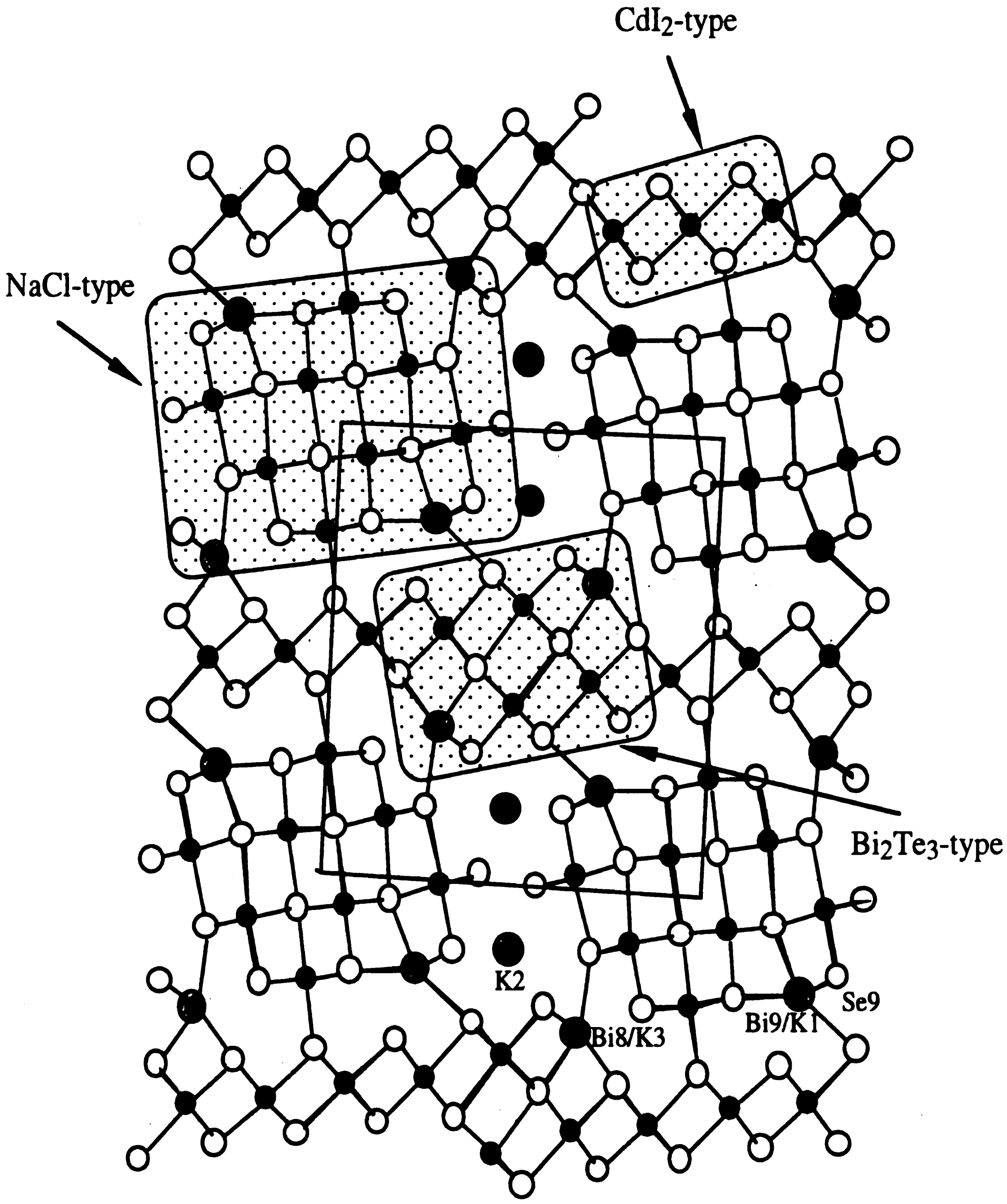
CdI2-type
NaCl-type
Bi2Te3-type
K2
Se9
Bi8/K3
Bi9/K1

Figure 85. Brillouin zone of β-$K_2Bi_8Se_{13}$.

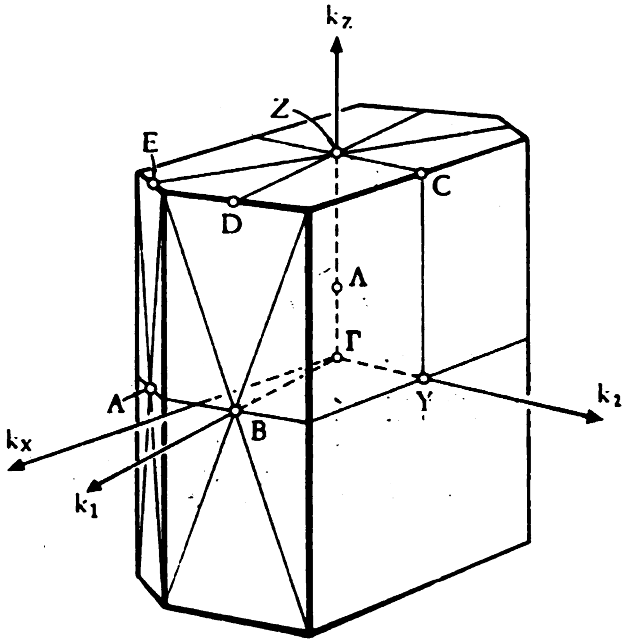

Our electronic structure program[55] cannot treat sites as partially occupied, such as in the virtual crystal approximation[164]. Therefore, we will perform preliminary band structure studies to understand the effects of disorder. Different configurations will be studied with the extreme occupancy of the K1/Bi9 and K3/Bi8 sites. As already mentioned, the site K1/B9 has 62% K and 38% Bi occupancy while the K3/Bi8 site has 62% Bi and 38% K occupancy.[16] The first arrangement, which will be called Configuration 1 will place K at the K1/Bi9 site and Bi at the K3/Bi8 site. Configuration 2 will have these positions reversed, Bi at the K1/Bi9 site and K at the K3/Bi8 site.

Configuration 1 seems closest to the structure seen experimentally.[16] Both before and after the inclusion of SOI, Configuration 1 yields a semi-metallic or metallic behavior (Figure 86) with some very flat bands along ΓY and ABΓ, in the plane perpendicular to the needle axis (defined in Figure 84).

Figure 86. Band structure of β-$K_2Bi_8Se_{13}$ - Configuration 1 (a) without and (b) with SOI.

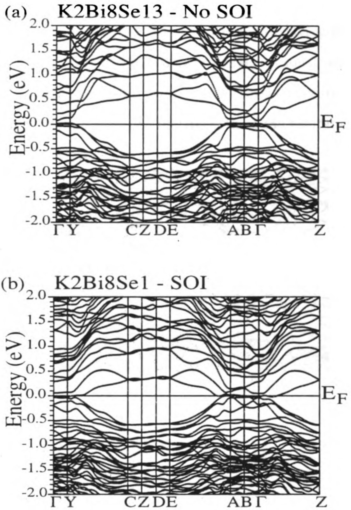

These flat regions existing at E_F are inconsistent with the measured band gap of 0.59 eV.[16] An orbital analysis of these bands shows that they correspond to Bi8 p and Se9 p states. (Figure 87) Se9 lies on the edge of the NaCl block next to the K atom in the disordered Bi9/K1 site. Also, the other bands crossing E_F correspond to the Bi atom in the Bi8/K3 site. It appears that the Se9-K1 bonding is too weak to form a bond so that the Se9 orbitals float to E_F to form a semi-metallic or metallic behavior.

Figure 87. Orbital character of (a) Bi8 and (b) Se9 overlying the band structure of β-$K_2Bi_8Se_{13}$ - Configuration 1 with SOI. The size of the circles overlying the band structure is directly proportional to the strength of the orbital character

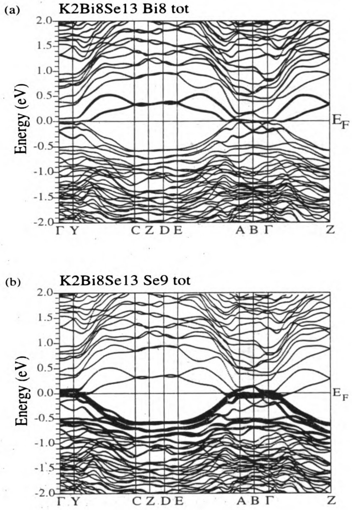

Configuration 2 has Bi is in the Bi9/K1 site and K is in the Bi8/K3 site. The total energy of this configuration is 1.49 eV/formula unit lower than that of Configuration 1. Before the inclusion of SOI, there is a band gap 0.38 eV, the VBM along the very flat bands along ABΓ and ΓY and the CBM along AB. While there is a band gap, the HVB is unusually flat, so that the bonding is very weak in some directions. After the inclusion of SOI, the band gap disappears and the band structure of Configuration 2 looks very similar to that of Configuration 1.

Figure 88. Band structure of β-$K_2Bi_8Se_{13}$ - Configuration 2 (a) without and (b) with SOI.

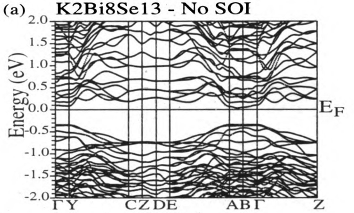

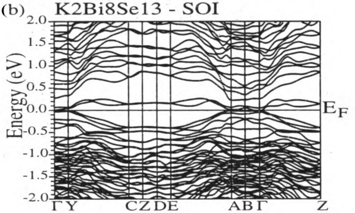

Figure 89. Band structure of β-$K_2Bi_8Se_{13}$ - Configuration 3 (a) without and (b) with SOI.

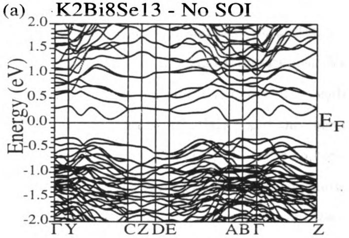

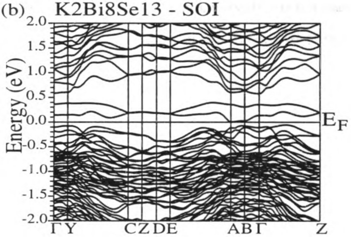

A third configuration has been tried which differs from Configuration 2 by exchanging Bi on the Bi9/K1 site with K on the K2 site. This type of disorder has been seen in $K_2Bi_8S_{13}$ but not in β-$K_2Bi_8Se_{13}$. This configuration has a slightly higher energy than Configuration 2, by 0.03 eV/formula unit. Before the inclusion of SOI, the CBM is at the A point while the VBM is between A and B to produce a gap of

0.35 eV. After the inclusion of SOI, the band gap decreases to 0.04 eV, smaller than the experimental value of 0.59 eV[16]. The HVB is much more dispersive along ABΓ and ΓY meaning the bonding along these directions is stronger.

While the Bi-K disorder in β-$K_2Bi_8Se_{13}$ has been suspected to reduce κ[16], this disorder also has a profound effect on the band structure near E_F. We have found either narrow-gap semiconducting or semi-metallic behavior depending on the position of the atoms on the disordered sites on the lattice and the calculated gap is much smaller than the measured value of 0.59 eV[16]. In order to better understand the band structure of this material, the band gap should be measured as a function of temperature to see if the low temperature value differs from the room temperature value (as in the lead salts[101]). Also, though the virtual crystal approximation[164] generally reduces the band gaps in semiconductors[59], such a calculation should be performed since the ratio of Bi/K atoms in the disordered sites is likely to have a profound effect on the band structure.

CHAPTER 8.

CONCLUSIONS

In this dissertation we have investigated the electronic structure of a wide variety of systems including an extensive study of the half-Heusler compounds and simple chalcogenides along with a detailed study of more complicated structures such as Zintl phases and complex chalcogenides. We have investigated the subtle properties of the gap formation in these semiconductors and used these results to understand their thermoelectric properties.

The focus of this dissertation is two-fold. First, we have used our calculations to understand which properties in the band structure are the best for thermoelectric properties and which materials display these properties. We have found that systems with highly anisotropic effective masses (though not large values) and multiply degenerate band extrema have the best thermoelectric properties, as predicted by the B parameter (Equation 24 in Chapter 2). The anisotropic effective masses seem even more important as they may describe reduced dimensionality in the charge transport in bulk materials which was found important in $CsBi_4Te_6$.[15] These are valuable criteria for finding new thermoelectric materials using band structure calculations.

Our analysis of a number of systems explained why certain materials were better thermoelectrics than others. We found that the six-fold degenerate VBM and CBM in Bi_2Te_3 and Sb_2Te_3 explain their improved thermoelectric performance compared to Bi_2Se_3 with CBM and VBM at the Γ point. Also, we found that the highly anisotropic masses in Bi_2Te_3 and $CsBi_4Te_6$ enhance their thermoelectric properties while the more isotropic effective masses in $BaBiTe_3$ lead to a less promising thermoelectric material. We have also predicted that the anisotropy in the CBM effective masses in the half-Heusler compounds would make the n-doped systems better for thermoelectric applications than the p-doped systems.

The second focus of this dissertation is to understand the gap formation of these narrow-gap semiconductors. Most of these semiconductors are formed from hybridization of different bands which lead to their small gaps. After the presentation of the numerous band structures which have been given in this dissertation, it is important to give a short critique of the methods we have used and how reliably we can trust these results. These include ground state properties, such as the total energies and band dispersions, and excited state properties, such as the band gaps.[30, 41]

The structural properties have been shown to be found correctly in DFT in many systems, such as in BCC Fe where GGA correctly finds this has a lower energy than FCC Fe while LDA did not.[45, 46] Our calculations found that in half-Heusler systems containing Ni, disorder of the Ni sublattice is energetically favorable to disorder of the NaCl substructure[11]. Experimentally one doesn't see Ni sublattice disorder at low T, instead higher energy defects are seen in the NaCl substructure (Zr-Sn disorder in ZrNiSn)[78]. Further theoretical and experimental study of disorder in the half-Heusler compounds is necessary to understand this result.

Relaxation of the lattice parameters within the electronic structure calculation also is valuable for obtaining reliable results. DFT is in general exact, but LDA/GGA are only approximate since the XC potential is treated approximately[31]. Therefore, a model crystal structure, such as relaxing the lattice parameters, often gives band gaps and total energies in better agreement with experiment. In PbS, PbSe, and PbTe, the lattice relaxation nearly reproduced the experimental band gaps[115]. The effects of lattice relaxations were not as profound in the other simple chalcogenides or half-Heusler systems which we have tried, while lattice relaxation on large systems becomes nearly impossible due to the number of configurations and time necessary to find the minimum energy structure. We strongly believe that lattice relaxation is necessary to obtain an accurate band structure.

The band dispersions (effective masses) are also ground state properties within DFT, so these should be predicted correctly because **k** is a good quantum number.[30, 41] The effective mass tensor is defined as $[\mathrm{m}]_{ij}^{-1} = \alpha_{ij} = \hbar^{-2}[\frac{\partial^2 E}{\partial k_i \partial k_j}]$.[22] In most cases when the correct orthogonal directions in the crystal are chosen, the off-diagonal terms of the mass tensor are small, so diagonal elements of the mass tensor, α_{ii}, accurately give the inverse of the effective mass parameters m_{ii} (i = 1, 2, 3). The effective masses of the semiconductors GaAs, InAs, and AlAs have been studied extensively both experimentally and theoretically. A good agreement is found between the most of the calculated values and the measured values[165] which confirms the belief that DFT calculations do a good job in measuring these ground-state properties. The large calculated effective masses of the half-Heusler compound ZrNiSn[7] agrees well with the measured value.[81] Even in the case where the bands are known to be nonparabolic, such as in Bi_2Te_3[11] and the lead salts[122], reasonable agreement can be found between theory and experiment. Since we found that anisotropic effective masses were very important for high values of ZT, finding systems with highly anisotropic effective masses is an effective use of electronic structure calculations in finding new thermoelectric materials.

One of the most well known problems in LDA/GGA is that semiconducting band gaps are usually found to be smaller than experiment. This is not surprising since the Kohn-Sham energies are related to the band gap by $\mathrm{E}_{gap} = \Delta_{xc} + \varepsilon_{N,N+1} - \varepsilon_{N,N}$ where $\Delta_{xc} = \varepsilon_{N+1,N+1} - \varepsilon_{N,N}$ is the shift of the exchange-correlation energy when adding an electron.[31] There is no way to estimate Δ_{xc}, so the LDA/GGA band gaps which have been reported are simply $E_{gap}^{LDA/GGA} = \varepsilon_{N,N+1} - \varepsilon_{N,N}$. The band gap is actually an excited state property because both I and A in E_{gap} = I - A are both excited state properties. Therefore, it is not surprising that the band gaps in LDA/GGA do not agree with experiment. In most group IV, III-V, and II-VI semiconductors, such as Si, Ge, InSb, GaAs, etc., the predicted band gap is smaller than what is seen experimentally.[31, 57, 58] The GW method explicitly adds and removes an electron to compensate for this problem and gives much better agreement between the theoretical and measured values for the band gaps.[31]

The semiconductors discussed above are either strongly covalent or strongly ionic compounds. In contrast to these compounds, we find that the band gaps in $BaBiTe_3$[11], Bi_2Te_3[11, 40, 130], and $CsBi_4Te_6$[15] agree very well with the experimental values. In the best thermoelectric materials which we have studied, the effects of SOI are very important. This may be a serious problem since LDA/GGA calculations within the scalar-relativistic method using second-variational treatment of SOI have been linked to poor prediction of the positions of the bands compared to full relativistic calculations for the 6*p* metallic elements Hg, Tl, Bi, and Pb.[36] However, the second-variational treatment of SOI has found good agreement in PbTe[37, 38, 39] and Bi_2Te_3.[11, 12, 13, 40] Is it possible that there is a happy cancellation taking place between these two approximations of SOI and LDA/GGA which leads to a better than expected agreement between experiment and theory? This point needs to be investigated further using fully-relativistic DFT calculations.[34]

The band gaps of some semiconductors are overestimated in LDA/GGA calculations. This is seen in the half-Heusler compounds, such as ZrNiSn with 0.50 eV compared to the measured value of 0.12 eV[7, 59]. This is difficult to reconcile with Equations 57 and 58 since Δ_{xc} should be positive and GW calculations give larger band gaps than LDA. Therefore, another explanations must be introduced. In ZrNiSn, it is claimed that virtual crystal calculations predict that 15% Zr-Sn disorder leads to a closing of the band gap in this material.[59] However, TiNiSn has the same structure and nearly the same predicted and measured band gaps as ZrNiSn. However, while anti-site disorder has been observed in ZrNiSn, no such disorder has been observed in TiNiSn, which makes the argument difficult to accept at best.[8, 66]

The above discrepancy is more evident in the Zintl-phase compounds where the gap formation is similar to that in the half-Heusler compounds. The calculated band gaps for the binary parent compound Th_3Sb_4 by Takegahara *et al.*[10] gives a negative gap compared to the experimental value of 0.48 eV. The calculated value of the gap for the ternary $Th_3Ni_3Sb_4$ is 0.36 eV compared to the experimental value of 0.07 eV.[10] Since disorder on the parent binary compounds substructure is expected to reduce the gap in the ternary compound, the discrepancy of finding a smaller band gap for the binary compound and a larger value for the ternary compound becomes harder to fathom. We suggest another possible mechanism discussed below.

It is well known that LDA/GGA calculations place the *d* orbitals of transition metals too high in energy while other methods, namely Hartree-Fock, place these *d* orbitals too low in energy.[97] As explained in greater detail in Chapter 5, shifting of the *d* levels down reduces the band gaps while moving them closer to E_F increases the gaps. The Co-containing half-Heusler compounds all had larger gaps than the Au-containing half-Heusler compounds. The lack of disorder in TiNiSn and the discrepancy between the gaps in the ternary Zintl phases and in their binary parent compounds make this a more believable explanation than reduction of the gaps through disorder. This should be studied further using GW[31] calculations and LSDA+U[73] within DFT calculations which better handle narrow *d*- and *f*-bands.

BIBLIOGRAPHY

References

[1] F. J. Disalvo, Science **285**, 703 (1999).

[2] G. Mahan, B. Sales, and J. Sharp, Phys. Today **50**, 42 (1997).

[3] T.M. Tritt, Science **272**, 1276 (1996).

[4] *Thermoelectric Materials 2000*, edited by T.M. Tritt, G.S. Nolas, G. Mahan, M.G. Kanatzidis, and D. Mandrus, MRS Symposium Proceedings No. **626** (Materials Research Society, Pittsburgh, 2000); *Thermoelectric Materials-The Next Generation Materials for Small-Scale Refrigeration and Power Generation Applications*, edited by T.M. Tritt, M.G. Kanatzidis, G.D. Mahan, and H.B. Lyon, Jr., MRS Symposium Proceedings No. **545** (Materials Research Society, Pittsburgh, 1999); *Thermoelectric Materials-New Directions and Approaches*, edited by T.M. Tritt, M.G. Kanatzidis, H.B. Lyon, Jr., and G.D. Mahan, MRS Symposium Proceedings No. **478** (Materials Research Society, Pittsburgh, 1997).

[5] M.G. Kanatzidis, Semicond. Semimet. **70**, 51 (2001).

[6] G.A. Slack, Solid State Physics **34**, 1 (1979).

[7] P. Larson, S.D. Mahanti, S. Sportouch, and M.G. Kanatzidis, Phys. Rev. B **59**, 15660 (1999).

[8] P. Larson, S.D. Mahanti, and M.G. Kanatzidis, Phys. Rev. B **62**, 12754 (2000).

[9] S. Sportouch, P. Larson, M. Bastea, P. Brazis, J. Ireland, C.R. Kannewurf, S.D. Mahanti, C. Uher, and M.G. Kanatzidis, *Thermoelectric Materials-The*

Next Generation Materials for Small-Scale Refrigeration and Power Generation Applications, edited by T.M. Tritt, M.G. Kanatzidis, G.D. Mahan, and H.B. Lyon, Jr., MRS Symposium Proceedings No. **545** (Materials Research Society, Pittsburgh, 1999), p. 421.

[10] K. Takegahara and T. Kasuya, Solid State Commun. **74**, 243 (1990); K. Takegahara, Y. Kaneta, and T. Kasuya, J. Phys. Soc. Japan **59**, 4394 (1990); K. Takegahara and Y. Kaneta, Prog. Theor. Phys. Suppl. **108**, 55 (1992).

[11] P. Larson, S.D. Mahanti, and M.G. Kanatzidis, Phys. Rev. B **61**, 8162 (2000).

[12] S.D. Mahanti, P. Larson, and M.G. Kanatzidis, *Proceedings of the 18th International Conference on Thermoelectrics*, edited by A. Ehrlich, Baltimore, MD, p. 52 (2000).

[13] S.D. Mahanti, P.Larson, D-Y Chung, S. Sportouch, and M.G. Kanatzidis, *Thermoelectric Materials-The Next Generation Materials for Small-Scale Refrigeration and Power Generation Applications*, edited by T.M. Tritt, M.G. Kanatzidis, G.D. Mahan, and H.B. Lyon, Jr., MRS Symposium Proceedings No. **545** (Materials Research Society, Pittsburgh, 1999), p. 23.

[14] P. Larson, S.D. Mahanti, D-Y Chung, and M.G. Kanatzidis, *Thermoelectric Materials 2000*, edited by T.M. Tritt, G.S. Nolas, G. Mahan, M.G. Kanatzidis, and D. Mandrus, MRS Symposium Proceedings No. **626** (Materials Research Society, Pittsburgh, 2000).

[15] P. Larson, S.D. Mahanti, D-Y Chung, and M.G. Kanatzidis, submitted to Phys. Rev. B.

[16] D-Y Chung, K-S Choi, L. Iordanidis, J.L. Schindler, P.W. Brazis, C.R. Kannewurf, B. Chen, S. Hu, C. Uher, and M.G. Kanatzidis, Chem. Mater. **9**, 3060 (1997).

[17] R.R. Heikes and R.W. Ure, Jr. *Thermoelectricity: Science and Engineering* (Interscience, New York, 1961).

[18] T.C. Harman and J.M Honig, *Thermoelectric and Thermomagnetic Effects and Applications* (McGraw-Hill, New York, 1967).

[19] G.D. Mahan in *Solid State Physics*, edited by H. Ehrenreich and F. Spaepen, Vol. **51** (Academic Press, Orlando, 1998), p. 81.

[20] G. Goldsmid, *Applications of Thermoelectricity* (John Wiley & Sons, London, 1960).

[21] P.H. Egli, *Thermoelectricity* (John Wiley & Sons, New York, 1960).

[22] N.W. Ashcroft and N.D. Mermin, *Solid State Physics* (Saunders College Publishing, Fort Worth, 1976).

[23] B.C. Sales, D. Mandrus, and R.K. Williams, Science **272**, 1325 (1996).

[24] L.D. Hicks and M.S. Dresselhaus, Phys. Rev. B, **47**, 16631 (1993); L.D. Hicks and M.S. Dresselhaus, *ibid.* , **47**, 12727 (1993).

[25] G.D. Mahan and J.O. Sofo, Proc. Natl. Acad. Sci. **93**, 7436 (1996).

[26] D-Y Chung, T. Hogan, P. Brazis, M. Rocci-Lane, C. Kannewurf, M. Bastea, C. Uher, and M.G. Kanatzidis, Science **287**, 1024 (2000).

[27] T.C. Harman, P.J. Taylor, D.L. Spears, and M.P. Walsh, J. Electron. Mater. **29**, L1 (2000).

[28] R. Venkatasubramanian, Phys. Rev. B **61**, 3091 (2000).

[29] Y-M Juna and E. Kaxiras, Phys. Rev B **48**, 14944 (1993); Y-M Juna and E. Kaxiras, *ibid.* **51**, 9521 (1995).

[30] W. Kohn, Rev. Mod. Phys. **71**, 1253 (1999).

[31] Wilfried G. Aulbur, Lars Jonsson, and John W. Wilkins, in *Solid State Physics*, edited by H. Ehrenreich and F. Spaepen, Vol. **54** (Academic Press, Orlando, 2000). p. 1.

[32] P. Novak, unpublished (1997).

[33] J. Kubler and V. Eyert, "Electronic structure calculations" in *Materials Science and Technology, Vol. 3A: Electronic and Magnetic Properties of Metals and Ceramics, Part I*, Edited by K.H.J. Buschow (VCH-Verlag, Weinheim, 1992), p. 1.

[34] M. Richter, J. Phys. D: Appl. Phys. **31**, 1017 (1998); H. Jansen, Phys. Rev. B **7**, 1912 (1988); A.K. Rajagopa and J. Callaway, *ibid.* **7**, 1912 (1973); H. Eschrig, G. Seifert, and P. Ziesche, Solid State Commun. **56**, 777 (1985).

[35] D. Singh, *Planewaves, Pseudopotentials, and the LAPW Method* (Kluwer Academic, Boston, 1994).

[36] A.H. MacDonald, W.E. Pickett, and D.D. Koelling, J. Phys. C: Solid St. Phys. **13**, 2675 (1980).

[37] S.H. Wei and A. Zunger, Phys. Rev. B **55**, 13605 (1997).

[38] M. Lach-lab, M. Keegan, D.A. Papaconstantopoulos, and M.J. Mehl, J. Phys. Chem. Solids **61**, 1639 (2000).

[39] E.A. Albanesi, C.M.I Okoye, C.O. Rodriguez, E.L.P.Y. Blanca, and and A.G. Petukhov, Phys. Rev. B **61**, 16589 (2000).

[40] S.K. Mishra, S. Satpathy, and O. Jepsen, J. Phys.: Condens. Matter **9**, 461 (1997).

[41] P. Hohenberg and W. Kohn, Phys. Rev. **136**, B864 (1964).

[42] W. Kohn and L.J. Sham, Phys. Rev. **140**, A1133 (1965).

[43] R.M. Dreizler and E.K.U. Gross, *Density Functional Theory: An Approach to the Quantum Many-Body Problem* (Springer-Verlag, Berlin, 1990).

[44] R.O. Jones and O. Gunnarsson, Rev. Mod. Phys. **61**, 689 (1989).

[45] P. Bagno, O. Jepsen, and O. Gunnarson, Phys. Rev. B **40**, 1997 (1989).

[46] J.P. Perdew, J.A. Chevary, S.H. Vosko, K.A. Jackson, M.R. Pederson, D.J. Singh, and C. Fiolhais, Phys. Rev. B **46**, 6671 (1992).

[47] J.P. Perdew and Y. Wang, Phys. Rev. B **45**, 13244 (1992).

[48] J.P. Perdew, K. Burke, and M. Ernzerhof, Phys. Rev. B **77**, 3865 (1996).

[49] D. Vanderbilt, Phys. Rev. B **41**, 7892 (1990).

[50] H.L. Skriver, *The LMTO Method: Muffin-Tin Orbitals and Electronic Structure* (Springer-Verlag, Berlin, 1984).

[51] O.K. Andersen, Phys. Rev. B **12**, 3060 (1975).

[52] T.L. Loucks, *Augmented Plane Wave Method: A Guide to Performing Electronic Structure Calculations* (W.A. Benjamin, Inc., New York, 1967).

[53] P. Blaha, K. Schwarz, J. Luitz, *WIEN97: A Full Potential Linearized Augmented Planewave Package for Calculating Crystal Properties User's Guide* (Techn. Universitat Wien, Austria, 2000).

[54] W.E. Pickett, Comp. Phys. Rep. **9**, 115 (1998).

[55] P. Blaha, K. Schwarz, and J. Luitz, **wien97**, A Full Potential Linearized Augmented Planewave Package for Calculating Crystal Properties (Karlheinz Schwarz, Techn. Universitat Wien, Austria), 1999. ISBN 3-9501031-0-4.

[56] F. Jensen, *Introduction to Computational Chemistry* (John Wiley & Sons, Chichester, England, 1999).

[57] F. Aryasetiawan and O. Gunnarsson, Rep. Prog. Phys. **61**, 237 (1998).

[58] X. Zhu and S.G. Louie, Phys. Rev. B **43**, 14142 (1991); M.S. Hybertsen and S.G. Louie, Phys. Rev. B **34**, 5390 (1986); M.S. Hybertsen and S.G. Louie, Phys. Rev. Lett. **55**, 1418 (1985).

[59] S. Ogut and K.M. Rabe, Phys. Rev. B **51**, 10443 (1995).

[60] J. Tobola and J. Pierre, J. Allloys Compd. **296**, 243 (2000); D. Jung, H-J Koo, and M-H Whangbo, J. Mol. Struct. **527**, 113 (2000).

[61] S.J. Poon, Semicond. Semimet. **70**, 37 (2001).

[62] G.J. McMullen and M.P. Roy, J. Phys.: Condens. Matter **4**, 7095 (1992).

[63] R.W.G. Wyckoff, *Crystal Structures* (Krieger, Melbourne, Fl, 1986), Vol. 2.

[64] J.C. Phillips, *Bonds and Bands in Semiconductors* (Academic Press, New York, 1973).

[65] N.V. Sidgwick, *The Electronic Theory of Valency* (Cornell University Press, Ithaca, New York, 1927).

[66] F.G. Aliev, N.B. Brandt, V.V. Moschalkov, V.V. Kozyrkov, R. V. Skolozdra, and A.I. Belogorokhov, Z. Phys. B. **80**, 353 (1990), and references therein; F.G. Aliev, *ibid.* **171**, 199 (1991); R. Kuentzler, R. Clad, G. Schmerber, and Y. Dossmann, J. Magn. Magn. Mater. **104-107**, 1976 (1992); H. Hohl, A.P. Ramirez, W.K. Fess, Ch. Thurner, Ch. Kloc, and E. Bucher, in *Thermoelectric Materials-New Directions and Approaches*, edited by T.M. Tritt, M.G. Kanatzidis, H.B. Lyon, Jr., and G.D. Mahan, MRS Symposium Proceedings No. **478** (Materials Research Society, Pittsburgh, 1997), p. 109.

[67] A.K. Solanki, A. Kashyap, S. Auluck, and M.S.S. Brooks, J. Appl. Phys. **75** 6301 (1994).

[68] S.K. Dhar, S. Rankakrishnan, R. Vijayaraghaban, G. Chandra, K. Satoh, J. Itoh, Y. Onuki, and K.A. Gschneider, Jr., Phys. Rev. B **49**, 641 (1994).

[69] I. Karla, J. Pierre, and R.V. Skolozdra, J. Alloys Compd. **265**, 42 (1998).

[70] J. Tobola, J. Pierre, S. Kaprzyk, R.V. Skolozdra, M.A. Kouacou, J. Magn. Magn. Mater. **159**, 192 (1996).

[71] A. Slebarski, A. Jezierski, S. Lutkehoff, and M. Neumann, Phys. Rev. B **57**, 6408 (1998); A. Slebarski, A. Jezierski, A. Zygmunt, S. Mahl, and M. Neumann, *ibid.* **57**, 9544 (1998); A. Wrona, A. Slebarski, A. Jezierski, A. Zygmunt, S. Plogmann, and M. Neumann, J. Magn. Magn. Mater. **213**, 157 (2000).

[72] A. Hasegawa, J. Phys. C **13**, 6147 (1980).

[73] V.I. Anisimov and O. Gunnarson, Phys. Rev B **43**, 7570 (1991); V.I. Anisimov, J. Zaanen, and O.K. Anderson, *ibid.* **44**, 943 (1991); V.I. Anisimov, I.V. Solovyev, M.A. Kortin, M.T. Czyzyk, and G.A. Sawatzky, *ibid.* **48**, 16929 (1993).

[74] E.K.R. Runge, R.C. Albers, N.E. Christensen, and G.E. Zwicknagl, Phys. Rev. B **51**, 10375 (1995).

[75] S.J. Youn and B.I. Min, Phys. Rev. B **51**, 10436 (1995); H. Ebert and G. Schutz, J. Appl. Phys. **69**, 4627 (1991); E. Kulatov and I.I. Mazin, J. Phys.: Condens. Matter **2**, 343 (1990); K.E.H.M. Hanssen and P.E. Mijnarends, Phys. Rev. B **34**, 5009 (1986).

[76] C. Hordequin, D. Ristoiu, L. Ranno, and J. Pierre, Eur. Phys. J. B **16**, 287 (2000); D. Orgassa, H. Fujiwara, T.C. Schulthess, and W.H. Butler, Phys. Rev. B **60**, 13237 (1999); K. Kaczmarska, J. Pierre, J. Tobola, and R.V. Skolozdra, *ibid.* **60**, 373 (1999); Ch. Hordequin, J. Pierre, and R. Currat, Physica B **234-236**, 605 (1997); Ch. Hordequin, E. Lelievre-Berna, and J. Pierre, *ibid.* **234-236**, 602 (1997); C. Hordequin, J. Pierre, and R. Currant, J. Magn. Magn. Mater. **162**, 75 (1996); J-S Kang, J.H. Hong, S.W. Jung, Y.P. Lee, J-G Park, C.G. Olson, S.J. Youn, and B.I. Min, Solid State Commun. **88**, 653 (1993).

[77] S. Ishida, T. Masaki, S. Fujii, and S. Asano, Physica B **237-238**, 363 (1997).

[78] F.G. Aliev, N.B. Brandt, V.V. Kozyr'kov, V.V. Moschalkov, R.V. Skolozdra, Yu. V. Stadnyk, and V.K. Pecharskii, Pis'ma Zh. Eksp. Teor. Fiz. **45**, 535 (1987) [JETP Lett. **45**, 535 (1987)]; F.G. Aliev, N.B. Brandt, V.V. Moshchalkov, V.V. Kozyr'kov, R.V. Skolozdra, and A.I. Belogorkhov, Z. Phys. B: Condens. Matter **75**, 167 (1989).

[79] F.G. Aliev, A.I. Belogorkhov, N.B. Brandt, V.V. Kozyr'kov, R.V. Skolozdra, and Yu.V. Stadnyk, Pis'ma Zh. Eksp. Teor. Fiz. **47**, 151 (1987) [JETP Lett. **47**, 184 (1987)]; F.G. Aliev, V.V. Kozyr'kov, V.V. Moshchalkov, R.V. Skolozdra, and K. Durczewski, Z. Phys. B: Condens. Matter **80**, 353 (1990); F.G. Aliev, Physica B **171**, 199 (1991).

[80] S.J. Poon, T.M. Tritt, Y. Xia, S. Bhattacharya, V. Ponnambalam, A.L. Pope, R.T. Littleton, and V.M. Browning, in *Thermoelectric Materials-New Directions and Approaches*, edited by T.M. Tritt, M.G. Kanatzidis, H.B. Lyon, Jr., and G.D. Mahan, MRS Symposium Proceedings No. **478** (Materials Research Society, Pittsburgh, 1997).

[81] C. Uher, J. Yang, S. Hu, D.T. Morelli, and G.P. Meisner, Phys. Rev. B **59**, 8615 (1999).

[82] Y. Xia, V. Ponnambalam, S. Bhattacharya, A.L. Pope, S.J. Poon, and T.M. Tritt, J. Phys.: Condens. Matter **13**, 77 (2001); S.J. Poon, Semiconduct. Semimet. **70**, 37 (2001).

[83] H. Hohl, A.P. Ramirez, C. Goldmann, G. Ernst, B. Wolfing, and E. Bucher, J. Phys: Condens. Matter **11**, 1697 (1999).

[84] T.T.M. Palstra, G.J. Nieuwenhuys, R.F.M. Vlastuin, J. van ben Berg, J.A. Mydosh, and K.H.J. Buschow, J. Magn. Magn. Mat. **67** 331 (1987); T.T.M. Palstra, G.J. Nieuwenhuys, J.A. Mydosh, and K.H.J. Buschow, *ibid.* **54-57**, 549 (1986); T.T.M. Palstra, G.J. Nieuwenhuys, R.F.M. Vlastuin, J.A. Mydosh, and K.H.J. Buschow, J. Appl. Phys. **63**, 4279 (1988).

[85] S. Kilibarda-Dalafave, H.K. Ng, T. Yuen, C.L. Lin, J.E. Crow, and D.B. Tanner, Phys. Rev. B **48**, 297 (1993).

[86] A. Johannis, C.R. Hebd. Seances Acad. Sci. **113**, 79 (1891); E. Zintl, J. Goubeau, W. Dullenkopf, Z. Phys. Chem. Abt. A **1**, 154 (1931); F. Laves, Naturwissenschaften **29**, 244 (1941).

[87] J.D. Corbett, Chem. Rev. **85**, 383 (1985).

[88] A disphenoid is a combinatorial polyhedron which has equivalent faces and vertices with opposite edges which are congruent. This is different from the distorted tetrahedra also discussed. See H.S.M. Coxeter *Regular Polytopes* (Pitman, New York, 1948).

[89] D. Young, K. Mastronardi, P. Khalifah, C-C Wang, R.J. Cava, and A.P. Ramirez, Appl. Phys. Lett. **74**, 3999 (1999).

[90] T. Takabatake, S-I Miyata, H. Fujii, Y. Aoki, T. Suzuki, T. Fujita, J. Sakurai, and T. Hiraoka, J. Phys. Soc. Japan **59**, 4412 (1990).

[91] Z. Fisk, P.C. Canfield, J.D. Thompson, and M.F. Hundley, J. Alloys Comp. **181**, 369 (1992).

[92] M. Kasaya, K. Katoh, and K. Takegahara, Sol. State Comm. **78**, 797 (1991); K. Takegahara, H. Harima, Y. Kaneta, and A. Yansese, J. Phys. Soc. Japan **62**, 2103 (1993).

[93] R.V. Skolozdra, P.S. Salamakha, A.L. Ganzyuk, and O.I. Bodak, Inorg. Mater. **29**, 26 (1993).

[94] M. Wang, R. McDonald, and A. Mar, Inorg. Chem. **38**, 3435 (1999).

[95] C.D.W. Jones, K.A. Regan, and F.J. Disalvo, Phys. Rev. B **58**, 16057 (1998).

[96] Z. Jingtai, S. Minghu, Z. Shankang, H. Zhongle, M. Jinxiao, and M. Shaoyu, J. Rare Earths **17**, 228 (1999).

[97] D.R. Salahub in *Ab Initio Methods In Quantum Chemistry II*, edited by K.P. Lawley (Wiley, New York, 1987), p. 447; R.G. Parr and W. Yang, *Density-Functional Theory of Atoms and Molecules* (Oxford University Press, New York, 1989).

[98] D.E. Bode, Phys. Thin Films **3**, 275 (1966).

[99] I. Melngailis and T.C. Harman in *Semiconductors and Semimetals* Vol. **5** edited by R.K. Willardson and A.C. Beer (Academic Press, New York, 1970), p. 111.

[100] T.C. Harman, A.R. Calawa, I. Melngailis, and J.O. Dimmock, Appl. Phys. Lett. **14**, 333 (1969).

[101] R. Dalven in *Solid State Physics*, edited by H. Ehrenreich, F. Seitz, and D. Turnbull, Vol. **28** (Academic Press, Orlando, 1973), p. 179.

[102] D.L. Mitchell and R.F. Wallis, Phys. Rev **151**, 581 (1966).

[103] L.E. Johnson, J.B. Conklin, Jr., and G.W. Pratt, Jr. Phys. Rev. Lett. **11**, 538 (1963); J.B. Conklin, Jr., L.E. Johnson, and G.W. Pratt, Phys. Rev. **137**, A1282 (1965).

[104] P.T. Bailey, Phys. Rev. **170**, 723 (1968).

[105] S. Rabii, Phys. Rev. **167**, 801 (1968); S. Rabii, Phys. Rev. **173**, 918 (1968).

[106] D.D. Buss and N.J. Parada, Phys. Rev. B **1**, 2692 (1970); N.J. Parada, Phys. Rev. B **3**, 2042 (1971).

[107] H. Overhof and U. Rossler, Phys. Status Solidi **37**, 691 (1970).

[108] F. Herman, R.L. Kortum, I.B. Ortenburger, and J.P. Van Dyke, J. Phys. (Paris) **29**, c4-62 (1968).

[109] G. Martinez, M. Schulter, and M.L. Cohen, Phys. Rev. B **11**, 651 (1975); G. Martinez, M. Schulter, and M.L. Cohen, *ibid.* **11**, 660 (1975).

[110] Y.W. Tung and M.L. Cohen, Phys. Rev. **180**, 823 (1969).

[111] P.J. Lin and K. Kleinman, Solid State Commun. **8**, 569 (1970).

[112] R.L. Bernick, L. Kleinman, Solid State Commun. **8**, 569 (1970).

[113] S.E. Kohn, P.Y. Yu, Y. Petroff, Y.R. Shen, Y. Tsang, and M.L. Cohen, Phys. Rev. B **8**, 1477 (1973).

[114] K.M. Rabe and J.D. Joannopoulos, Phys. Rev. B **32**, 2302 (1985).

[115] D. Agassi and J.B. Restorff, J. Phys.: Condens. Matter **6**, 1497 (1994); D. Agassi and J.B. Restorff, J. Phys.: Condens. Matter **6**, 4673 (1994).

[116] J. A. Valdivia and G.E. Barberis, J. Phys. Chem. Solids **56**, 1141 (1995).

[117] A. Delin, P. Ravindran, O. Eriksson, and J.M. Wills, Int. J. Quant. Chem. **69**, 349 (1998).

[118] A. Santoni, G. Paolucci, G. Santoro, K.C. Prince, and N.E. Christensen, J. Phys.: Condens. Matter **4**, 6759 (1992).

[119] G. Nimitz and B. Schlicht, *Narrow-Gap Semiconductors* (Springer-Verlag, New York, 1985), and references therein.

[120] KALEIDAGRAPH (Synergy Software, Inc., Reading, PA, 1999).

[121] H. Yokoi, S. Takeyama, N. Miura, and G. Bauer, Phys. Rev. B **44**, 6519 (1991).

[122] D.L. Mitchell, E.D. Palik, and J.N. Zemel in *Proceedings of the International Conference on Physics of Semiconductors* (Dunod Cie, Paris, 1964).

[123] H.J. Goldsmid, *Thermoelectric Refrigeration* (Plenum, New York, 1964); A.F. Ioffe, *Semiconductor Thermoelements and Thermoelectric Cooling* (Infosearch, London, 1957).

[124] G.A. Thomas, D.H. Rapke, R.B. Van Dover, L.F. Mattheis, W.A. Surden, L.F. Schneemaper, and J.V. Waszczak, Phys. Rev. B **46**, 1553 (1992).

[125] P.M. Lee and L. Pincherlee, Proc. Phys. Soc. London **81**, 461 (1963).

[126] F. Borghese, and E. Donato, Nuovo Cimento Soc. Ital. Fis. B **53**, 283 (1968).

[127] Shin-ichi Katsuki, J. Phys. Soc. Japan **26**, 58 (1969).

[128] R. Togei and G.R. Miller, J. Phys. Chem. Solids suppl. **32**, 349 (1971).

[129] E.V. Oleshhko and V.N. Koryshin, Fiz. Tverd. Tela (Leningrad) **27**, 2856 (1985) [Sov. Phys. Solid State **27**, 1723 (1985)].

[130] S.J. Youn and A.J. Freeman, Phys. Rev. B **63**, 5112 (2001).

[131] H. Kohler, Phys. Status Solidi B **73**, 95 (1976).

[132] B. Schroeder, A. Von Middlendorff, H. Kohler, and G. Landwehr, Phys. Status Solidi B **59**, 561 (1973).

[133] H. Kohler, Phys. Status Solidi B **74**, 591 (1976).

[134] S. Aliev, Sh. S. Ismailov, and I.G. Tagiev, Fiz. Tverd. Tela (St. Petersburg) **37**, 2851 (1995) [Phys. Solid State **37**, 1573 (1995)].

[135] L. Hedin and B.I. Lundqvist, J. Phys. C **4**, 2064 (1971).

[136] P. Pecheur and G. Toussaint, Phys. Lett. A **135**, 223 (1989).

[137] V.A. Davidenko, J. Phys. (USSR) **4**, 170 (1941); E. Mooser and W.B. Pearson, Phys. Rev. **101**, 492 (1956); J. Black, E.M. Conwell, L. Seigle, and C.W. Spencer, J. Phys. Chem. Solids **2**, 240 (1957); P.P. Konorov, Zh. Tekh. Fiz. **26**, 394 (1956).

[138] H. Kohler, Phys. Stat. Sol. B **58**, 91 (1973); H. Kohler and J. Hartmann, Phys. Stat. Sol. B **63**, 171 (1974).

[139] P. Larson, V.A. Greanya, W.C. Tonjes, R. Liu, S.D. Mahanti, and C.G. Olson, submitted to Phys. Rev. B.

[140] J. Olivier-Fourcade, P-E Lippens, J-C Jumas, M Womes, I. Lefebvre, and M. Lannoo, Eur. J. Solid State and Inorg. Chem. **30**, 139 (1993).

[141] R.S. Erofeev and E.I. Shcherbina, Inorg. Mater. **18**, 1546 (1982).

[142] B. Chen, C. Uher, L. Iordanidis, and M.G. Kanatzidis, Chem. Mat. **9**, 1655 (1997).

[143] J.J. Loferskic, Proceedings of the Workshop on Photovoltaic Conversion of Solar Energy for Terrestrial Application, sponsored by the National Science Foundation, USA **1**, 27 (1973); M. Schoijet, Sol. Ener. Mater. **1**, 43 (1979).

[144] H. Mizoguchi, H. Hosono, N. Ueda, and H. Kawazoe, J. Appl. Phys. **78**, 1378 (1995); J. Lukose and B. Pradeep, Sol. State Commun. **78**, 535 (1991).

[145] S. Hufner, *Photoelectron Spectroscopy* (Springer, New York, 1995).

[146] V.A. Greanya, W.C. Tonjes, R. Liu, C.G. Olson, D-Y Chung, and M.G. Kanatzidis, Phys. Rev. B **62**, 16425 (2000).

[147] V.A. Greanya, W.C. Tonjes, R. Liu, C.G. Olson, D-Y Chung, and M.G. Kanatzidis, submitted to Phys. Rev. B.

[148] T.P. Debies and J.W. Rabalais, Chem. Phys. **20**, 277 (1977).

[149] Y. Ueda, A. Furtuta, H. Okuda, M. Nakatake, H. Sato, H. Namatame, and M. Taniguchi, J. Electron Spectroscopy Sp. Iss. **103**, 677 (1999).

[150] V.B. Nascimento, V.E. de Carvalho, R. Paniago, E.A. Soares, L.O. Ladeira, and H.D. Pfannes, J. Electron Spectroscopy Sp. Iss. **104**, 99 (1999).

[151] G. Nolas, J.L. Cohn, G. Slack, and S.B. Schujman, Appl. Phys. Lett. **73**, 178 (1998).

[152] R.T. Littleton, T.M. Tritt, C.R. Feger, J. Kolis, M.L. Wilson, M. Marone, J. Payne, D. Verebeli, and F. Levy, Appl. Phys. Lett. **73**, 178 (1998).

[153] D-Y Chung, S. Jobic, T. Hogan, C.R. Kannewurf, R. Brec, J. Rouxel, and M.G. Kanatzidis, J. Am. Chem. Soc. **119**, 2505 (1997).

[154] D-Y Chung, T. Hogan, J. Schindler, L. Iordanidis, P. Brazis, C.R. Kannewurf, B. Chen, C. Uher, and M.G. Kanatzidis in *Thermoelectric Materials-New Directions and Approaches*, edited by T.M. Tritt, M.G. Kanatzidis, H.B. Lyon, Jr., and G.D. Mahan, MRS Symposia Proceedings No. **478** (Materials Research Society, Pittsburgh, 1997), p. 333.

[155] M.G. Kanatzidis, T.J. McCarthy, T.A. Tanzer, L. Chen, L. Iordanidis, T. Hogan, C.R. Kannewurf, C. Uher, and B. Chen, Chem. Mater. **8**, 1456 (1996).

[156] R. Brec and S. Jobic (unpublished).

[157] M.G. Kanatzidis, D-Y Chung, L. Iordanidis, K-S Choi, P. Brazis, M. Rocci, T. Hogan, and C.R. Kannewurf, *Thermoelectric Materials-The Next Generation Materials for Small-Scale Refrigeration and Power Generation Applications*, edited by T.M. Tritt, M.G. Kanatzidis, G.D. Mahan, and H.B. Lyon, Jr., MRS

Symposium Proceedings No. **545** (Materials Research Society, Pittsburgh, 1999), p. 233.

[158] P. Brazis, M. Rocci, D-Y Chung, M.G. Kanatzidis, and C.R. Kannewurf, *Thermoelectric Materials-The Next Generation Materials for Small-Scale Refrigeration and Power Generation Applications*, edited by T.M. Tritt, M.G. Kanatzidis, G.D. Mahan, and H.B. Lyon, Jr., MRS Symposium Proceedings No. **545** (Materials Research Society, Pittsburgh, 1999), p. 75.

[159] V.A. Greanya, W.C. Tonjes, R. Liu, C.G. Olson, D-Y Chung, and M.G. Kanatzidis, submitted to Phys. Rev. B.

[160] Z.B. Zhang, J.Y. Ying, and M.S. Dresselhaus, J. Mat. Res. **13**, 1745 (1998).

[161] T.J. McCarthy, S.P. Ngeyi, J.H. Liao, D.C. DeGroot, T. Hogan, C.R. Kannewurf, and M.G. Kanatzidis, Chem. Mater. **5**, 331 (1993).

[162] M.G. Kanatzidis, T.J. McCarthy, T.A. Tanzer, L-H Chen, L. Iordanidis, T. Hogan, C.R. Kannewurf, C. Uher, and B. Chen, Chem. Mater. **8**, 1465 (1996); B. Chen, C. Uher, L. Iordanidis, and M.G. Kanatzidis, *ibid.* **9**, 1655 (1997).

[163] G. Cordier, H. Schafer, and C. Schwidetzky, Rev. Chim. Miner. **22**, 676 (1985).

[164] M. Podgorny, G. Wolfgarten, and J. Pollman, J. Phys. C **19**, L141 (1986).

[165] W. Nakwaski, Physica B **210**, 1 (1995).

MICHIGAN STATE LIBRARIES
3 1293 02200 7367